Study of Radiation Outbursts in the Vicinity of a Supermassive Black Hole - Flare Statistics of Sgr A*

INAUGURAL-DISSERTATION

zur
Erlangung des Doktorgrades
der Mathematisch-Naturwissenschaftlichen Fakultät
der Universität zu Köln

vorgelegt von

Matthias Oliver Subroweit
aus Münster, Deutschland

Köln 2021

Berichterstatter:	Prof. Dr. Andreas Eckart
(Gutachter)

Prof. Dr. Peter Schilke

Tag der mündlichen Prüfung:	11. Februar 2022

Abstract

The center of our Galaxy, the Milky Way, conceals one of the most fascinating astrophysical phenomena of the universe. Located approximately 28000 light-years away from our Solar system in the constellation Sagittarius close to the border to Scorpius, it harbors a bright radio source, Sagittarius A* (Sgr A*). It is nowadays strongly believed, that Sgr A* is the radiative counterpart of a Supermassive Black Hole (SMBH) with a mass of approximately four million solar masses. Astrophysicists have strong evidence that most regular galaxies contain a SMBH in their center. Due to its proximity, Sgr A* provides us with an unique opportunity to study such an object with the highest obtainable resolution. Investigating Sgr A* may thus not only help us to understand the physical processes in the heart of our Galaxy but might also be a blueprint for a more general understanding of galactic nuclei.

Sgr A* has been first detected as a steady radio source. Ongoing observations at different wavebands with increasing resolution and sensitivity have revealed that on top of the steady, so-called quiescent emission, Sgr A* shows radiation outbursts, also referred to as flares, across the entire frequency regime. It has been found that these flares must have their origin in the innermost accretion flow onto Sgr A*. Therefore, their investigation and understanding might be crucial to shed light on the physical conditions in the direct vicinity of a SMBH.

The concrete physical mechanisms in the accretion flow onto Sgr A* giving rise to the flares are not yet fully understood. Although most models include some form of synchrotron emission to explain the occurring flares from the radio to the NIR regime, the mechanisms behind X-ray flares are highly disputed. Mainly two concurrent models are currently debated: high energy synchrotron, or synchrotron self-Compton (SSC) emission. Both possible explanations differ significantly in terms of the predicted electron energies and plasma densities. In this thesis I present three papers (two of them already published, the last one to be submitted) which statistically elaborate on

the putative emission mechanism.

In the first paper, I present both submillimeter (submm) data obtained with the LArge BOlometer CAmera (LABOCA), which was mounted at the Atacama Pathfinder EXperiment (APEX) telescope, and radio data from the Australia Telescope Compact Array (ATCA). I analyze the flux density distribution of these lightcurves and find that both distributions can be described by power-laws with similar scaling indices. An almost identical scaling index has previously been found by another group for the near-infrared (NIR) emission. This strongly suggests that the flaring emission at these three wavebands originate in the very same source regions. That finding is furthermore compatible with a physical model of adiabatically expanding, self-absorbed synchrotron plasmons.

In the second paper, I investigate X-ray data from the Chandra X-ray Observatory (CXO) obtained during the X-ray Visionary Project (XVP) campaign. Here, the analytical challenge is that X-ray lightcurves are subject to instrumental pile-up phenomena and low count rate Poisson statistics. I present a count rate distribution fitting routine, which is based on Approximate Bayesian Computation (ABC). Having developed this fitting routine I am able to describe the X-ray count rate distribution as a power-law with an exponential cutoff and estimate its parameters. Using analytical considerations, I deduce that the X-ray flares are most likely produced by an SSC mechanism.

In the third paper, I again present and analyze APEX/LABOCA submm data. Our workgroup conducted new observations in 2016 and 2017. I compare this data with the already published data from the first paper. I find that the statistical description of both datasets is very similar, i.e., that the flaring mechanism was stationary at least between 2008 and 2017. This is particularly interesting as an object called G2/DSO had its closest approach to Sgr A* in spring 2014. It has been speculated whether this flyby might lead to an increased accretion rate onto Sgr A* and therefore to increased flaring activity. I am able to rule out such an increase at least up to 2017.

Altogether, my statistical analyses reveal, that the observed lightcurves of Sgr A* at different wavebands are fully compatible with the following emission model: adiabatically expanding synchrotron blobs are the origin of the observed radio to NIR flares. The X-ray flares are most probably produced by an SSC mechanism.

Zusammenfassung

Das Zentrum unserer Galaxie, der Milchstraße, birgt eines der faszinierendsten astrophysikalischen Phänomene des Universums. Etwa 28000 Lichtjahre von unserem Sonnensystem entfernt, im Sternbild Schütze an der Grenze zum Skorpion liegend, beinhaltet es eine helle Radioquelle, Sagittarius A* (Sgr A*). Es wird heutzutage stark davon ausgegangen, dass Sgr A* der radiative Gegenpart eines supermassiven Schwarzen Loches (englisch: Supermassive Black Hole, SMBH) mit einer Masse von ungefähr vier Millionen Sonnenmassen ist. Astrophysiker haben starke Belege dafür, dass die meisten regulären Galaxien ein SMBH in ihrem Zentrum besitzen. Aufgrund seiner Nähe bietet uns Sgr A* die einzigartige Gelegenheit, ein solches Objekt mit der höchsten erreichbaren Auflösung zu untersuchen. Die Erforschung von Sgr A* kann daher nicht nur dabei helfen, die physikalischen Prozesse im Herzen unserer Galaxie zu verstehen, sondern könnte auch eine Blaupause für ein allgemeineres Verständnis von galaktischen Kernen liefern.

Sgr A* wurde zunächst als stetige Radioquelle entdeckt. Fortwährende Beobachtungen in verschiedenen Wellenbändern mit zunehmender Auflösung und Empfindlichkeit haben gezeigt, dass Sgr A* neben der stetigen, sogenannten Ruheemission auch Strahlungsausbrüche, die auch als Flares bezeichnet werden, über den gesamten Frequenzbereich zeigt. Es wurde festgestellt, dass diese Flares ihren Ursprung im innersten Akkretionsfluss auf Sgr A* haben müssen. Daher könnte ihre Untersuchung und ihr Verständnis entscheidend dafür sein, die physikalischen Bedingungen in der unmittelbaren Umgebung eines SMBH zu erhellen.

Die konkreten physikalischen Mechanismen im Akkretionsfluss auf Sgr A*, welche die Flares hervorrufen, sind bisher nicht vollständig verstanden. Auch wenn die meisten Modelle eine Form von Synchrotronstrahlung beinhalten um die auftretenden Flares vom Radio- bis zum NIR-Bereich zu erklären, sind die Mechanismen hinter der Röntgenstrahlung äußerst umstritten. Hauptsächlich zwei konkurrierende Modelle werden

derzeit debattiert: hochenergetische Synchrotron-, oder Synchrotron-Selbst-Compton-Emission (SSC). Beide Erklärungsversuche unterscheiden sich signifikant hinsichtlich der prognostizierten Elektronenenergien und Plasmadichten. In dieser Arbeit stelle ich drei Artikel vor (zwei davon bereits veröffentlicht, der letzte muss noch eingereicht werden), welche die vermuteten Emissionsmechanismen statistisch untersuchen.

Im ersten Artikel stelle ich sowohl Daten aus dem Submillimeter (submm) vor, die mit der LArge BOlometer CAmera (LABOCA) gewonnen wurden, das am Atacama Pathfinder EXperiment (APEX) montiert war, als auch Radiodaten vom Australia Telescope Compact Array (ATCA). Ich analysiere die Flussdichteverteilung dieser Lichtkurven und stelle fest, dass beide Verteilungen durch ein Potenzgesetz mit einem ähnlichen Skalierungsindex beschrieben werden können. Ein fast identischer Skalierungsindex ist zuvor von einer anderen Gruppe für die Emission im Nahinfrarot (NIR) gefunden worden. Dies deutet stark darauf hin, dass die Flareemissionen in diesen drei Wellenbändern aus denselben Quellregionen stammen. Dieser Befund ist zudem mit einem physikalischen Modell adiabatisch expandierender, selbstabsorbierter Synchrotronplasmen vereinbar.

Im zweiten Artikel untersuche ich Röntgendaten des Chandra-Röntgenobservatoriums (CXO), die während der X-ray Visionary Project (XVP) Kampagne gewonnen wurden. Hier besteht die analytische Herausforderung darin, dass die Röntgenlichtkurven instrumentellen Pile-up-Phänomenen und Poisson-Statistiken mit niedriger Zählrate unterliegen. Ich präsentiere eine Routine zum Fitten der Zählratenverteilung, die auf Approximate Bayesian Computation (ABC) basiert. Nach der Entwicklung dieser Anpassungsroutine kann ich die Zählratenverteilung der Röntgenstrahlung als Potenzgesetz mit exponentiellem Abfall beschreiben und seine Parameter abschätzen. Mit Hilfe analytischer Überlegungen komme ich zu dem Schluss, dass die Röntgenflares höchstwahrscheinlich durch einen SSC-Mechanismus erzeugt werden.

Im dritten Artikel präsentiere und analysiere ich erneut APEX/LABOCA-submm-Daten. Unsere Arbeitsgruppe führte in den Jahren 2016 und 2017 neue Beobachtungen durch. Ich vergleiche diese Daten mit den bereits veröffentlichten Daten aus dem ersten Artikel. Dabei stelle ich fest, dass die statistische Beschreibung beider Datensätze sehr ähnlich ist, d.h., dass der Flaremechanismus zumindest zwischen 2008 und 2017 stationär war. Dies ist besonders interessant, da ein Objekt namens G2/DSO seine naheste Annäherung an Sgr A* im Frühjahr 2014 hatte. Es ist spekuliert worden, ob dieser Vorbeiflug zu einer erhöhten Akkretionsrate auf Sgr A* und damit zu einer gesteigerten Flareaktivität führen könnte. Ich kann eine solche Zunahme zumindest bis 2017 ausschließen.

Insgesamt ergeben meine statistischen Analysen, dass die beobachteten Lichtkurven von Sgr A* in verschiedenen Wellenbändern vollständig mit dem folgenden Model kompatibel sind: adiabatisch expandierende Synchrotronblobs sind die Quelle der beobachteten Flares vom Radio bis zum NIR. X-ray flares werden höchstwahrscheinlich von einem SSC-Mechanismus generiert.

Contents

1

Astrophysical Background

1.1 The Milky Way and its Place in the Universe

One of the most prominent astronomical objects in the nightly sky is the Milky Way (MW). In every culture one finds tales that tell about the bright band of light which stretches across the firmament and can be observed during dark and cloudless nights. For the Inca people of the Andes that band was the *Mayu*, the celestial river, which is connected to the Earth and is the wellspring of all water on Earth. The Aboriginal Australian Euahlayi people saw the *Gawarrgay*, the figure of an emu in the dark clouds covering the MW, whose change of shape and position during the seasons was supposed to be closely related to terrestrial events (Fuller et al., 2014). In Ancient Greek mythology it was the goddess Hera who created the MW by having spilled milk over the sky while breastfeeding Heracles. The word *galaxy* actually stems from the old Greek word *galaxías* (γαλαξίας) which is derived from *gala* (γάλα), meaning "milk". People from Saxony called the MW *Iring's Way*, according to their god of light and protection. The 11th century Arabic author Ibn Raḥīq described the MW in his astronomical work as the "mother of stars" and "split in the heavens" (شرج السماء, Eckart 2019). In the more than 2500 years old *Shijing*, the Book of Songs, a story of "The Cowherd and the Weaver Girl" is told. It is a tale about the forbidden love between Zhinü and Niulang, which were dispelled to opposite sides of the heaven, separated by the "Silvery River" (銀河), the MW. Only once per year the Emperor of Heaven let the lovers meet, on the seventh day of the seventh month.

The modern, scientific "tale" about the MW starts in 1920, with the "great Debate" between the astronomers Harlow Shapley and Heber Curtis. They discussed whether the MW encompasses the entirety of the cosmos (Shapley) or if there are objects outside the MW (Curtis) and our Galaxy is just one among other galaxies. Shortly after that debate took place, in the mid-1920s, Edwin Hubble was able to show that some "spiral nebulae" were too distant to be part of the MW. Up to 1929, he was able to identify at least 46 distant galaxies (Hubble, 1929) and to determine their distances and redshifts. Hubble also discovered that the redshift for far away galaxies increases with their increasing distance. This, and other theoretical considerations let astronomers develop the idea of an expanding universe that began in a singularity event, the Big Bang (BB, Lemaître 1931). At the latest, the discovery of the Cosmic Background Radiation (CMB) by Penzias and Wilson (1965) established the BB theory and astronomers were able to estimate the age and therefore the dimensions of the universe.

According to human imagination, these dimensions are inconceivable. The time since the BB and thus the age of the universe has been estimated to be about 13.8 billion years (Planck Collaboration et al., 2016). Since then, spacetime has expanded, so that the observable universe reached a radius of 45.7 billion light-years. The universe is also a very empty space. Its average density is about $9 \times 10^{-27}\,\mathrm{kg\,m^{-3}}$ (Spergel et al., 2007) which corresponds to approximately six hydrogen atoms per cubic meter[1]. However, matter is not uniformly distributed in space (that would make the universe a very boring place) but clumped in structures. An elementary building block of these structures are galaxies, which are ensembles of stars, planets, gas clouds, dust and dark matter, gravitationally bound together. Typical galaxies contain about 10^9 to $10^{13}\,M_\odot$ of matter and have diameters between 3000 and 300000 light-years. The visible universe contains about 200 billion galaxies, though recent observations have suggested that this number might be underestimated by a factor of 10 (Conselice et al., 2016). Galaxies are also not distributed homogeneously in space but form honeycomb- or foam-like superstructures, i.e., they form clusters and filaments around almost empty regions, so-called voids. Our Galaxy, the MW, is part of the Laniakea supercluster (Tully et al., 2014). It contains about 10^5 galaxies ($\sim 10^{17}\,M_\odot$) and has an expansion of about 500 million light-years. Within the Laniakae supercluster, several substructures can be observed, one of which is the Virgo Supercluster, also called the Local Supercluster (LC, Chon et al. 2015) with a mass of $\sim 10^{15}\,M_\odot$ and a diameter of about 100 million light-years. The LC, in turn, can also be subdivided into smaller galaxy groups. One of these groups is the Local Group (LG). The LG has a diameter of about 10 million light-years, a total mass of $\sim 4 \times 10^{12}\,M_\odot$ (González et al., 2014) and harbors more than 50 galaxies. The two biggest galaxies inside the LG are the Andromeda galaxy (M31) with a mass of $\sim 1.5 \times 10^{12}\,M_\odot$ and the MW with a similar mass (McMillan, 2017). Both, the MW and M31, have a diameter of about 200000 light-years and are approximately 2.5×10^6 light-years apart (Ribas et al., 2005). The Triangulum galaxy (M33) is the third largest galaxy of the LG, whereby its mass is already more than one order of magnitude smaller than M31 or the MW ($\sim 5 \times 10^{10}\,M_\odot$). The MW builds a substructure of the LG: the Milky Way subgroup. It consists of the MW itself and several smaller orbiting satellite galaxies. Two of the

---

[1]In fact, the ratio between dark matter and visible matter is roughly six to one. That means, that the average density of protons per cubic meter is even less.

most prominent satellite galaxies are the Large and the Small Magellanic Cloud (LMC and SMC). The LMC has a mass of approximately $1 \times 10^{10}\,M_\odot$, a diameter of 25000 light-years and a distance of 160000 light-years from the MW, the corresponding values for the SMC are $2 \times 10^9\,M_\odot$, 15000 light-years and 210000 light-years. The closest orbiter of the MW is the dwarf galaxy Canis Major (CMa Dwarf). It has a distance from the center of the Milky Way of 42000 light-years. Interestingly, it is only 25000 light-years away from our solar system which is a bit less than the distance from our Solar system to the center of the Milky way.

The MW itself is a Hubble type SBc galaxy with a diameter of about 50 kpc. SBc galaxies are spirals with S-shaped, loosely wound arms and a bar-shaped central stellar structure instead of a spherical core. It is believed that the MW contains at least 4 major spiral arms: the Perseus Arm, the Norma Arm, the Scutum–Centaurus Arm and the Carina-Sagittarius Arm. Several minor spiral arms have also been observed, one of them is the Orion–Cygnus Arm. Our Solar system is part of the Orion-Cygnus Arm and lies on its inner rim, facing toward the center of the Galaxy at a distance of about 8.3 kpc (Gillessen et al., 2009). The entire Galactic plane is enshrouded by a sparse stellar halo of about $10^9\,M_\odot$ which extends up to 100 kpc (Cooper et al., 2010). As only about 10% of the total virial mass of the MW can be attributed to luminous matter, it is nowadays believed that the MW is also surrounded by a dark matter halo. Its volume density has been estimated to be around $0.009\,M_\odot/\mathrm{pc}^{-3}$ (Kafle et al., 2014). The Galactic plane consists of two layers: the thin disk with a scale height of about 350 pc and a young stellar population and the thick disk with a scale height of about 1 kpc containing predominantly older stars. The scale height of the thin disk increases toward the center where it finally dissolves in the central bulge with a scale height of 3 kpc. For SB-type galaxies as the MW the central bulge is not spheroidal but bar-shaped. The inner kpc of the bulge is dominated by a stellar structure called the Nuclear Bulge (not to be confused with the Galactic bulge itself) with a stellar mass of approximately $10^9\,M_\odot$ (Launhardt et al., 2002). It consists of a disk-like structure, the Nuclear Stellar Disk, with a radius of ~ 230 pc and a scale height of ~ 45 pc, and a spherical inner structure of a few pc in diameter, the so-called Nuclear Star Cluster (NSC). The exact dimensions and definition of the NSC is not unambiguous (see Neumayer et al., 2020 for a general review on galactic NSCs). In the context of the MW one can define the NSC as the region of up to 15 pc around Sgr A*, where the number density of bright stars down to ~ 0.5 pc can be well described by a power-law of the form $\rho(r) \propto r^{-2}$. The power-law index of ~ 2 suggests a thermalized, i.e., old population of stars. At smaller radii, i.e. $r < 1$ pc or 25$''$, where the gravitational sphere of influence of Sgr A* becomes relevant, the power-law breaks and exhibits a flatter distribution (Fritz et al., 2016). Within this sphere the enclosed stellar mass is approximately as big as the mass of the central black hole, i.e., of the order of $10^6\,M_\odot$. The stars in the innermost arcsec of this region are called S-cluster stars. Depending on their brightness, the orbital movement around Sgr A* can nowadays be traced. This will be further discussed in the next section.
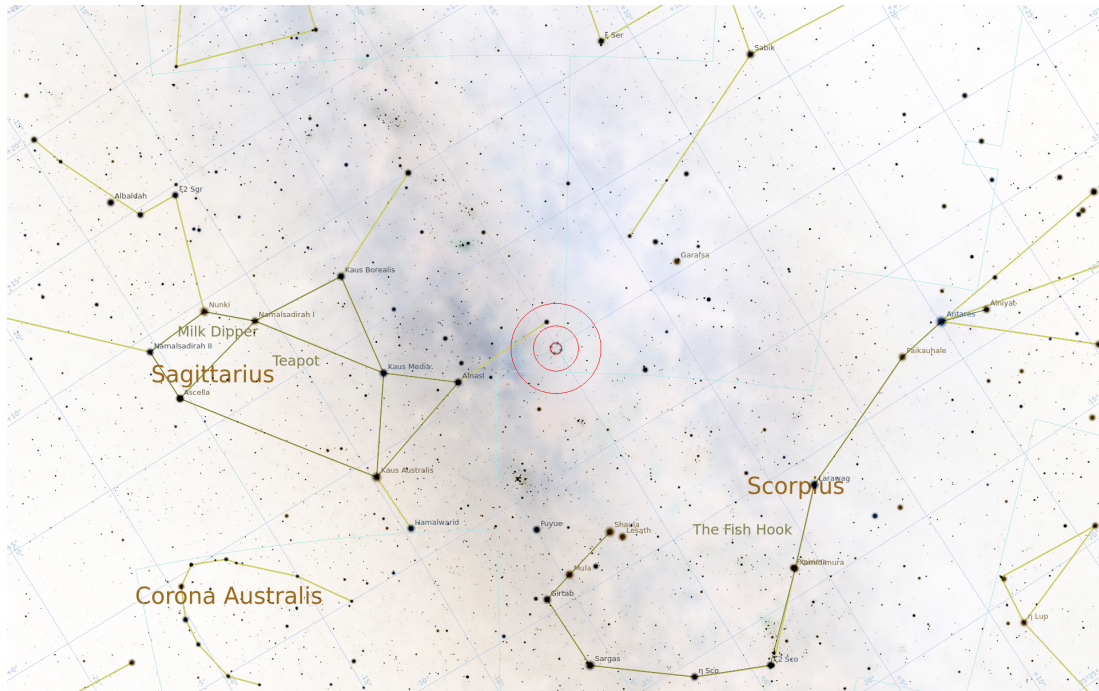
Figure 1.1: *Simulated view on the Galactic center (GC) with the constellations of Sagittarius, Scorpius and Corona Australis as seen from Earth with a field of view ~ 35 deg using inverse colors. The GC is marked with concentric red circles at the center of the map. The image was created (own work) with the software* `stellarium` *(Zotti et al., 2021).*

1.2   The Galactic Center and its Supermassive Black Hole

From the Earth's perspective, the barycenter of the MW lies close to the constellation Sagittarius (see Fig. 1.1). In this direction the "band" of the Galaxy appears to be brightest and densest. The observational challenge when monitoring the Galactic Center (GC) is the band of dust in the Galactic plane, almost completely blocking optical and ultraviolet (UV) radiation from that region and a dense population of stars which confuses observation especially in the infrared (IR). Radio, IR and X-ray emission can pass through the dust layers so that the GC is observable from our position in the Galaxy. The atmosphere of the Earth in turn, blocks X-ray radiation entirely and attenuates IR emission significantly. Radio waves with frequencies between 15 and 100 GHz pass through the atmosphere with almost no attenuation. This frequency band is also called the "radio window". Thus, ground-based radio, high altitude IR and space-based IR and X-ray telescopes are best suited to observe the GC.

The radiative counterpart of the dynamical center of the MW was first spotted by Karl Jansky, one of the pioneers of early radio astronomy, in 1932. By that time, he was an employee at Bell Telephone Laboratories and tried to find out the origin of interference which caused problems in the transatlantic radio communication at 20 GHz. He build a rotatable radio dish (Jansky, 1932) and found that there is a strong radio emitter outside of the Solar system in the direction of the GC (Jansky, 1935). This finding was later reproduced, e.g., by Reber (1940), Bolton and Westfold (1950) and Piddington

and Minnett (1951). Early detailed maps of the Galactic radio emission at different radio frequencies with a clearly identifiable bright structure, the so called Sagittarius A complex, or in short Sgr A, in the direction of the GC can be found in Burke (1965). Shortly after that, the first IR maps of the GC were compiled (Becklin and Neugebauer, 1968; Rieke and Low, 1973), also yielding strong infrared emission from the direction of Sgr A. Finally, Balick and Brown (1974) observed the very center of Sgr A with the National Radio Astronomy Observatory (NRAO) radio interferometer at 3.7 and 11 cm. They report on a "bright", "unresolved", i.e., $\theta \leq 0.1''$ structure at the very center of Sgr A, "unique in the Galaxy" and conclude:

> "The unusual nature of the sub-arcsecond structure and its positional coincidence with the inner 1-pc core of the galactic nucleus strongly suggests that this structure is physically associated with the galactic center (in fact, defines the galactic center)."

Because of its unique- and brightness, Brown (1982) later coined the term "Sagittarius A*", or in short, "Sgr A*" as

> "[...]the bright nonthermal radio core of Sgr A (which we hereafter refer to as Sgr A*)."

Before addressing further research on the properties of the point-like radiation source Sgr A* itself, I will first take a step back and briefly discuss its closest environment. Looking in detail at the Sgr A complex, prominent substructures become visible. Two major components can be identified: Sgr A East and Sgr A West. Sgr A East is a non-thermal, 6-9 pc in diameter, shell-like structure and might be a supernova remnant (Ekers et al., 1983; Zhou et al., 2021). However, it is still subject of ongoing observations and theoretical consideration, details of the state of research can be found in Lee et al. (2006) or Zhou et al. (2021). Sgr A West on the other hand is a seemingly spiral-like structure with three arms of ionized gas streams, the so-called minispiral, with Sgr A* close to its center. The term "spiral" is misleading though as it is a 3-dimensional structure which only resembles the spiral-like appearance on the 2-dimensional plane of sky. A detailed analysis of its spatial structure can be found in Zhao et al. (2010). Nevertheless, the three apparent arms are called Northern and Eastern arm and the Western Arc. All components meet in a bar-like structure, located 0.1-0.2 pc south of Sgr A*, and contain in total a mass of approximately 60 $M_\odot$. Along the arms, a mass transport toward the center can be observed. It is estimated to be of the order of 10^{-3} $M_\odot$ yr^{-1} (Lo and Claussen, 1983). The minispiral is surrounded (and probably fed) by a torus-shaped structure, mostly containing gas and dust, the Circum Nuclear Ring (CNR), sometimes also called Circum Nuclear Disk (CND). Depending on the observed wavelength, the CNR has an inner and outer radius between 1.5-2 and 2-5 pc, respectively (Montero-Castaño et al., 2009; Tsuboi et al., 2018). Its total mass is surprisingly uncertain, estimates go from 6×10^2 to 2×10^5 $M_\odot$ (Lau et al., 2013; Smith and Wardle, 2014). The CNR rotates around Sgr A* with a velocity of approximately 100 km s^{-1} and a distance of 2 pc (Guesten et al.,

1987). A multi-waveband image of Sgr A West can be seen in Fig. 1.2.

From the analysis of gas motion in the CNR and the minispiral mass estimates on the enclosed mass could be derived. Wollman et al. (1977) concluded from line emission and assuming orbital motion that the total mass within the central one parsec had to be approximately $4 \times 10^6 M_\odot$. Lacy et al. (1982) estimated the total mass to be about $6 \times 10^6 M_\odot$, where only $3 \times 10^6 M_\odot$ could be attributed to distributed mass, the remaining $3 \times 10^6 M_\odot$ had to be concentrated in a central massive black hole. Similar results were reproduced by follow-up observations of gas motion, e.g., by Serabyn et al. (1988). Herbst et al. (1993) could show that $\sim 4 \times 10^6 M_\odot$ of mass had to be within the central 0.17 pc and that the barycenter coincides with the position of Sgr A*. Nevertheless, gas kinematics is not only affected by gravitation. Therefore, a mass determination of the central object from gas dynamics kept being uncertain. More accurate mass estimates
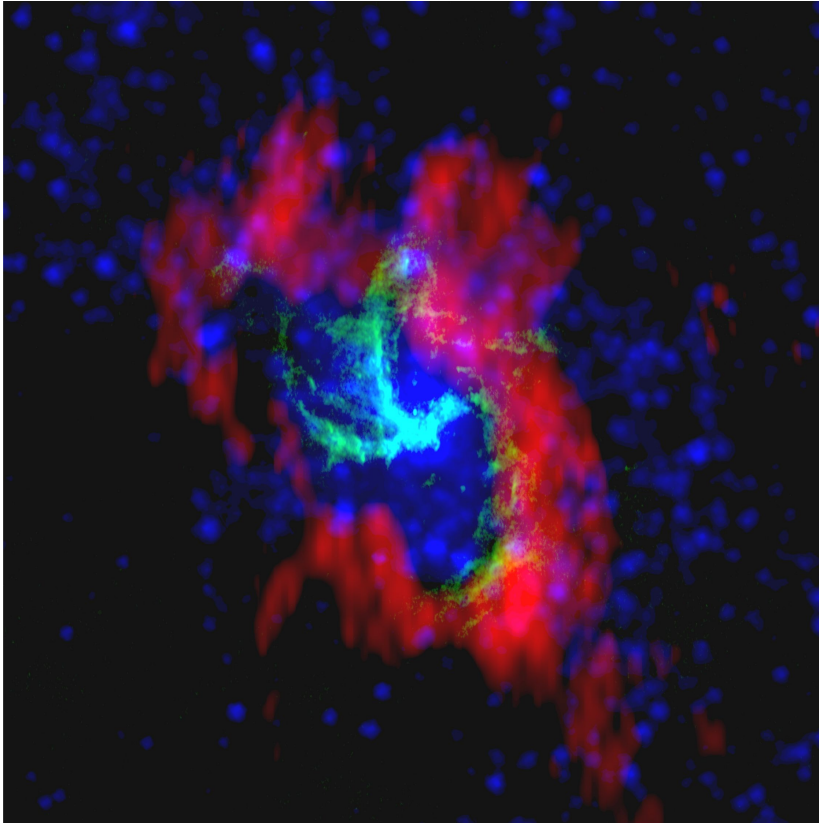

Figure 1.2: *Multi-waveband image of Sagittarius (Sgr) A West with a field of view of 120×120 as and Sgr A* at its very center. Green and red colors show radio data from the Very Large Array (VLA) and the Berkeley-Illinois-Maryland Association (BIMA) telescope, respectively. In blue infrared data from the Spitzer Space Telescope (SST) is depicted. Cold gas from the circum nuclear ring (CNR) as well as hot gas from the minispiral is clearly visible. The blue point-like sources indicate stars orbiting Sgr A*. Image credit: Legacy Astronomical Images, "Stars and Gas Orbiting the Massive Black Hole," NRAO Archives, accessed November 3, 2021, https://www.nrao.edu/archives/items/show/33428.*

can be done by observing stellar dynamics. Measuring the velocity dispersion of two dozen blue supergiants, Krabbe et al. (1995) were able to roughly calculate the central

mass by using the virial theorem. The first conclusive estimates of the barycenter's mass could be obtained by the detection of proper motion of stars orbiting Sgr A* in the innermost few arcseconds, also called the S-cluster (Eckart and Genzel, 1996, 1997; Genzel et al., 1997; Ghez et al., 1998). All papers concluded a central mass of approximately $2.5 \times 10^6 M_\odot$. Finally, several groups were able to first determine parts of, later complete individual orbits of S-cluster stars (Eckart et al., 2002; Schödel et al., 2002; Ghez et al., 2003). Solving the equation of motion yields the central mass. Since then, ongoing observations with increasing astrometric precision have revealed detailed knowledge of the orbits of more than 40 S-cluster stars (Gillessen et al., 2009; Peißker et al., 2020; Ali et al., 2020). A black hole mass of $4.3 \times 10^6 M_\odot$ seems to be the most cited value nowadays (Parsa et al., 2017; Gillessen et al., 2017). Fitting the equations for a two body problem also allows the determination of the distance R_0 between our Solar system and the GC. So far, the most accurate distance estimate has been made by Gravity Collaboration et al. (2019). They determined R_0 with an accuracy of 0.3%, the value to memorize is $R_0 \approx 8.2\,\text{kpc}$.

In the last paragraph of this section I will again return to the radiative source Sgr A* itself. As mentioned earlier, Sgr A* was first detected in the radio regime, observations in other waveband regimes followed such that the steady spectral energy distribution (SED) of Sgr A* was relatively well known in the late 1990s. It can roughly be described as follows: in the radio regime we observe an inverted power-law spectrum with a $S_\nu \propto \nu^{1/3}$, or $\nu^{4/3}$ in the νL_ν display, respectively (Falcke et al., 1998). The spectrum rises up to a peak in the submillimeter (submm), the so called "submm bump" at approximately 350 GHz (Zylka et al., 1995). Here, the flux density S_ν is about 3 Jy, which corresponds to a flux $\nu L_\nu \approx 5 \times 10^{35}$ erg/s. Toward higher frequencies, the SED steeply drops. In the far-infrared (FIR), the upper limits for the flux densities have been reported to be ~ 1.1, ~ 0.6 and ~ 0.8 Jy at 160, 100 and 70 μm, respectively (von Fellenberg et al., 2018). Schödel et al. (2011) have not detected Sgr A* in the mid-infrared (MIR), and therefore give an upper limit of ~ 84 mJy at 8.6 μm. They furthermore report on ~ 4, ~ 5 and ~ 1.5 mJy at 4.8, 3.8 and 2.2 μm, respectively. Faint emission at a few keV ($\sim 2 \times 10^{33}$ ergs/s, Quataert 2002) can be considered as the upper end of the observable SED of Sgr A*. A graphical display of the observed SED and an over-plotted emission model from different electron populations (see Yuan et al. 2003) can be seen in Fig. 1.3. Integrating over the entire SED, Sgr A* shows a remarkable low bolometric luminosity of $L \approx 10^{36}$erg s^{-1} which is just a few hundred times brighter than the Sun. In terms of the Eddington luminosity L_{edd}, the total bolometric luminosity of Sgr A* can be expressed as $L \leq 10^{-8} L_{\text{edd}}$. This luminous faintness can either be explained by very low accretion rates onto Sgr A*, radiative inefficient accretion flows (RIAF) or a combination of both. Modelling the accretion flow onto SMBHs is its own field of research and often requires complex magnetohydrodynamic (MHD) simulations. I would like to refer the interested reader to, e.g., the publications of Yuan and Narayan (2014) or Mościbrodzka et al. (2014) and references therein. The SED, as discussed in this paragraph, describes the steady emission of Sgr A*, i.e., the emission that is always observable. In the next section I will show, that the SED changes from time to time, namely whenever Sgr A* shows radiation outbursts and enters a temporal "active" state. Therefore, the state, which I have described in this section, is called the "quiescent" state and the observed
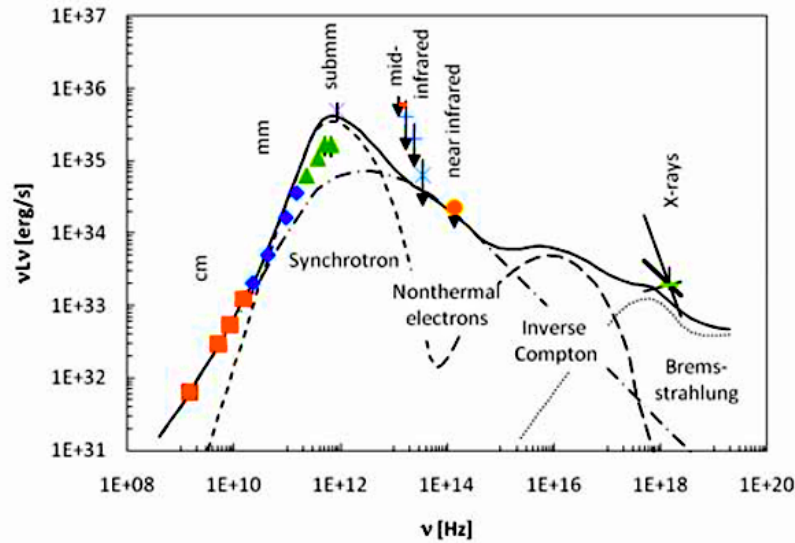
Figure 1.3: *Quiescent spectral energy distribution (SED) of Sagittarius A* (Sgr A*) from the radio to the X-ray regime with data and overplotted model from Genzel et al. (2010) and references therein. The short dashed line shows the emission from thermal synchrotron electrons, the dash-dotted line represents the synchrotron spectrum from non-thermal, power-law distributed electrons. Inverse Compton effects lead to a secondary hump in the optical/ultraviolet (long dashed line). In the X-ray regime thermal bremsstrahlung can be observed (dotted line). Image credit: Genzel et al. (2010)*

radiation "quiescent emission".

1.3   Flares from Sagittarius A*

Shortly after the detection of Sgr A*, Brown and Lo (1982) reported about long term variability of the radio emission. They observed Sgr A* over a period of 3 years (1976-1978) with the Green Bank radio-link Interferometer (GBI) at 2695 and 8085 MHz and detected monthly flux density variations of 25% and 40%, respectively. They interpreted these alterations as "flickering" source size changes of the emitter. Zhao et al. (1989) reported on observations between 4 and 20 cm between 1974 and 1987 and detected magnitude variabilities in the range of 15 to 20%. However, they attributed this variability to interstellar refractive scintillation. In the years 1990 and 1991 they monitored Sgr A* at 1.5, 5, 8.4, 15 and 22.4 GHz (Zhao et al., 1992). At 8.4 GHz and above they reported on significant flux density variations, with increasing magnitude toward higher frequencies. They also stated three clearly identifiable "radio outbursts". Their interpretation of the flux density modulations changed from scintillation to "intrinsic activity". Wright and Backer (1993) report on flux density variations of 0.8 to 2.3 Jy in their 3 mm observations between 1985 and 1990. This is also one of the first papers where the term *flare* is used in the context of Sgr A*. Six years later the term flare for the radiation outbursts of Sgr A* seems to have established, Tsuboi et al. (1999) report on a "Flare of SGR A* at Short Millimeter Wavelengths". It has to be mentioned though, that despite the fact that flares had certainly been observed in the radio regime,

toward the submm and even higher frequencies the existence of intrinsic variability was not clearly confirmed. Calibration problems and measurement uncertainties left the question whether observed flux density variations were real or just instrumental effects. These problems were debated, e.g., in Beckert et al. (1996).

Nevertheless, flares of Sgr A* had been detected successively across the entire wavelength regime: Baganoff et al. (2001) were the first who observed an X-ray flare in the 2-8 keV band with a peak luminosity ~ 40 times brighter as in the quiescent state. Goldwurm et al. (2003) mentioned another X-ray flare, 20-30 times brighter than the steady count rate. The flare detected by Porquet et al. (2003) exceeded the quiescent level by a factor of 160. In the NIR, observations of the galactic center are more difficult due to dust absorption and stellar confusion. The enhanced adaptive optics (AO) technology in the early 2000s finally made it possible to also observe Sgr A* at these frequencies with sufficient accuracy. Genzel et al. (2003) were the first to identify flaring NIR activity. With an AO instrument they observed at least one flare at $1.65\,\mu$m and two flares at $2.16\,\mu$m. The peak fluxes were three times larger than the background level. Using the Keck telescope at $3.8\,\mu$m, Ghez et al. (2004) identified Sgr A* as a "variable point source" with flux density variations between 4 and 17 mJy. The aforementioned papers were just the earliest of a bunch of following papers which all clearly identified Sgr A* as a point-like source with radiation outbursts. The tendency for the wavelength dependency of the flare magnitudes was already recognizable in the aforementioned early publications and was later established (Herrnstein et al., 2004; Miyazaki et al., 2004; Bélanger et al., 2005; Gillessen et al., 2006). From the radio to the X-ray regime the amount of variability steadily increases: in the radio regime one observes flux density variations of the order of 50%, in the submm, infrared and X-ray peak amplitudes with factors of up to 2, 20 and 200, respectively (see, e.g., Fig. 1.4 for a typical X-ray light curve). I want to stress that these numbers are not statistically hardened quantities but just a rule of thumb to get an easy to memorize overview of the occurring magnitudes across the entire observed wavelength regime.
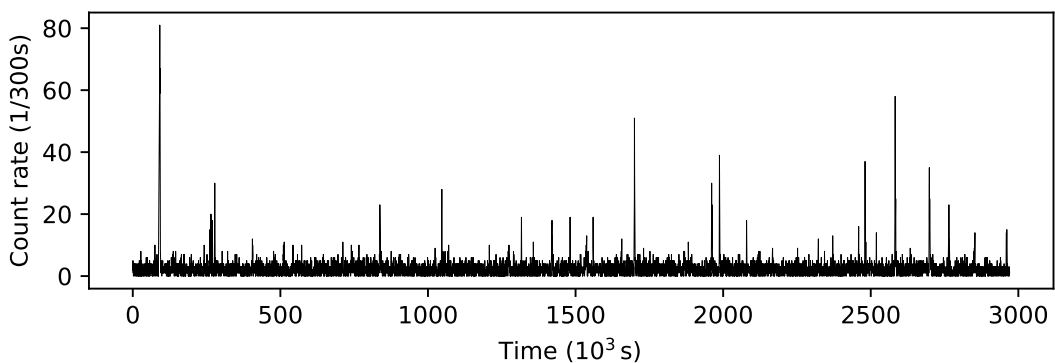

Figure 1.4: *Concatenated X-ray light curve obtained with the Chandra X-ray Visionary Project (XVP) campaign in 2012. Sagittarius A* (Sgr A*) is most of the time in a quiescent state and shows only emission of a few counts per 300 s. From time to time distinct emission outbursts can be observed, exceeding the quiescent emission by almost up to two orders of magnitude.*
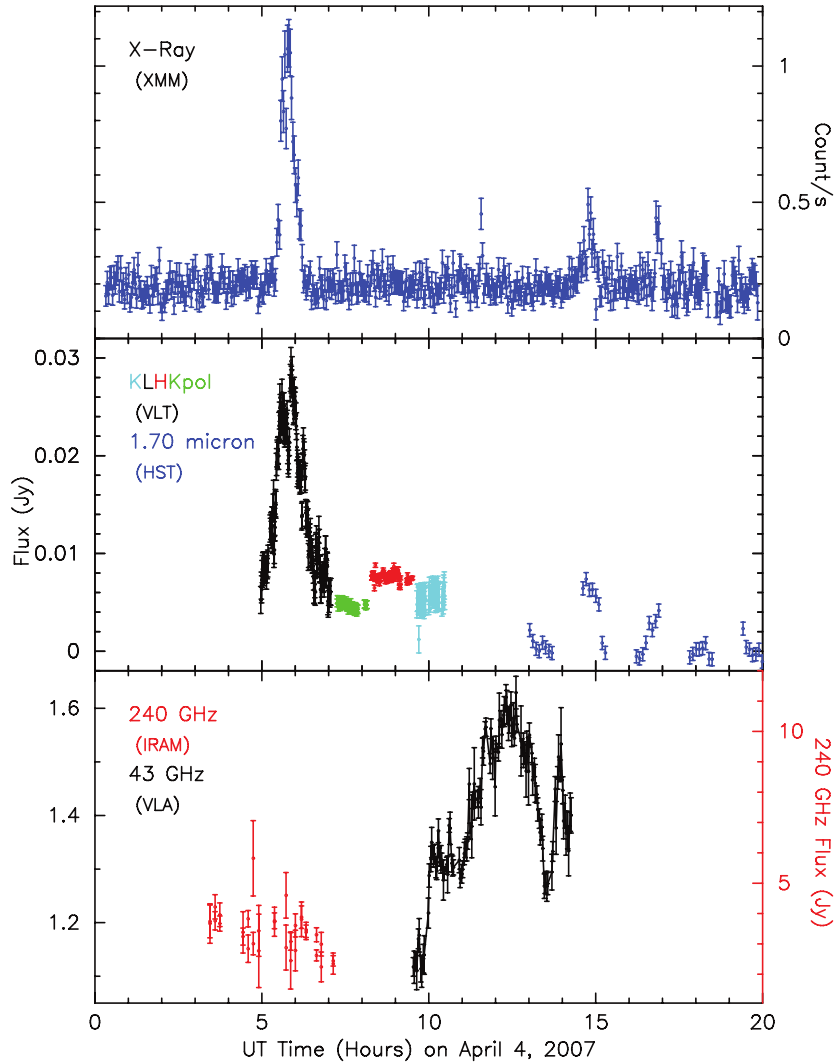
Figure 1.5: *Parallel monitoring of Sagittarius A* (Sgr A*) at different wavebands. The upper panel shows an X-ray light curve, the middle near-infrared (NIR) and the bottom submillimeter and radio observations. The tight temporal correlation between X-ray and NIR flares is obvious, they occur simultaneously. A 43 GHz flare follows with a time delay of several hours. Image credit: Yusef-Zadeh et al. (2009)*

Nowadays there is a consensus that the source regions which give rise to the flares have to originate from very compact regions in the innermost accretion flow around Sgr A*. Light travel arguments strongly suggest compactness of the regions. Do et al. (2019) detected a brightness change of Sgr A* during a flare by a factor of 9 within 2 minutes, which corresponds to ~3 Schwarzschild radii (R_S) for the mass of Sgr A*. From an expanding source model and from typical flare rise times of ~ 30 minutes, Eckart et al. (2012) derived a source region size of 2.7 R_S. Gravity Collaboration et al. (2018) reported on the direct observation of compact and bright regions orbiting Sgr A* during "flaring state" and estimated a distance of these "blobs" of about ~9 R_S from Sgr A* and a source diameter of ~5 R_S (see also Gravity Collaboration et al. 2020). Furthermore, it

has been detected that flares are linearly polarized in the submm and NIR (Marrone et al., 2007; Shahzamanian et al., 2015). This and the observed spectral index of ~ 0.6 in the NIR (see, e.g., Bremer et al. 2011 or Witzel et al. 2014b and references therein) strongly indicates that synchrotron emission plays a predominant role in the emission mechanism.

Multi-waveband campaigns (see Fig. 1.5 for an example) have also revealed that radio flares follow NIR and submm flares with increasing time delays toward lower frequencies (Brinkerink, 2015; Marrone et al., 2008). This has been successfully modeled within the framework of expanding synchrotron blobs, which initially turnover close to the submm regime and become successively optically thin toward lower frequencies due to adiabatic expansion (Yusef-Zadeh et al., 2009; Mossoux et al., 2016) . The relation between NIR and X-ray emission has been debated more controversially. Observationally, it has manifested that there is a tight temporal correlation between flares in both regimes: every X-ray flare seems to go together with an NIR flare (Eckart et al., 2004; Trap et al., 2010), the opposite is not always true: NIR flares without an X-ray counterpart have been observed (e.g., Hornstein et al. 2007). In general, NIR flares occur approximately four times a day whereas on average only once per day an X-ray burst can be detected (Baganoff et al., 2003; Eckart et al., 2006). A time delay between flares at both frequencies is not ascertainable (Boyce et al., 2019). At the moment, two concurrent models are proposed that try to explain the tight correlation between flares at both wavelengths: pure synchrotron models and combined synchrotron and synchrotron self-Compton (SSC) models (see Sec. 1.4). In the former scenario, the optically thin synchrotron spectrum extends from the NIR to the X-ray regime, i.e, the observed X-ray emission is part of the synchrotron spectrum (e.g., Dodds-Eden et al. 2009; Ponti et al. 2017). In the SSC case, the synchrotron spectrum cuts-off somewhere between the NIR and the optical. X-ray emission is produced due to inverse Compton scattering within the synchrotron source (Sabha et al., 2010; Eckart et al., 2012; Mossoux et al., 2016). Both models have different physical implications: while a pure synchrotron model needs very high energetic electrons in the synchrotron plasma, an SSC scenario is less demanding in terms of electron energies but presumes higher volume densities. Therefore, the question which model fits the observed flaring activity better yields answers about concrete physical conditions in the innermost accretion flow onto Sgr A*.

1.4 General Emission Mechanisms

In this section, I will give a brief overview of some of the emission mechanisms that play a relevant role in the radiative processes around Sgr A* and SMBHs in general. In my humble opinion, excellent textbooks, in which most of the here mentioned mechanisms are exhaustively discussed are, e.g., Rybicki and Lightman (1979), Lang (1999) or Ghisellini (2013).

Thermal emission

Thermal black body emission is one of the most fundamental emission mechanisms. All matter, regardless of its state of aggregation, emits thermal radiation if it has a temperature above absolute zero. An idealized thermal emitter, i.e., an object which is in local thermodynamical equilibrium (LTE) and absorbs all incident radiation, is

called a black body. Although this ideal state rarely occurs in the real world, the black body approximation is omnipresent in physical models. First, many astronomical objects nearly behave like black bodies: stars, planets, dust particles, to name just a few. Secondly, the black body approximation plays an important role in many theoretical derivations. For instance, no thermal, incoherent emitter can radiate more efficiently than a black body. Therefore, black body radiation can often be used as an upper limit for the radiance of an emission process. The spectral radiance of a black body is given by

$$B(\nu, T) = \frac{2h\nu^3}{c^2} \frac{1}{\exp(h\nu/k_b T) - 1} \,. \tag{1.1}$$

For astronomers, Wien's displacement law is one of the most important applications of Planck's law. Given a temperature T, the displacement law gives the frequency ν at which $B(\nu, T)$ becomes maximal. Formally, it can be derived by differentiating $B(\nu, T)$ with respect to ν, set the derivative to zero and (numerically) solve for ν. This yields

$$\nu_{\mathrm{max}} \approx 5.8789 \times 10^{10} \frac{\mathrm{Hz}}{\mathrm{K}} \cdot T \,. \tag{1.2}$$

For instance, cold dust in the CND around Sgr A* can have temperatures below $10\,\mathrm{K}$. That means that its thermal emission peaks below $600\,\mathrm{GHz}$, i.e., in the submm regime. Accretion disks around SMBHs reach temperatures of several $10^6\,\mathrm{K}$ and more, so that the thermal spectrum might be relevant up to the X-ray regime (e.g., the thermal spectrum of a $10^7\,\mathrm{K}$ hot object peaks at $\sim 1\,\mathrm{keV}$).

Thermal bremsstrahlung

From the basic theory of electromagnetism it is known that de- and accelerated charged particles emit radiation. In astronomy, this typically happens when electrons get deflected in the Coulomb-field of ionized atoms or atomic nuclei. The kinetic energy which is lost by the electron is emitted in form of photons. It is beyond the scope of this basic introduction to derive explicit formulae for different kinds of bremsstrahlung. Here, I will only give the formula for bremsstrahlung from hot, i.e., thermal plasma. In general, the volume emissivity is given by

$$\epsilon_\nu \propto \frac{n_\nu N_e}{4\pi} \int P_r(v, \nu) f(v) \mathrm{d}v \,, \tag{1.3}$$

with the refraction index n_ν, electron density N_e, the total bremsstrahlung power in a frequency interval $P_r(v, \nu)\mathrm{d}\nu$ and the electron velocity distribution $f(v)$. $P_r(v, \nu)$ depends on the number of ions N_i, the velocity of the electrons v and the radiation cross section (which is in turn a function of the proton number Z). One can show that if the velocity distribution $f(v)$ is Maxwellian, i.e.,

$$f(v)\mathrm{d}v = \left(\frac{m}{2\pi kT}\right)^{3/2} 4\pi v^2 \exp\left(-\frac{mv^2}{2kT}\right)\mathrm{d}v \,, \tag{1.4}$$

Eq. 1.3 becomes

$$\epsilon_\nu \propto \frac{8}{3}\left(\frac{2\pi}{3}\right)^{1/2} \frac{n_\nu Z^2 e^6}{m^2 c^3}\left(\frac{m}{k_B T}\right)^{1/2} N_i N_e g(\nu, T)\exp(-h\nu/k_B T) \,. \tag{1.5}$$

Here, $g(\nu, T)$ is the free-free Gaunt factor which accounts for quantum mechanical corrections and often calculates to the order of unity.

Bremsstrahlung, self-absorption

To get the total brightness of an emitting source one needs to consider radiative transfer, i.e., not only the emissivity ϵ_ν but also the absorption coefficient α_ν. Thus, obtaining the full spectrum of thermal bremsstrahlung requires an expression for α_ν. I assumed that the electrons have a thermal, i.e., Maxwellian distribution. If one now additionally considers the plasma to be at a LTE, Kirchhoff's law applies and the source function S in the LTE can be written as

$$S = \frac{\epsilon_\nu}{\alpha_\nu} = B(\nu, T), \tag{1.6}$$

with the radiance of a black body $B(\nu, T)$ as given in Eq. 1.1. Calculating this out and omitting the numerical constants, one obtains

$$\alpha_\nu = \frac{B(\nu, T)}{\epsilon_\nu} \propto \frac{Z^2 N_e N_i}{T^{1/2}} \frac{1 - \exp(h\nu/k_b T)}{\nu^3} g(\nu, t) \tag{1.7}$$
$$\approx N_e^2 T^{-1/2} \nu^{-3} \left(1 - \exp(-h\nu/k_B T)\right).$$

Considering that the optical depth is given by

$$\tau = \alpha_\nu \mathrm{d}s, \tag{1.8}$$

one can see that toward lower frequencies (due to $\alpha_\nu \propto \nu^{-3}$) thermal bremsstrahlung sources tend to be optically thick ($\tau \gg 1$) and therefore absorbed. Looking at the specific intensity I_ν in the radiative transfer equation

$$I_\nu = S \cdot (1 - \exp(-\tau)), \tag{1.9}$$

it is also easy to see that for sources above some densities ($\alpha_\nu \propto N_e^2$) and below some temperatures ($\alpha_\nu \propto T^{-1/2}$), the entire frequency spectrum becomes optically thick. Then, the bremsstrahlung spectrum approaches the spectrum of a black body with $I_\nu = S = B(\nu, T)$.

Synchrotron emission

The physical mechanism behind synchrotron emission is basically the same as the principle of bremsstrahlung. Charged particles (mostly electrons) get accelerated and thus produce electromagnetic radiation. The difference compared to classical bremsstrahlung is that *a)* the electrons have relativistic velocities, i.e., $v \lesssim c$, and *b)* the force which accelerates the electrons is produced by magnetic fields, i.e., is the Lorentz force[2]. The acceleration **a** on an electron with rest mass m and total energy E in a magnetic field **B** is given by

$$\mathbf{a} = \frac{e}{\gamma mc} \mathbf{v} \times \mathbf{B} = \frac{ec}{E} \mathbf{v} \times \mathbf{B}, \tag{1.10}$$

---

[2]In older publications, often the term *magnetobremsstrahlung* is used instead of *synchrotron* radiation. In my opinion the former nomenclature should have prevailed as it labels the radiation mechanism, namely *bremsstrahlung* in a *magnet*ic field very precisely.

where e is the charge of the electron. Here,

$$\gamma = \frac{1}{\sqrt{1 - \frac{v^2}{c^2}}} = \frac{1}{\sqrt{1 - \beta^2}} \tag{1.11}$$

is the so-called Lorentz factor and can be considered as a measure for the "relativity" of the electrons. For simplicity, I assume that the path of an electron is helical around the magnetic field line **B**. At non-relativistic energies, i.e., $\gamma \sim 1$, the electron emits dipole radiation with the cyclotron frequency

$$\nu_L = \frac{eB \sin \theta}{2\pi mc} \approx 2.8 \cdot 10^6 \, \text{Hz/Gs} \cdot B \,. \tag{1.12}$$

For relativistic electrons with $\gamma \gg 1$ the gyration frequency is reduced to

$$\nu_g = \frac{\nu_L}{\gamma} \,. \tag{1.13}$$

In the relativistic regime, also the geometry of the dipole radiation has to be transformed from the electron's rest frame (ERF) to the observer's frame of reference (ORF). If ζ' is the opening angle of the forward lobe in the ERF, it can be shown that in the ORF it is given by

$$\zeta = \frac{\sin \zeta'}{\gamma(1 + \beta \cos \zeta')} = \frac{1}{\gamma} \,. \tag{1.14}$$

If I now imagine a distant ORF, where "distant" means that the opening cone completely fills the observer's field of view (FoV), the observer would repeatedly (with the Doppler-shifted gyration frequency) see synchrotron pulses. One can show that the duration of each pulse is given by

$$\Delta t \approx \frac{1}{2\pi \gamma^3 \nu_g} \,. \tag{1.15}$$

Vice versa, the inverse of that timescale defines a frequency ν_c at which the observer receives the most power from the signal. Then we have

$$\nu_c = \frac{1}{2\pi \Delta t} = \gamma^3 \nu_g = \gamma^2 \nu_L = \gamma^2 \frac{eB \sin \theta}{2\pi mc} \,. \tag{1.16}$$

To get the full spectrum, the entire electric field in the synchrotron pulse has to be calculated and Fourier-transformed. The resulting power spectrum is

$$p(\nu, \gamma) = \frac{\sqrt{3}e^3 B \sin \theta}{mc^2} \cdot F(\nu/\nu_c) \,, \tag{1.17}$$

where

$$F(\nu/\nu_c) = \frac{\nu}{\nu_c} \int_{\nu/\nu_c}^{\infty} K_{5/3}(y) \mathrm{d}y \,. \tag{1.18}$$

$K_{5/3}$ is the modified Bessel function of the order 5/3. It can be shown that

$$F(\nu/\nu_c) \approx \begin{cases} \frac{4\pi}{\sqrt{3}\Gamma(1/3)} \left(\frac{\nu}{2\nu_c}\right)^{1/3} & \text{for } \nu \ll \nu_c \\ \left(\frac{\pi}{2}\right)^{1/2} \left(\frac{\nu}{\nu_c}\right)^{1/2} \exp(-\nu/\nu_c) & \text{for } \nu \gg \nu_c \end{cases} \,. \tag{1.19}$$

This means that the power spectrum of a single synchrotron electron can be approximated with a power-law with a slope of 1/3 up to the critical frequency and an exponential decay for higher frequencies.

Ensemble of synchrotron electrons

In astrophysical cases, one does not observe synchrotron radiation from single electrons rather from ensembles of them, for instance from a plasma in the magnetic field next to a SMBH. The spectral volume emissivity of such an ensemble is given by

$$\epsilon_\nu = \frac{1}{4\pi} \int_0^\infty N(E) p(E, \nu) \mathrm{d}E \,, \tag{1.20}$$

if we assume isotropic synchrotron emission[3]. With $E = \gamma m c^2$, we already have an expression for $p(E, \nu)$ by Eq. 1.17. For the energy distribution of astronomical synchrotron sources one often finds power-law distributions. Thus, in the energy range between E_1 and E_2 one can write

$$n(E) dE = N_0 E^{-p} \mathrm{d}E \,. \tag{1.21}$$

The volume emissivity of the ensemble of electrons is therefore given by

$$\epsilon_\nu = C_1 \cdot N_0 \, B \int_{E_1}^{E_2} E^{-p} F(\nu/\nu_c) \mathrm{d}E \,. \tag{1.22}$$

The integral can be solved and written as

$$\epsilon_\nu = C_2 \cdot G(\nu, p) \cdot N_0 B^{(p+1)/2} \nu^{-(p-1)/2} \tag{1.23}$$

It can be shown that within a reasonable range of energy limits and power-law indices, the function $G(\nu, E_1, E_2, p)$ does not change the total expression by more than 10% (Moffet, 1975), so can often be neglected. Thus, for the emissivity the simple expression can be noted:

$$\epsilon_\nu \propto \nu^{-(p-1)/2} = \nu^{-\alpha} \,. \tag{1.24}$$

This is a remarkable result: a synchrotron plasma with power-law distributed electron energies $\sim E^{-p}$ will yield an emission spectral index $\sim \nu^{-(p-1)/2}$. Vice versa, if a synchrotron source with a power-law SED and spectral index α is observed, one can automatically infer that the underlying electron energy distribution is also a power-law with $p = 2\alpha + 1$[4].

Synchrotron self-absorption

As for any radiation, also for synchrotron emission radiative transfer has to be considered. To derive the absorption coefficient for a synchrotron emitter, two lines of reasoning can be followed: first the mathematically and physically exhaustive and stringent method using radiative transfer equations and Einstein coefficients. Secondly, one can use a more heuristic argumentation which I will use here for simplicity: I have mentioned that for many astronomical synchrotron sources the electron energy distribution is a

---

[3]This assumption is often made when performing simple synchrotron calculations: an isotropic energy distribution of electrons and tangled magnetic fields with no preferred orientation of the magnetic field lines.

[4]For typical astronomical synchrotron sources one often observes the "canonical" spectral index $\alpha \sim 0.7$ and therefore $p \sim 2.4$. Caution is advised when referring to a cited spectral index. Depending on the context and convention, some authors omit the sign of α, i.e., a given spectral index of $\alpha = 0.6$ could either mean $\epsilon_\nu \propto \nu^{0.6}$ or $\epsilon_\nu \propto \nu^{-0.6}$.

power-law as in Eq. 1.21, not thermal as in Eq. 1.4. Nevertheless, one can imagine the power-law distribution as a superposition of Maxwellians. Thus, one can formally associate the energy of an electron with a corresponding effective temperature via

$$3k_B T_e = \gamma m c^2 = \left(\frac{\nu}{\nu_g}\right)^{1/2} mc^2 \,. \tag{1.25}$$

For a completely absorbed thermal emitter, the Rayleigh-Jeans law for the relation between brightness temperature T and radiance I_ν can be used:

$$I_\nu = \frac{2 k_b T_e \nu^2}{c^2} \,. \tag{1.26}$$

Plugging in Eqs. 1.12, 1.25 and 1.26, one obtains

$$I_\nu \propto \frac{\nu^{5/2}}{B^{1/2}} \,. \tag{1.27}$$

This is again a remarkable result. The spectral index of optically thick synchrotron emission does not depend on the underlying energy distribution of the electrons but calculates to the fixed value of 5/2. This also means that for an absorbed synchrotron source one can directly derive the strength of the magnetic field from the observation of the flux density (knowing its angular dimension, see below). Using the definition of the source function S, it can additionally be shown that the synchrotron absorption coefficient α_ν has to scale with

$$\alpha_\nu \propto \nu^{-(p+4)/2} \,. \tag{1.28}$$

One can now combine what has so far been shown about the emissivity and absorption of a spherical synchrotron source. Introducing the angular diameter of the source as θ and integrating over the angular dimension, one finds an expression for the entire synchrotron spectrum:

$$S(\nu) = \begin{cases} C_1 B^{1/2} \theta^2 \nu^{5/2} & \text{if } \nu \ll \nu_m \\ C_2 N_0 B^{(p+1)/2} \theta^3 \nu^{-(p-1)/2} & \text{if } \nu \gg \nu_m \end{cases} \,. \tag{1.29}$$

Here, ν_m is the so-called turnover frequency, i.e., the frequency at which the emission turns from optically thick to thin, i.e, where $\tau \approx 1$.

Synchrotron self-Compton:

A well known phenomenon is the so-called Compton effect: high energetic photons scatter with electrons, lose energy, and thus change their frequency. The energy difference is transferred to the kinetic energy of the electrons. This is expressed by the famous Compton scattering formula $\Delta\lambda = (1 - \cos\theta)h/m_e c$ for the wavelength shift. Yet, in high energy physics the inverse effect might also happen: relativistic electrons scatter with photons and transfer parts of their energy such that the photons get "up-scattered" to higher frequencies. External photons might enter a high energetic plasma and gain energy by scattering. In the astrophysical community, this is then often specified as external Comptonization or simply inverse Compton (IC). Another scenario is also possible and was considered in my research: high energetic electrons produce synchrotron emission

and these synchrotron photons get up-scattered by the very same electron population. Very suggestively, this process is referred to as synchrotron self-Compton (SSC, see also Sec. 1.3). The formal derivation of IC and SSC formulae is beyond the scope of this introduction as it requires certain mathematical and physical effort. Details can be found in, e.g., Blumenthal and Gould (1970) or Gould (1979). Here, I will only show the, in the context of this thesis, relevant results for the SSC mechanism. First, there is a simple relation between the total power emitted due to synchrotron emission P_{syn} and SSC emission P_{SSC}. If $u_{mag} = B^2/2\mu_0$ is the magnetic, and $u_{rad} = S_\nu/c$ the radiative energy density, the ratio is given by

$$\frac{P_{SSC}}{P_{syn}} = \frac{u_{rad}}{u_{mag}} = \frac{2S_\nu\mu_0}{cB^2} \,. \tag{1.30}$$

In addition, the scaling of the (first order) SSC with the synchrotron flux density can be simply expressed as

$$S_\nu^{1,SSC} \propto N_0\theta S_\nu^{syn} \ln(\nu_2/\nu_m) \,, \tag{1.31}$$

where N_0 is the electron density and ν_2 the upper synchrotron cutoff frequency given by $E_2 = \gamma_2 mc^2$ and $\nu_2 = 2.8 \cdot 10^6 B/\text{Gs}\, \gamma_2^2$ Hz. If photons gain energy by multiple scattering events, higher order SSC flux densities then scale with

$$S_\nu^{n,SSC} \propto N_0\theta S_\nu^{(n-1),SSC} \,, \tag{1.32}$$

whereas second and higher order scattering only appear in physically extreme cases (ultra-relativistic electron energies and very high plasma densities) and are mostly used to explain observed GeV to TeV emission, e.g., from blazars. For my research on Sgr A*, all higher than first order SSC is negligible, thus I will always assume that $S_\nu^{SSC} = S_\nu^{1,SSC}$. The SSC formalism was further developed and adapted to concrete astrophysical use-cases by Marscher (1983, 1987). He introduced relativistic bulk motion of the synchrotron source (important for SSC, e.g., in jets or relativistic orbits) and accurate formulae to calculate SSC flux densities from observable variables. First, for the bulk motion, the boosting factor δ is introduced which is given by

$$\delta = \frac{1}{\gamma(1 - \beta\cos\phi)} \,, \tag{1.33}$$

with the Lorentz factor γ and relativistic velocity β as in Eq. 1.11 and the angle ϕ between the velocity vector and the line of sight. It can be shown that the synchrotron flux density then scales as

$$S(\nu) \propto \begin{cases} B^{-1/2}\theta^2\nu^{5/2}\delta^{1/2} & \text{if } \nu \ll \nu_m \\ B^{1+\alpha}\theta^3\nu^{-\alpha}\delta^{3+\alpha} & \text{if } \nu \gg \nu_m \end{cases} . \tag{1.34}$$

Thus, one obtains formulae for the Doppler-boosted synchrotron flux (Eq. 1.34) and the SSC flux density (Eq. 1.31). In principle, all variables are directly observable, except the magnetic field B and the electron density N_0. Both quantities can be expressed in terms of the turnover frequency ν_m and flux density $S_m = S_\nu(\nu/\nu_m)^{-\alpha}$. This is a very "canonical" point in the spectrum: at the turnover frequency, both optically thin and thick properties of the source can be observed. From the formulae for the optically thick part, the magnetic field B can be derived with

$$B \propto \theta^4\nu_m^5 S_m^{-2} \tag{1.35}$$

and from the optical thin properties one can get an expression for the electron density N_0 with

$$N_0 \propto \theta^{-(4\alpha+7)} \nu_m^{-(4\alpha+5)} S_m^{2\alpha+3} \,. \tag{1.36}$$

Combining Eqs. 1.31, 1.35 and 1.36 and considering numerical constants, we obtain an "accurate formula for the self-Compton X-ray flux density" (Marscher, 1983):

$$S_\nu^{\text{SSC}}(E_{\text{keV}}) \approx d(\alpha)\theta^{-2(2\alpha+3)} \nu_m^{-3\alpha+5} S_m^{2(\alpha+2)} (h\nu)_{\text{keV}}^{-\alpha} \ln\left(\frac{\nu_2}{\nu_m}\right) \delta^{-2(\alpha+2)} \,\text{mJy} \,. \tag{1.37}$$

Here, all frequencies are given in units of keV, the dimensionless parameter $d(\alpha)$ is tabulated in the literature and is, for instance, approximately 20 for a spectral index $\alpha = 0.7$. A note on the here presented equations: in the literature, in all formulae for the Doppler-boosted synchrotron and SSC flux densities (e.g., Eqs. 1.34 and 1.37) one finds an additional term for the luminosity distance expressed by the cosmological redshift z. As I only investigated Sgr A*, the redshift can be completely ignored and the z-term omitted. A final remark has to be done about the validity of Eq. 1.37: it only strictly applies within the limits

$$5.5 \times 10^{-9} \left(\frac{E_1}{mc^2}\right)^2 \nu_m \lesssim (h\nu)_{\text{keV}} \lesssim 5.5 \times 10^{-9} \left(\frac{E_2}{mc^2}\right)^2 \nu_2 \,, \tag{1.38}$$

where the frequencies ν_m and ν_2 are given in GHz. Below and above these energy boundaries the spectrum cuts off.

Adiabatically expanding synchrotron sources

In the former synchrotron formalism it was assumed that the source stays spatially invariant, i.e., that the angular diameter θ remains constant over time. Motivated by the observation of supernova remnants and their expanding synchrotron shells, several authors introduced models to describe the time dependency of such synchrotron spectra (Shklovskii, 1960; Kellermann and Pauliny-Toth, 1967). Here, I will briefly present the formalism as elaborated by van der Laan (1966) where the following scenario is considered: given is a spherical self-absorbed synchrotron source with initial radius r_0 and turnover frequency $\nu_{m,0}$. The source now expands adiabatically with a constant velocity v, such that $r(t) = r_0 + v \cdot t$. Then the angular diameter scales with

$$\theta(t) = \theta_0 \left(\frac{r(t)}{r_0}\right) = \theta_0 \cdot \rho \,, \tag{1.39}$$

where ρ is a dimensionless parameter for the temporal evolution with $\rho(t) = r(t)/r_0$[5]. Adiabatic expansion implies that the magnetic flux and the total energy is conserved, so it holds that

$$B(\rho) = B_0 \rho^{-2} \quad \text{and} \tag{1.40}$$

$$E(\rho) = E_0 \rho^{-1} \,. \tag{1.41}$$

It can be shown that the turnover frequency then evolves with

$$\nu_m(\rho) = \nu_{m,0} \rho^{-(4p+6)/(p+4)} \,. \tag{1.42}$$

---

[5]In principle ρ allows for other expansion models $r(t)$ than simple constant velocity.

For the time-dependent flux densities one finally obtains

$$S(\nu,\rho) = \begin{cases} S_0(\nu)\rho^3 & \text{if } \nu \ll \nu_m(\rho) \\ S_0(\nu)\rho^{-2p} & \text{if } \nu \gg \nu_m(\rho) \end{cases} . \tag{1.43}$$

The interpretation of this formula is quite suggestive: if we observe an adiabatically expanding, self-absorbed synchrotron source over time, the optically thin synchrotron flux densities will continuously decrease. The decrease of the volume density of electrons is the physical reasoning for this phenomenon. However, for some wavelength in the initially optically thick part of the spectrum, the flux density will first increase (physically, due to the increase of the emitting surface area), up to that time where that frequency becomes optically thin. Thinking of simultaneously observed light curves at different frequencies (see, e.g., Fig. 1.5 for a parallel NIR and radio light curve of Sgr A*), the time delay between flare peaks is easily explainable. The source is initially optically thick in the radio regime and optically thin in the NIR regime and adiabatically expands. Although the flux density in the NIR is already dropping, the flux density in the radio has not yet reached its maximum. It increases until the turnover frequency $\nu_m(\rho)$ lies in the radio regime from where on the radio flux also decreases. Both light curves are correlated but time delayed.

2 Observational Background

During my PhD-research, my main focus was the statistical investigation and interpretation of pre-reduced data. Neither did I conduct any observation nor did I perform any data reduction by myself. For all three manuscripts (Chaps. 4, 5 and 6) the credit for the data reduction goes in each case to the second author (and the fourth author for paper I). Nevertheless, in my opinion this thesis would be incomplete if I had not at least briefly discussed the used telescopes and some of their underlying techniques. Therefore, in this section I will give a short introduction to the involved facilities and their working principles. For a deeper understanding and more explanations I would like to refer the reader to the references given in each section or to standard astronomical textbooks.

2.1 Radio and Submillimeter Observations

Compared to optical observations, radio astronomy is a relatively young branch of science (optical observations contain both observations with the naked eye, as ancient astronomers did, as well as observations with early types of refracting telescopes whose invention is attributed to Galileo Galilei at the beginning of the 17th century). As already mentioned in Sec. 1.2, it was Karl Jansky who built the first radio telescope for astronomical observations in the early 1930s, followed by Grote Reber's research in the early 1940s. During World War II, enormous efforts were spent to intensively research and use radar (Radio Detection and Ranging) technology. This knowledge played an important role in the development of radio astronomy during and after the war. For instance, in February 1942, British radar stations detected extraordinary strong noise always coming from a distinct direction (Elgarøy, 1982). First assuming that the noise stems from an enemy interfering transmitter, British scientists soon found out that the source was the Sun with strong sunspot activity by that time. The newly detected "window" to the sky was then extensively used to conduct radio observations of the Sun, the Moon and the Milky Way (Unsöld, 1947). In 1948, the first radio interferometer was constructed (a so called "sea interferometer" which uses the reflection of radio waves from the ocean as second ray path) and, for instance, the radio source Cygnus A was identified (Bolton and Stanley, 1948). In the following decades, radio astronomy

greatly improved. Progressively, larger and larger telescopes with better sensitivity were constructed, here I just want to give a brief overview of historically important single-dish radio telescopes: The Ohio State Big Ear telescope, which is famous for the observed "*Wow!*"-signal in 1977, was build in 1963 (Kraus, 1963). It had a collecting area of $103 \times 33 \, \text{m}^2$. The Arecibo Telescope, also completed in 1963, had a reflector of more than 300 m in diameter. It was the largest radio telescope for more than half a century. Main parts of it spectacularly collapsed in 2020. The Effelsberg Radio Telescope (Wielebinski, 1970) located near Cologne: it started its operation in 1973 and has a steerable dish of 100 m in diameter. For almost 30 years, it was the biggest rotatable radio telescope. The reflector is build in such a way that gravitational deformation always preserves the parabolic shape. Nowadays, the largest steerable radio telescope it the Green Bank Telescope (GBT) with a collection area of $100 \times 110 \, \text{m}^2$. The largest non-steerable radio telescope is the Five-hundred-meter Aperture Spherical radio Telescope (FAST) with a diameter of its main mirror of about 520 m.

Principles of a radio telescope

Technically, most modern radio telescopes are reflectors. In practical terms, this means that a curved mirror is used to reflect the incident radio waves to a feed antenna. This antenna can be as simple as a dipole, yet mostly a small horn antenna, the feed horn is used. The feed can either be directly mounted in the focal point of the mirror or a subreflector in the focal point is used to concentrate the light beam onto the feed. From here, the signal is send to a receiver and an amplifier system. Due to the usually little power of astronomical radio sources (a mobile phone on the moon would be one of the strongest sources for radio astronomy), the receiver system needs to be very sensitive and thus cooled down to very low temperatures. Additionally, due to their weakness, radio signals have to be amplified to be able to detect and post-process them. Unfortunately, most amplifiers perform very bad at GHz frequencies. Therefore, the radio signals first need to be down-converted to the so-called intermediate frequency (ν_{IF} or simply IF). Typically the desired IF is of the order of a few hundred MHz. The down-conversion is done by mixing, also called heterodyning, the incident signal with frequency ν_{radio} with the signal of a local oscillator (LO) with a fixed frequency ν_{LO}. Mixing can be performed with any device that shows a non-linear current-voltage relationship such as a diode. From the mixed signal, the lower heterodyne frequency

$$\nu_{\text{IF}} = |\nu_{\text{LO}} - \nu_{\text{radio}}| \tag{2.1}$$

is filtered out, passed to the amplifier chain and finally to the evaluation electronics.

In radio astronomy, the strength of a signal is often measured in terms of the flux density S_ν. It describes the spectral (per frequency) rate (per time) of energy which is received by the detectors surface (per projected area). Thus, in SI-units the flux density is given by

$$[S_\nu] = \frac{\text{J}}{\text{Hz} \, \text{m}^2 \, \text{s}} = \frac{\text{W}}{\text{Hz} \, \text{m}^2} \, . \tag{2.2}$$

Due to the low received energies in radio astronomy, in this branch the unit Jansky was established:

$$1 \, \mathrm{Jy} = 10^{-26} \frac{\mathrm{W}}{\mathrm{Hz \, m^2}} = 10^{-23} \frac{\mathrm{erg}}{\mathrm{s \, Hz \, cm^2}} \tag{2.3}$$

The right side of Eq. 2.3 is given in cgs-units, which are also still often used in the radio community. For most thermal radio sources, the Rayleigh-Jeans-approximation of Planck's radiation law can be applied ($h\nu \ll k_B T$) and the flux density can therefore be converted to a corresponding brightness temperature T_B given by

$$T_B = \frac{S_\nu c^2}{2\nu^2 k_B \Omega} \, , \tag{2.4}$$

where Ω is the effective solid angle of the antenna beam. The association with a physical temperature can certainly only be made for thermal emitters. Nevertheless, the term brightness temperature is also used for non-thermal sources (e.g. synchrotron sources, see Sec. 1.4).

Radio telescopes are particularly different from optical telescopes in terms of dish sizes and surface textures: from optics, it is known that the diffraction-limited resolution θ of a circular aperture is approximately given by

$$\theta \approx 1.22 \frac{\lambda}{D} \, , \tag{2.5}$$

where D is the diameter of the aperture[1]. For instance, if a diffraction-limited resolution of 10 arcsec is desired with a NIR K-band (2.2 μm) telescope, a 5 m dish had to be built. If the same resolution is wanted to be achieved at 3 cm (100 GHZ), the dish needed to have a diameter of more than 750 m. On the other hand, mirrors for radio telescopes are technically less demanding than for higher frequencies. The surface accuracy of the reflector has to be of the order of fractions of the incident radiation (Mar and Liebowitz, 2003). This means, that the construction of mirrors toward higher frequencies becomes increasingly challenging as the requirements on the surface accuracy also increase.

Principles of radio interferometry

Although interferometry is mostly and extensively used in radio astronomy (I will explain the reason later), the first interferometer for astronomical observation was optical. Michelson and Pease (1921) tried to measure the angular diameter of stars, which appeared as unresolved, point-like sources for a single telescope. They created a device, where the light rays coming from the star were first split into two different beam paths separated by an adjustable distance D, and then brought to interference. If the star was an unresolvable point source, interference patterns as known from a double slit experiment would be observed. If the source was extended, then different points on the source's surface create different interference patterns, leading to a mixture of various interference patterns. The regions of positive (bright) and destructive (dark) interference are called fringes. The relative amplitudes of bright (B_+) and dark (B_-)

---

[1]For practical calculations, the conversion 1 rad = 206264 arcsec has to be applied.

fringes define the so-called visibility, which is an important function in interferometry:

$$V = \frac{B_+ - B_-}{B_+ + B_-}\,.$$

(2.6)

One can show that fringe patterns disappear if the condition

$$\theta = \frac{\lambda}{2D}$$

(2.7)

is satisfied. Comparing this with Eq. 2.5, the basic benefit of interferometry can be seen: in the former equation, the obtainable resolution was limited by the telescope's dish diameter D, now high resolution is obtained by a spatial separation D of two telescopes and the interference of their signals. This is called aperture synthesis. The distance vector $\mathbf{D}$ of the telescopes is in interferometric terms often referred to as the baseline.

Modern interferometers may consist of arrays of multiple telescopes separated by different baselines. The Earths rotation is then used to let the projected baselines "sweep" over the source on the plane of sky. It can be shown (Zernike, 1938) that the complex visibility function $V(\mathbf{D})$ is the Fourier-transformed brightness function I_ν of the source,

$$V(\mathbf{D}) = \int I_\nu(\mathbf{s}) \exp\left(-2i\pi\nu\mathbf{Ds}/c\right) d\Omega\,,$$

(2.8)

where $\mathbf{s}$ denotes the unity vector in the direction of the source. Eq. 2.8 is the so-called Van Cittert-Zernike theorem. As it can be seen, the observed quantity in interferometry is the visibility in the coordinate system of the baseline $\mathbf{D}$, where $\mathbf{D}$ is defined in the so called (u, w)-plane. The physically interesting and tangible quantity though is the brightness function I_ν in the (l, m)-plane, where l and m are the direction cosine of $\mathbf{s}$. The inverse Fourier transformation

$$I(l, m) = \int V(u, v) \exp\left(2i\pi\nu(ul + vm)/c\right) dudw$$

(2.9)

is often mathematically difficult and not unambiguous as most observations only cover tiny fractions of the entire (u, w)-plane. Techniques for deducing $I(l, m)$ from $V(u, v)$ go under the term "image reconstruction" and are beyond the scope of this brief overview.

A final note on the technical difficulties of interferometry: earlier in this section, I mentioned that interferometry has been mostly used in the radio domain. In the IR and optical domain, interferometric multi-telescope instruments have only been introduced in the early 1980s (see, e.g. Gravity Collaboration 2017 for a most recent development). This has the following reasons: first, with increasing frequency, the precision of the optics becomes more demanding. Along the whole optical path, the light has to be kept coherent, optical accuracies below fractions of a micron have to be achieved. Secondly, in radio astronomy, especially when the different telescopes of an array are separated by very long baselines (VLBI), the signals from the single telescopes can first be recorded and later be superimposed in a central correlator. This also requires the recording of accurate timestamps for the precise correlation. High frequency signals would need such a high time resolution, that the recording of the received signals is not feasible. Therefore, IR and optical interferometers need fast real-time correlation of the signals, which puts additional high demands on the involved facilities.

Principles of a bolometer

Bolometers are special kinds of thermal detectors that are often used in submm astronomy. In principle, incident radiation is absorbed, converted into heat and then electrically read out. Bolometers are a very effective radiation detection method especially in the submm regime. Toward higher frequencies, charge-coupled devices (CCDs) are better suited to fully convert the incident energy into a measurable signal, toward lower frequencies the photon energies are so low that absorption becomes inefficient and heterodyne receivers are preferable. The working principle of a bolometer can be described as follows (see Hollister 2009): a thermistor with resistance $R(T)$ is embedded in an absorption material with heat capacity C. The absorber is also thermally coupled via a heat link with heat conductance G to a low temperature heatsink of temperature T_0. Incident radiation heats up the absorber and induces an amount of heat Q. The absorber's temperature therefore increases by ΔT. This changes the resistance of the thermistor, which then can be used, e.g., by a simple electric voltage divider circuit, to measure the incident signal.

Two main parameters describe the performance of a bolometer: first, the time constant τ which is a measure for the speed of a temperature change due to incident radiation with power $P = dQ/dt$. This constant is given by

$$\tau = \frac{C}{G}.\tag{2.10}$$

Secondly, it is the Noise Equivalent Power (NEP). It is defined as the minimum strength of an input signal that outputs a signal with power P_R as strong as the instrument's noise power P_N at a given bandwidth:

$$\text{NEP} = \frac{P_N}{P_R}.\tag{2.11}$$

It can be shown (Richards, 1994) that the NEP critically depends on the bolometer's temperature (simply put, the cooler, the less noise). Therefore, for best performance the heat sink has to be cooled down to fractions of a Kelvin.

2.1.1 The Australia Telescope Compact Array (ATCA)

The Australia Telescope Compact Array (ATCA) is an aperture synthesis interferometric array of six 22 m telescopes. Taken into service in September 1988, it is located at the Paul Wild Observatory 30 km east of Narrabri in New South Wales Australia. Operated by the Commonwealth Scientific and Industrial Research Organisation (CSRIO), it is one of the four telescopes of the Australia Telescope National Facility (ATNF). ATCA is an Earth-rotation interferometer and can operate at frequencies between 1 and 100 GHz (Frater et al., 1992). Five of the six antennas are mounted on a 3 km long railway track with a 214 m long, rectangular spur and can be moved separately for the desired array configuration. A sixth antenna is fixed at a distance of another 3 km. This means that as a single interfermometer, ATCA has a maximum baseline of 6 km. Together with the other three ATNF telescopes, i.e., the Parkes Observatory, the Mopra Observatory, and the Australian Square Kilometre Array Pathfinder (ASKAP), ATCA can be also used for

Figure 2.1: *Image of the Australia Telescope Compact Array (ATCA). Five of the six 22 m radio antennas can be seen. Different array configurations can be achieved by moving the dishes on the railway track. The east-west railway is 3 km long, the north-south (not yet constructed when this photo was taken) 214 m. Image credit: CSIRO, licensed under CC BY 3.0*

VLBI. In standalone mode, ATCA can be operated in seven observing bands: 20 cm, 13 cm, 6 cm, 1 cm, 7 mm and 3 mm. The angular resolution depends on the observed waveband, ranging from 6 arcsec at 20 cm down to 0.1 arcsec at 3 mm (Wilson et al., 2011).

2.1.2 The Atacama Pathfinder EXperiment (APEX) and the LArge Bolometer CAmera (LABOCA)

The Atacama Pathfinder EXperiment (APEX) is a mm to submm (1.5 to 0.2 mm) telescope located at an altitude of more than 5000 metres in the Atacama desert in Northern Chile. It is operated jointly by the Max Planck Institute for Radio Astronomy (MPIfR), the European Southern Observatory (ESO) and the Swedish Onsala Space Observatory (OSO) at the site of the Atacama Large Millimeter Array (ALMA) radio interferometer and saw its first light in 2005. With a dish diameter of 12 m, it is the largest submm telescope in the southern hemisphere. After assembly, the dish, with its 264 aluminium panels, had a surface accuracy of about 40 μm rms. With near-field holography conducted with a $\sim$ 90 GHz transmitter under an elevation of 13 deg, the surface accuracy was re-calibrated to even less than 15 μm. For higher elevations, gravitational deforma-

Figure 2.2*: Image of the Atacama Pathfinder EXperiment (APEX) telescope. It can be seen that the 12 m dish consists of different aluminium panels (264 in number). Image credit: ESO, licensed under CC BY 4.0*

tions reduce the surface accuracy by a few micron (Güsten et al., 2006).

A crucial parameter for ground based submm observations is the precipitable water vapour (PWV), which is defined as the total amount of water (in mm) in an atmospheric column above a location if all the water vapor in that column would condense:

$$PWV = \int_0^h \rho_w(h) \mathrm{d}h \,. \tag{2.12}$$

At 345 GHz, the atmospheric transmission has for instance a value of ~ 0.9 for PWV = 0.2 mm and ~ 0.8 for PWV = 1 mm, but drops to ~ 0.5 for PWV = 3.75 mm (Güsten et al., 2006; Plume et al., 2007). The location of the APEX telescope is best suited for ground-based submm observations, as it is one of the driest places on Earth with a median value of PWV ≈ 1 mm for the telescope operation time from April to December (Lundgren et al., 2010).

One of the science instruments mounted at APEX was the LArge APEX Bolometer CAmera (LABOCA, Siringo et al. 2009). It had been developed at the MPIfR in Bonn, was installed at APEX in 2006 and operated since 2007. LABOCA was a multi-channel

bolometer array, composed of 295 single bolometers. Operating at a central frequency of 345 GHz with a spectral bandpass of 60 GHz, it was cooled down during operation to a temperature of ~285 mK. Each single bolometer was fed by a horn antenna, the individual beam shapes had been determined to be a circular Gaussian with a FWHM ≈ 19.2 arcsec. With its hexagonal arrangement and a channel separation of 36 arcsec, the total FoV was 11.4 arcmin. LABOCA's noise-equivalent flux density (NEFD) had been determined to be 60 mJy s$^{1/2}$ (Lundgren et al., 2010)[2]. Over the years, technical difficulties arose with an increasing number of single channels (see Fig. 2.3). Thus, LABOCA has been decommissioned in December 2020 (Lundgren et al., 2020).
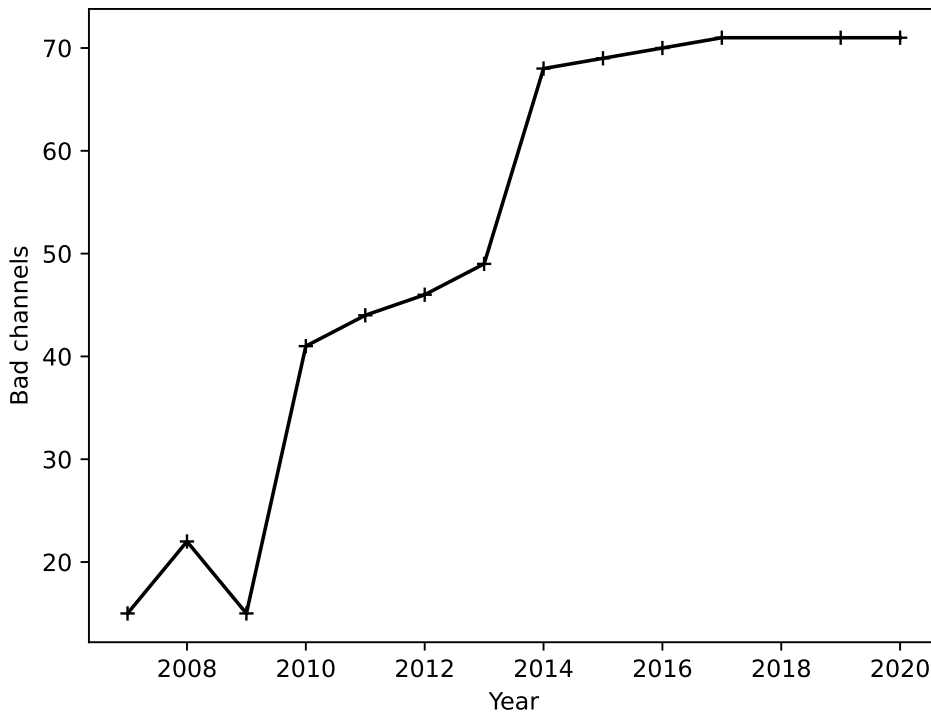
Figure 2.3: *The LArge BOlometer CAmera (LABOCA) suffered from aging effects over the years. This plot show the number of bad channels at the end of each year, the data is taken from the "channel-flags-*"-files available at* `https://www.apex-telescope.org/bolometer/laboca/calibration/array/`. *The true number of defunct bolometers from all 295 single channels was even higher as some channels were sealed with an absorber, showed cross-talk or were not connected at all. LABOCA was taken out of operation in December 2020.*
.

2.2   X-ray Observations

As already mentioned earlier, the Earth's atmosphere is not transparent for X-ray radiation. This is due to the photo-electric effect where atoms in the atmosphere absorb X-ray

---

[2]The NEFD is defined as NEFD≈ NEP/(Aν), where A is the the detectors collection area, ν the frequency bandwidth and the NEP is given by Eq. 2.11.

photons and emit electrons. Thus, almost no X-ray photons reach the Earth's surface, making X-ray astronomy a difficult and relatively new observational branch. One has to get to high layers of the atmosphere, e.g., with balloons or rockets, or even above, to space, to be able to observe extraterrestrial X-ray radiation. One of the earliest astronomical X-ray campaigns was started in the late 1940s with sounding rockets based on the German V2s (Friedman, 1963). The solar X-ray emission was continually observed for more than 11 years, i.e., a full sunspot cycle. In 1960, only three years after the first-ever launch of a satellite, namely Sputnik, the first successful X-ray satellite mission was launched, SOLRAD 1, followed by a series of SOLRAD missions (Evans and Pounds, 1968). Not only that these missions successfully monitored the Sun's X-ray spectrum, they also detected strong solar variability, so-called flares, in the X-ray. The first satellite dedicated exclusively for X-ray observations was Uhuru in 1970. For the first time, an exhaustive all-sky X-ray survey was conducted. Amongst other achievements, the mission confirmed the detection of the variable X-ray source Cygnus X-1 (Oda et al., 1971), which can be considered as the first-ever detected black hole candidate. In 1983, the European Space Agency (ESA) started its own X-ray satellite programme with the European X-ray Observatory Satellite (EXOSAT). Due to its highly eccentric orbit with a ~90 hours period, it was capable of long continuous monitoring of X-ray sources. Therefore, it was able to observe the count rate variability of active galactic nuclei (AGNs, McHardy 1988). The first X-ray satellites which exhaustively monitored Sgr A* were the X-ray Multi-Mirror (XMM-Newton) mission and the Chandra X-ray Observatory (CXO), both launched in 1999 and still in operation.

Basic principles of an X-ray mirror
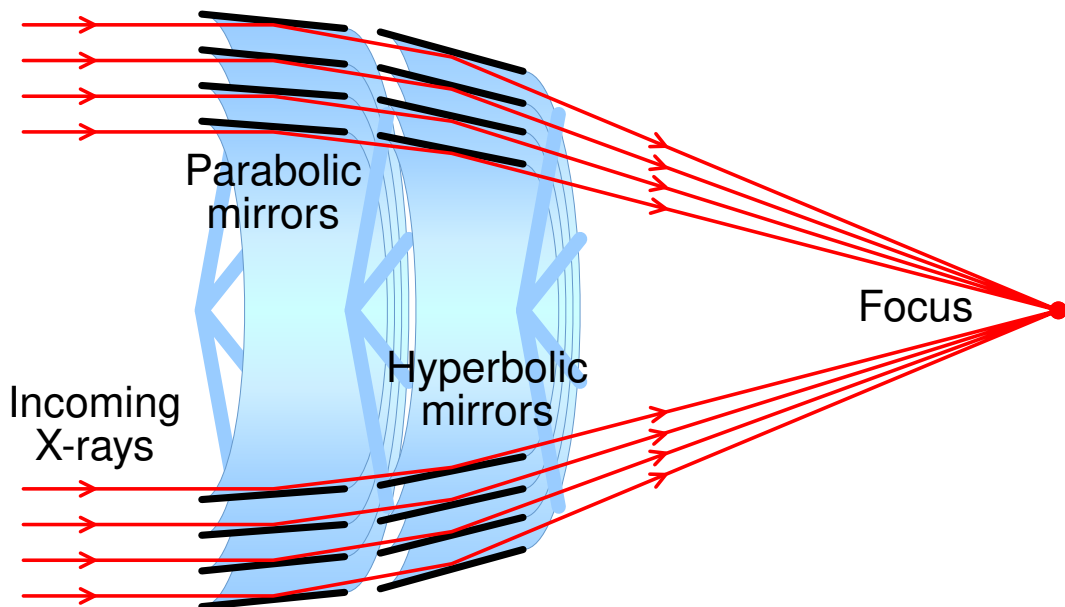
Figure 2.4: *Schematic view of a nested Wolter Type-I mirror. This optics is a combination of paraboloid and hyperboloid mirrors. The incoming beam is almost parallel to the optical axis to obtain total external reflection. The positioning of both mirrors in a single setup allows for nesting several layers of mirrors to increase the optical aperture. Image Credit: CMG Lee, licensed under CC BY 4.0 (a label was removed from the original image)*

X-ray telescopes are different in design compared to telescopes that operate at smaller frequencies. Refracting optics are difficult to build for X-rays as most materials which are transparent to these frequencies have a refraction index close to unity. Due to their high energies, standard designs for reflecting mirrors are also not possible: under larger incidence angles, X-ray photons just pass through or get absorbed by most reflecting mirrors due to their high energies. Only under small incidence angles, X-ray photons can get reflected. For materials with refraction indices below unity and smooth surfaces, it is possible to get total external reflection (TER) for the X-ray beam. If the complex refraction n is given by

$$n = 1 - \delta - \mathrm{i}\beta \tag{2.13}$$

and $1 - \delta < 1$, one can show that the critical angle, under which TER occurs, is given by

$$\cos\alpha_{\mathrm{TER}} = 1 - \delta \tag{2.14}$$

and for $\delta \ll 1$

$$\alpha_{\mathrm{TER}} = \sqrt{2\delta}. \tag{2.15}$$

One can also show that for the parameter δ it holds that

$$\delta \propto \frac{Z}{A}\rho\lambda^2 \,, \tag{2.16}$$

where Z is the proton number, A is the mass number, ρ is the mass density of the reflectors material, and λ is the X-ray's wavelength. This suggests heavy and dense materials as X-ray reflectors. In so-called grazing incidence mirrors, TER is used to effectively focus X-rays. One of the most common type of a grazing incidence mirror is a Wolter Type-I mirror (Wolter, 1952). In this kind of telescope, the beam is first reflected on a paraboloid mirror, followed by a hyperboloid mirror. To guarantee for TER, the optical axis is almost parallel to the incoming beam. This setup has two major advantages: first, it has a relatively short focal length. Secondly, it allows for nesting several shells of mirrors. This gives the possibility to build compact telescopes with a large aperture. A sketch of a nested Wolter Type-I optics is shown in Fig. 2.4.

2.2.1   The Chandra X-ray Observatory (CXO)

The Chandra X-ray Observatory (CXO, or just Chandra) satellite was launched on July 23, 1999. It is named after the famous astrophysicist Subrahmanyan Chandrasekhar and was delivered to space by the Space Shuttle Columbia. Chandra carries two focal plane science instruments: the Advanced CCD Imaging Spectrometer (ACIS) and the High Resolution Camera (HRC). In addition to the two primary instruments, Chandra is also equipped with diffraction gratings for high resolution spectroscopy: the High Energy Transmission Grating (HETG), and the Low Energy Transmission Grating (LETG). HETG is mostly used with ACIS, the LETG with HRC (Weisskopf et al., 2000). The former configuration was used for the GC observations during the X-ray Visionary Project (XVP) campaign. Therefore, I will briefly summarize some of its operating principles:

ACIS consists of ten CCDs, each of them with a FoV of approximately 8.3 arcmins. Four of the CCDs are arranged in a 2x2 array used for imaging (and therefore called ACIS-I), giving the entire array a FoV of $\sim$ 16 arcmin. The other six CCDs are assembled
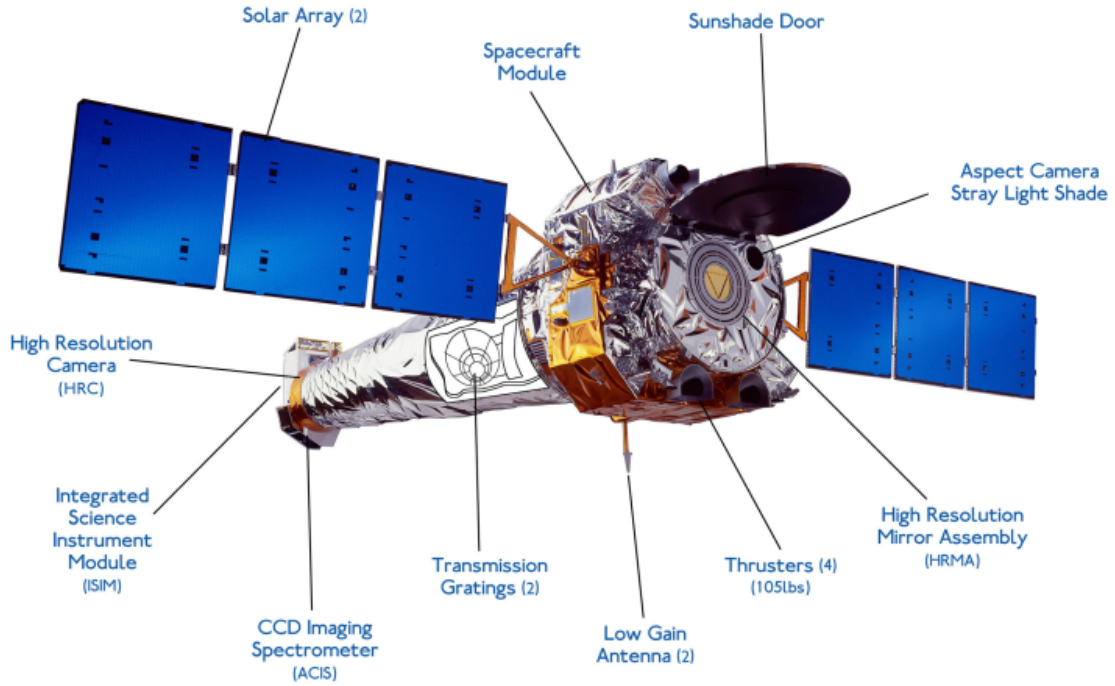
Figure 2.5: *Schematic view of the Chandra X-ray Observatory. For the Galactic Center observations during the X-ray Visionary Project (XVP) campaign, the High Energy Transmission Grating (HETG) transmission grating and the Advanced CCD Imaging Spectrometer (ACIS) CCD were used. The High Resolution Mirror Assembly (HRMA) consists of four concentric grazing incidence Wolter Type-I mirrors. Image credit: NASA/CXC/NGST, Public domain, via Wikimedia Commons*

in an 1x6 array. This array (called ACIS-S) can either be also used for imaging or for energy spectroscopy. Spectroscopy is conducted via the HETG. This diffraction grating can be optionally inserted into the X-ray beam. From the theory of diffraction gratings, it is known that the dispersion angle ϕ depends on the wavelength λ, the spacing between the slits d and the diffraction order n:

$$\phi = \arcsin\left(\frac{n\lambda}{d}\right). \tag{2.17}$$

Thus, the dispersion angle is a measure for the photon's energy and can be used for spectral analysis. Photons passing undispersed through the grating to the central CCDs are called 0th-order photons, dispersed photons $\pm 1^{st}$-order photons. 0th-order photons represent the spatial image of the source, higher order photons the spectral information. It has to be kept in mind that 0th-order photons are often affected by pile-up. This is an observational phenomenon which can occur with X-ray photon counting CCDs. Simply put, pile-up is the inability of a CCD to distinguish between single and multiple photon detection events within a readout frame. Two scenarios have to be considered here:

- Multiple photons hit the detector within a readout frame and the cumulated sum of the photon energies exceeds the limit of the energy bandpass. Then the readout software will reject the detection for the respective readout frame and zero counts are detected.

- Multiple photons hit the detector within a readout frame and the cumulated sum of the photon energies does not exceed the limit of the energy bandpass. The detector software will report a single count with an energy equal to the sum of the individual energies.

In either case, pile-up will lead to an underestimation of the incident source count rate. The brighter the source the more pile-up has to be considered. In Sec. 3.3.1, I discuss the implicated mathematical and statistical challenges in more detail.

3 Statistical Background

3.1 Basic Statistical Concepts

In this chapter, I will introduce some basic concepts which are important for the statistical analyses I conducted throughout my PhD-research. Especially this first section might appear as too basic and textbook-like, but I nevertheless deem it to be an important part of this thesis. During my PhD-studies, I had the impression that in parts of experimental physics, statistics is considered to be a subordinate subject. Thus, when it comes to probability theory, I sometimes noticed subtle misconceptions. To address this issue, I will first introduce some very basic definitions of probability distributions. Later, in Sects. 3.2, 3.3 and 3.3.1, I will discuss some of the statistical tools that were necessary to analyze the given light curves of Sgr A*.

In all three manuscripts I analyzed distribution functions, continuous flux density distributions in the case of submm and radio data, discrete count rate distributions in the case of X-ray data. Some of the underlying questions are:

- What is the probability of observing a certain flux density or count rate? (This is more a question of *descriptive statistics*.)

- Which model and which model parameters describe the probability function? (This question belongs to the field of *inferential statistics*.)

Let me first begin with the very basic question: *What is a probability?* For discrete values, this question is straightforward to answer. The probability is described by a function f_X which assigns each (discrete) value x, i.e., each possible outcome of an experiment, a certain probability between zero and one. This function is called the probability mass function (PMF),

$$f_X(x) = \Pr(X = x) \, , \tag{3.1}$$

and X is called a random variable. Of course all probabilities must add up to one (there is a 100% chance that any of all possible events will occur). As a simple example, one may write down the PMF of a fair six-sided dice as

$$\Pr(X = i) = \frac{1}{6} \quad \text{for } i = 1, 2, \dots, 6. \tag{3.2}$$

Another example of a PMF is the probability of observing n photon counts within a certain readout cycle or time bin. For instance, steady, low count rate processes are often described by a Poissonian PMF

$$\Pr(X = x) = \frac{\lambda^x}{x!} \exp(-\lambda), \tag{3.3}$$

where λ is both the expected value and the variance of the distribution.

For continuous random variables, the concept of probabilities is slightly different. The probability that a random variable takes exactly one value is in fact -leastways due to uncertainties- zero (*How big is the probability that an object is observed with a flux density of 3 Jy? Zero, as the flux density will never be **exactly** 3 Jy*). One can only define the probability of a value falling into a specific range of values as

$$\Pr(a \le X \le b) = \int_a^b f_X(x)dx. \tag{3.4}$$

Then $f_X(x)$ is called the probability density function (PDF). This function has to be normalized, i.e., $\int_{-\infty}^{\infty} f_X(x)dx = 1$, always non-negative and of course integrable. Considering an infinitesimally small interval (a, b), one can also formally write for the PDF

$$f_X(x) = \frac{d\text{Pr}}{dx}. \tag{3.5}$$

Closely related to the PDF is the so-called cumulative distribution function (CDF). This function gives the probability of a random variable being less or equal a certain value x (*How big is the probability that I observe 3 Jy or less?*):

$$F_X(x) = Pr(X \le x) \tag{3.6}$$

Thus, the CDF is given by the integral over the PDF:

$$F_X(x) = \int_{-\infty}^x f_X(x)dx \tag{3.7}$$

It is often useful to consider the complementary question, namely what is the probability that a random variable is above a certain value:

$$S_X(x) = Pr(X > x) = 1 - F_X(x) \tag{3.8}$$

This function is called the complementary cumulative distribution function (CCDF) or the survival function. Later we will see that, e.g., for power-law distributions, it is more convenient to work with the CCDF than with the CDF.

In descriptive statistics, the task is often to obtain model-free estimators either for the PDF or the CDF of a given sample of random variables. PDFs have the main advantage that their meaning is often directly and intuitively understandable. For instance, the statement "*The probability that Sgr A* exhibits a flux density between 2.5 and 3.5 Jy is 50%*" might be considered as easier to understand than the statement "*The probability that the flux density is less than 2.5 is 35% and that it is less than 3.5 Jy is 85%*". Without claiming general validity, I tend to say that human beings think more in PDFs than in CDFs. This might also be caused by the fact that the PDF of a standard normal distribution, namely

$$f(x) = \frac{1}{\sqrt{2\pi}} \exp\left(-\frac{x^2}{2}\right), \tag{3.9}$$

is well known and easy to understand, whereas its CDF, given by

$$F(x) = \frac{1}{\sqrt{2\pi}} \int_{-\infty}^{x} \exp\left(-\frac{t^2}{2}\right) dt = \frac{1}{2}\left[1 + \mathrm{erf}\left(\frac{x}{\sqrt{2}}\right)\right], \tag{3.10}$$

does not appear to be similarly intuitive. Additionally, the graph of a PDF often tends to be easier to interpret and seems to give more directly tangible information than the corresponding CDF (see Fig. 3.1). Nevertheless, the use of a CDF has one major advantage compared to a PDF: it is directly accessible from the data without additional choices and biases. To construct an estimator for a PDF, two of the most commonly applied techniques are histograms and kernel density estimations (KDEs). A histogram of N samples is defined by its j bins, each of which contains c_i observations. For a histogram, it holds that:

$$N = \sum_{i=1}^{j} c_i. \tag{3.11}$$

It is easy to understand that the number of bins j is a crucial parameter in the construction of histograms. If j is chosen too low, the PDF estimator tends to over-smooth potentially interesting features of the data. Choosing a too high j leads to a clustered histogram with many spikes and empty bins. Estimating the best number of bins for a histogram is its own field of research and has exhaustively been discussed in, e.g., Knuth (2006) or Shimazaki and Shinomoto (2007). KDEs are subject to a similar problem. A KDE is given by

$$\hat{f}(x) = \frac{1}{nb} \sum_{i=1}^{n} k\left(\frac{x - x_i}{b}\right) \tag{3.12}$$

with a kernel k and a bandwidth b. Again, the obtained estimator depends on the made choices, i.e., the chosen kernel and the smoothing bandwidth (Shimazaki and Shinomoto, 2010). Both applications, histograms and KDEs, therefore always go together with information loss and biases. Conversely, CDF estimators can be constructed as functions, which take the observations as only input parameter. If X is a sample of n random variables given by an observation, an expression for the empirical CDF is given by

$$F_n(x) = \frac{1}{n} \sum_{i=1}^{n} \mathbb{1}\{X_i \leq x\} \tag{3.13}$$
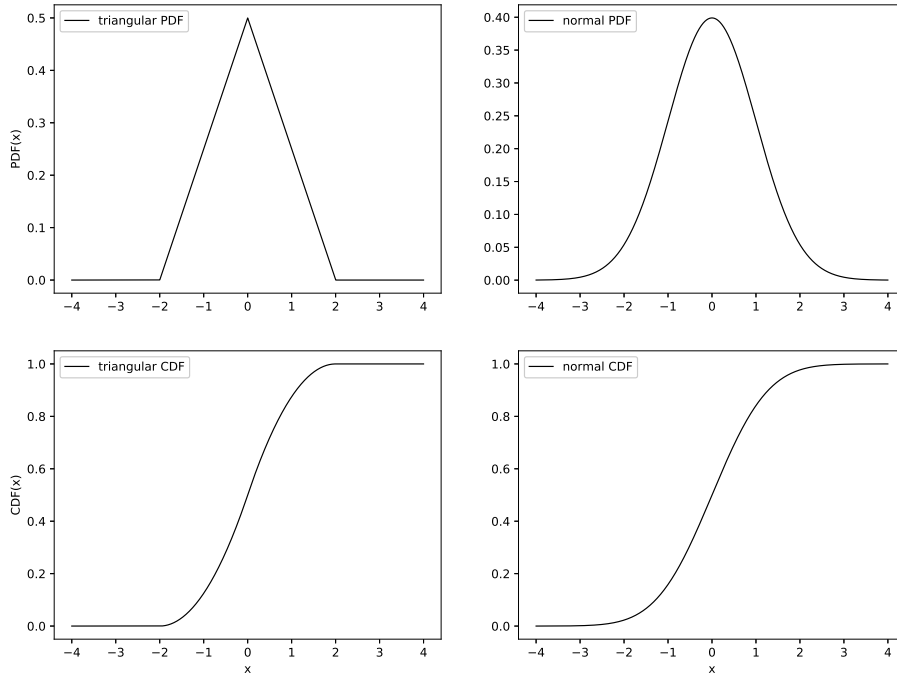
Figure 3.1*: Comparison of the visual impression of probability density functions (PDFs) and cumulative distribution functions (CDFs) for a triangular (left side) and a standard normal distribution (right side). In the upper panels, the respective PDFs are shown, in the bottom panels both CDFs. The PDFs are visually and intuitively distinguishable, whereas this is more difficult for the CDFs. That is one of the main reasons for using PDF estimator when visualizing data, whereas CDF estimators are mathematically more informative (see text for details).*

where

$$\mathbb{1}\{X_i \leq x\} = \begin{cases} 1 & X_i \leq x \\ 0 & \text{else} \end{cases} \tag{3.14}$$

is the indicator function. No additional choices about other parameters such as number of bins, kernel selection or bandwidths have to be done and the complete information of the observed random variables is preserved. Because of this property, CDFs are preferably used to define distance metrics between probability distributions or their realization in form of a given sample of random variables. Popular applications of CDF-based distances are, e.g., the Kolmogorov-Smirnov (Kolmogorov, 1933) or the Anderson-Darling (Anderson and Darling, 1952) test.

Inverse transform sampling

The CDF can also be used to draw random numbers from the underlying distribution if the CDF is invertible, i.e., if we are able to write down CDF^{-1}. This is called inverse transform sampling or the inversion method. The procedure for generating n samples X can be given as follows:

1. Draw a random number u from the uniform distribution between $[0, 1]$

2. Calculate $x = \text{CDF}^{-1}(u)$

3. Repeat n times

Algorithm 3.1: *Scheme for inverse transform sampling. Knowing the cumulative distribution function (CDF) of a probability distribution allows for generating random numbers from that distribution.*

The random variables X will follow the distribution given by its CDF (Devroye, 1986). As I will show later (Sec. 3.3 about Bayesian inferential statistics), it is often very useful to be able to create simulated data from a given model. If the CDF of that model is known, inverse transform sampling can be conveniently used as mock data generator.

Distribution fitting, maximum likelihood estimation (MLE)

In the last paragraph of this section, I want to briefly discuss a widely used method to estimate the parameters θ of a PDF model p from a set of given samples x. (To take up the earlier introduced nomenclature, this is part of inferential statistics.) Without loss of generality, I assume a one-dimensional sample, i.e., there is one quantity which is observed multiple times. If one wants to estimate the best fit parameters of an assumed PDF, one might be tempted to create a histogram or KDE as introduced above, interpret this as a function $p(x; \theta)$ in an (x, y)-plane and perform an ordinary curve fitting routine, for instance a minimum chi-square estimation. For several reasons, this is not the mathematically correct approach though. First, least square fitting assumes that the errors of a data point are symmetric around zero. This cannot be true for a function which is only allowed to take non-negative values. Secondly, least square fitting expects the different data points to be independent and identically distributed (i.i.d.). This is also not true for a probability distribution which has to be normalized (for a histogram that means, if the heights of all bins up to the second last are known, the heights of the last bin is automatically determined as the sum of all bin heights has to be one). Thus, curve fitting techniques are not applicable for PDFs. Instead, one tries to maximize the so-called likelihood function $\mathcal{L}$, defined as

$$\mathcal{L}(x|\theta) = \prod_{i=1}^{n} p(x_i|\theta) \,. \tag{3.15}$$

$\mathcal{L}$ describes the joint probability of observing x given a model described by its PDF with parameters θ. The greater the value of the product, the more likely it is that the data was "generated" from the assumed model. The maximum of $\mathcal{L}$ can either be found by analytically solving the equations

$$\frac{\partial \mathcal{L}}{\partial \theta_i} = 0 \,, \tag{3.16}$$

or, if these equations have no analytical solution, by numerically solving Eq. 3.16 by varying θ. Often it is more convenient not to use the likelihood function itself, but its logarithm, the log-likelihood $\ln(\mathcal{L})$. This has the computational advantage that the

product as given in Eq. 3.15 becomes a sum, which is numerically easier to handle:

$$\ln(\mathcal{L}(x|\theta)) = \sum_{i=1}^{n} \ln\left(p(x_i|\theta)\right) . \tag{3.17}$$

3.2 Power-law Distributions

Power-law distributions are omnipresent not only in natural but also in social sciences. From the energy of solar flares (Lu and Hamilton, 1991), the diameter of moon craters (Young, 1940), the initial mass function of stars (Salpeter, 1955), the magnitude of earthquakes (Gutenberg and Richter, 1956), the size and duration of neural avalanches (Friedman and Landsberg, 2013), the distribution of wealth in modern societies (Pareto, 1964), Zipf's law of the frequency of words in languages (Powers, 1998) to the number of links to websites in the world wide web (Adamic et al., 2000): power-laws seem to able to describe a wide range of different phenomena. Additionally, as I will also show in this thesis, the flux density distribution of flares from Sgr A* at different wavebands are also well modeled with power-law distributions (Witzel et al., 2012; Neilsen et al., 2015; Subroweit et al., 2017, 2020). In this section, I will therefore discuss general mathematical properties of power-laws.

Our daily life is based on subconsciously assessing probabilities of certain events and the evolution has giving us a decent sense for this assessments. For instance, we know how much time it approximately takes to do the grocery shopping at the supermarket. We have an intuition about how many people might approximately attend to the talk we will give in the lecture hall or how likely it is that is rains tomorrow. But human common sense is in some situations also subject to cognitive biases and may fatally fail. In my opinion, this is often caused by the lack of intuition toward processes where exponential growth or shrinkage leads to "non-Gaussian behaviour", i.e., where the underlying probability distribution differs significantly from a normal distribution. There is a famous example which is often given when it comes to misconceptions in understanding the properties of heavy-tailed, e.g., power-law distributions: we imagine a situation where a room is filled with 50 people. Now one estimates the average height μ of all attendants according to $\mu = 1/N \sum x_i$. Some people will be taller, some shorter, but one would possibly find that on average the people are about 1.75 m tall with a standard deviation $\sigma = (1/N \sum (x_i - \mu)^2)^{1/2}$ of, say 20 cm. Now the tallest person on Earth enters the room. Let us assume he or she is 2.5 m tall. It is easy to calculate that the average height of all people inside the room has only increased by less than 2 cm to now approximately 1.77 m. The updated standard deviation is 22 cm.[1] Now we make another evaluation: we calculate the average income off all people inside the room. Some may be professors, some construction workers, some unemployed, so there is some span in their income. Let us assume we have determined the average income to be 40000 € per year with a standard deviation of 20000 €. Now the richest person on Earth enters the room. Say, his or her annual income is 3 billion €. Now the statistics yields that the average income in the room increased to about 59 million € per year with a standard deviation of 420 million €. The question arises what commonly

---

[1]The update standard deviation σ_n is given by $\sigma_n = ((n-2)\sigma_{n-1} + (x_n - \mu_n)(x_n - \mu_{n-1}))/(n-1)$

used statistical descriptions, like the mean or the standard deviation, really tell about the underlying distribution of income and how we can make predictions from our observations. For instance, if another person enters the room, what properties are expected? A good bet would be to say the person is probably around 1.8 m tall, but it is obviously not a good assumption that this person earns approximately 60 million € per year! This "odd" behavior of the income statistics stems from the underlying distribution of income, namely the Pareto or power-law distribution. Similar statistical caveats have to be considered, to come back to the astrophysical topic of this thesis, when the flaring activity of Sgr A* is statistically analyzed. I will later show that the flux density distributions also follow power-laws. For that reason, one has to keep in mind that typical behavior, as expected by a normal distributed processes, cannot be assumed for Sgr A*'s flaring activity. Thus, some questions cannot be answered with common sense, i.e., in a Gaussian manner. For instance, if we have previously observed a light curve and have found that the maximum value is, e.g., 4 Jy, how likely is it that we observe a flare twice as bright in the future? And if we observe a radiation outburst of, say, 10 Jy, how does this newly obtained value change the statistical description of the emission process? Is the old model still valid or does it need to be adjusted or even completely rejected? And finally, if we assume that a power-law process is at work, how can we estimate the parameters of that distribution? To be able to answer this questions one needs to get familiar with the basic math of power-law distributions. Therefore, I will briefly describe some of their statistical properties in the following paragraphs.

The PDF of a simple power-law is given by

$$\mathrm{PDF}(x) \propto x^{-\alpha}. \tag{3.18}$$

This function approaches infinity for $x \to 0$ and is not defined for $x = 0$ (division by zero). Thus, there has to be a lower bound $x_{\min}$ only above which the power-law distribution is defined. Because a PDF has to normalized, i.e., the integral over the whole domain has to be unity, the PDF must contain a normalization constant C. This constant can easily be calculated:

$$\int_{x_{\min}}^{\infty} \mathrm{PDF}(x) = C \cdot \left. \frac{x^{-\alpha+1}}{-\alpha+1} \right|_{x_{\min}}^{\infty} = C \cdot \frac{-x_{\min}^{-\alpha+1}}{-\alpha+1} \overset{!}{=} 1 \tag{3.19}$$

$$\Rightarrow C = \frac{\alpha-1}{x_{\min}^{-\alpha+1}}. \tag{3.20}$$

Thus, the complete PDF of a power-law writes as

$$\mathrm{PDF}(x) = \begin{cases} 0 & \text{for } x \leq x_{\min} \\ \frac{\alpha-1}{x_{\min}} \left(\frac{x}{x_{\min}} \right)^{-\alpha} & \text{otherwise}. \end{cases} \tag{3.21}$$

By the definition in Eq. 3.7, it then follows that the CDF of a power-law is given by

$$\mathrm{CDF}(x) = \begin{cases} 0 & \text{for } x \leq x_{\min} \\ 1 - \left(\frac{x}{x_{\min}} \right)^{-\alpha+1} & \text{otherwise}. \end{cases} \tag{3.22}$$

and thus the respective CCDF as given in Eq. 3.8:

$$\begin{cases} 0 & \text{for } x \leq x_{\min} \\ \left(\frac{x}{x_{\min}} \right)^{-\alpha+1} & \text{otherwise}. \end{cases} \tag{3.23}$$

The result is remarkable and a special property of power-laws: the survival function of a power-law is a power-law again, the scaling index is just shifted by one. This is a very useful relation because, as we have seen in Eq. 3.13, the empirical CDF can directly be constructed from a given sample without further assumptions or information loss. Thus, if $(1 - \text{CDF})$ yields a power-law with a scaling index of β, the slope of the underlying PDF is automatically determined to be $\beta - 1$.

Moments of a power-law

Some surprising properties of power-laws can be understood when looking at the raw moments, i.e., the moments about zero, of these distributions. The nth raw moment is defined as:

$$m_n = \langle x^n \rangle = \int_{x_{\min}}^{\infty} x^n \text{PDF}(x) \mathrm{d}x = \frac{\alpha - 1}{x_{\min}^{-\alpha+1}} \int_{x_{\min}}^{\infty} x^{-\alpha+n} \mathrm{d}x \qquad (3.24)$$

$$= \frac{\alpha - 1}{x_{\min}^{-\alpha+1}(-\alpha + n + 1)} \cdot x^{-\alpha+n+1} \Big|_{x_{\min}}^{\infty} \qquad (3.25)$$

It can be seen, that Eq. 3.24 only converges, if the condition $\alpha > n + 1$ is satisfied. Then the nth moment is given by

$$m_n = \frac{\alpha - 1}{\alpha - n - 1} x_{\min}^n \qquad (3.26)$$

where m_1 is the expression for the mean value. Thus, for $\alpha < 2$ the mean and all higher moments are infinite, for $2 < \alpha < 3$ the mean is defined, but the distribution has an infinite variance. This is the reason for the "strange" results we obtained for the income example in the introduction of this chapter. If a quantity (as wealth and income) is power-law distributed and the slope is shallow enough, it is not meaningful to calculate the sample mean or variance.

For the sake of completeness I will also give the analytical formula for the nth central moment, i.e., the moment about the mean m_1, namely $m'_n = \int_{x_{\min}}^{\infty} (x - m_1)^n \text{PDF}(x) \mathrm{d}x$. One can show (Papoulis, 1984) that the following relations hold:

$$m'_2 = m_2 - m_1^2 \qquad (3.27)$$

$$m'_3 = m_3 - 3m_1 m_2 + 2m_3$$

$$m'_4 = m_4 - 4m_1 m_3 + 6m_1^2 m_2 - 3m_1^4 \qquad (3.28)$$

Thus, with Eqs. 3.26 and 3.27 we have a closed-form expression for the mean, the variance, the skewness and the kurtosis of a power-law.

MLE for power-laws

The likelihood function of a power-law is given by

$$\mathcal{L}(x_{\min}, \alpha) = p(x|x_{\min}, \alpha) = \prod_{i=1}^{n} \frac{\alpha - 1}{x_{\min}} \left(\frac{x_i}{x_{\min}} \right)^{-\alpha}. \qquad (3.29)$$

Taking the logarithm we obtain the following expression for the log-likelihood:

$$\log \mathcal{L} = \log p(x|x_{\min}, \alpha) = n \log(\alpha - 1) - n \log x_{\min} - \alpha \sum_{i=1}^{n} \frac{x_i}{x_{\min}}. \tag{3.30}$$

Here, the crucial point is that the PDF is only defined for values $x_i \geq x_{\min}$, otherwise it is zero (see Eq. 3.21). As a consequence, there is neither an analytic expression for the maximum likelihood in respect to $x_{\min}$ nor a numerical way of maximizing the likelihood function for this parameter. The larger $x_{\min}$ becomes, the larger will be $\mathcal{L}$. This means that the MLE for $x_{\min}$ will always yield the highest values of all x_i. As a result, only for a fixed value of $x_{\min}$ an MLE for α can be given:

$$\frac{\partial \mathcal{L}}{\partial \alpha} = 0 \tag{3.31}$$

$$\Rightarrow \alpha = 1 + n \left(\sum_{i=1}^{n} \log \frac{x_i}{x_{\min}} \right) \tag{3.32}$$

The best fit value for $x_{\min}$ has to determined by other means.

Slope of a power-law

Power-laws are often identified by plotting their PDF estimator (histogram or KDE) in a log-log diagram. The PDF transforms to a linear relation with a slope $m = \alpha$:

$$\log \text{PDF}(x) \propto -\alpha \log x \tag{3.33}$$

The same applies to the log-log plot of the (information-preserving) CCDF, the slope now is $\beta = \alpha + 1$. Thus, a naive power-law slope estimation would be a linear fit in the log-log space. However, in Sec. 3.1, I have argued that it is not the mathematically correct approach to apply curve fitting techniques to distributions. Nonetheless, one could argue that it is sufficient for a rough estimate of the power-law slope. In the following, I will show that the slope in a log-log diagram only represents the power-law scaling index, if we have a pure, not modified power-law. For other types of power-laws, namely shifted, bound and exponentially truncated power-laws (I will define this terms later) the slope of the log-log plot may significantly deviate from the scaling index α (see Fig. 3.2). Therefore, it should be avoided to identify power-law parameters by "graphical" means.

Shifted power-law

A power-law distributed random variable might be superimposed by a constant shift s. Thinking in terms of a random number generator, this means that for every drawn random value a constant s is added or subtracted. Such a situation is physically often given; one can think about power-law distributed flux densities of an object that are enhanced by some constant background radiation. Flares of Sgr A* are a concrete example: the observed flux densities of a flare come on top of the steady quiescent emission. An opposite case can be imagined as a power-law process that is attenuated by some constant value. The resulting distribution can be called a shifted power-law
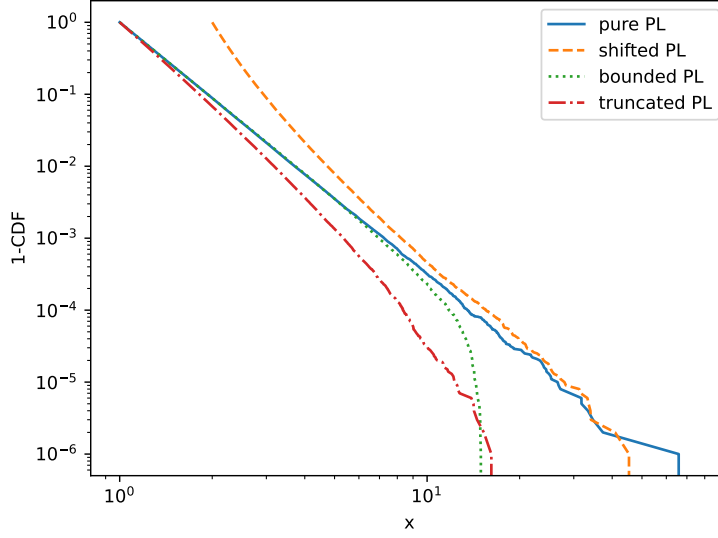
Figure 3.2: *Comparison of survival functions of different power-law types. All shown power-laws have a scaling index α = 4.5 and left side limit $x_{\min}$ = 1. The blue solid line shows a pure power-law, all other power-laws are generated with the following parameters: shifted power-law (dashed orange line): s = 1, bounded power-law (dotted green line): $x_{\max}$ = 15, exponentially truncated power-law (dash-dotted red line): λ = 0.2. Although all power-laws share the same "slope" α, it is obvious that this parameter cannot be estimated by linear regression in the log-log-plane. Depending on the type of power-law, the "true" slope is either identifiable in the left or right tail. Combinations of deviations from a pure power-law (e.g., a shifted power-law with an upper bound) can even lead to a situation where the complementary cumulative distribution function (CCDF) is completely S-shaped, without any linear section. The plot does deliberately not show the analytical functions but empirical CCDFs from randomly generated data so that the under-sampling in the high end tail becomes visible.*

and its PDF is given by

$$\text{PDF}(x) = \begin{cases} 0 & \text{for } x \leq x_{\min} + s \\ C_1 \cdot \left(\frac{x-s}{x_{\min}-s}\right)^{-\alpha} & \text{otherwise}\,. \end{cases} \tag{3.34}$$

Following basic definitions, one obtains for the CDF of a shifted power-law the following expression:

$$\text{CDF}(x) = \begin{cases} 0 & \text{for } x \leq x_{\min} + s \\ 1 - \left(\frac{x-s}{x_{\min}}\right)^{-\alpha+1} & \text{otherwise}\,. \end{cases} \tag{3.35}$$

In the case of a shifted power-law, the aforementioned linearity of the power-law in a log-log plane (Eq. 3.33) does not hold anymore. If we take the PDF, the logarithmic application gives

$$\log \text{PDF}(x) \propto -\alpha \log x - \alpha \log\left(1 - \frac{s}{x}\right), \tag{3.36}$$

and thus no longer a liner relation. Again, it can be seen that other fitting methods than linear regression in the log-log space have to be used to fit general power-law models.

Bounded power-law

Another modification of a pure power-law is the introduction of a fixed upper limit for the possible outcome of the stochastic process. This then yields a distribution that I call a bounded power-law. It can be imagined as a stochastic process with a physically limited reservoir from which random variables can be drawn. For instance, the size of forest fires have often been modeled with a power-law distribution (Malamud et al., 1998) and it is obvious that the size of such a fire is limited by the largest connected forest area. Another example, from the context of my work, is that it has been proposed by Neilsen et al. (2015) that the X-ray count rate distribution follows a bounded power-law (which I questioned in my publication because no physical reasoning was given, see Chap. 5). The PDF of a bounded power-law is given by

$$\text{PDF}(x) = \begin{cases} 0 & \text{for } x \le x_{\min} \text{ and } x \ge x_{\max} \\ C_2 \cdot x^{-\alpha} & \text{otherwise}, \end{cases} \tag{3.37}$$

its CDF by

$$\text{CDF}(x) = \begin{cases} 0 & \text{for } x \le x_{\min} \text{ and } x \ge x_{\max} \\ \frac{x^{-\alpha+1} - x_{\min}^{-\alpha+1}}{x_{\max}^{-\alpha+1} - x_{\min}^{-\alpha+1}} & \text{otherwise}. \end{cases} \tag{3.38}$$

Exponentially truncated power-law

Power-law distributions can show a decay in their tail. If this decay is described by an exponential, the resulting distribution is called exponential truncated power-law. Although, this kind of distribution can certainly also be introduced in a strictly mathematical way, I prefer to see them as a trade-off between a bounded and a pure power-law: in some situations a power-law distributed quantity is observed where it makes sense to introduce a sharp upper limit as in a bounded power-law. Often, though, it is not justifiable to define such a hard upper cutoff. On the other hand, I have shown that for power-law exponents below some threshold (three and two), the variance and the expected value, respectively, become infinite. For many real world examples, this seems unrealistic. A prototype for such a situation would be the distribution of group sizes of herd animal populations (Minasandra and Isvaran, 2018): neither an upper limit can be given nor infinitely large populations can be expected. Thus, an exponential truncation seems a sensible modification to "tame" the power-law's tail. Mathematically, the PDF of this distribution is given by

$$\text{PDF}(x) = \begin{cases} 0 & \text{for } x \le x_{\min} \\ C_2 \cdot x^{-\alpha} \exp(-\lambda x) & \text{otherwise}. \end{cases} \tag{3.39}$$

The CDF is expressed via the generalized incomplete gamma function $\Gamma(a, b, \infty)$ as

$$\text{CDF}(x) = \begin{cases} 0 & \text{for } x \le x_{\min} \\ \frac{\Gamma(-\alpha+1, \lambda \cdot x)}{\lambda^{-\alpha+1}} & \text{otherwise}. \end{cases} \tag{3.40}$$

In Subroweit et al. (2020) (Chap. 5), I demonstrated a concrete use case for an exponentially truncated power-law. I analyzed the X-ray count rate distribution of Sgr A* and found that using this kind of distribution yields a very canonical explanation of the observed emission statistics.

3.3   Bayesian Distribution Fitting, Markov Chain Monte Carlo (MCMC) and Approximate Bayesian Computation (ABC)

Bayesian statistics and Markov Chain Monte Carlo (MCMC) methods have evolved to become an important tool in astronomy during the past two decades. Fig. 3.3 shows the immense growth of popularity of these methods in astronomical papers since the early 2000s. In this section I will briefly explains these methods and demonstrate why they are so beneficial in modern astrophysics.
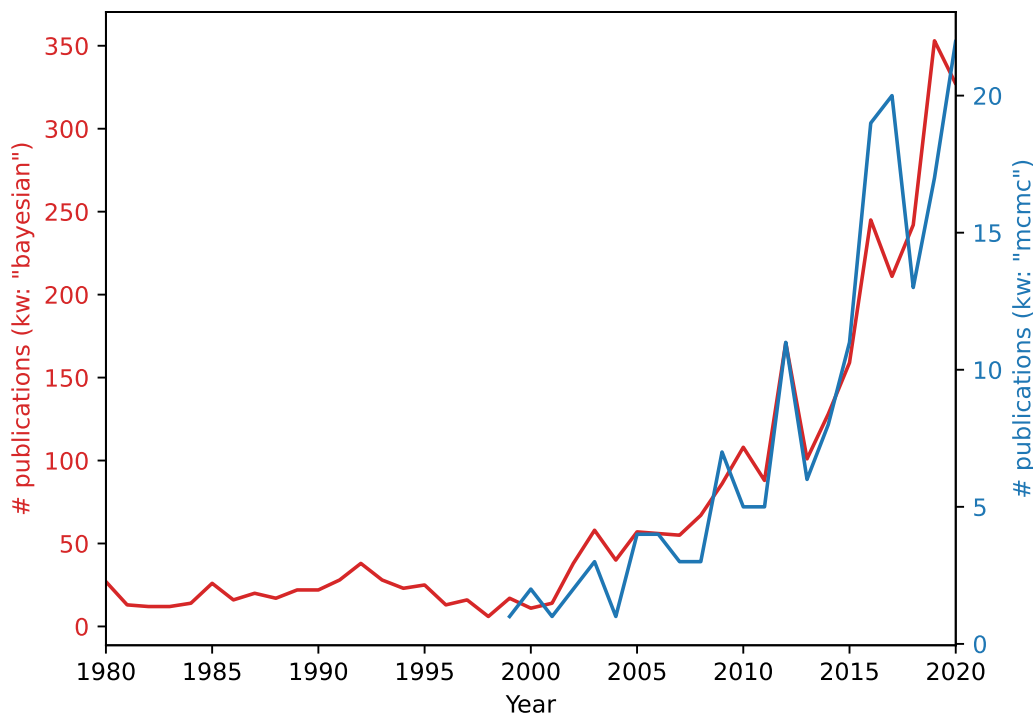

Figure 3.3: *Number of refereed papers published on the Astrophysics Data System (ADS) with the keywords "bayesian" (red) and "mcmc" (blue). The almost exponential rise of publications containing these keywords in the last 20 years is remarkable and shows the increasing importance of these fields of statistics.*

   Let me first start to explain one of the main differences between Bayesian and frequentist statistics: the concept of probability. In the frequentist approach, the probability of an event A, p_A, is the relative frequency of the event A in many trials. If n is the number of trials and n_A is the number of events where A is true, the frequentist definition of the probability of A is given by $p_A = n_a/n$. In the frequentist approach, the probability has a true, yet at the beginning of an experiment hidden, value which can be determined by following the law of large numbers. This means that if an experiment is repeated a large number of times, the relative frequency of an event will approach its true probability: $p_A = \lim_{n\to\infty} n_a/n$. Vice versa, this definition of a probability leads directly to the concept of the likelihood function $\mathcal{L} = p(x|\Theta)$. In the frequentist's world,

a system is described by a model with its true parameters θ and an experiment randomly yields measurements or data x drawn from that model. The likelihood function thus answers the question *How likely is the observed data x given the system's parameter's θ?*. The Bayesian concept of probability differs from the frequentist's definition. In Bayes theory, the probability for an event A is the reasonable expectation that the event A occurs, data updates the degree of belief for the probability p_A. As a consequence, the concept of true, only hidden, parameters θ of a system is weakened. The parameters itself become random variables with some probability after the observation of events x. Thus, an important quantity in Bayesian statistics is the posterior distribution $p(\Theta|x)$ which answers the question *How likely are system parameters Θ given the observed data x?*.

Closely related to the Bayesian concept of probability is Bayes' theorem which I will give in a form which is required later:

$$p(\theta|x) = \frac{p(\theta)p(x|\theta)}{p(x)} \tag{3.41}$$

Here, $p(\theta|x)$ and $p(x|\theta)$ are the aforementioned posterior and likelihood functions, $p(\theta)$ is called the prior and $p(x)$ the evidence. The prior represents the prior belief of the parameters θ as a distribution[2], the evidence is the total probability of observing x irrespective of the knowledge about θ. Generally $p(x)$ is often difficult to calculate as it requires the integration about all possible states of a given system. This might be the reason why Bayesian inference, though known since more than 250 years, has just recently become so popular. Some Bayesian evaluations tend to be computationally more expensive than frequentist approaches. The steadily increasing availability of computational power in the past 50 years has certainly led to a revival of Bayesian methods.

Another important development, which is closely related to the increase of computational power, is the use of Monte-Carlo-simulation in mathematical problems. Up to the first half of the 20th century, most physical systems were analytically analyzed. Monte-Carlo-simulations use methods of repeated random sampling and stochastic variables, e.g., to estimate uncertainties, perform numerical integration and draw random numbers from probability distributions. One important application are Monte-Carlo-Markov-chain algorithms which can sample from a given distribution, the so called target distribution. This is done by constructing a Markov-Chain with properties of the desired target distribution. Markov-Chains describe "memoryless" stochastic processes where different states of that process are connected with each other through transition probabilities. In this context "memoryless" means that the knowledge of just a few previous states is sufficient to make predictions about future states. This condition for the chain is

---

[2]I want to point out that I deem the introduction of priors as one of the main advantages of Bayesian statistics. Although, it seems subjective to introduce prior knowledge or beliefs into an equation, in my opinion this is a more "honest", objective way compared to some classical frequentist approaches. In the latter case, often boundary conditions and initial guesses are introduced or solutions are dismissed as "non-physical". That means, also frequentist statistics often uses implicit a priori beliefs without an underlying clearly defined mathematical concept. I my opinion, the explicit use of priors in Bayesian inference makes the approach more "objective".

also called the Markov property. Most chains need some number of initial transitions between different states until they reach the Markov property or so-called equilibrium state. This is often referred to as the "burn-in"-time. Let me give an example of an early and famous MCMC-algorithm, which is called the Metropolis-Hastings-algorithm (Hastings, 1970). It can be used to draw samples from an arbitrary target distribution $p(\phi)$. We define a transition distribution, $Q(\phi|\phi')$, which gives the probability of a state transition between ϕ' and ϕ. Often a symmetric transition distribution is chosen, so that $Q(\phi|\phi') = Q(\phi'|\phi)$. Then the algorithm is only called Metropolis-algorithm. We construct our Markov-chain as follows:

I Initialize random state ϕ

II Propose new state $\phi \rightarrow \phi'$ with $Q(\phi'|\phi)$

III Accept new state with probability $a(\phi', \phi) = \min\left[1, \frac{p(\phi')\, Q(\phi'|\phi)}{p(\phi)\, Q(\phi|\phi')}\right]$

IV If ϕ' is accepted, push it to sample chain, else go to step II)

V Set $\phi = \phi'$, go to step II)

Algorithm 3.2: *Schematics of the Metropolis-Hastings algorithm.*

It can be shown that this algorithm constitutes a random number generator for the target distribution $p(\phi)$, a chain of stochastic samples from p will be generated.

  I have now introduced some basic concepts of Bayesian inference and MCMC sampling. The question remains how this is useful for an astronomer having to deal with a probability distribution. To give an astrophysical example of what the posterior distribution actually is, the following situation can be imagined: given is a light curve x of an emitting source and we want to estimate the parameters of an assumed generative process with parameters θ. We are not only interested in the best fit parameters, but also in their uncertainties. The solution is given by the posterior distribution $p(\theta|x)$. If we knew that distribution we would know about, e.g., the mean (best fit) or standard deviation (uncertainty) values of θ. With Bayes theorem and the MCMC-algorithm, we are able to sample from $p(\theta|x)$ and thus numerically estimate it. The only difference to the MCMC sampling from a simple target distribution as shown before, is that we now replace the target distribution with the $p(\theta|x)$ as given in Eq. 3.41. If we plug that into the MCMC algorithm, we obtain an acceptance ratio

$$a(\theta', \theta) = \min\left[1, \frac{p(\theta)p(x|\theta)\, Q(\theta'|\theta)}{p(\theta')p(x|\theta')\, Q(\theta|\theta')}\right]. \tag{3.42}$$

It is important to note that the evidence term $p(x)$ as given in Eq. 3.41 has canceled out as it appears both in the numerator and the denominator of the fraction. Thus, the often very expensive calculation of $p(x)$ is no more necessary in the MCMC algorithm. The priors for θ can be chosen according to the prior knowledge of their parameters,

estimated from an independent previous observation.[3] In this context, "independent" could mean an estimate from another observation campaign (ideally with another instrument), a theoretical prediction and so forth. If no prior knowledge about θ is available, uninformative priors have to be used. Having chosen the prior distribution, one can now utilize the likelihood function to generate samples from the posterior using Alg. 3.2. Figure 3.4 depicts a simple example of the evolution of different sampler during an MCMC run.
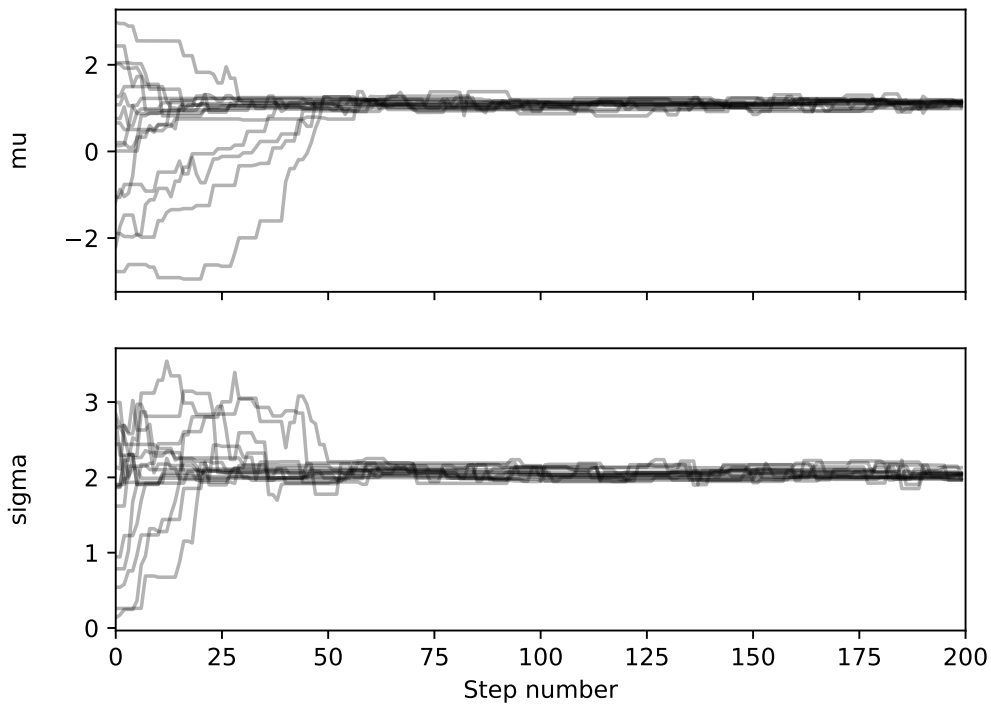
Figure 3.4: *Markov Chain Monte Carlo (MCMC) samples produced by the Metropolis-Hastings algorithm with 16 walkers per parameter. In this simple example, a normal distribution is fit to a randomly generated sample with parameters $\mu = 1$ and $\sigma = 2$. For each parameter, uniform priors were used. It can be seen that after the "burn-in" phase of approximately 60 iteration steps, the walkers have reached their equilibrium state. The Markov chains are memoryless, i.e., independent from their previous states. No matter of the initial starting position, each walker generates samples from the posterior distribution.*

---

[3]Sometimes a shortcut for constructing the priors of the parameters θ is used: the best fit parameters are estimated using some traditional, frequentist optimization, e.g., MLE and these estimates are taken to form informative prior distributions for θ. Strictly taken this violates the condition for Bayes' theorem, namely that the prior has to come from prior knowledge. The given data cannot be utilized twice to both get the prior and the posterior. Although seen in some publications, this is considered bad practice and called "double-dipping".

Intractable likelihoods and ABC

A crucial point to perform these kind of MCMC analyses is the knowledge of the likelihood function. In the previous paragraphs, I have assumed that one is able

- to write down the likelihood function and

- to calculate it with reasonable computational expense.

The first point might often be satisfied: either one knows an analytical expression for the likelihood or is able to calculate it via its basic definition (see Eq. 3.15). If two or more probability densities are given and the convolution integrals cannot be solved analytically, it is also possible to numerically calculate them and thus create an "empirical" likelihood function. For function fits, it can furthermore be shown that the logarithmic likelihood function is simply half of the negative χ^2-value (Berkson 1980 and references therein). But what can be done if the likelihood-function cannot be written down or cannot be efficiently calculated? Examples for the first case are some quantile distributions (McVinish, 2012), which are only defined via their quantiles without an explicit probability density, power-laws, as we have previously seen because there is no MLE estimator for the parameter $x_{\min}$ (see also Pilgrim and Hills 2021) or, in general, many dynamical evolution processes. For the latter case, it is easy to imagine that, especially for high dimensional systems, the calculation of the likelihood function tends to be time consuming if not completely unreasonable (this is sometimes called the *curse of dimensionality*). In Subroweit et al. (2020) (paper II, Chap. 5), I describe a situation where the likelihood function for an X-ray count rate distribution is given by a complicated mixture of multiple probability densities, Poisson noise and instrumental pile-up effects. This likelihood can certainly be considered as intractable. Here, a relatively new Bayesian technique comes into play, called Approximate Bayesian Computation (ABC). Imagine the following situation: given is some dataset of discrete samples. We have an intractable likelihood, but a generative model, i.e., a simulator, which can produce random samples x with the given parameters θ. Rubin (1984) propose the following algorithm:

  I Draw a proposal θ' from the prior $p(\theta)$

 II Simulate data x' with the generative model and θ'

III Accept θ' if $x' = x$

IV Go to I)

Algorithm 3.3: *Schematics of a simple Approximate Bayesian Computation (ABC) rejection algorithm for discrete data. Samples are accepted if the simulation yields exactly the same result as the observed data.*

As all proposals, which do not fulfill the condition $x' = x$, are rejected, this scheme is also called *simple rejection*. Rubin (1984) argue that this algorithm is equivalent to

sampling from the posterior:

$$p\left(\theta|(x' = x)\right) = p(\theta|x) \tag{3.43}$$

This means that without knowing and calculating the likelihood function we are able to draw samples from the posterior distribution. This is therefore also called *likelihood free inference*. Of course, the proposed algorithm has two major disadvantages: first, it only works with discrete data, as it needs an exact identity between simulated and observed data. Secondly, it is also computational ineffective as the acceptance ratios tend to be small. Most proposed parameters will be rejected and the sampler chain only slowly fills. To circumvent these problems, Pritchard et al. (1999) used a slightly modified approach. By defining some distance metric $\rho(x, y)$ between two datasets x and y, the algorithm is given by

   I Draw a proposal θ' from the prior $p(\theta)$

  II Simulate data x' with the generative model and θ'

 III Accept θ' if $\rho(x', x) \leq \epsilon$

 IV Go to I)

Algorithm 3.4: *Schematics of a simple Approximate Bayesian Computation (ABC) rejection algorithm for continuous data. Samples are accepted if the simulation yields approximately the same result as the observed data.*

Using this scheme, we now sample from

$$p\left(\theta|\rho(x', x) \leq \epsilon\right) \approx p(\theta|x) \quad \text{for small } \epsilon, \tag{3.44}$$

thus, from an approximation to the true posterior. What values of ϵ are small enough to have a good approximation depends on the specific case. Anyhow, this algorithm is now also applicable to continuous data.

Nevertheless, this algorithm may also lack computational efficiency. Depending on the size of ϵ, the rejection rate still might be high. Also, the distance between observed and modeled data has to be calculated in each iteration step. In the case of one-dimensional data this could for instance be the Kolmogorov-Smirnov or the Anderson-Darling distance, to name just two examples. In general, the calculation of the distance can still be expensive if the the dataset is large in numbers or dimensions (I mentioned the so-called curse of dimensionality earlier). Therefore, Beaumont et al. (2002) proposed an updated version of an ABC algorithm. The idea is that if one finds a *summary statistics* $S(x)$, which summarizes the data x sufficiently enough, one can use the distance between summary statistics instead of the data itself, which can significantly reduce the computational effort:

   I Draw a proposal θ' from the prior $p(\theta)$

  II Simulate data x' with the generative model and θ'

  III Calculate the summary statistics $S(x')$

  IV Accept θ' if $\rho(S(x'), S(x)) \leq \epsilon$

   V Go to I)

Algorithm 3.5: *Schematics of an Approximate Bayesian Computation (ABC) rejection algorithm using summary statistics. Samples are accepted if the summary statistics of the simulation and the observed data are approximately identical.*

It can be shown that

$$p\left(\theta|\rho(S(x'), S(x)) \leq \epsilon\right) \approx p(\theta|x) \quad \text{for small } \epsilon \text{ and sufficient } S. \tag{3.45}$$

The term *sufficient* is, of course, crucial in this context. Whether some data is decently summarized by some statistics is case dependent. Nonetheless, to give a simple example, it is obvious to see that two normal distributed samples are decently summarized by their mean and some quantile. It is not necessary to compare the entire datasets, e.g., by a CDF-based metric.

   It is beyond the scope of this thesis to give an exhaustive overview of the most recent developments in ABC-based statistics. As a final example of an optimization of the aforementioned algorithms, I want to mention another enhanced ABC-scheme. All previously introduced procedures still may be subject to low acceptance ratios. Marjoram et al. (2003) introduce a new approach which finally connects ABC with MCMC methods. Their recipe can be summarized as follows:

     I Initialize some initial θ

    II Propose a new θ' according to the proposal distribution $Q(\theta'|\theta)$

   III Simulate data x' with the generative model and θ'

   IV Calculate the summary statistics $S(x')$

    V If $\rho(S(x'), S(x)) \leq \epsilon$ go to VI, else return to II)

   VI Accept θ' with probability $a(\theta', \theta) = \min\left[1, \frac{p(\theta')\,Q(\theta'|\theta)}{p(\theta)\,Q(\theta|\theta')}\right]$

  VII If θ' is accepted, push it to sample chain, else go to II)

 VIII Set $\theta = \theta'$ and return to II)

Algorithm 3.6: *Schematics of an Approximate Bayesian Computation - Markov Chain Monte Carlo (ABC-MCMC) algorithm using summary statistics. Samples from the approximated posterior function are generated by Markov chains.*

Conceptually, this algorithm closes the gap between ABC and classical MCMC approaches. ABC sampling is now performed via a Markov Chain. In the given scheme the Markov Chain is implemented via the Metropolis-Hastings algorithm. Nevertheless,

the Metropolis-Hastings algorithm is just one among other procedures that fulfills the
Markov-Chain criteria. Many optimized algorithms have been developed in the last
15 years. For instance, ABC - Sequential Monte Carlo (SMC, Sisson et al., 2007) is
one of those schemes. The principal idea behind SMC to sequentially (i steps) create
populations of sampled parameters θ_n, i (each population contains n so called particles)
with successively decreasing thresholds $\epsilon_0 > ... > \epsilon_i \geq 0$. The particles of the first
population are drawn from the prior distributions, following populations are drawn
from the perturbed[4] population. Therefore, the populations are supposed to sequentially
evolve toward the desired posterior distribution (see Fig. 3.5 for an example of an
ABC-SMC sampling). Good overviews and more explanations about ABC-SMC are, for
instance, given in Toni et al. (2009) or Beaumont (2010). Some examples for MCMC
and ABC libraries which I often used throughout the course of my PhD-studies are emcee
Foreman-Mackey et al. (2013), PyMC Salvatier et al. (2016) and pyABC Klinger et al.
(2018).
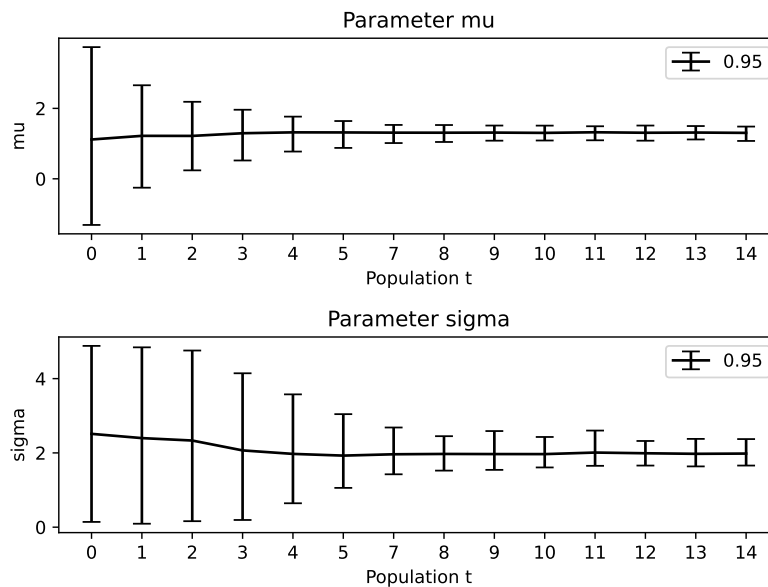
Figure 3.5: *Example of a Sequential Monte Carlo - Approximate Bayesian Computation (SMC-ABC) sampling routine. The same data as in Fig. 3.4 is fitted, i.e., samples from a normal distribution with $\mu = 1$ and $\sigma = 2$. As a summary statistics, I used the 50th and 68th percentile, $P_{50\%}$ and $P_{68\%}$. The distance function was defined as L2-metric between the vectors $(P_{50\%}, P_{68\%})$ of the original and the simulated data. A population size of 1000 was chosen and uniform priors used. It can be seen that the 95th confidence interval of the approximate posterior distribution contracts and converges increasingly with consecutive populations. The true posterior can be considered as well approximated, the chosen summary statistics and metric as sufficient (see the text for details).*

---

[4]ABC SMC requires the use of a perturbation kernel. That means that an accepted particle is taken and
its parameter vector is randomized to sufficiently explore the parameter space

3.3.1 Astrophysical Example of an Intractable Likelihood and ABC: Pile-up on an X-ray CCD

In the previous section, I have motivated the use of ABC by intractable likelihoods. Though I have not demonstrated yet how this was relevant in my concrete astrophysical research. In the following, I will describe in more detail why ABC significantly facilitated my statistical analyses. As mentioned in Sec. 2.2.1, X-ray observations with Chandra are often affected by pile-up. Additionally, the X-ray count rate from Sgr A* are so low that Poisson statistics has to be applied. Thus, both effects have to be incorporated into a parametric description of the emission process. I will now show, how a likelihood function for the X-ray count rate distribution had to be constructed, why this is a difficult task and how ABC is relatively easy to implement for this kind of problem.

First, I want to address the problem of Poissonian photon noise in the field of X-ray observations of Sgr A*. The observed count rates are in general very low, i.e., even for the brightest flares the count rates rarely exceed 0.1 counts per second (30 counts in a 300 s bin). Therefore, any estimate for the count rate distribution has to consider Poisson statistics. Let $\mathrm{d}N/\mathrm{d}r$ be the noise-free PDF of the count rate r, but r underlies Poisson noise. Then the PDF for the observed variable r' is given by

$$\frac{\mathrm{d}N}{\mathrm{d}r'} = \int \frac{r^{r'}}{r'!} \exp(-r)\frac{\mathrm{d}N}{\mathrm{d}r}\mathrm{d}r, \tag{3.46}$$

and the process is called a Cox-process. This formula is quite suggestive: the PDF of the random variable r' is a "poissonized realization" of the PDF of r. In principle, one can now formulate a model for $\mathrm{d}N/\mathrm{d}r$ (for instance, a truncated power-law), plug it in into Eq. 3.46 and utilize the outcome for the likelihood function. Nevertheless, one has to keep in mind that r is not the incident count rate Λ_i, i.e., the count rate as theoretically expected from the emission model, but the pile-up reduced, observed count rate. Following the official Chandra guidelines (see Subroweit et al. 2020 and references therein), the fraction of photon counts which are lost due to pile-up, f_d, can be estimated by

$$f_d = 1 - \frac{(\exp(\alpha - \Lambda_i) - 1)\exp(-\Lambda_i)}{\alpha\Lambda_i}. \tag{3.47}$$

Here, α is the grade migration parameter and Λ_i is the incident, that means the true source count rate. The parameter α describes the probability $p(e) \sim \alpha^{n-1}$, that an event e is detected, when n photons hit the detector within a readout frame without exceeding the energy limit. Often, α has to be determined as a free parameter through spectral fits. Due to the faintness of Sgr A*, α can safely be assumed to be ~ 1, though. Eq. 3.47 can also be formulated in a slightly different way: if r is the observed count rate, it is given by

$$r = \Lambda_i \cdot (1 - f_d(\Lambda_i)). \tag{3.48}$$

This is obviously true, as $1 - f_d$ is the fractions of photons **not** lost due to pile-up. If all photons were affected by pile-up, Eq. 3.48 would fully describe the relation between observed and incident count rate due to pile-up. However, only non-dispersed, 0th-order photons are affected by pile-up, for dispersed, higher order (mainly 1st-order) photons pile-up is negligible. Thus, r is given by

$$r = r_0 + r_1. \tag{3.49}$$

This means that if an observed, pile-up affected count rate r is given, one first needs to know about the ratio of 0th to 1st-order photons. Then, one can calculate r_0 and r_1. For the data I used, one empirically finds that the ratio of 0th to 1st-order photons is given by

$$\frac{\Lambda_{i,0}}{\Lambda_{i,1}} = 1.6. \tag{3.50}$$

$$\Rightarrow \Lambda_{i,0} = 1.6\Lambda_{i,1} \quad \text{and} \quad \Lambda_{i,1} = 0.625\Lambda_{i,0}, \tag{3.51}$$

where the total number of counts Λ_i is, of course, given by

$$\Lambda_i = \Lambda_{i,0} + \Lambda_{i,1}. \tag{3.52}$$

Thus, we have

$$\Lambda_i = 1.6\Lambda_{i,1} + \Lambda_{i,1} = 2.6\Lambda_{i,1} \quad \text{and} \quad \Lambda_i = \Lambda_{i,0} + 0.625\Lambda_{i,0} = 1.625\Lambda_{i,0} \tag{3.53}$$

$$\Rightarrow \Lambda_{i,0} = \frac{1}{1.625}\Lambda_i \approx 0.6154\Lambda_i \quad \text{and} \quad \Lambda_{i,1} = \frac{1}{2.6}\Lambda_i \approx 0.3846\Lambda_i \tag{3.54}$$

We can now bring Eqs. 3.48, 3.49 and 3.54 together to get a final expression for the observed count rate r, given as a function of the incident photon count Λ_i:

$$r(\Lambda_i) = \left(\exp(1 - 0.6154\Lambda_i) - 1\right)\exp(-0.6154\Lambda_i) + 0.3846\Lambda_i. \tag{3.55}$$

Thus, if we have a model for the PDF of the incident count rate $dN/d\Lambda_i$, we can write down a formula for the noise-free, pile-up affected count rate distribution as

$$\frac{dN}{dr} = \frac{dN}{d\Lambda_i}\frac{d\Lambda_i}{dr}. \tag{3.56}$$

Together with Eq. 3.46, which accounts for photon noise, we obtain for the observed, piled-up up count rate

$$\frac{dN}{dr'} = \int \frac{r^{r'}}{r'!}\exp(-r)\frac{dN}{d\Lambda_i}\frac{d\Lambda_i}{dr}dr. \tag{3.57}$$

In the concrete case, I assumed that an exponentially truncated power-law with $dN/d\Lambda_i \propto \Lambda_i^{-\alpha} \cdot \exp(-\lambda\Lambda_i)$ (see Eq. 3.39) describes the incident count rate. $d\Lambda_i/dr$ can be calculated according to Eq. 3.55. However, without writing down the final equation, it is easy to see that the resulting PDF and the respective likelihood function tends to be very unwieldy. In addition, to get the full description of the entire emission mechanism, Eq. 3.57 has to be convolved with another Poisson distribution which accounts for the quiescent background emission (due to the low count rates, pile-up can be neglected for the quiescent emission). Thus, the calculation becomes computationally very expensive, especially when repetitively computed hundreds or thousands of times in an optimization routine. This is exactly what can been called an intractable likelihood function and what initially motivated the use of ABC.

Let me now consider the given case within an ABC framework. I recall that for implementing an ABC sampler, the knowledge of the likelihood function is not necessary, the only requirement is the ability to simulate data according to a given model. Power-law distributed random variables can efficiently be generated by inverse transform

sampling because we know the analytical expression for the CDF (see Eq. 3.40 for an exponentially truncated power-law). Applying pile-up corrections (as given in Eq. 3.55) and Poisson noise is also straightforward. Thus, we can construct a random number generator that simulates observational data according to the power-law emission model. In each ABC iteration step, mock data is created, and the distance to the observed data is calculated, to sample from the posterior of the parameters θ. The resulting fitting routine is depicted in Fig. 3.6 and can schematically be summarized as follows:

- Generate incident count rate:
  inverse transform sampling from power-law model $\rightarrow \Lambda_i(\theta)$

- Simulate pile-up $\rightarrow r(\Lambda_i)$

- Apply Poissonian photon noise $\rightarrow r'(r)$

- Compare r' with the observed data

This scheme can be plugged in into an efficient ABC sampler as described in Sec. 3.3. In this specific case, the ABC approach is easier to implement and computational less expensive compared to classical likelihood-based fitting routines.
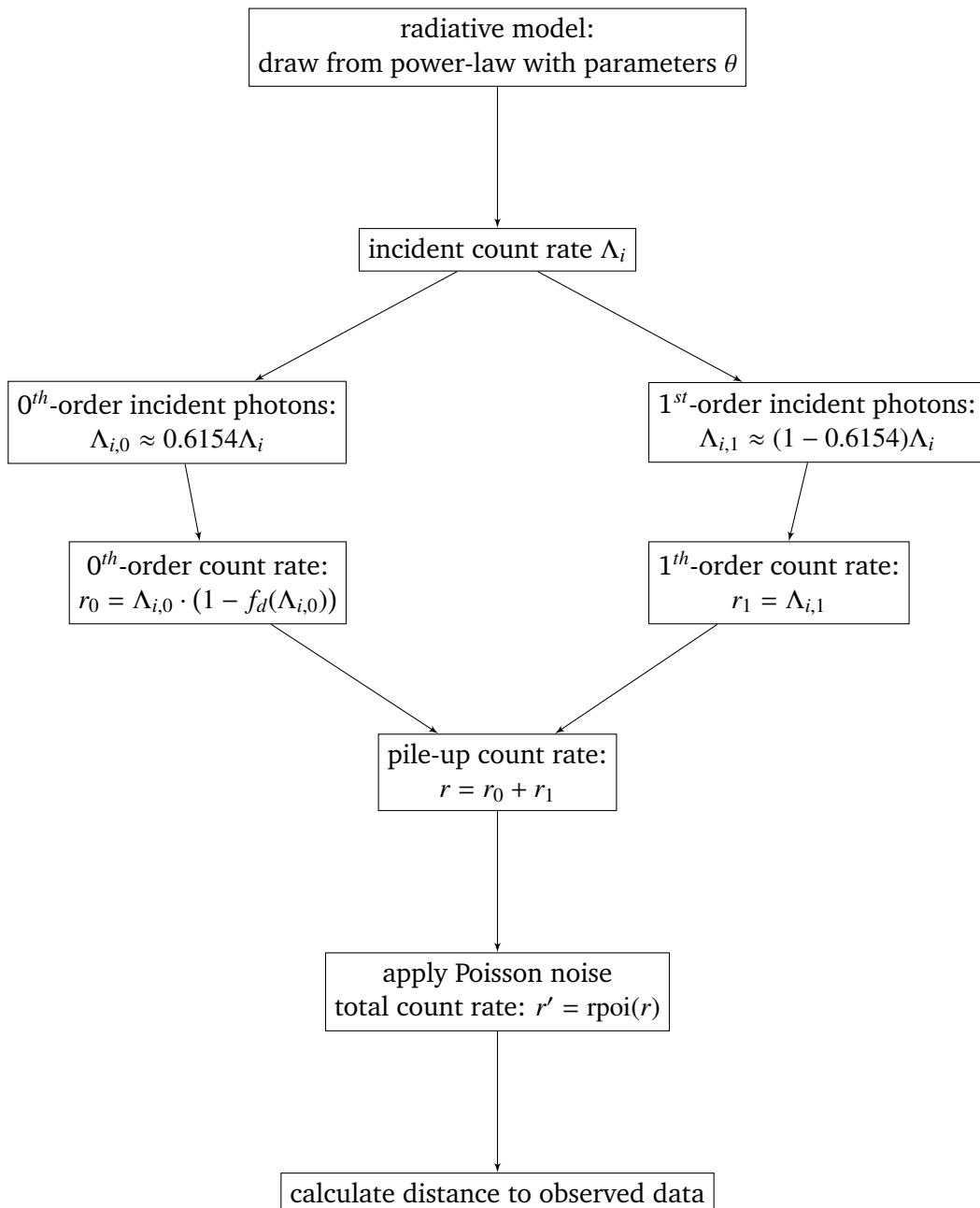
Figure 3.6: *Scheme of the count rate simulation used in the Approximate Bayesian Computation (ABC) sampling in Subroweit et al. (2020) (Chap. 5). It is easy to generate mock data from a model with parameters θ and compare it to the observed data with a custom metric, but not to write down and calculate the explicit likelihood $\mathcal{L}(x|\theta)$. This makes the perfect case for ABC. The division into two paths for the 0th and 1st order count rates is not necessary (see Eq. 3.55) but helps to intuitively understand the underlying observational process and to mathematically keep track of the count rate contributions.*

Paper I: Submillimeter and Radio Variability of Sagittarius A* - A Statistical Analysis

4

Over almost three decades, the flaring activity of Sgr A* has been monitored at different wavebands. One of the most comprehensive studies was published by Witzel et al. (2012). Using K-band (2.2 μm) lightcurves obtained between 2003 and 2010 using the Nasmyth Adaptive Optics System (NAOS) - Near-Infrared Imager and Spectrograph (CONICA) instrument, in short NaCo, at the Very Large Telescope (VLT), the authors presented an analysis of the NIR flux density distribution. They found that above the detection limit of the instrument, all observed flares can be described by a pure power-law with a scaling index $\alpha = 4.2$. Due to spectral index (Bremer et al., 2011) and polarization measurements (Shahzamanian et al., 2015), it is evident that the NIR flares are optically thin synchrotron emission. Additionally, it has been observed that flares in the radio regime follow NIR flares with time delays of several 10 minutes to hours Yusef-Zadeh et al. (2009). This suggest that the flare emitting source regions are initially optically thick in the radio regime and become optically thin after a source expansion has taken place. The modeling of individual multi-waveband observations has also revealed that the initial transition between optically thin and thick emission, the so-called synchrotron turnover frequency, lies approximately in the submm regime (Eckart et al., 2012). In this paper, I analyze the flux density distribution of two data sets: first, 350 GHz submm lightcurves obtained with APEX/LABOCA between 2008 and 2014 with additional data taken from the literature from 2004 to 2009 with similar frequencies. Secondly, 100 GHz radio lightcurves obtained with ATCA between 2010 and 2014. The ATCA data had previously been published by Borkar et al. (2016). I am able to show that, within the uncertainties, the flux density distributions at both wavelengths can also be described by a power-law with scaling index $\alpha \sim 4$. This implies that the variability in the radio, submm and NIR share a common origin. Furthermore, it is compatible with an adiabtically expanding plasmon model.

In general the fitting of power-law distributions in observational data requires special techniques as described in this paper. It is neither sufficient to identify a power-law by its slope in the log-log-space nor is it possible to conduct classical MLE. Special fitting

techniques are described and successfully applied in the paper. Here, the identification of the submm flux density distribution as a shifted power-law (see Sect. 3.2) was the crucial point in the analysis, otherwise too steep power-law could have mistakenly been identified.

As mentioned earlier, all the data acquisition and reduction has not been performed by me. The LABOCA data was reduced by the second author of this paper, Macarena García-Marín, the ATCA data by the fourth author, Abhijeet Borkar. The rest of the analysis was conducted by myself.

Astronomy & Astrophysics

Submillimeter and radio variability of Sagittarius A*

A statistical analysis⋆

M. Subroweit[1], M. García-Marín[1,2], A. Eckart[1,3], A. Borkar[1], M. Valencia-S.[1], G. Witzel[4],
B. Shahzamanian[1], and C. Straubmeier[1]

[1] I. Physikalisches Institut der Universität zu Köln (PH1), Zülpicher Straße 77, 50937 Köln, Germany
   e-mail: subroweit@ph1.uni-koeln.de
[2] Space Telescope Science Institute, 3700 San Martin Drive, Baltimore, MD 21218, USA
[3] Max-Planck-Institut für Radioastronomie (MPIfR), Auf dem Hügel 69, 53121 Bonn, Germany
[4] Dep. of Physics and Astronomy, University of California Los Angeles (UCLA), 465 Portola Plaza, Los Angeles, CA 90095, USA

ABSTRACT

We report on a statistical analysis of the 345 GHz submillimeter (submm) and 100 GHz radio flux density distribution of Sagittarius A* (Sgr A*). The submm data set consists of 345 GHz data obtained from different Large Apex Bolometer Camera (LABOCA) campaigns between 2008 and 2014, and additional literature data from 2004 to 2009 at comparable wavelengths. The radio observations were carried out with the Australia Telescope Compact Array (ATCA) between 2010 and 2014. We used a combined maximum likelihood estimator (MLE) and Kolmogorov-Smirnov (KS) statistics method to test for a possible power-law distribution in the high flux density excursions (flares) at both wavebands. We find that both flux density distributions can be described by a shifted power-law of the form $p(x) \propto (x - s)^{-\alpha}$ with $\alpha \sim 4$ (submm: $\alpha = 4.0 \pm 1.7$; radio: $\alpha = 4.7 \pm 0.8$). The same power-law index was previously found for the near-infrared (NIR) flux density distribution. These results may strengthen our preferred flare emission model: a combined synchrotron self-Compton (SSC) and adiabatically expanding self-absorbed synchrotron blob model where the flaring activity across all wavebands stem from the same source components and the variable emission can be described by a single state red noise process. Within the framework of the expanding blob model the similarity of the radio and the submm flux density distribution may also narrow down possible initial synchrotron turnover frequencies ν_0 to be mainly around 350 GHz and possible expansion velocities $v_{\exp}$ to be predominantly around 0.01 c.

Key words. black hole physics – galaxies: statistics – Galaxy: nucleus – radio continuum: general – submillimeter: general – Galaxy: center

1. Introduction

Observations of stellar motions in the nuclear star cluster (S-cluster) and the fitting of individual S-cluster star orbits have brought compelling observational evidence for a supermassive black hole (SMBH) at the very center of the Milky Way (Eckart & Genzel 1996; Genzel 2000; Schödel et al. 2002). The position of this compact and massive object coincides with an uncertainty of less than a few milliarcseconds with the position of the emission source Sagittarius A* (Sgr A*) (Trippe et al. 2006). Therefore the gravitational center of the Galactic center (GC) and the radio emission source are associated with the same object.

Sgr A* is, in terms of the Eddington luminosity L_{Edd}, a faint galactic nucleus with a total bolometric luminosity of only $10^{-8} \times L_{\mathrm{Edd}}$. First detected in the radio regime by Balick & Brown (1974), over the past decades Sgr A* has been monitored across various wavebands. Though optical and ultraviolet emission of the source is not detectable due to the absorption of the Galactic plane's dust band, the radio, submillimeter (submm), infrared (IR) and X-ray spectrum is relatively well known. Most

of the energy is emitted in the submm regime, therefore this area in the spectral energy distribution (SED) is also referred to as the "submm bump". The steady quiescent flux density emitted in the submm regime has been found to be about 3 Jy (García-Marín et al. 2011; Dexter et al. 2014). This corresponds to a luminosity $L_{\mathrm{submm}} \sim 10^{35}$ erg s^{-1}. Sgr A* is also always bright at radio bands (1–300 GHz). The rise of the spectrum from radio frequencies to the submm-bump can roughly be described as a power-law with an exponent of one third (Falcke et al. 1998). The existence of a quiescent IR emission is still debated, only strong upper limits for a possible steady emission could be constrained so far (Hornstein et al. 2002; Genzel et al. 2003; Sabha et al. 2010). The SED of Sgr A* shows a rapid drop from the submm bump to the IR regime. Faint quiescent X-ray emission has been observed to be about $L_{2-10\,\mathrm{keV}} \sim 10^{33}$ erg s^{-1} (Baganoff et al. 2003; Quataert 2002).

Sgr A* also shows flaring activity across all observed wavelengths. Typically, these emission outbursts occur on timescales of approximately one hour (Ghez et al. 2004; Herrnstein et al. 2004). Light-travel arguments imply that the flaring mechanism originates from compact regions on scales of a few Schwarzschild radii (Genzel et al. 2003). Very long baseline interferometry (VLBI) observations have also revealed, that these regions are located in the innermost accretion region in the direct

---

vicinity of the SBMH (Doeleman et al. 2009). Therefore the investigation of the flaring activity of Sgr A* provides important information about emission processes next to the SMBH.

The highest variabilities can be found in the X-ray regime, where flaring events with flux densities reaching to two orders of magnitude above the quiescent state can be observed approximately once a day (Porquet et al. 2003; Neilsen et al. 2014). Concurrent multi-waveband observations have also revealed that these X-ray flares are always accompanied by IR flares, but not vice versa (Eckart et al. 2008a; Dodds-Eden et al. 2009; Yusef-Zadeh et al. 2009). Flaring events with maximum flux densities of about one order of magnitude above the quiescent state are detected in the near-infrared (NIR) regime approximately four times a day. The simultaneity of IR and X-ray flares indicates that both emission types stem from the same source components. This can conveniently be explained by a synchrotron self-Compton (SSC) process (Marscher 1983; Eckart et al. 2012): the same population of electrons that emits optically thin NIR synchrotron radiation interacts with the produced synchrotron photons again and scatters them in an inverse Compton process to X-ray energies. High flux density excursions in the submm regime of a factor of up to two above the quiescent emission have been detected (Yusef-Zadeh et al. 2006a; Trap et al. 2011). Toward radio frequencies the amount of variability continuously decreases. Herrnstein et al. (2004) report on rms variations at 43 GHz and 14 GHz of 21% and 15%, respectively, and according to Falcke (1999) the variation at 8.3 GHz and 2.3 GHz decreases to 6% and 2.5%, respectively.

Simultaneous multi-wavelength campaigns have revealed that the radio, submm, NIR and X-ray emission are correlated. Submm flares seem to follow concurrent NIR and X-ray outbursts with time delays ~1 h (Marrone et al. 2008; Trap et al. 2011; Eckart et al. 2012). Delayed flares can also be observed at lower frequencies. Yusef-Zadeh et al. (2008) report on time delays of about 0.75 h between submm and 40 GHz flares. Additionally, time delays of about 0.5 h between 40 GHz and 20 GHz have been reported by the same authors (Yusef-Zadeh et al. 2006b). These delayed low frequency flares can be described with a model of adiabatically expanding electron clouds that emit through the synchrotron self-absorbed mechanism (later also referred to as blobs or synchrotron clouds, Eckart et al. 2012, 2009; Marrone et al. 2008; van der Laan 1966). Hence, a combined SSC/expanding blob model is well suited to interpret the flaring activity of Sgr A* across all observed wavebands: synchrotron clouds with initial turnover frequencies ν_0 in the submm or above[1] emit optically thin ($\nu > \nu_0$) IR emission and optically thick ($\nu < \nu_0$) radio to submm emission. An SSC process simultaneously gives rise to the X-ray flares. These synchrotron blobs expand adiabatically which leads to a decrease of the turnover frequency and therefore to delayed flares throughout the radio frequencies.

Albeit, at the moment there is no consensus about the physical origin of flares. Possible other explanations are, without any claim to completeness, orbiting hotspots (Broderick & Loeb 2006), mildly relativistic jet outflows (Falcke et al. 2009), accretion instabilities (Tagger & Melia 2006), shock heating (Dexter & Fragile 2013), tidal disruption of asteroids (Zubovas et al. 2012), self-organized criticality (Li et al. 2015) or general relativistic magnetohydrodynamic (GRMHD) models (Chan et al. 2015).

Over the past decades sufficient data sets have been compiled that it is also possible to analyze the flaring emission of Sgr A* with statistical methods (e.g., Yusef-Zadeh et al. 2011; Dexter et al. 2014; Neilsen et al. 2014). These statistical investigations can put additional constraints on emission models of the SMBH. Witzel et al. (2012) presented a comprehensive analysis of the K_S-band (2.2 μm) NIR emission. They found that the high-flux part of the K_S-band emission is well described by a single state power-law distribution of the form $p(x) \sim x^{-\alpha}$ with an index $\alpha \sim 4$. Shahzamanian et al. (2015) have also successfully described the distribution of the polarized K_S-band flux density with a power-law distribution of the same index. In the framework of a combined SSC/expanding blob model the NIR flux density distribution ought to be tightly linked to the flux density distributions at other wavebands.

In this paper we present a statistical analysis of the 345 GHz (submm) and 100 GHz (radio) emission under the hypothesis of a power-law distribution. In Sect. 2.1 we present the submm data and in Sect. 2.2 the radio data. The statistical analysis of the submm and radio data is shown in Sects. 3 and 4, respectively. Sect. 3.4 might be of general interest, as we review a power-law fitting technique introduced by Rácz et al. (2009), hereinafter RKE09, which is perfectly suited for situations, where a power-law distribution is superimposed by a strong steady contribution. This may be the case for the submm dataset. The fitting algorithm is able to estimate and separate the quiescent contribution from the power-law distributed variable emission. In Sect. 5 we discuss the results in the context of the adiabatic expanding blob model. Finally we summarize our findings in Sect. 6.

2. Observations and data reduction

2.1. The submm data

Our analysis of the submm flux density distribution of Sgr A* is based on two different data resources. First, we used data coming from the Large Apex Bolometer Camera (LABOCA) mounted at the Atacama Patfinder Experiment (APEX) telescope (Siringo et al. 2009). The light curves were obtained between 2008 and 2014. Secondly, to have a more statistically significant sample, we extended our data set with literature data.

2.1.1. LABOCA observations

LABOCA is a multi-channel bolometer array, consisting of 295 channels, installed at the APEX telescope. APEX is a 12 m radio telescope located at the Llano de Chajnantor Observatory 50 km east of San Pedro de Atacama in northern Chile. It is situated at an altitude of 5014 m. LABOCA operates in the 345 GHz (870 μm) atmospheric window and has a bandwidth of 60 GHz. The beam shape can be described as a circular Gaussian with a full width half maximum (FWHM) ~19″. For a detailed description of the observational process and data reduction we refer the reader to Eckart et al. (2008a,b). Here we only give a short overview:

The GC observations were performed using the On-the-fly (OTF) mapping technique with about 280 s integration time, map sizes of about 0.7° × 0.4°, with a fully sampled map[2] of 0.5° × 0.17°. For different observations the position angle of the scan with respect to the Galactic plane was changed to average out artificial scanning effects. During observations in 2008 and 2009 we switched the angle between 10°, 0° and −10°;

---

[1] This can be derived from polarization measurements of flare emission (Eckart et al. 2007; Marrone et al. 2008).

[2] No measurement gap larger than half of the beamwidth.

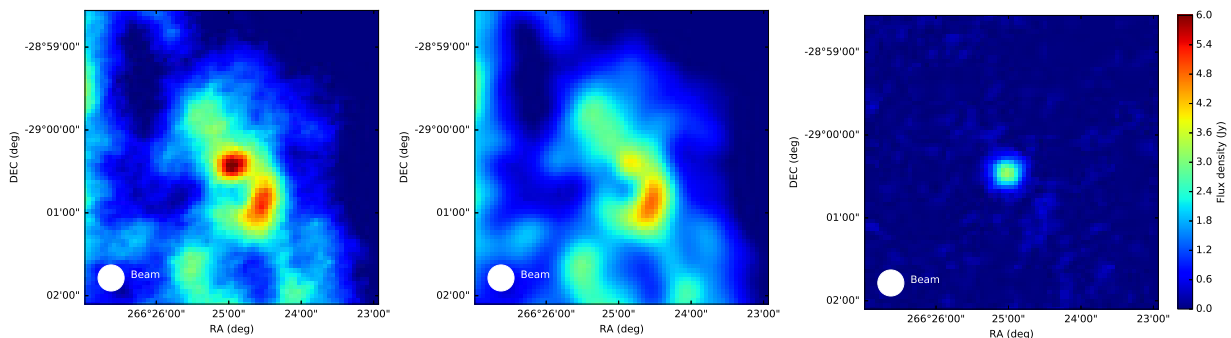M. Subroweit et al.: Submillimeter and radio variability of Sagittarius A*

Fig. 1. Data reduction process for the LABOCA campaigns. All maps are zoomed to the innermost 3.5′ × 3.5′. *Left*: a single measurement map of the GC from 2009-05-17T04:19:58. *Center*: model of the extended submm emission from the GC: co-added maps with subtracted point source at the position of Sgr A*. *Right*: remaining map for the 2009-05-17T04:19:58 map after subtraction of the GC model for the extended emission. The point like source represents the submm emission from Sgr A* itself.

all other observing campaigns used a random angle between −47° and −17°. Furthermore, measurements of secondary calibrators (G10.62, IRAS 16293-2422) and skydips were carried out for different observations. Skydips allow to determine the opacity of the atmosphere as a function of elevation and secondary calibrators are close to the GC and therefore allow calibration with a minimum amount of telescope driving time.

Data reduction was done with the Bolometer Array Analysis Software (BoA, Schuller 2012). This involves the following steps: atmospheric correction, flat-fielding, de-spiking, (spatially correlated) sky noise removal, correlated instrumental noise removal and a correction for pointing offset. In the left panel of Fig. 1 we show a resulting GC map after having applied these corrections.

We present data obtained in a time span of seven years, with variable observing conditions. In this context one of the parameters that changes the most is the atmospheric opacity. With the LABOCA data there are three different options to estimate it: skydips[3], radiometer values[4], or a combination of both. It has been studied that opacities estimated with skydips tend to underestimate the flux density[5], whereas those derived with the radiometer tend to overestimated it[6]. A weighted average of both radiometer and skydips gives an intermediate result that occasionally[7] is better adjusted (A. Weiss, priv. comm.). We performed all three estimations for every observing night, and chose the technique that optimized the agreement between the secondary calibrator values as well as the individual maps and the co-added reference map (see below). The variations in respect with the corresponding reference values result in an estimate of the relative uncertainty in the light curve measurements of the order of 4% (1σ). After this initial step all good quality

images of one campaign were co-added, in other words aligned, added and normalized to the total number of added images. A Gaussian point source was fit at the position of Sgr A*. This point source was subtracted from the co-added GC map leaving a model of the extended submm emission of the GC (Fig. 1, middle). Afterwards this model was subtracted from each individual map (Fig. 1, right). On the remaining flux density map again a Gaussian point source was fit at the position of Sgr A*. The peak of the Gaussian is supposed to yield the flux density of Sgr A* at the observation time. From all 8 LABOCA campaigns between 2008 and 2014 we obtained 24 light curves with a total of 792 data points.

2.1.2. Literature data

We extended the submm data set with archival data at comparable wavelengths (see Table 1). Though there is a small scatter in the observed central frequencies, in a good approximation all measurements can be treated equally. The difference between 850 and 890 μm is negligible (Fig. 1 in Marrone et al. 2006b). The literature datasets contain additional 345 data points in total. Thus the complete submm sample consists of 1137 flux density values. Figure 2 gives an overview of all used observations in the decade between 2004 and 2014.

2.2. The radio data

To investigate the flux density distribution of Sagittarius A* in the radio regime we used data from the Australia Telescope Compact Array (ATCA) at a frequency of 100 GHz which are already published in Borkar et al. (2016). For more details about the observation campaigns and data reduction we refer the reader to their paper. Here we only give a brief overview.

ATCA is an array of six 22-m antennas of which five are available for 100 GHz observations. It is located at the Paul Wild Observatory, about 25 kilometers west of Narrabi in Australia and at an altitude of 234 m. Differential flux density light curves were collected for a total of 16 observation days during 2010 and 2014. Four observation days were excluded from our data set due to bad weather conditions.

As the antenna gain of ATCA is highly dependent on the elevation angle, calibrators within 10° from the GC were used (mainly PKS 1741-312 as a flux density and visibility calibrator). After each observation a flux density calibration was carried

---

[3] By measuring the emission of the atmosphere as a function of elevation, proportional to $(1 − e^{−τ})$, the atmospheric opacity $τ$ can be determined.

[4] Measuring a water line intensity with a water vapor radiometer the precipitable water vapor column density along the line of sight (and therefore the atmospheric opacity $τ$) can be determined.

[5] Skydips are usually taken under good weather conditions whereas the conditions for the measurements may be less preferential.

[6] Positive biases toward the detection of precipitable water overestimates the opacity.

[7] For instance if the weather conditions differ in both directions from average conditions under which the calibration was done; using a weighted average is less susceptible to excursions in the weather conditions.

Table 1. Literature data used to extend the submm sample.

Source	Telescope	Wavelength (μm)	Frequency (GHz)	Dates	Beam
Eckart et al. (2009)	SMA	890	340	5–7 July 2004	$1\overset{''}{.}5 \times 3\overset{''}{.}0$
Yusef-Zadeh et al. (2006a)	CSO	850	350	2–4 Sept. 2004	$21''$
Yusef-Zadeh et al. (2008)	CSO	850	350	16–17 July 2006	$20''$
Yusef-Zadeh et al. (2009)	CSO	850	350	6 April 2007	$18\overset{''}{.}8$
Trap et al. (2011)	LABOCA	870	345	1–5 April 2009	$19''$
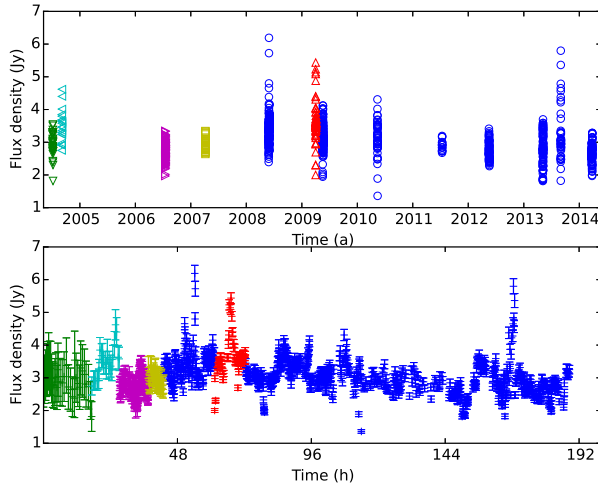
Fig. 2. *Top*: all available submm light curves between 2004 and 2014. The plot contains both the LABOCA data (blue circles) and the literature data (green down-pointing triangles: Eckart et al. 2009; cyan left-pointing triangles: Yusef-Zadeh et al. 2006a; magenta right-pointing triangles: Yusef-Zadeh et al. 2008; yellow squares: Yusef-Zadeh et al. 2009; red up-pointing triangles: Trap et al. 2011). *Bottom*: a concatenated light curve of the submm data. Time gaps greater than 10 min were replaced by gaps of 300 s.

Fig. 3. *Top*: all ATCA 100 GHz light curves obtained between 2010 and 2014. The flux density values are averaged over a window of 300 s. *Bottom*: concatenated light curve of the averaged radio data after background reduction and removal of negative values. Time gaps greater than 10 min were replaced by gaps of 300 s.

out using Uranus. Only observational data from elevations above 40° were processed. At smaller elevations gravitational deformation of the dishes, atmospheric effects and shadowing may lead to unreliable measurements. The observations were predominantly carried out in the H214 configuration with a maximum available baseline of 214 m. At a frequency of 100 GHz this corresponds to a synthesized beam of $2''$. For the GC observations this means, that the correlated flux densities on different baselines are dominated by the extended emission[8] from the surroundings of Sgr A* on size scales of 20 to 30 arcseconds with peak flux density contributions at 100 GHz of the order of 0.1–0.2 Jy per beam; hence, the integrated values per baseline and hour angle are larger. To obtain the intrinsic variability of Sgr A* a method introduced by Kunneriath et al. (2010) was used (see also Borkar et al. 2016). Though the authors provide a formula for the time depend uncertainty of the differential flux density, $\delta S(t)$, we took the median of these values, $\widetilde{\delta S} = \pm 0.15$ Jy, as an estimate of the overall uncertainty.

The used Compact Array Broadband Backend (CABB) has an average time resolution of 10 s. As we do not expect intrinsic flux density variations at timescales below minutes (in Borkar et al. 2016 it is shown that the structure functions of the

daily differential light curves are flat up to time lags of approximately 10 min), and to make the time resolution comparable to the LABOCA data, we averaged the differential flux density values over 300 s. Rough calculations have shown that the estimated distribution parameters (see Sect. 4) do not change significantly by averaging over timescales of up to several minutes[9]. The differential light curves contain both negative and positive values. To obtain the physically relevant value, namely the positive deviation from the quiescent state, we subtracted the lowest 10th percentile of the complete data set from the binned light curves. Finally we omitted all remaining negative flux density values. The original data sample contains 24 877 data points, after averaging and background subtraction we end up with 613 and 552 flux density values, respectively. A concatenated light curve of these values is shown in Fig. 3.

3. Statistical analysis of the submm flux density distribution

For the distribution analysis of the submm (and later also the radio) light curves we assume that all single flux density measurements can be treated as interchangeable random values. While this is not strictly true for short time scales (flux density values within distinct flaring events follow a temporal sequence typically of the order of one hour), these correlations

---

[8] For a detailed discussion of the extended mm emission from the inner few parsecs of the GC we refer to Kunneriath et al. (2012) and Moser et al. (2017).

[9] For example we performed a power-law fit with the later introduced CSN07 method to differently averaged data sets. The obtained estimator $\alpha = 4.7$ for the power-law index is stable up to an averaging over 7 min and only slightly diverges to higher values, for instance 5.0 for an average over 10 min.
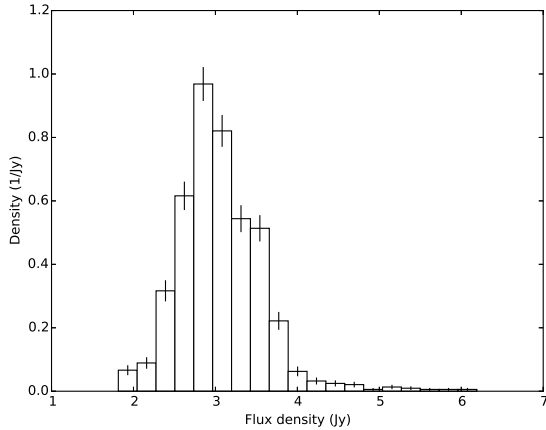
Fig. 4. Histogram of the submm flux density values. The steady quiescent emission leads to the average of ~3 Jy, the high-flux tail up to ~6 Jy is supposedly power-law distributed.

disappear on larger time scales of the order of days or even years (Yusef-Zadeh et al. 2011; Dexter et al. 2014; Bower et al. 2015). Thus, for a long-term analysis all flux density values can be handled in a good approximation as uncorrelated stochastic variables.

To get a first impression of the underlying distribution several methods of visualizing the data can be considered. A common way is to create a histogram of the flux density values. Histograms though face the problem of properly binning the data, which is connected to additional analytic challenges (e.g., Knuth 2006 or Shimazaki & Shinomoto 2007). If the number of bins is chosen too large, a histogram will overemphasize statistical fluctuations, while a too small number of bins may cause a loss of information of the underlying data structure. Without going into detail we used the algorithm introduced in Knuth (2006) to determine the optimal number of bins for the data sets, yielding 17 bins for the submm data (Fig. 4) and later seven bins for the radio data (Sect. 4). For the logarithms of the submm and radio data used in log-log histograms the optimal number of bins computes to 16 and ten, respectively.

3.1. Modeling a power-law distribution

We begin the flux density distribution analysis by introducing some basic definitions and considerations about power-law distributions. The probability density function (PDF) of a power-law distributed variable can be written as

$$p(x) = C \cdot x^{-\alpha} = \frac{\alpha - 1}{x_{\min}} \left(\frac{x}{x_{\min}} \right)^{-\alpha}, \tag{1}$$

where $x_{\min}$ is the domain's lower bound, α the power-law index and $C = (\alpha - 1)x_{\min}^{\alpha-1}$ the normalization constant. The cumulative distribution function (CDF) is then given by

$$P(x) = 1 - \left(\frac{x}{x_{\min}} \right)^{-\alpha+1}, \tag{2}$$

with the survival function or complementary cumulative distribution function (CCDF)

$$F(x) = 1 - P(x) = \left(\frac{x}{x_{\min}} \right)^{-\alpha+1}. \tag{3}$$

A commonly used indicator for an underlying power-law is a linear behavior of the empirical PDF or CCDF tail in a log-log plot with $\log p(x) \propto -\alpha \log x$. The slope of this graph then indicates the power-law index α.

If we now consider a power-law with a constant shift s, for instance a red noise emission process superimposed with a steady quiescent contribution, the form of the power-law changes to what we call a shifted power-law:

$$p(x) = \frac{\alpha - 1}{x_{\min} - s} \left(\frac{x - s}{x_{\min} - s} \right)^{-\alpha}. \tag{4}$$

In a log-log view, a shifted power-law does not show the linear behavior unless for large values of x, as

$$\log p(x) \propto -\alpha \log x - \alpha \log(1 - s/x). \tag{5}$$

The second term at the right-hand side of Eq. (5) leads to a curvature in a log-log plot as shown in Fig. 5. This term is determined by the ratio between quiescent and flaring emission and therefore is crucial particularly for the analysis of the submm flux density distribution. Only for $x \gg s \Rightarrow s/x \to 0$ the slope converges to α. If we consider a steady quiescent submm emission of about 3 Jy and flaring peaks of up to 6 Jy (Fig. 4), we expect s/x-ratios of about 0.5 or higher. That implies, that even if the variable radiation is generated by a power-law distributed process, the steady quiescent emission causes a curvature in a logarithmic probability plot. This might lead to a premature rejection of a power-law hypothesis or a broken power-law conjecture. Figure 6 shows a log-log histogram of the submm data. A negative curvature in the histogram's high-flux tail ≳3.5 Jy is visible. Therefore, the challenge for the submm analysis is to separate the quiescent from the variable flaring emission. In the following sections we present two methods of doing so:

– A heuristic method, which is based on physical and observational considerations (Sect. 3.2). After having subtracted a heuristic model for the quiescent emission from the light curve, the remaining flux density sample can be tested for an unshifted power-law distribution (Sect. 3.3) as in Eq. (1).
– A numerical method (Sect. 3.4) which is based on Eq. (4) (a shifted power-law) and contains a mathematical estimator for the quiescent emission, s.

The analysis of the radio data (Sect. 4) copes without the additional estimator s as the method of taking differential light curves already inherently includes the subtraction of a quiescent contribution.

3.2. Heuristic estimation of the quiescent submm emission

Possible estimators for the quiescent radiation can be found by simple heuristic considerations. For instance, our submm sample spans a flux density range from about 2 Jy to 6 Jy. Thus, as a lowest bound for an estimator we may just take the lowest 1st percentile of the sample (~2 Jy). This can be seen as the lowest possible quiescent baseline. An upper limit for a constant estimator is the 50th percentile (median, ~3 Jy). This value is based on the idea, that if all radiation stems from one quiescent process, meaning that the variable emission is negligible, the median flux density value is a good estimator for the most probable flux density value. If we now consider two combined emission processes, one quiescent process and a flaring activity, the median surely is the upper limit for the quiescent emission estimator. However, this constant estimator s may take all values between the 1st and the 50th percentile.
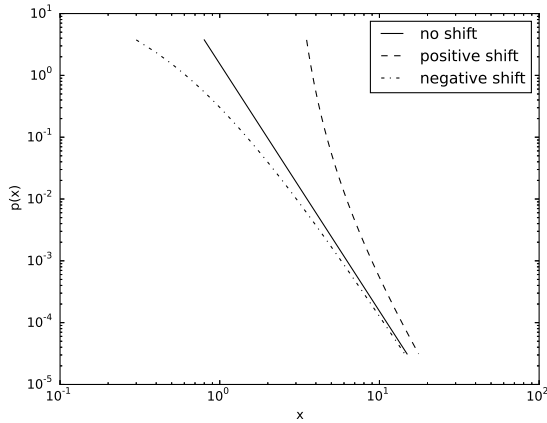
Fig. 5. PDFs for shifted power-laws ($\alpha = 12$, $x_{\min} = 3.5$) with different shifts, solid line without shift, dashed line with positive, dash-dot line with negative shift. The slope only becomes constant for large x.
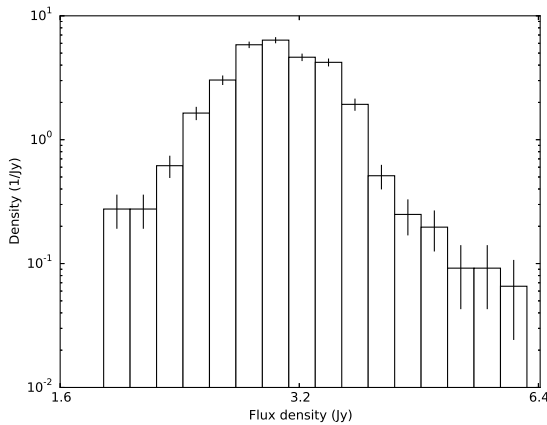

Fig. 6. log-log histogram of the submm data. The curvature of the high-flux tail $\gtrsim 3.5$ Jy indicates a shifted power-law of the form $p(x) \sim (x - s)^{\alpha}$.

Another consideration can be given to the temporal development of the quiescent emission: though long term observations of Sgr A* have shown, that on time scales above days no periodicities can be found (Dexter et al. 2014), the possibility of long term variations can not completely be ruled out (Pierce-Price et al. 2003). Therefore we have to consider a possible change in the quiescent emission over longer timescales. As no further information about a putative temporal development of the quiescent flux density distribution is available, we used three simplistic models for the long term variability: a linear trend, a constant quiescent level per each observing campaign and a third polynomial order trend modeled by a cubic spline. In summary, we define 4 models, which may possibly represent the steady quiescent emission:

A Constant quiescent flux density contribution (Fig. 7): we assumed a constant low-flux contribution yielding a global estimator s for the quiescent emission. As possible values for s we took the range of the $[1, 5, 10, 30, 50]$th percentile of the flux density values.
B Quiescent flux density contribution with linear trend (Fig. 8): we calculated the mean flux density value for each observing

campaign. A trend line was fit to these values, the difference between the trend line and the global mean was subtracted from the light curves. After having detrended the data a global value for the quiescent emission was assumed (according to the model described in A).
C Non-parametric variable quiescent flux density contribution (Fig. 9): we supposed a long term variability in the quiescent emission without assuming a parametric equation. Instead, for each observing campaign we took the lowest nth ($[1, 5, 10, 30, 50]$th) percentile. To not overestimate outliers we introduced a threshold of 30 data points per campaign. If an campaign contains less data we calculated the quiescent emission's value by a linear interpolation of the two neighboring campaigns.
D Variable quiescent flux density contribution modeled by a cubic spline (Fig. 10): we modeled the variability in the quiescent emission with a third order polynomial. The nth percentile of each campaign was calculated and a cubic spline fit was performed on these values.

The resulting models were then subtracted from the observed light curves to obtain the variable emission.

3.3. Fitting the variable submm emission

We used a distribution fitting formalism which has been introduced by Clauset et al. (2007), hereinafter CSN07. This formalism is briefly summarized in Appendix A. We point out, that the CSN07 algorithm is only applicable to unshifted power-laws, meaning that it only yields estimators for $x_{\min}$ and α, not for a possible shift s. Thus we had to subtract the quiescent emission using the heuristic metholody described in Sect. 3.2 and fit the remaining dataset with a power-law model. The results of this procedure are summarized in Table 2.

If we choose a significance level of 0.05, some power-law fits have to be rejected due to their low p-value (see Appendix A). The corresponding data set is unlikely power-law distributed. Although we note that higher p-values can not be used for model verification, we can nevertheless formulate the results as follows: we found some heuristic models for the quiescent emission which yield, after subtraction, high flux density samples that can be described by power-law distributions. The power-law distribution fits yield a range of best estimators for α and $x_{\min}$:

$$\alpha \in [(3.3 \pm 0.3), (6.9 \pm 0.7)] \text{ and} \tag{6}$$

$$x_{\min} \in [(0.46 \pm 0.07), (1.50 \pm 0.08)] \text{Jy}. \tag{7}$$

The mean of the obtained parameters from all non rejected fits is

$$\alpha = (4.8 \pm 1.2) \quad \text{and} \quad x_{\min} = (0.9 \pm 0.3) \text{Jy}. \tag{8}$$

The statistical meaning of Eq. (8) might be weak, as the different fits were performed on different data sets. Though it gives an impression of the numerical size of α and $x_{\min}$.

In Table 2 we also include a column with a new parameter $x^{*}_{\min}$. Before we applied a power-law fitting routine we subtracted different models for the unknown quiescent emission from the original sample. Thus, the resulting $x_{\min}$ is the flux density value where the power-law begins for the data where the quiescent emission has been subtracted. Instead $x^{*}_{\min}$ indicates where the power-law tail starts in the original sample. Hence, from an observer's perspective, $x^{*}_{\min}$ is the more interesting parameter. To obtain this value, the estimator for $x_{\min}$ needs to be re-shifted again, such that $x^{*}_{\min} = x_{\min} + s$. For models C and D
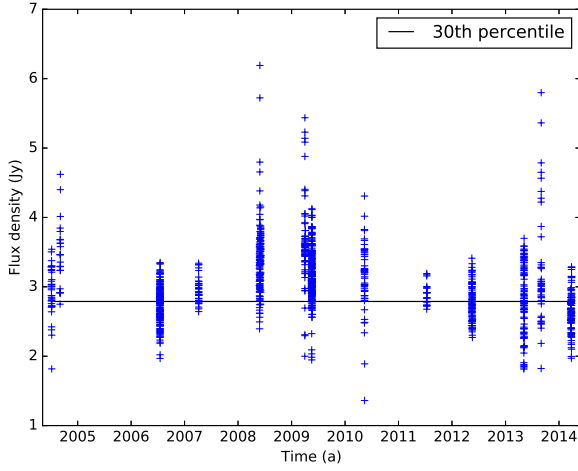
Fig. 7. Quiescent emission model A: subtraction of a constant contribution from the data. In this example the steady contribution is the lowest 30th percentile of all data points.
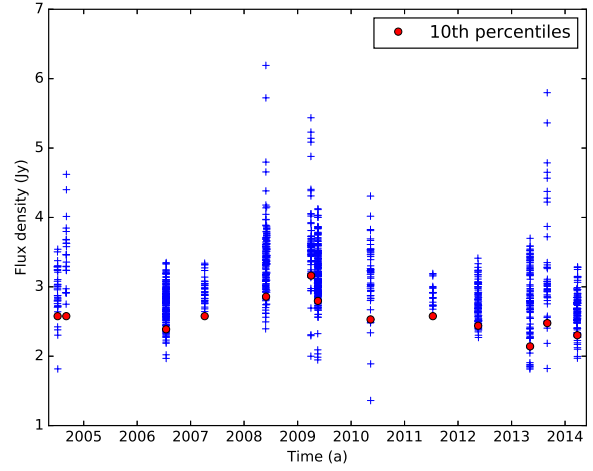

Fig. 9. Quiescent emission model C: subtraction of a variable quiescent emission. In this example for each campaign the 10th percentiles of the campaign's data is subtracted.
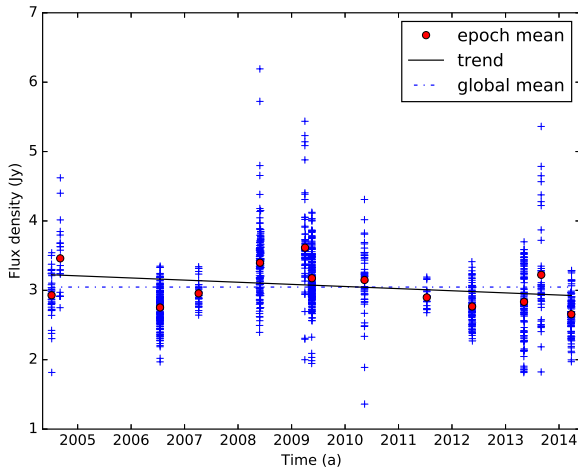

Fig. 8. Quiescent emission model B: linear detrending, followed by the subtraction of a global constant for the quiescent emission (not depicted in this plot).
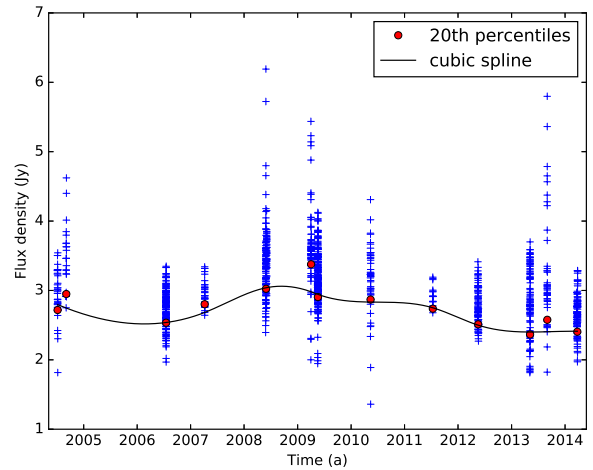
Fig. 10. Quiescent emission model D: the variable quiescent emission is modeled by a cubic spline. Here the spline fit is applied to the 20th percentile values of each campaign.

we added a single value s although we had subtracted a function for the quiescent radiation (i.e., a per campaign value and a cubic spline). As the different values for x^*_{min} mostly serve for consistency comparison, a decent approximation for this re-shifting is to take the nth percentile from the original data (depending on the percentile parameter we used in the corresponding model) and add this value to the calculated x_{min}. For model B we added the nth percentile of the detrended data. This method yields only rough estimates for x^*_{min}, and thus we omit uncertainty considerations.

3.4. Numerical estimation of the quiescent and variable submm emission

In the previous section we analyzed the submm flux density distribution by introducing several heuristic models for the non-flaring, quiescent emission of Sgr A*. We subtracted these models from the measured data sets and performed a power-law hypothesis test according to CSN07 on the remaining data.

Under the assumption of a constant quiescent contribution it is also possible to numerically obtain an estimator s for the quiescent emission out of the given data set. This method was proposed by RKE09. We briefly describe the fitting procedure in the following:

As we have already discussed in Sect. 3.1, a quiescent contribution to a power-law process leads to a curvature in a log-log representation of the flux density distribution (Fig. 5 and Eq. (4)). RKE09 inverse the argument, such as the curvature of such a plot is vice versa a direct mathematical indicator for the unknown power-law shift s. That is, in this context, the steady quiescent emission. The estimator for s can be found by straightening out the log-log plot through adding an appropriate constant to the flux density distribution. The constant, that minimizes the deviation from a best linear fit is an estimator s for the steady shift of the power-law. Once we obtained s, it is possible to test the sample for a shifted power-law hypothesis. The resulting

Table 2. Best fit parameters for the variable submm emission after having subtracted the quiescent emission using the heuristic methodology described in Sect. 3.2.

Model	Percentile	$x_{\min}$ (Jy)	$x^*_{\min}$ (Jy)	α	p-value
*A(raw)	0	3.4 ± 0.1	3.4	12.1 ± 1.6	0.02
A	1	1.50 ± 0.08	3.4	6.8 ± 0.7	0.17
A	5	1.13 ± 0.07	3.4	5.6 ± 0.5	0.30
A	10	0.96 ± 0.07	3.4	5.0 ± 0.4	0.38
A	20	0.76 ± 0.08	3.4	4.4 ± 0.8	0.46
A	30	0.67 ± 0.08	3.5	4.1 ± 0.4	0.60
A	50	0.6 ± 0.1	3.6	3.5 ± 0.3	0.37
B	1	1.5 ± 0.2	3.5	6.4 ± 0.9	0.84
*B	5	0.7 ± 0.2	3.0	4.0 ± 0.8	0.03
*B	10	0.6 ± 0.2	3.1	3.6 ± 0.6	0.00
*B	20	0.7 ± 0.1	3.4	3.9 ± 0.5	0.03
*B	30	0.6 ± 0.1	3.4	3.6 ± 0.5	0.02
*B	50	0.5 ± 0.1	3.5	3.6 ± 0.5	0.04
C	1	1.41 ± 0.07	3.2	6.9 ± 0.7	0.13
C	5	0.96 ± 0.05	3.2	5.3 ± 0.5	0.32
C	10	0.84 ± 0.04	3.3	4.8 ± 0.4	0.41
C	20	0.67 ± 0.05	3.4	4.2 ± 0.3	0.56
C	30	0.56 ± 0.05	3.4	3.8 ± 0.3	0.67
C	50	0.46 ± 0.07	3.5	3.3 ± 0.3	0.68
D	1	1.3 ± 0.1	3.2	6.0 ± 0.7	0.63
*D	5	0.80 ± 0.09	3.2	4.4 ± 0.5	0.01
*D	10	0.8 ± 0.1	3.3	4.3 ± 0.5	0.03
*D	20	0.7 ± 0.1	3.4	4.1 ± 0.5	0.04
D	30	0.61 ± 0.09	3.4	3.8 ± 0.4	0.36
D	50	0.52 ± 0.09	3.5	3.5 ± 0.4	0.18

Notes. For an explanation of the different models and percentile values see the text. Rows with rejected power-law fits are marked with a leading asterisk.

fitting procedure for a shifted power-law according to RKE09 can briefly be described as follows:

– Sort the elements of the data set: $\{X_1, \ldots, X_N\} \to \{x_1, \ldots, x_N\} =: \mathcal{S}$ with $x_1 \leq \ldots \leq x_N$.
– For each value x_i in $\mathcal{S}$ assume it to be $x_{\min}$ (i.e., $x_i = x_{\min,i}$) and create a new ordered data set $\mathcal{T}_i := \{x_{\min,i}, \ldots, x_N\}$.
– For each possible value s_j in a given shift range $\{s_{\min}, \ldots, s_{\max}\}$ shift $\mathcal{T}_i$ with s_j: $\mathcal{T}_{i,j} := \mathcal{T}_i + s_j$. For the possible shift range we assume the range between −5 and 5 Jy with iteration steps of 0.1 Jy.
– For each $\mathcal{T}_{i,j}$ calculate the empirical survival function $\tilde{F}(\mathcal{T}_{i,j})$ (see Eq. (A.4)) and do a linear fit in a log-log representation.
– The value s_j that minimizes the R^2-value of the linear fit, is the shift estimator s_i for a given $x_{\min,i}$.
– Shift the data set with the shift estimator s_i: $\mathcal{S}_i := \mathcal{S} + s_i$ and calculate the Hill estimator for α_i (see Eq. (A.3)) with $x_i^* \geq x^*_{\min} = x_{\min,i} + s_i$.
– For each $x_{\min,i}$ calculate the KS-distance D between the empirical survival function $\tilde{F}(\mathcal{S}_i)$ (see Eq. (A.4)) and the theoretical survival function $F(\mathcal{S})$ with α_i, s_i and $x_{\min,i}$:

$$D = \max_{x > x_{\min}} \left| \tilde{F}(\mathcal{S}_i) - F(\mathcal{S}) \right|. \tag{9}$$

For a shifted power-law, $F(x)$ is given by

$$F(x) = \left(\frac{x - s}{x_{\min} - s} \right)^{-\alpha+1}. \tag{10}$$
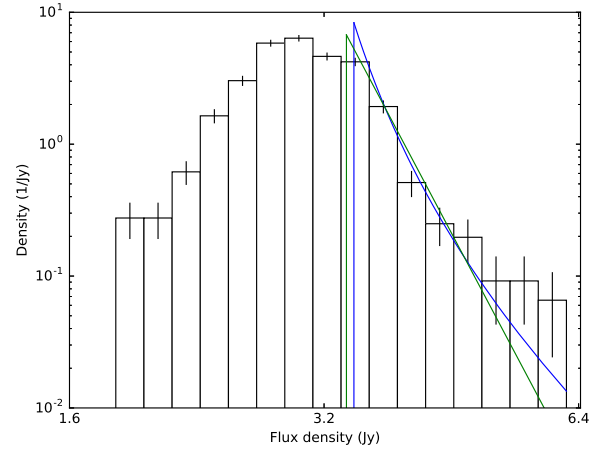
Fig. 11. log-log histogram of the submm flux density with shifted power-law fit (blue line) from the RKE09 algorithm and a pure power-law fit (green line) according to CSN07. The obtained power-law indices for the RKE09 and CSN07 method are $\alpha \sim 4$ and $\sim$12, respectively.

– As best fit accept the estimators $x_{\min,i}$, s_i and α_i which minimize the parameter D.
– Error estimations and a goodness of fit value are obtained by the bootstrapping techniques described in Appendix A.

Applying this method to the submm sample yields the shifted power-law parameters:

$$x_{\min} = (0.6 \pm 0.1)\,\text{Jy}, \alpha = 4.0 \pm 1.7, s = (2.8 \pm 0.6)\,\text{Jy} \tag{11}$$

with a p-value of 0.53.

Figure 11 demonstrates the difference between both power-law fitting methods we presented: the CSN07 algorithm fits an unshifted power-laws without the additional parameter s, so the fit in the log-log plot will always be linear. The shown fit corresponds to the first row in Table 2. The RKE09 fitting procedure can reproduce the internal shift by a quiescent contribution which is manifested as the curvature of the probability density distribution. Although both fits look similar, the resulting power-law indices are very different.

In Table 3 we compare the mean results (Eq. (8)) from Sect. 3.3 (I) with the results from the RKE09 method (II) from this section. Within uncertainties, both results appear to be in agreement and suggest, that the power-law index α is consistent with a value of four. Moreover we compare the RKE09 results to a specific model from Sect. 3.3: model A (a constant quiescent emission) with a percentile parameter of 30% (III). This percentile parameter corresponds to a value of 2.79 Jy. The motivation for comparing the RKE09 with this specific model is the following: although we have considered different models for a varying quiescent emission (models B–D), the simplest model (a constant quiescent emission) should always be preferred until observational evidence demands for more complexity (e.g., a significant detection of long-term periodicities in the quiescent emission). The fact that applying a CSN07 fit to this specific model is in good agreement with the RKE09 results primarily only shows, that both fitting approaches yield unbiased estimators and work accordingly. Moreover, we are able to suggest a statistical model of the submm emission which is both heuristically and analytically consistent: a power-law with an intrinsic

M. Subroweit et al.: Submillimeter and radio variability of Sagittarius A*

Table 3. Comparison of the results for the submm data from parameter estimation approaches.

Method	α	$x_{\min}$ (Jy)	s (Jy)	$x^*_{\min}$ (Jy)
I	4.8 ± 1.2	0.9 ± 0.3	–	3.4 ± 0.1
II	4.1 ± 0.4	0.67 ± 0.08	2.79 ± 0.01	3.46 ± 0.08
III	4.0 ± 1.7	0.6 ± 0.1	2.8 ± 0.6	3.4 ± 0.6

Notes. (I) shows the mean results from the CSN07 fits to the models shown in Sect. 3.3; (II) shows the results from the RKE09 algorithm and (III) from the CSN07 fit after having subtracted the lowest 30th percentile.
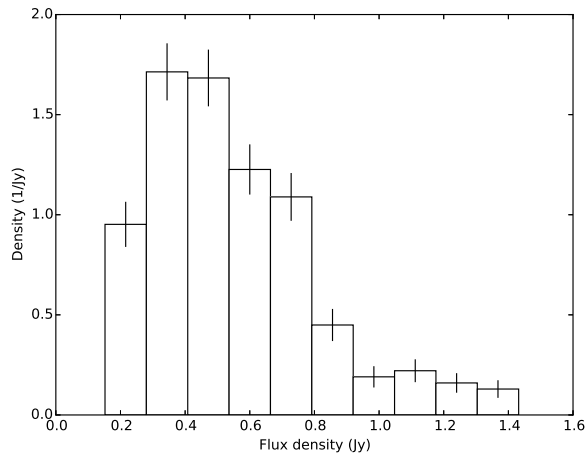
Fig. 12. Histogram of the 100 GHz flux density values.

lower bound $\sim$0.6 Jy[10] and an index $\alpha \sim 4$ which is superimposed by a constant quiescent emission with an average flux density of about 2.8 Jy. Though, if more complexity is demanded in the modeling of the quiescent emission, we have also shown that the results for the submm emission model do not change significantly. In the later discussion we refer to the parameters found with the RKE09 method as we deem this the superior approach.

4. Statistical analysis of the radio flux density distribution

The results from the previous section show, that the variable submm emission can be described by a power-law with an index of about four. A power-law analysis of the 100 GHz ATCA data (shown in a histogram in Fig. 12) can be done accordingly. With the introduced methods (CSN07 and RKE09) power-law distributions in differential light curves (the ATCA radio data) and in light curves with absolute flux density values (the submm data) can directly be compared. In differential light curves the quiescent emission is already pre-subtracted; hence a pure power-law (CSN07) can be assumed. Absolute light curves may additionally contain the quiescent emission, so that a shift estimator has to be included (RKE09). Thereby, the RKE09 estimator for the power-law index α is shift invariant. Thus, the fitting algorithm of CSN07 for pure power-laws can be applied to the ATCA data

---

[10] As explained in Appendix B the real value for $x_{\min}$ might indeed be smaller if one considers the possible influence of uncertainties (uncertainties in the light curves, variability in the quiescent emission, etc.). The value for α, which is the parameter from which we later draw conclusions, is not effected by these uncertainties though.

Table 4. Comparison of the results (for the radio data) from the CSN07 fitting method (I) to the results from the RKE09 algorithm (II).

Method	α	$x_{\min}$ (Jy)	s (Jy)	p-value
I	4.7 ± 0.8	0.65 ± 0.04	0	0.08
II	4.8 ± 1.1	0.63 ± 0.08	0.1 ± 0.2	0.46
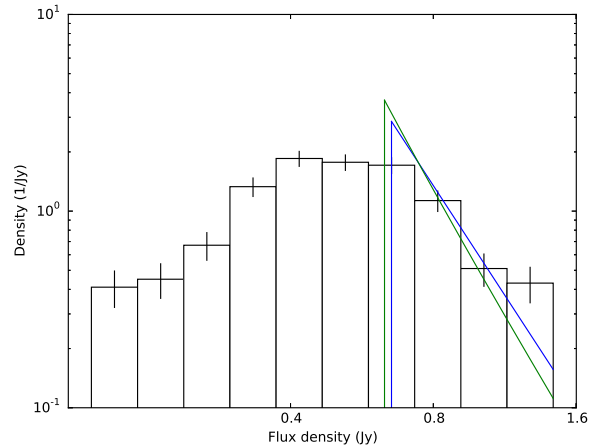
Fig. 13. log-log histogram of the radio flux density with power-law fits. Both the CSN07 (green line) and the RKE09 (blue line) method yield similar fits, the power-law slopes are within uncertainties consistent with $\alpha \sim 4$.

and the submm and radio power-law indices can directly be compared. For the 100 GHz data we find as best fit parameters[10]

$$x_{\min} = (0.65 \pm 0.04)\text{Jy} \quad \text{and} \quad \alpha = 4.7 \pm 0.8 \qquad (12)$$

with a p-value of 0.08. To check for consistency we also perform a fit based on the RKE09 method. Table 4 shows, that the results from both fitting techniques are in good agreement. Figure 13 depicts a log-log histogram with both the best unshifted (CSN07) and shifted (RKE09) power-law fit. Within uncertainties, the power-law index is consistent with the one found in the NIR and submm distributions, namely approximately four.

5. Consequences for the model of adiabatically expanding blobs

The fact that at 100 GHz and 350 GHz we find power-law flux density distributions with exponents $\alpha \sim 4.0$ suggests that the (sub)mm- and NIR-flares are linked to each other and have the same origin. Witzel et al. (2012) find in the NIR a power-law with $\alpha = 4.2 \pm 0.1$. Under the assumption that the NIR spectra are the optically thin extension of the submm flare component spectra, a different flux density distribution in the submm domain than a power-law would be inconsistent with the NIR measurements. The similar nominal value of the power-law indices at different wavebands (mm, submm and NIR) can also put additional constraints on the model of adiabatically expanding self-absorbed synchrotron blobs:

Previous measurements have already suggested that contributions from flares with initial turnover frequencies below 100 GHz are less likely as the variability drops toward lower frequencies (see Sect. 1 and references therein). A significant
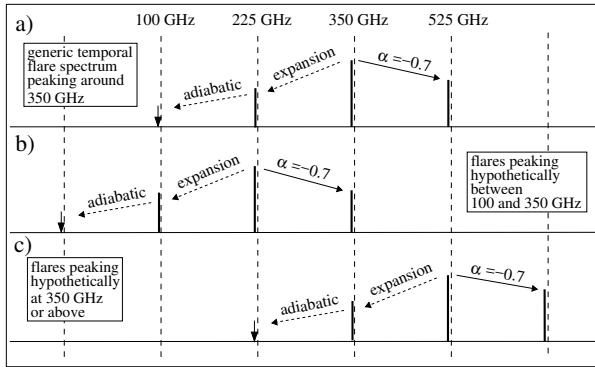
Fig. 14. Schematic representation of possible peak contributions to different frequency channels from different temporal spectra of adiabatically expanding flares.

population of flares peaking at or below 100 Hz would contradict this trend. A substantial contribution from flares peaking between 100 GHz and 350 GHz has the same problem. Flares with initial turnover frequencies well above 350 GHz are also probably rare as the overall spectrum drops strongly toward the far-infrared in the frequency range of 300–400 GHz (Marrone et al. 2006a,b; Marrone 2006; Eckart et al. 2012). In the following we investigate this formaly.

In Fig. 14 we show a schematic representation of possible peak contributions to different frequency channels from different temporal spectra of adiabatically expanding flares. With respect to the peak frequency, contributions to higher frequencies are due to the optically thin synchrotron part of the contaminating flare component spectrum. In the (sub)mm domain flare components of Sgr A* have not yet been isolated spectrally or spatially. As we are only considering frequently observed strong flares with amplitudes between a few tenths and a few Janskys, we assume that the optically thin synchrotron spectral index is also close to the one measured in the infrared, that is around $\alpha_{sync} = -0.7$. Steeper spectral indices in the NIR wavelength domain are most likely due to synchrotron losses and do not reflect the intrinsic optically thin spectral index (see Bremer et al. 2011 and Witzel et al. 2014 for details).

Contributions to lower frequencies are mainly due to the adiabatic expansion process. Low frequency contributions due to the optically thick part of the synchrotron components are not considered as the spectrum there rises with a very steep index of ∼+2.5. In Fig. 14a we show a generic temporal spectrum peaking around 350 GHz. In Fig. 14b we show the case of a spectrum peaking between 100 GHz and 350 GHz. The optically thin synchrotron spectrum and the adiabatic expansion process result in contributions at the neighbouring frequencies. In Fig. 14c we show the case of a spectrum peaking above 350 GHz. Here, only the adiabatic expansion process results in contributions at the lower frequencies. In case of the presence of contaminating flares like the ones shown in Fig. 14bc their contribution should be added to the generic flare spectrum peaking at 350 GHz as shown in Fig. 14a. In both cases the contaminating flares below and above 350 GHz contribute to the high or low end of the flux density distribution at 100 GHz and 350 GHz.

In the following we use the concept of Fig. 14 to quantify the effect the contaminating flare populations have on the flux density power-law index of the generic flare spectrum shown in Fig. 14a. We use D to denote the dynamic range, defined as

the ratio between brightest and faintest (significant) flare fluxes that contribute to the power-law section of the flux density histogram. The flux densities are corrected for the constant s by which the power-law has been shifted and normalized to unity by division by x_{min}. The frequencies of occurrence are also normalized (so that highest frequency becomes unity). From our (sub)mm-light curves we find D in the range of ∼2.5–5. Then the frequencies of flare amplitudes at the low and high end of the power-law part of the distribution are unity and P and the power-law index α is defined as:

$$\frac{\log(1) - \log(P)}{\log(1) - \log(D)} = \alpha. \tag{13}$$

Here the frequencies and dynamic range values can now be modified according to the situations at the different observing wavebands resulting in power-law indices for the simple extreme cases. If we assume that the nominal value of the power-law index of our generic (sub)mm-flare spectrum peaking at 350 GHz is the same as the index $\alpha = -4.2$ found in the NIR, one can show that the corresponding power-law index of the contaminated flare flux density spectrum can be described via

$$\alpha = -4.2 \pm \Delta\alpha = -4.2 \pm \frac{\log(R)}{\log(D)}. \tag{14}$$

Here, R is the factor by which the flux density frequency is increased due to the contamination, which means that $R = 2$ for a 100% additional contribution from contaminating flares. The varying operation signs reflect that the index can be lowered or enlarged depending on whether the faint of bright end of the distribution is enhanced. As a result we find that with the current typical uncertainty in the power-law index in the (sub)mm-regime around $\Delta\alpha = 1$, we can only exclude contamination flare flux contributions that increase the flux density frequencies by a factor of about 5. However, if we assume an intrinsic power-law index equals that found in the NIR and the power-law index uncertainty that is not larger than the value $\Delta\alpha = \pm 0.1$ derived from the NIR, then the contaminating contributions to the uncontaminated flux density frequencies at 100 GHz and 350 GHz of around 15% to 20% can be excluded. This assumption implies that the measured difference between the submm and the radio power-law indices and the NIR power-law index are entirely due to measurement uncertainties and (currently) smaller statistics in the submm and radio domain. This then supports the picture, that most of the flares are indeed borne within the 300–400 GHz domain and are to first order of similar nature consistent with the spectral index and power-law distribution index information found in the NIR and the (sub)mm domain.

Accepting that the bulk of observed flares have the same origin and initially peak at ∼350 GHz and above, consequences for the possible expansion velocity of the adiabatic expansion can be inferred: according to van der Laan (1966) the peak frequency, ν_m, decreases as:

$$\nu_m = \nu_{m0} \left(\frac{R(t)}{R_0}\right)^{-(4p+6)/(p+4)} = \nu_{m0} \left(\frac{R(t)}{R_0}\right)^{\Gamma}, \tag{15}$$

where p is the power-law index of the energy spectrum of the synchrotron emitting electrons with $n(E) \propto E^{-p}$, ν_{m0} the initial peak frequency, R_0 the initial source size and $R(t)$ the source size after the expansion time t. $R(t)$ can be modeled by linear expansion at constant expansion speed, ν_{exp}, as

$$R(t) = v_{exp}(t - t_0) + R_0. \tag{16}$$

M. Subroweit et al.: Submillimeter and radio variability of Sagittarius A*

If one again assumes the measured NIR spectral information, namely $p = 2\alpha_{\text{sync}} + 1 \approx 2.4$ with the synchrotron spectral index α_{sync}, as also being valid for the (sub)mm flares, the exponent Γ of the right-hand side of Eq. (15) becomes ≈ -2.44. Therefore

$$\frac{R(t)}{R_0} \approx \left(\frac{\nu_{\text{m}}}{\nu_{\text{m0}}}\right)^{-1/2.44} = \left(\frac{100 \text{ GHz}}{350 \text{ GHz}}\right)^{-1/2.44} \approx 1.67. \quad (17)$$

We note that Eq. (17) is only mildly sensitive to p. If one assumes extreme cases, such as p in the range between 1 and 9 (e.g., Yusef-Zadeh et al. 2006a or Hornstein et al. 2007), the normalized expansion radius $R(t)/R_0$ would range from 1.87 to 1.47, and thus the result would deviate only by $\sim 10\%$.

Using Eqs. (15) and (16) the time delay $t_4 - t_3$ between peaks at two arbitrary frequencies ν_4 and ν_3 can be calculated if the time lag $t_2 - t_1$ between peaks at two frequencies ν_2 and ν_1 is known:

$$t_4 - t_3 = \frac{\nu_{\text{m4}}^{1/\Gamma} - \nu_{\text{m3}}^{1/\Gamma}}{\nu_{\text{m2}}^{1/\Gamma} - \nu_{\text{m1}}^{1/\Gamma}} \times (t_2 - t_1). \quad (18)$$

Yusef-Zadeh et al. (2006b, 2008) found time delays between peaks at 44 and 23 GHz to be ~ 0.5 h, in Brinkerink et al. (2015) the time lag between a peak at 100 and 19 GHz was measured as ~ 1.1 h. Thus, typical time delays between peaks at 350 GHz and 100 GH are expected to be ~ 0.5 h. Therefore, using Eqs. (16) and (17), we get

$$v_{\text{exp}} \times 0.5 \text{ h} \approx 0.67 R_0. \quad (19)$$

R_0 can additionally be constrained to be of a typical size scale of the order of 1 Schwarzschild radius (R_S) (Doeleman et al. 2009; Fish et al. 2011; García-Marín et al. 2011; Eckart et al. 2012). Hence,

$$v_{\text{exp}} \approx 1.34 R_S/\text{h}. \quad (20)$$

For Sgr A* an expansion velocity of 1 c corresponds to about 100 R_S per hour. If one introduces the terms fast, intermediate and slow expanding synchrotron blobs for expansion velocities of 0.1, 0.01 and 0.001 c, respectively, it can be seen that under the aforementioned assumptions the bulk of observed flares expand at intermediate velocities, meaning that $v_{\text{exp}} \sim 0.01$ c. Fast and slow expansion velocities would require initial blob sizes R_0 of the order of 10 and 0.1 R_S, respectively.

6. Conclusions

We compiled both submm light curves obtained mainly from LABOCA observation campaigns extended with literature data and 100 GHz radio data from observations carried out with ATCA. Having investigated these data sets we found that the variable flux density distribution for both wavelength regimes are well described by a single state power-law distributed emission process with a power-law index $\alpha \sim 4$. This finding may put general constraints on any emission model for the observed flares of Sgr A*. The fact, that the NIR flaring emission follows the same distribution can be seen as an additional indicator that the radio, submm and NIR variability stem from the same source components. This has already been predicted by the model of adiabatically expanding synchrotron blobs, which is capable to fit simultaneous multi-wavelength light curves. Our statistical findings may strengthen this model. A situation, where the radio, submm and NIR emissions stem from different source components or even different mechanisms and are describable by the same flux density distribution is possible though, but unlikely.

Inside the framework of a model of adiabatically expanding synchrotron blobs we may also conclude, that the initial turnover frequencies ν_0 of the synchrotron sources are predominantly around 350 GHz. Otherwise the radio flux density distribution would either yield a significantly different power-law index than approximately four or be a completely different distribution. Moreover, the conclusion that the bulk of observed flares are of similar nature may also infer an average expansion velocity of the synchrotron blobs of the order of ~ 0.01 c.

References

Baganoff, F. K., Maeda, Y., Morris, M., et al. 2003, ApJ, 591, 891
Balick, B., & Brown, R. L. 1974, ApJ, 194, 265
Borkar, A., Eckart, A., Straubmeier, C., et al. 2016, MNRAS, 458, 2336
Bower, G. C., Markoff, S., Dexter, J., et al. 2015, ApJ, 802, 69
Bremer, M., Witzel, G., Eckart, A., et al. 2011, A&A, 532, A26
Brinkerink, C. D., Falcke, H., Law, C. J., et al. 2015, A&A, 576, A41
Broderick, A. E., & Loeb, A. 2006, MNRAS, 367, 905
Chan, C.-k., Psaltis, D., Özel, F., et al. 2015, ApJ, 812, 103
Clauset, A., Rohilla Shalizi, C., & Newman, M. E. J. 2007, ArXiv e-prints [arXiv:0706.1062]
Dexter, J., & Fragile, P. C. 2013, MNRAS, 432, 2252
Dexter, J., Kelly, B., Bower, G. C., et al. 2014, MNRAS, 442, 2797
Dodds-Eden, K., Porquet, D., Trap, G., et al. 2009, ApJ, 698, 676
Doeleman, S. S., Fish, V. L., Broderick, A. E., Loeb, A., & Rogers, A. E. E. 2009, ApJ, 695, 59
Eckart, A., & Genzel, R. 1996, in The Galactic Center, ed. R. Gredel, ASP Conf. Ser., 102, 196
Eckart, A., Schödel, R., Meyer, L., et al. 2007, in Black Holes from Stars to Galaxies – Across the Range of Masses, eds. V. Karas, & G. Matt, IAU Symp., 238, 181
Eckart, A., Baganoff, F. K., Zamaninasab, M., et al. 2008a, A&A, 479, 625
Eckart, A., Schödel, R., García-Marín, M., et al. 2008b, A&A, 492, 337
Eckart, A., Baganoff, F. K., Morris, M. R., et al. 2009, A&A, 500, 935
Eckart, A., García-Marín, M., Vogel, S., et al. 2012, A&A, 537, A52
Falcke, H. 1999, in The Central Parsecs of the Galaxy, eds. H. Falcke, A. Cotera, W. J. Duschl, F. Melia, & M. J. Rieke, ASP Conf. Ser., 186, 113
Falcke, H., Goss, W. M., Matsuo, H., et al. 1998, ApJ, 499, 731
Falcke, H., Markoff, S., & Bower, G. C. 2009, A&A, 496, 77
Fish, V. L., Doeleman, S. S., Beaudoin, C., et al. 2011, ApJ, 727, L36
García-Marín, M., Eckart, A., Weiss, A., et al. 2011, ApJ, 738, 158
Genzel, R. 2000, in Astronomische Gesellschaft Meeting Abstracts, ed. R. E. Schielicke, 16
Genzel, R., Schödel, R., Ott, T., et al. 2003, Nature, 425, 934
Ghez, A. M., Wright, S. A., Matthews, K., et al. 2004, ApJ, 601, L159
Herrnstein, R. M., Zhao, J.-H., Bower, G. C., & Goss, W. M. 2004, AJ, 127, 3399
Hill, B. M., et al. 1975, Ann. Stats., 3, 1163
Hornstein, S. D., Ghez, A. M., Tanner, A., et al. 2002, ApJ, 577, L9
Hornstein, S. D., Matthews, K., Ghez, A. M., et al. 2007, ApJ, 667, 900
Knuth, K. H. 2006, ArXiv Physics e-prints [arXiv:physics/0605197]
Kunneriath, D., Witzel, G., Eckart, A., et al. 2010, A&A, 517, A46
Kunneriath, D., Eckart, A., Vogel, S. N., et al. 2012, A&A, 538, A127
Li, Y.-P., Yuan, F., Yuan, Q., et al. 2015, ApJ, 810, 19
Marrone, D. P. 2006, Ph.D. Thesis, Harvard University, USA
Marrone, D. P., Moran, J. M., Zhao, J.-H., & Rao, R. 2006a, ApJ, 640, 308
Marrone, D. P., Moran, J. M., Zhao, J.-H., & Rao, R. 2006b, J. Phys. Conf. Ser., 54, 354
Marrone, D. P., Baganoff, F. K., Morris, M. R., et al. 2008, ApJ, 682, 373
Marscher, A. P. 1983, ApJ, 264, 296

Moser, L., Sánchez-Monge, Á., Eckart, A., et al. 2017, A&A, in press DOI: 10.1051/0004-6361/201628385
Neilsen, J., Nowak, M. A., Gammie, C., et al. 2014, in The Galactic Center: Feeding and Feedback in a Normal Galactic Nucleus, eds. L. O. Sjouwerman, C. C. Lang, & J. Ott, IAU Symp., 303, 374
Pierce-Price, D., Jenness, T., Richer, J., & Greaves, J. 2003, Astron. Nachr. Suppl., 324, 413
Porquet, D., Predehl, P., Aschenbach, B., et al. 2003, A&A, 407, L17
Quataert, E. 2002, ApJ, 575, 855
Rácz, É., Kertész, J., & Eisler, Z. 2009, ArXiv e-prints [arXiv:0905.3096]
Sabha, N., Witzel, G., Eckart, A., et al. 2010, A&A, 512, A2
Schödel, R., Ott, T., Genzel, R., et al. 2002, Nature, 419, 694
Schuller, F. 2012, in SPIE Conf. Ser., 8452, 1
Shahzamanian, B., Eckart, A., Valencia-S., M., et al. 2015, A&A, 576, A20
Shimazaki, H., & Shinomoto, S. 2007, Neural computation, 19, 1503
Siringo, G., Kreysa, E., Kovács, A., et al. 2009, A&A, 497, 945

Tagger, M., & Melia, F. 2006, ApJ, 636, L33
Trap, G., Goldwurm, A., Dodds-Eden, K., et al. 2011, A&A, 528, A140
Trippe, S., Gillessen, S., Ott, T., et al. 2006, J. Phys. Conf. Ser., 54, 288
van der Laan, H. 1966, Nature, 211, 1131
Witzel, G., Eckart, A., Bremer, M., et al. 2012, ApJS, 203, 18
Witzel, G., Morris, M., Ghez, A., et al. 2014, in The Galactic Center: Feeding and Feedback in a Normal Galactic Nucleus, eds. L. O. Sjouwerman, C. C. Lang, & J. Ott, IAU Symp., 303, 274
Yusef-Zadeh, F., Bushouse, H., Dowell, C. D., et al. 2006a, ApJ, 644, 198
Yusef-Zadeh, F., Roberts, D., Wardle, M., Heinke, C. O., & Bower, G. C. 2006b, ApJ, 650, 189
Yusef-Zadeh, F., Wardle, M., Heinke, C., et al. 2008, ApJ, 682, 361
Yusef-Zadeh, F., Bushouse, H., Wardle, M., et al. 2009, ApJ, 706, 348
Yusef-Zadeh, F., Miller-Jones, J., Roberts, D., et al. 2011, in The Galactic Center: a Window to the Nuclear Environment of Disk Galaxies, eds. M. R. Morris, Q. D. Wang, & F. Yuan, ASP Conf. Ser., 439, 285
Zubovas, K., Nayakshin, S., & Markoff, S. 2012, MNRAS, 421, 1315

M. Subroweit et al.: Submillimeter and radio variability of Sagittarius A*

Appendix A: Power law fitting: the Clauset algorithm (CSN07)

The likelihood function of a power-law is given by

$$\mathcal{L}(\Theta; X) = \prod_{i=1}^{n} \frac{\alpha - 1}{x_{\min}} \left(\frac{x_i}{x_{\min}} \right)^{-\alpha} \tag{A.1}$$

with Θ as free parameters, here $x_{\min}$ and α.

The logarithm of the likelihood function is then given by

$$\ln \mathcal{L} = n \ln(\alpha - 1) - n \ln x_{\min} - \alpha \sum_{i=1}^{n} \ln \frac{x_i}{x_{\min}}. \tag{A.2}$$

Maximum Likelihood Estimations (MLEs) face a special problem when applied to power-laws: the parameter $x_{\min}$ is both a variable of the density function and a lower bound for the function's domain. As the likelihood function increases monotonically with decreasing domain, the MLE for $x_{\min}$ converges to ∞ or $\max(x_i)$. For this reason maximization of the likelihood function is only possible for the parameter α with a conditioned $x_{\min}$. If we set $\partial \ln \mathcal{L}/\partial \alpha = 0$ we obtain an estimator for the scaling parameter α:

$$\alpha = 1 + n \left(\sum_{i=1}^{n} \ln \frac{x_i}{x_{\min}} \right)^{-1}. \tag{A.3}$$

Equation (A.3) is known as the Hill estimator (Hill et al. 1975).

Common approaches for getting an estimator for $x_{\min}$ used visual inspection of log-log plots of the distribution function or so called Hill plots (α vs. the conditioned $x_{\min}$). CSN07 introduced an algorithm where the best estimator for $x_{\min}$ is obtained by applying Kolmogorov-Smirnov (KS) statistics. For every value x_i in the order statistics (the set of the ordered values of the sample) one assumes this value is $x_{\min}$ and calculates the corresponding Hill estimator $\alpha(x_{\min})$. One also calculates the KS-statistics for this value, which is defined as the maximum difference between the empirical survival function

$$\tilde{F}(x) = 1/n \sum_{i}^{n} I(x_i \geq x) \tag{A.4}$$

(where I is the indicator function, that takes the value 1 if the argument is true and 0 otherwise) and the theoretical survival (see Eq. (3)) function with that $x_{\min}$ and α. As best fit one accepts the estimators $x_{\min}$ and $\alpha(x_{\min})$ which minimize the KS-statistics.

For the error estimation of the parameters CSN07 suggest the following bootstrapping technique: first, about 1000 samples each of length n are created by bootstrapping with replacement. For each sample, a power-law fit is performed. The errors for $x_{\min}$ and $\alpha(x_{\min})$ are then given by taking the standard deviation of the 1000 bootstrapped values for $x_{\min}$ and $\alpha(x_{\min})$.

A goodness of fit parameter is derived by a modified bootstrapping technique. About 2500 surrogate samples of length n are created. Let n_{tail} be the length of the power-law tail with
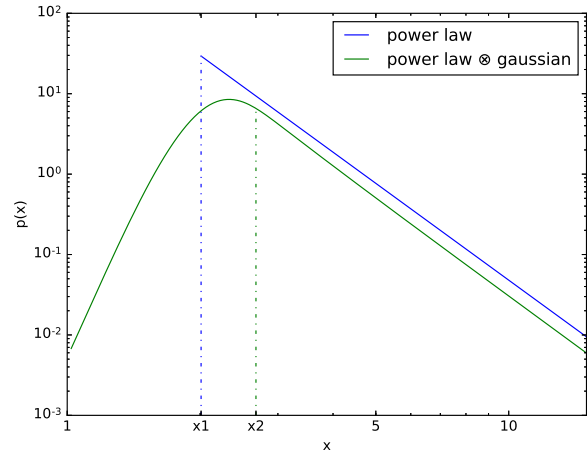
Fig. B.1. Schematic example for the convolution of a power-law with a Gaussian distribution and its effect on the apparent $x_{\min}$. Due to the influence of the Gaussian uncertainty distribution the fitted lower bound x_2 takes a higher value than the intrinsic paramter x_1.

$x_i \geq x_{\min}$. Then each value of a surrogate sample is generated as follows: with a probability of n_{tail}/n a random variable from the fitted power-law with $x_{\min}$ and α is drawn, with a probability of $1 - n_{\text{tail}}/n$ a value from the original data set with $x < x_{\min}$. For each of the surrogate samples a power-law fit is performed and the KS value is noted. The goodness of fit (p-value) is defined as fraction of surrogate data sample which have larger KS-values than the original data set. If the p-value is below a chosen significance level (e.g., 0.05), the power-law hypothesis is rejected. In this case there are only 5% of the surrogate samples with KS-statistic larger than the one of the "best" fit, meaning that most of the "fake" data fit better the model. In the opposite case, where the p-values are large, the majority of the fake samples have KS-statistics larger than our best fit, so its KS-statistic can be seen as a statistical fluctuation.

Appendix B: Convolution of a pure power-law with a Gaussian distribution

Here we show the influence of uncertainties and noise in the data acquisition on the obtained power-law parameter $x_{\min}$. We assume an power-law distributed random variable and an error statistics which can be modeled by a Gaussian distribution. Provided that both probabilities are independent the joint probability density is given by the convolution. A schematic representation of this convolution is depicted in Fig. B.1. It can be seen that the apparent lower bound of the power-law, that is the parameter $x_{\min}$ which is obtained by a power-law fitting routine, takes a higher value due to the uncertainty distribution. Nevertheless the power-law index α does not change significantly. A detailed quantitative discussion about power-laws convolved with a Gaussian can be found in Sect. 3.2 of Witzel et al. (2012).

Paper II: Synchrotron Self-Compton Scattering in Sgr A* Derived from NIR and X-Ray Flare Statistics

In the previous paper (Chap. 4, Subroweit et al. 2017), I analyzed radio and submm lightcurves and was able to show that the radio, submm and NIR emission can be described by a similar flux density distribution. I took this as a strong evidence that the flares at these wavebands originate from the very same source components. Theoretical considerations also revealed that the most probable emission mechanism is self-absorbed synchrotron emission, perhaps combined with an adiabatically expansion of the emitting source region.

The physical relation between flares from the radio to the NIR on one hand and the observed X-ray flares on the other hand have been discussed more controversial. The tight temporal correlation between X-ray and NIR flares also indicates common source components for both types of radiation. Nevertheless, the concrete emission mechanism giving raise to the observed X-ray outbursts is disputed. It has been proposed that the X-ray emission can either be the high energy part of an overall synchrotron spectrum (Dodds-Eden et al., 2009) or the Compotonized emission from lower frequency synchrotron radiation which has a energy cut-off shortly after the NIR (Marrone et al., 2008). Both models have different physical consequences: the synchrotron scenario requires ultra-relativistic electrons in the vicinity of Sgr A* whereas the SSC scenario requires higher electron densities in this region.

In this paper, I re-analyzed already published data from the Chandra X-ray Visionary Project (XVP) campaign. This campaign was conducted between February and October 2012 and collected in total 3 Msec of observation of Sgr A*. By that time, this almost doubled the available X-ray data of Sgr A* and therefore provided a very unique dataset. The publicly available data was reduced by the second author of this paper, Enmanuelle Mossoux (Mossoux and Grosso, 2017). Using this data, I show that the observed count rate distribution can be explained when assuming an SSC mechanism at work. As in the previous paper, the crucial point of this work is the descent application of power-law

theory. Another workgroup previously conducted a statistical analysis using a bounded power-law (BPL) to describe the count rate distribution of the same data (Neilsen et al., 2015). Using this model, the authors obtained a power-law scaling index of $\alpha \sim 1.9$. I argue that a BPL is physically difficult to motivate because a hard upper limit for possible count rates cannot be theoretically justified. I alternatively suggest an exponentially truncated power-law (TPL) which accounts for the observed decay in the high energy tail of the count rate distribution as well as for potentially brighter X-ray flares than the ones so far been observed.

Fitting a power-law distribution to the count rate statistics of Sgr A* has turned out to be a theoretically and technically challenging task. Combining Poisson photon statistics and instrumental pile-up effects prohibits the use of "classical" parameter estimation techniques. Therefore I have explored an - up to that point unknown to me - field of statistics: Approximate Bayesian Computation (ABC, see Sec. 3.3). Using this method, I am able to estimate the parameters of the TPL model and obtain a scaling parameter for the power-law of $\alpha \sim 1.6$. I am then able to show that this value can be naturally explained within the framework of an SSC model.

Synchrotron Self-Compton Scattering in Sgr A* Derived from NIR and X-Ray Flare Statistics

Matthias Subroweit[1] , Enmanuelle Mossoux[2], and Andreas Eckart[1,3]

[1] I. Physikalisches Institut, Universität zu Köln Zülpicher Str. 77 D-50937 Köln, Germany
[2] Institut d'Astrophysique et de Géophysique Allée du Six Août, 19C B-4000 Liège, Belgium
[3] Max-Planck-Institut für Radioastronomie Auf dem Hügel 69 D-53121 Bonn, Germany

Abstract

The flaring activity of Sagittarius A* (Sgr A*) can be analyzed by statistical means to test emission models for its accretion flow. A particular modeling question is whether the observed X-ray flares are the high-energy end of a synchrotron spectrum or if they arise from self-Comptonized photons of a lower-energy synchrotron process. We use already published Chandra X-ray Visionary Project data to statistically investigate the X-ray count-rate distribution of Sgr A*. Two previous workgroups have already undertaken such an analysis on that data. They modeled the flaring part of the emission with a bounded power law, i.e., a power-law distribution with a hard cutoff at the highest measured count rate. With this model, both teams obtain a power-law index $\alpha_X \sim 2$. We show that the flare count-rate distribution can also be well described by a truncated, i.e., an exponentially decaying power law. We argue that an exponential truncation is a more natural model than a hard cutoff. With this alternate model, our fit yields a power-law index $\alpha_X \sim 1.66$. We find that this slope can be canonically explained by a synchrotron self-Compton (SSC) process. Therefore, we argue that SSC models are the best ones suitable to explain the observed X-ray count-rate distribution.

Unified Astronomy Thesaurus concepts: Active galactic nuclei (16); Galactic center (565); Supermassive black holes (1663); X-ray active galactic nuclei (2035)

1. Introduction

The radio object Sagittarius A* (Sgr A*) is considered to coincide with the gravitational center of our Galaxy (Balick & Brown 1974; Brown & Lo 1982; Goss et al. 2003). Observations of gas clouds and stellar motions have revealed that at a distance of 8 kpc, Sgr A* is associated with a central mass of $\sim 4 \times 10^6 M_\odot$ concentrated in a very small volume (Lacy 1980; Herbst et al. 1993; Horrobin et al. 2004; Boehle et al. 2016). Such a high-mass concentration indicates that Sgr A* is most likely a supermassive black hole (SMBH; Eckart et al. 2002; Gillessen et al. 2009; Eckart et al. 2017; Gravity Collaboration et al. 2018a, 2018b). Nowadays it is assumed that SMBHs exist in the center of every massive galaxy and play an important role in the evolution of galaxies (Silk & Mamon 2012). Furthermore, SMBHs are supposed to be the central engine of active galactic nuclei (AGNs), one of the most energetic phenomena in the universe (Shields 1999). Therefore, these objects are subject of highest interest and comprehensive investigations in modern astrophysics. Due to its relative vicinity of a few kpc, Sgr A* is the perfect candidate to use for studying physics in the strong-gravity environment of a SMBH.

Most of the time Sgr A* resides in a quiescent, faint state, predominately emitting and always visible in the radio to submillimeter regime. The spectral energy distribution (SED) shows an inverted spectrum in these domains with a peak at the so called "submm bump." Typical mean-flux density values are, e.g., 1 Jy at 100 GHz and 3 Jy at 350 GHz. After a turnover in the 300–400 GHz regime, the SED shows a steep drop. While von Fellenberg et al. (2018) report on a detectable mean quiescent flux of Sgr A* in the far-infrared, in the mid- and near-infrared (NIR), so far only upper limits for a quiescent emission have been constraint (Schödel et al. 2007, 2011).

Sgr A* is not visible in the optical and UV band, due to extinction by dust along the line of sight through the Galactic plane. In the X-ray regime, it "reapears" as a faint source (e.g., $\sim 10^{-8}$ Jy in the 2–10 keV band, Baganoff et al. 2003). Modeling the entire SED, Sgr A*'s bolometric luminosity is of the order of $\sim 10^{36}$ erg s^{-1} (Narayan et al. 1998), which corresponds to $\sim 100 L_\odot$. The underluminous nature of Sgr A* ($\sim 10^{-9}$ times the Eddington luminosity) makes the case for both low mass accretion rates toward the SMBH and inefficient radiation processes. It is still not yet clear if our Galactic center has to be classified as an inactive, quiescent galactic nucleus, or if it is on the borderline to low-luminous AGNs (Ho 2008; Eckart et al. 2017).

However, Sgr A* shows intermittent, short time scaled (~ 1 ks) radiation outbursts, also referred to as flares, across all observed wave bands. Light travel arguments imply that these events have their origin in the innermost accretion flow toward the black hole. Thus, the investigation of flaring processes is a unique possibility to derive physical parameters from regions near the black hole's event horizon.

Generally speaking the flare amplitudes (compared with the quiescent level or with the upper detection limit) increases with increasing frequency. Herrnstein et al. (2004) report on variations of up to 55%, 75%, and 85% at 15, 23, and 43 GHz, respectively (see also Yusef-Zadeh et al. 2006a). At 100 and 140 GHz, flux density peaks of $\sim 100\%$ above the quiescent ~ 1 Jy level were observed (Tsuboi et al. 1999; Borkar et al. 2016), the same order of magnitude variations can be seen at 350 GHz (Dexter et al. 2014; Subroweit et al. 2017). In the NIR flare, peak flux densities of 30 mJy and more have been observed, which is a factor of 10 higher then the detection limit (Genzel et al. 2003; Ghez et al. 2004; Sabha et al. 2010; Witzel et al. 2012). X-ray flare peak count rates can exceed the quiescent level by a factor of 100 (Baganoff et al. 2001;

Porquet et al. 2008; Nowak et al. 2012; Mossoux & Grosso 2017).

Simultaneous multiwave band observations have revealed tight temporal correlations between flares at different frequencies. X-ray flares seem to always be accompanied by NIR flares with little, i.e., of the order of a few minutes, or no time delays (Marrone et al. 2008; see Boyce et al. 2019). The opposite is not always true (Eckart et al. 2004, 2006; Yusef-Zadeh et al. 2012; Mossoux et al. 2016; Capellupo et al. 2017). Lower-frequency flare peaks appear to follow with increasing time delays of up to several hours in the mm regime (Yusef-Zadeh et al. 2006a; Brinkerink et al. 2015; Capellupo et al. 2017). The observed temporal links between flares at different frequencies hint toward common spatial source components, although at the moment there is no consensus about the physical origin of these flares. Possible explanation models span from magneto-hydrodynamical turbulences, orbiting hotspots, jets, expanding plasmon blobs, and magnetic reconnections in an accretion disk (Markoff et al. 2001; Yusef-Zadeh et al. 2006b; Mościbrodzka et al. 2009; Karssen et al. 2017; Li et al. 2017) to name but a few. Models of adiabatically expanding synchrotron blobs may be of particular importance in this context as they imply a quite naturally explanation of the observed time delays between flare peaks (van der Laan 1966).

While polarization measurements in the NIR indicate that synchrotron radiation plays a predominant role in the radiative process of flares (Eckart et al. 2008; Shahzamanian et al. 2015), it is still being debated how the X-ray counterpart is to be interpreted. Some authors prefer pure synchrotron models where the X-ray flares are the high-energy part of a synchrotron spectrum with a possible additional cooling break between the NIR and the X-rays (Dodds-Eden et al. 2009; Ponti et al. 2017). Other authors have interpreted X-ray flares as a result of synchrotron self-Compton (SSC) emission from a synchrotron spectrum that does not extend to keV energies (Marrone et al. 2008; Eckart et al. 2012; Dibi et al. 2016). SSC models have already been fit to individual (multiwave band) light curves so that physical source parameters of the emission process, such as synchrotron turnover and cutoff frequencies, electron energies and densities, etc., have been successfully constrained (Sabha et al. 2010; García-Marín et al. 2011; Eckart et al. 2012; Mossoux et al. 2016).

Apart from the analysis of individual flare events, during the past three decades Sgr A* has been monitored sufficiently enough, so that it is also possible to investigate the flaring behavior with statistical means. For the context of this paper the following results should be mentioned:

1. The NIR variability of Sgr A* can be described as a single state, red noise like process (Do et al. 2009; Meyer et al. 2014). The flux density distribution in this wave band can be described by a power law with a scaling parameter $\alpha_{\mathrm{NIR}} \sim 4.2$ (Witzel et al. 2012).
2. The 350 GHz flux density distribution follows a power law with a slope $\sim$4, very similar to the NIR flux density distribution (Subroweit et al. 2017).
3. The 2–8 keV count-rate distribution can also be modeled by a power law. Using a power-law model with an upper bound (details will be mathematically described in Section 3), Li et al. (2015 hereafter L15) and Neilsen et al. (2015, hereafter N15) derived a power-law slope $\alpha_X \sim 2$.

4. The spectral index ζ (with $S_\nu \propto \nu^{-\zeta}$) in the NIR approaches $\sim$0.6 for bright flares. Fainter flares seem to have a steeper spectrum (Bremer et al. 2011; Witzel et al. 2018, but also see the discussion in Section 6).
5. For X-ray flares, ζ is less well constrained. In the literature, one mostly finds values between 0.3 (Baganoff et al. 2001; Bélanger et al. 2005) and 1 (Nowak et al. 2012; Yuan et al. 2018) generally consistent with a value of 0.6. Albeit even extremer spectra have been reported (Goldwurm et al. 2003; Ponti et al. 2017).

In this paper we statistically reanalyze X-ray Visionary Project (XVP) data published in Mossoux & Grosso (2017, hereafter M17; see Section 2). The same observations were already analyzed by L15 and N15. These groups model the flaring X-ray count-rate distribution with a bounded power law. By contrast, in Section 3 we introduce a new model for the flaring emission: an exponentially truncated power law. We reason an exponential truncation of the count-rate distribution to be a more physical approach compared with a hard cutoff with a fixed upper limit. In Section 4 we then derive the main parameter of the count-rate distribution, i.e., the power-law index α_X and find $\alpha_X \approx 1.66$. In Section 5 we introduce an algebraic derivation of α_X under the assumption of a simple SSC scattering model with a constant synchrotron spectral index ζ. The algebraically predicted parameter $\alpha_X = 1.6$ convincingly matches the empirically derived parameter $\alpha_X \approx 1.66$ from Section 5. In Section 6 we discuss and validate the assumption of a constant and common spectral index for both the optically thin synchrotron and the SSC emission. We then interpret our results in the context of the pure synchrotron versus SSC debate and argue that SSC models should be favored over pure synchrotron models.

2. Data Selection

From the data presented in M17 we solely use the XVP campaigns for our analysis. This data frame does not suffer from instrument aging, time-dependent calibration problems or the lack of angular resolution. By restricting our analysis on this data, our results also become directly comparable with N15 and L15.

The light curves of Sgr A* were constructed in exactly the same way as presented in M17: the data were reduced using the Chandra Interactive Analysis of Observations package (version 4.7) and the calibration database (CALDB; version 4.6.9). The source and background events were then extracted from a $1''25$-radius disk centered on the radio position of Sgr A* and from a $8''2$-radius disk at $0'.54$ south of Sgr A*. During the XVP campaign, Sgr A* was observed with the High Energy Transmission Grating (HETG), which disperses the source events on the detector. We thus extracted the dispersed events from wide rectangle of $2''5$ width. The light curves in a 2–10 keV energy range were then created by merging zero-order and ± 1-order events and grouping the events using a time bin of 300 s.

Due to the nature of its CCD detectors, count-rate measurements with Chandra are subjected to pile-up effects. These effects occur whenever two or more photons arrive at a single CCD in the same readout interval. Instead of resolving multiple photon counts, the detector associates the sum of the photon energies with a single event. This can even lead to a nondetection if the sum of the single photons energies exceed

Subroweit, Mossoux, & Eckart

the energy bandpass of the detector. Thus, pile-up phenomena both distort measured spectra and count rates.

According to the "The Chandra ABC Guide to Pile-up"[4] the fraction of counts lost due pile-up, f_r, is given by

$$f_r = 1 - \frac{[\exp(\alpha \Lambda_i) - 1]\exp(-\Lambda_i)}{\alpha \Lambda_i}, \tag{1}$$

where α is the grade migration parameter (which we assume to be $\alpha = 1$) and Λ_i is the incident count rate measured in counts per frame (a frame is 3.14 s for HETG observations). However it must be held that only zero-order photons are affected by pile-up, not dispersed $\pm$1st-order events. We find that on average the ratio of zero- to first-order events is approximately 1.6. This agrees with the ratios mentioned in Nowak et al. (2012) and Bouffard et al. (2019).

With this relations, we are able to incorporate pile-up into the count-rate distribution models. Methodologically, we note that we do not "unpile" the observational data but simulate pile-up effects on generated mock data as described in the next section.

3. Count-rate Distributions and Photon Statistics

In this section we introduce the probability density functions (pdfs), which we assume to be able to summarize both the quiescent and the flaring emission and discuss the challenges of fitting low count-rate distributions. We assume that the convolution of two pdfs make up the observed X-ray count-rate distribution of Sgr A*: a pdf for the steady quiescent emission and a pdf for the flaring component which can be described by some realization of a power-law distribution.[5] The power laws we take into consideration are either a bounded power law with

$$\text{PDF}(x) = \begin{cases} 0 & \text{for } x \leqslant x_{\min} \\ C_1 \cdot x^{-\alpha} \\ 0 & \text{for } x \geqslant x_{\max} \end{cases} \tag{2}$$

and parameters $\Theta = (x_{\min}, \alpha \text{ and } x_{\max})$, or a truncated power law with

$$\text{PDF}(x) = \begin{cases} 0 & \text{for } x \leqslant x_{\min}, \\ C_2 \cdot x^{-\alpha} \exp(-\lambda x) \end{cases} \tag{3}$$

and parameters $\Theta = (x_{\min}, \alpha \text{ and } \lambda)$. For physical reasons, we deem a truncated power law to be the better approach compared with a bounded power-law model. An exponential truncation is more physical than a hard cutoff. With a bounded power law, the probabilities for count rates $\geqslant x_{\max}$ approach zero.[6] This implies that if brighter flares were observed (e.g., in future observations), the model had to be adjusted (refitted). By contrast, a truncated power law assigns a nonvanishing probability to higher count rates, and therefore naturally includes potentially brighter, not yet observed flares. X-ray

---

[4] https://cxc.harvard.edu/ciao/download/doc/pileup_abc.pdf
[5] By "realization of a power law," we mean that the underlying power-law pdf has to be pile-up corrected and treated as a Poisson process. Mathematical details will be discussed later.
[6] If one considers additional counting noise, the probability of observing count rates $\geqslant x_{\max}$ are not exactly zero. For instance, count rates of up to $x_{\max} + \sqrt{x_{\max}}$ still are in the 1σ-interval for the expected maximum values. Nevertheless, a bounded power law introduces a hard physical constraint on predicted flux densities and count rates where a truncated power law does not.

echoes detected near the Galactic center suggest that brighter flares indeed occurred in the past (Koyama et al. 2008; Ryu et al. 2013). Also, the history of X-ray flare observations shows that the upper flare flux density increase steadily as the monitoring time increases. Furthermore, exponentially truncated power laws are a common description of quasi-scale free processes which are constrained by limited mass, volume, or energy reservoirs. For instance, Schechter (1976) found a exponentially truncated power law for the luminosity function of galaxies, Abod et al. (2019) model the mass and size distribution of planetesimals with a similar distribution. Synchrotron spectra of jets (Meisenheimer & Heavens 1986), SSC spectra of blazars (Schlickeiser & Röken 2008), and spectra of X-ray binaries (Cadolle Bel et al. 2006) also exhibit exponential truncation of power laws at high energies. In general, sharp cutoff power laws are harder to justify and need evident and compelling physical boundaries. Although we therefore question the idea of a hard cutoff of Sgr A*'s X-ray count-rate distribution as in a bounded power law, we implemented that model to check our routines for consistency with N15 and L15.

In the following, we discuss some statistical subtleties that need to be considered when fitting Sgr A*'s X-ray count-rate distribution: standard approaches for fitting a distribution PDF(Z) to observed data Z commonly involve first constructing the likelihood function $\mathcal{L} = \prod_i \text{PDF}(z_i) = P(Z|\Theta)$ and then performing a maximization routine for $\mathcal{L}$. Without pile-up effects and counting noise, and assuming that there is a simple conversion factor between observed count rates and flux densities S (see N15 or Nowak et al. 2012), finding an expression for $\mathcal{L}$ would be straightforward. In a generic, simple model, the flaring emission may be assumed to follow a pure power law of the form $p(S) \propto S^{-\alpha}$ and the quiescent emission a normal distribution $g(S) \propto \exp(-(S - P)^2/\sigma^2)$ with mean value P and variance σ. Then the convolution of both distributions and thus the likelihood function is easy to form. As a simple example, in the idealized limit of negligible variance $g(S)$ can formally be reduced to a delta distribution $g(S) \approx \delta(S - P)$. The PDF(S) would then be given by

$$\text{PDF}(S) = f(S) * g(S) = f(S - P) = (S - P)^{-\alpha}. \tag{4}$$

This is called a shifted power law. We comprehensively analyzed such a model for submm data in Subroweit et al. (2017).

However, in case of the X-ray distribution examined here, the situation is unfortunately more complicated. First, as mentioned above, the data is affected by pile-up effects. This implies that if the PDF for a variable X is know, but a piled-up quantity X' with $X' = \mathcal{P}(X)$ is observed, the probability density function for X' is given by $dN/dX' = dN/dX \cdot dX/dX'$. second, the pile-up corrected variable is governed by Poisson statistics, i.e., it is subject to counting noise. We then call the observed variable X'' and its distribution dN/dX'' is given by

$$\frac{dN}{dX''} = \int_0^\infty \left(\frac{X'^{X''}}{X''!} \exp(-X') \frac{dN}{dX'} \right) dX'. \tag{5}$$

Such a distribution is referred to as doubly stochastic Poisson or Cox process.

As for the quiescent emission, Equation (5) can be reduced to a simple form: if we assume a constant quiescent background process (which could be expressed by a δ-distribution as explained above) and neglect pile-up effects (i.e., $X = X'$, which is justified by the low count rates in the quiescent emission), Equation (5) becomes

$$\frac{dN}{dk}\bigg|_{P} = \int_{0}^{\infty} \frac{X^{k}}{k!} \exp(-X)\delta(X - P)dX$$

$$= \frac{P^{k}}{k!} \exp(-P). \tag{6}$$

Here we have set $k := X''$ for better readability where k is the observed discrete count rate. Thus, the quiescent emission can be described by a simple homogeneous Poisson distribution which is completely determined by its only parameter P.

For a power-law process with pile-up effects and counting noise though, the integral in Equation (5) can in general not easily be simplified. For instance, the resulting probability mass function from an underlying truncated power law is given by

$$\frac{dN}{dk}\bigg|_{x_{\min},\alpha,\lambda} = \int_{x_{\min}}^{\infty} \frac{X'^{k}}{k!} \exp(-X') \frac{dX}{dX'} (\mathcal{P}^{-1}(X'))^{-\alpha}$$

$$\times \exp(-\lambda \cdot \mathcal{P}^{-1}(X'))dX'. \tag{7}$$

The total count-rate distribution, i.e., the combination of both the quiescent and the flaring emission, then has to be computed by convolving Equations (6) and (7). Hereafter, we will refer to it as a BPL model, if we plug in a bounded power law into Equation (5), and a TPL model if we use the truncated power law.

4. ABC Fitting

In the previous section we proposed that the entire count-rate distribution of Sgr A* can be expressed by the convolution of two pdfs. However, although this convolution can in principle be computed numerically and then be used to calculate the likelihood function $\mathcal{L}$, these calculations tend to be complicated and time intensive. For instance, setting up an Markov chain Monte Carlo routine to draw samples from the posterior distribution $P(\theta|Z)$ needed the convolution integral to be computed at least several 10^{4}–10^{5} times for good convergence. While it is difficult and expensive to draw samples from $P(\theta|Z)$ (due to what is also called a intractable likelihood), it is comparatively easy to generate mock data according to the aforementioned class of models. This makes the case for a parameter estimation strategy referred to as approximate Bayesian computation (ABC). The idea behind ABC is to not draw samples directly from the exact posterior distribution $P(\Theta|Z) = P(\Theta)P(Z|\Theta)$ but from an approximation to $P(\Theta|Z)$. If Z is the observed data, M is a mock sample generated by simulation, D is a distance metric, and ϵ a distance threshold, it can be shown (Marjoram et al. 2003) that $P(\Theta|D(M|Z) \leqslant \epsilon)$ is a good approximation for the "true" posterior distribution if ϵ is sufficiently small and D is a sensible metric.[7]

To implement an ABC parameter estimation routine, we thus first need to define the simulator for the mock data M. If X are

Table 1
Parameter Priors

Model	P (10^{-3} cts s^{-1})	$x_{\min}$ (10^{-4} cts s^{-1})	α_{X}	λ (s ct s^{-1})
BPL	$u(1-20)$	$u(0.1-10)$	$u(1.1-3)$	$\cdots$
TPL	$u(1-20)$	$u(0.1-10)$	$u(1.1-3)$	$u(0-20)$

Note. Priors for the ABC fitting, u stands for a uniform prior within a given range.

samples from the quiescent emission and Y from the flaring emission, the expected count rate $M = X + Y$ can be simulated as follows: for the quiescent emission we draw samples from a Poisson random number generator rpoi(P) with a mean value P (see Equation (6)). The flaring emission can be simulated by first generating a power law distributed random variable $x = $ rpl($\cdot$), apply pile up corrections to this variable, i.e., $x' = \mathcal{P}(x)$ and account for counting noise by drawing from a Poisson distribution so that $x'' = $ rpoi(x'). Here, the power law random number generator rpl($\cdot$) is a placeholder for the respective power law used in the two models. We note that only for the BPL there exists a closed analytical form for the random number generator. For the TPL model we generated random numbers by numerical inverse transform sampling. The resulting mock data generator for the X-ray emission can now be written as

$$M = X + Y = \text{rpoi}(P) + \text{rpoi}(\mathcal{P}(\text{rpl}(\cdot))). \tag{8}$$

We draw samples from $P(\Theta|D(M|Z) \leqslant \epsilon)$ by setting up a sequential Monte Carlo (SMC) ABC routine. In ABC–SMC the posterior distribution is approximated sequentially by iteratively reducing the acceptance threshold ϵ and thus creating intermediate distributions of Θ, called populations. The first population of parameters is created by drawing from the priors $P(\Theta)$. We then accept those parameters with $D(M(\Theta)|Z) \leqslant \epsilon_{1}$. Accepted parameters are also called particles. After a specific number of particles have been collected the next iteration step will be executed. In the following iteration the prior gets replaced by the perturbed, i.e., weighted and randomized[8] previous particle ensemble and ϵ_{i} with $\epsilon_{i+1} < \epsilon_{i}$. Thus, consecutive particle ensembles are supposed to approximate $P(\theta|Z)$ increasingly better. Our ABC–SMC sampler is implemented in the Python framework pyabc (Klinger et al. 2018). As distance function D between M and Z we use the energy distance (Székely & Rizzo 2013) defined as square root of

$$D^{2}(M, Z) = 2 \int_{-\infty}^{\infty} (F(x) - G(x))^{2}dx \tag{9}$$

where F and G are the cumulative distribution functions (CDFs) of M and Z. The used priors are listed in Table 1.

We set up the ABC sampler with a fixed particle number of 10,000 per population. As a stop condition for the sampler we define $D(M, Z) \leqslant \epsilon = 0.01$. This is an empirical choice that has no influence on the outcome of the investigation if the chosen ϵ is sufficiently small. By tracking the parameter convergence over several particle ensembles it can be shown

---

[7] In ABC it has to be examined for each use case what is a "sufficiently small distance" and a "sensible metric." If, for instance, the algorithm reproduces results obtained by other methods these conditions can be considered as fulfilled.

[8] A detailed mathematical description of particle perturbations can be found in, e.g., Toni et al. (2009).
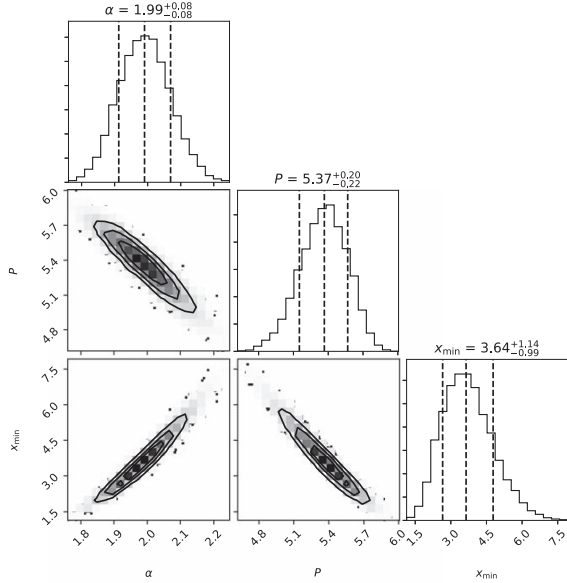
(a)
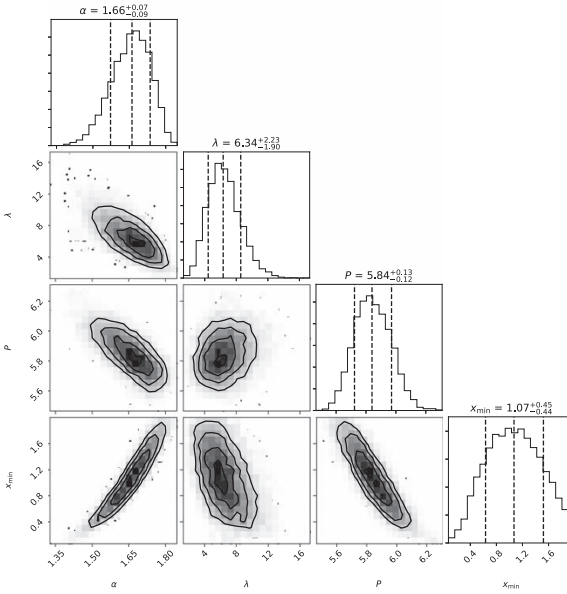
(b)

Figure 1. (a) Corner plot of the BPL parameters. (b) Corner plot of the TPL parameters. The marginalized posterior distributions of the estimated parameters are almost Gauss-shaped which indicates a good convergence of the fits.
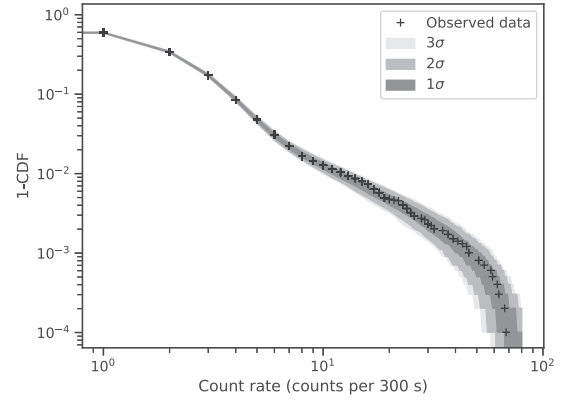
Table 2
ABC–SMC Fitting Results

Model	P (10^{-3} cts s^{-1})	x_{min} (10^{-4} cts s^{-1})	α_X	λ (s ct s^{-1})
BPL	$5.4^{+0.2}_{-0.3}$	4^{+2}_{-1}	$1.99^{+0.08}_{-0.08}$	⋯
TPL	$5.9^{+0.2}_{-0.2}$	$1.1^{+0.5}_{-0.4}$	$1.66^{+0.07}_{-0.09}$	6^{+3}_{-2}

Note. For the later analysis, the scaling parameter α_X is the most interesting. It differs significantly depending on the used fitting model.

(a)
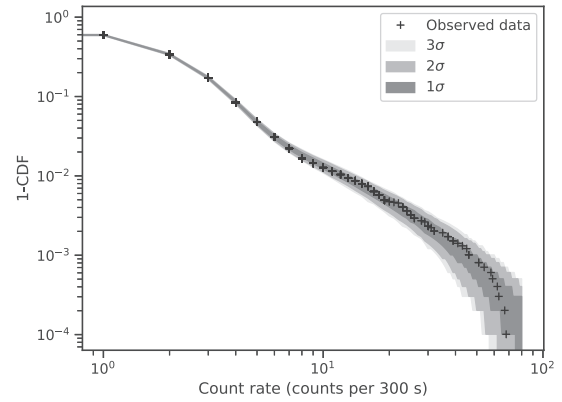
(b)

Figure 2. (a) ECDF of the simulated data according to the best-fit BPL model. (b) ECDF of the simulated data according to the best-fit TPL model. Both plots show the ECDF of the observed data as well as the 1σ, 2σ, and 3σ intervals of the ECDF given by simulations. For each model we generated 1000 synthetic samples with the best-fit parameters and calculated the resulting ECDF on the same grid. The σ intervals shown in different gray levels are evaluated by taking the respective percentile functions. Both models seem to fit the data equally well. Although the visual impression of both models is similar, the underlying power-law models are different ($\alpha_X = 1.99$ for the BPL vs. $\alpha_X = 1.66$ for the TPL model favored by us). The estimated scaling parameter of the power-law distribution is very sensitive toward the behavior at the high count-rate tail (i.e., hard cutoff vs. exponential truncation).

(we omit the demonstration here) that this distance is appropriately small, so that the particle distributions have stabilized. We therefore can safely consider the last generated particle ensemble as good approximation of the posterior distribution.

In Figure 1 we show scatter plots of the last particle ensembles from both models. It can be seen that the posterior distributions are well-behaved and not degenerate. The best-fit parameter estimates and their errors are listed in Table 2. The respective empirical cumulative distribution functions (ECDFs) are shown in Figure 2 (see the caption for details). Our ABC
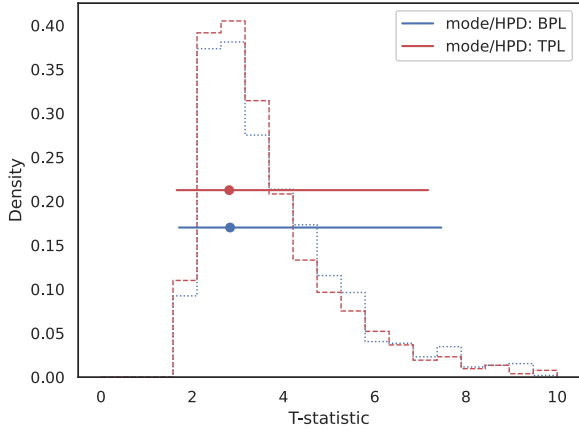
Figure 3. Distribution of T-statistics for both the BPL (blue) and the TPL(red) model and the corresponding HPD intervals (see the text for details). Lower values indicate a better fit. The lower mode and HPD interval range of the TPL model distribution may suggest a preference for this model albeit both models seem to perform comparably.

parameter estimation approach reproduces the results of N15. With a BPL model we find a Poisson parameter $P = (5.4^{+0.2}_{-0.3}) \times 10^{-3}$ cts s^{-1} and a power-law slope of $\alpha_X = 1.99^{+0.08}_{-0.08}$. This is consistent with $P = (5.24 \pm 0.08)$ cts s^{-1} and $\alpha_X = 1.92^{0.03}_{0.02}$ from N15. L15 found $\alpha_X \sim 2.2$ which is inconsistent with N15 but lies within the 3σ-interval of our value.

We finally compare the statistical performance of the the BPL and the TPL model by using the standard test for equality of distributions in the energy distance framework, namely the T-statistics (Szekely & Rizzo 2004): if $D(M, Z)$ is the energy distance between the observed data Z with length n and a simulated sample M of length m, the T-statistic is defined as

$$ T = \frac{nm}{n + m} D^2(M, Z). \tag{10} $$

For each model we generated 1000 samples M_i with the best-fit parameters given in Table 2 and calculated the respective T-statistic. The results are shown in histograms in Figure 3. For the BPL model we obtain a mode of 2.83 and a highest posterior density (HPD) interval of (1.71–7.46). The mode of the TPL T-statistic is 2.81 with a HPD interval of (1.66–7.17). This suggests that the TPL model performs marginally better (lower mode and HPD interval) without giving a strong decisive criterion for that model. Nevertheless we can demonstrate that the TPL model fits the data at least comparably well as the BPL model. This backs up our former heuristic preference for the TPL model.

5. The Link between X-Ray and NIR Distributions: Plausibility of an SSC Scenario

In Section 3 we have argued that a TPL model should be preferred over a BPL model, and have shown in Section 4 that the power-law index of the count-rate distribution is then given by $\alpha_X = 1.66$. Now we present an approach to interpret this finding particularly in the context of the pure synchrotron versus SSC debate.

If one considers a pure synchrotron model with $S_\nu \propto \nu^{-\zeta}$, the X-ray count rates are always proportional to the NIR flux densities. A straightforward deduction then would be that both the NIR and the X-ray flare distributions simply share the same power-law index α: the X-ray distribution just inherits the statistics of the lower, optically thin frequencies. Alternatively, recent models involve a synchrotron power law $\propto \nu^{-\zeta}$ that is continued with a steeper power-law spectral index $\propto \nu^{-(\zeta+1/2)}$ after a cooling break at ν_c between the NIR and X-ray domain. This additional assumption of a (constant or stochastically distributed) cooling break does not weaken the former statement about the similarity of both distributions: though the spectra in the X-ray regime are steeper in this case, the scaling behavior of the distribution after the cooling break stays the same. N15 have already shown, that in the case of this pure synchrotron model only an unphysical positive correlation between the cooling break frequency ν_c and the NIR flux density S_{NIR} would be able to explain the smaller X-ray power-law index (see their discussion in Section 5).

Here we suggest another approach which might explain the link between NIR and X-ray statistics. If one accepts that both the NIR and the X-ray distributions are power-law distributed (i.e., $PDF(S_{NIR}) = S_{NIR}^{\alpha_{NIR}}$ and $PDF(S_X) = S_X^{\alpha_X}$), and furthermore claims a functional relationship between X-ray count rate and NIR flux density of the form $S_X = f(S_{NIR})$, the scaling invariance suggests that the function f can also be written as some power law, i.e.,

$$ S_X \propto S_{NIR}^\beta. \tag{11} $$

Under this condition, and using the formal approach $PDF(S_X) = dN/dS_X = dN/dS_{NIR} \cdot dS_{NIR}/dS_X$ N15   have shown (see their Equations (8)–(11)) that it holds that

$$ \alpha_X = 1 + \frac{\alpha_{NIR} - 1}{\beta}. \tag{12} $$

Moreover, Witzel et al. (2012) have found, that $\alpha_{NIR} \sim 4.2$. It then follows that

$$ \alpha_X \cong 1 + \frac{3.2}{\beta}. \tag{13} $$

If we now assume approximately spherical and homogeneous plasma blobs (which are optically thin in the NIR) as source regions of the flares, we can implement the SSC formalism of Marscher (1983). In this framework, the entire spectrum of synchrotron photons gets upscattered by the synchrotron radiation emitting ensemble of electrons. With $S_{NIR} = S_m(\nu_{NIR}/\nu_m)^{-\zeta}$, the first-order Compton flux density can be written as

$$ S_{xray}^{SSC} \propto S_{NIR}^{2(\zeta+2)} \nu_m^{-\zeta(2\zeta+7)-5} \Theta^{-2(2\zeta+3)} $$
$$ \times \ln(\nu_c/\nu_m)\delta^{-2(\zeta+2)} \tag{14} $$

where S_m is the flux density at the synchrotron turnover frequency ν_m, ζ the spectral index for the optically thin synchrotron emission, ν_c the upper cutoff frequency of the synchrotron spectrum, Θ the angular diameter of the source region and δ the relativistic boosting factor. For typical values of ν_c (i.e., between 10^2 and 10^6 THz) and ν_m (i.e., of a few hundred GHz) the term $\ln(\nu_c/\nu_m)$ can be approximated by $\ln(\nu_c/\nu_m) \approx c_1(\nu_c/\nu_m)^{c_2}$, with $c_2 \sim 0.07$ (see Eckart et al.

2012). This means that due to the small exponent c_2 this term can be neglected here. Furthermore, we assume only mildly relativistic bulk motion of the emitting source regions as, e.g., derived in Subroweit et al. (2017) so that in a first approximation relativistic boosting also does not need to be considered. Therefore, in this context Equation (14) reduces to

$$S_{\text{xray}}^{\text{SSC}} \propto S_{\text{NIR}}^{2(\zeta+2)} \nu_{\text{m}}^{-\zeta(2\zeta+7)-5} \Theta^{-2(2\zeta+3)}. \qquad (15)$$

From synchrotron theory it is known that the occurring quantities are interdependent. For instance, in stationary synchrotron sources with magnetic field B and electron density n_e the synchrotron flux density for some optically thin frequency scales with $S_{\text{SYN}} \propto n_e \nu^{-\zeta} \Theta^3 B^{\zeta+1}$. The self-Compton flux density is then given by $S_{\text{SSC}} \propto n_e \Theta S_{\text{SYN}}$. B and n_e in turn can be expressed by $B \propto \Theta^4 \nu_{\text{m}}^5 S_{\text{m}}^{-2}$ and $n_e \propto \Theta^{-(4\zeta+7)} \nu_{\text{m}}^{-(4\zeta+5)} S_{\text{m}}^{2\zeta+3}$. Therefore, without further considerations, it is not easy to recognize that Equation (14) can in this statistical context be approximated with a form similar to Equation (11).

Let us first focus on the three physical parameters S_{NIR}, ν_{m}, and Θ in Equation (15). S_{NIR} is the one with the highest observed variability: Witzel et al. (2012) have shown, that flux density variations in the NIR of factors 30 and above can be observed. In contrast to that, the emitting source size Θ is considered to have significantly smaller variations: time travel arguments and modeling results imply, that Θ is at least approximately 1 R_{S} (Mossoux et al. 2015; Karssen et al. 2017). On the other hand, recent observations have revealed orbital motions of these emitting regions at a distance of $\sim 4 R_S$ (Gravity Collaboration et al. 2018a), which therefore we use as an upper limit for the source size. Thus, source size variations are only of the order of unity. Similar small variations can be assumed for the synchrotron turnover frequencies ν_{m}. Although the distribution of ν_{m} for different flares has not been directly observed yet as this would require full spectral measurements of multiple flares, modeling approaches have shown that the bulk of flares seem to have a turnover point near the submm bump, again with variations of only a few times unity (Eckart et al. 2012; Mossoux et al. 2016). Thus, from basic considerations about the likely variations of the physical parameters in Equation (15) it appears that the flux density variations in S_{NIR} presumable play the dominant role for the inter-flare variations in the SSC process.

It is therefore legitimate to approximate the general behavior of the SSC flux density with

$$S_{\text{xray}}^{\text{SSC}} \propto S_{\text{NIR}}^{2(\zeta+2)} \tilde{\nu}_{\text{m}}^{a(\zeta)} \tilde{\Theta}^{b(\zeta)}, \qquad (16)$$

where $\tilde{\nu}_{\text{m}}$ and $\tilde{\Theta}$ are mean values and $a(\zeta)$ and $b(\zeta)$ exponents as given in Equation (15). The distribution of $S_{\text{xray}}^{\text{SSC}}$ can be imagined as the product of the random variables ν_{m}, Θ and S_{NIR}, where the pdfs of ν_{m} and Θ have such narrow variances, that the pdf of S_{NIR} dominates the shape of the product distribution.[9] Therefore, for the statistical average of an

---

[9] In the Appendix, we also demonstrate that under the additional assumption of adiabatic expansion as mechanism for intra-flare flux density variations at different wave bands the dominance of S_{NIR} on variations in $S_{\text{xray}}^{\text{SSC}}$ becomes even more evident.

ensemble of flares it is valid to write

$$S_{\text{xray}}^{\text{SSC}} \propto S_{\text{NIR}}^{2(\zeta+2)} \propto S_{\text{NIR}}^{\beta}. \qquad (17)$$

Coming back to Equation (13) we then obtain

$$\alpha_{\text{X}} \cong 1 + \frac{3.2}{\beta} \cong 1 + \frac{3.2}{2(\zeta+2)}. \qquad (18)$$

Considering that the synchrotron spectral index for bright NIR flares has been derived to be $\zeta \sim 0.6$ (a detail discussion on that value can be found in Sections 1 and 6), we expect β to be ~ 5.2 and thus

$$\alpha_{\text{X}} \approx 1.6. \qquad (19)$$

This value is in good agreement with the previously obtained $\alpha_{\text{X}} = 1.66_{-0.09}^{+0.07}$ derived via the ABC analysis.

6. Conclusions

We have shown that the X-ray emission of Sgr A* is well described by a convolution of a (quiescent) Poisson and a realization of a (flaring) exponentially truncated power-law count-rate distribution. An ABC analysis yields a power-law index $\alpha_X = 1.66$. Within a theoretical SSC framework we have also derived that for a constant synchrotron spectral index of $\zeta = 0.6$ one expects the X-ray flux density distribution to follow a power law with scaling parameter $\alpha_X \approx 1.6$. The theoretically expected and the empirically derived value are statistically consistent.

However, for the theoretical derivation we used a constant spectral index of $\zeta = 0.6$. While that value seems to be valid for the bulk of bright NIR flares (Eisenhauer et al. 2005; Hornstein et al. 2007; Bremer et al. 2011; Witzel et al. 2014), Witzel et al. (2018) have also shown, that the NIR spectral index ζ is a function of flare brightness. For fainter flares ζ tends to be significantly steeper and approaches 0.6 only for brighter flares. As outlined by Eckart et al. (2006), Bremer et al. (2011) and Witzel et al. (2018) most of the variation can be explained by alterations of the synchrotron loss cutoff frequency ν_2. This explains the spectral steepening toward faint infrared flares. Bright NIR flares are dominated by a spectral index around 0.6 as expected for optically thin synchrotron radiation (Hornstein et al. 2007; Witzel et al. 2018).

Furthermore, SSC theories imply that the spectral index of the optically thin synchrotron emission is preserved and therefore should also be observed in the X-ray regime. As already mentioned in Section 1, the measured X-ray spectral indices scatter significantly around the predicted value of 0.6 (e.g., Bélanger et al. 2005; Barrière et al. 2014; Zhang et al. 2017; Haggard et al. 2019). It could be argued that this might be contraindicative for an SSC scenario in the case of Sgr A*. Nevertheless, the following arguments have to be considered here.

1. The derived spectral indices in the X-ray regime are in general subject to high uncertainties. Not only that the low 2–8 keV flare count rates of Sgr A* lead to high uncertainties in the obtained spectra but also the spectral fits are highly model dependent (e.g., models for dust scattering and the N_{H} column density). Regardless of this, the spectral index of bright X-ray flares is to within the uncertainties consistent with or shows the tendency to approach the spectral index expected from SSC scattering

of a synchrotron spectrum with $\zeta \sim 0.6$ (see Figure 7 in Eckart et al. 2017).

2. The demand for similarity of both the spectral indices in the optically thin and the X-ray emission in SSC models only holds for the instantaneous, in situ spectra without cooling effects. Chiang & Böttcher (2002) have shown that if synchrotron radiation is the dominant cooling mechanism the time-averaged SSC spectral index can become significantly steeper (up to $\zeta_{SSC} = (3 + 2\alpha)/4$). Thus, although we have not incorporated such a time-dependent analysis here, possible steeper X-ray spectral index than $\zeta = 0.6$ do not exclude an SSC scenario.

Other authors have presented SSC models where the location of the SSC flux peak lies close to or within the 2–8 keV band (Dodds-Eden et al. 2009). Then the assumption of a common in situ spectral index ζ in the NIR and the observed X-ray regime as required by Equation (14) would not apply. These models presuppose seed photons with distinct frequencies (either submm or NIR) scattering with IR emitting synchrotron electrons. In contrast to that, in the SSC framework we are considering here the entire spectrum of synchrotron photon interacts with the entire ensemble of synchrotron emitting electrons.[10] Following standard synchrotron theory we are assuming a power-law distribution for the ensemble of synchrotron electron Lorentz factors, with $N(\gamma) \propto \gamma^{-p}$ within the limits $\gamma_1 \leqslant \gamma \leqslant \gamma_2$. Then, according to Marscher (1987), the limits for which Equation (14) is valid and, thus, for which a common spectral index can be assumed, is given by

$$5.5 \times 10^{-9} \gamma_1^2 \nu_m < E_{keV} < 5.5 \times 10^{-9} \gamma_2^2 \nu_2, \qquad (20)$$

where ν_m and ν_2 are the synchrotron turnover and upper cutoff frequency given in units of GHz. The observed synchrotron spectrum ranges at least from the submm bump ($\nu_m = 350$ GHz) to the NIR ($\nu_2 \sim 200$ THz). Magnetic fields can be assumed to be of a few ten Gauss (10–30 G). If we now imagine the observed synchrotron spectrum as sum of single electron spectra which emit most at their energy at the critical frequency $\nu_{crit} = 4.2 \times 10^6 B \gamma^2$, the spectrum of Lorentz factors roughly spans from 50 to 2000. Using Equation (20) we find that the used SSC formalism should approximately be valid for SSC energies between $5 \text{ eV} < E_{keV} < 5 \text{ MeV}$. Neither the lower cutoff frequency nor the higher frequency cutoff are predicted to lie in the 2–8 keV band. Any putative spectral structure in that range is therefore unlikely to be due to the underlying SSC mechanism. Hence, in consideration of general properties of Sgr A*'s synchrotron mechanism, a common in situ spectral index ζ in the NIR and the observed X-ray regime can from a theoretical perspective safely be assumed.

We conclude that the predictions made by a first principle SSC model are generally fully consistent with the observed X-ray count-rate distribution. We find that not only detailed modeling of individual NIR/X-ray flares (Eckart et al. 2012; Mossoux et al. 2016) but also the statistical analysis (as presented here) of the flare fluxes and the spectral index behavior supports the dominant presence of an SSC mechanism. Additionally, an SSC mechanism is less demanding on the electron acceleration process compared with a pure synchrotron process. In the SSC case electrons with $\gamma \leqslant 1000$ are sufficient to explain the observed X-ray flux density (Markoff et al. 2001; Eckart et al. 2012). The electrons efficiently scatter the seed spectrum that stretches from the submm turnover peak to the optically thin NIR with a cooling break in or short of the NIR domain (Bremer et al. 2011; Witzel et al. 2018). Such a spectral behavior is also well know for powerful extragalactic synchrotron sources (Meisenheimer et al. 1996; Shi et al. 2007). Producing the X-ray spectrum out of the optically thin submm to infrared spectrum by an SSC mechanism requires higher volume densities of relativistic particles. However, $\rho = 10^8$–10^9 cm^{-3} for SSC compared with $\rho = 10^6$–10^7 cm^{-3} for pure synchrotron solution is not excessive at all (Markoff et al. 2001; Eckart et al. 2012). Densities in the 10^8–10^9 cm^{-3} range are also required by the radiative-transfer model of the mid-plane of the accretion stream onto Sgr A* as presented in Table 1 by Mościbrodzka & Falcke (2013). Such densities of relativistic electrons are also favorable to explain the large Faraday rotation measure observed on the line of sight close to Sgr A* (Beckert & Falcke 2002; Bower et al. 2018). Furthermore, an SSC mechanism explains quite naturally the presence of extremely bright flares in the past that have been reported in the X-ray domain (Sunyaev & Churazov 1998; Revnivtsev et al. 2004; Terrier et al. 2010). These flares may simply be a result of not yet observed very bright NIR flares compatible with a power-law NIR flux statistics and an SSC scenario as explained by Witzel et al. (2012).

Appendix
SSC Flux Density Variations and Adiabatic Expansion

Models of adiabatic expansion or compression of emitting synchrotron blobs have been successfully used to explain the time delay between flare peaks from higher to lower frequencies. Here we consider how that mechanism can be linked with the SSC formalism we introduced earlier and how it may strengthen the argument, that the NIR flux density variations dominate the variation in the SSC X-ray flux density.

If $R(t)$ is the source radius at any given time and R_0 is the initial source size, the parameter $\rho(t) = R(t)/R_0$ determines the temporal evolution of physical quantities due to adiabatic expansion or compression. According to van der Laan (1966)

---

[10] Synchrotron radiation flare spectra are red in the S_ν versus ν spectral representation. This is important because the energy density in the radiation field is $U = Nh\nu$, with the photon energy $h\nu$ and photon density N with $N \sim S_\nu/h\nu$. So we have $U \sim S_\nu$. As S_ν in the submm is a few Janskys compared with a few milli-Janskys in the NIR, the radiation field in the submm is $\sim$1000 times stronger. This is exactly the reason why the bulk of the photons at the submm peak flux S_m with peak frequency ν_m is scattered to the bulk of the X-ray spectrum at energies around $\gamma_1^2 \nu_m$, i.e., for the low energy X-ray spectrum the NIR SSC scattered photons are less relevant.

Subroweit, Mossoux, & Eckart

ORCID iDs

Matthias Subroweit https://orcid.org/0000-0001-6165-8525
Andreas Eckart https://orcid.org/0000-0001-6049-3132

Figure A1. Exponents of $\rho(t)$ depending on the spectral index ζ according to Equation (A6). S, ν and Θ are the parameters whose temporal evolutions has been expressed by the $\rho(t)$ (see text for details). The dominance of the flux density term (ρ_S) on the total value of the exponent of $\rho(t)$ is visible. The solid horizontal line represents the most likely spectral index $\zeta = 0.6$ for which the exponents have been calculated in Equation (A7).

Θ, ν_m and S_{NIR} then scale as follows:

$$\Theta(t) = \Theta_0 \rho(t)$$
$$\nu_m(t) = \nu_{m0}\rho(t)^{-(8\zeta+10)/(2\zeta+5)}$$
$$S_{NIR}(t) = S_{NIR0}\rho(t)^{-2(2\zeta+1)}. \quad (A1)$$

Thus, combining adiabatic expansion with the SSC formalism of Equation (14) we obtain the the following relations:

$$S_{xray0}^{SSC} \propto S_{NIR0}^{2(\zeta+2)} \nu_{m0}^{-\zeta(2\zeta+7)-5} \Theta_0^{-2(2\zeta+3)} \quad (A2)$$

$$S_{xray}^{SSC}(t) \propto S_{NIR}(t)^{2(\zeta+2)} \times \nu_m(t)^{-\zeta(2\zeta+7)-5}\Theta(t)^{-2(2\zeta+3)} \quad (A3)$$

$$\propto (S_{NIR0}\rho(t)^{-2(2\zeta+1)})^{2(\zeta+2)}$$
$$\times (\nu_{m0}\rho(t)^{-(8\zeta+10)/(2\zeta+5)})^{-\zeta(2\zeta+7)-5} \times (\Theta_0\rho(t))^{-2(2\zeta+3)} \quad (A4)$$

$$\propto S_{xray0}^{SSC}(\rho_S(t)^{-2(2\zeta+1)})^{2(\zeta+2)}$$
$$\times (\rho_\nu(t)^{-(8\zeta+10)/(2\zeta+5)})^{-\zeta(2\zeta+7)-5} \times \rho_\Theta(t)^{-2(2\zeta+3)}. \quad (A5)$$

The subscripts S (which here is a short form of S_{NIR}), ν and Θ of $\rho(t)$ in the last equation denote whose parameter's temporal evolution has been expressed by ρ in each case. We thus arrive at an equation which describes the relative impact of each parameter's variation on the temporal variation of the SSC flux:

$$\frac{S_{xray}^{SSC}(t)}{S_{xray0}^{SSC}} \propto \rho_S(t)^{-4(2\zeta^2+5\zeta+2)}$$
$$\times \rho_\nu(t)^{2(8\zeta^3+38\zeta^2+15\zeta-25)/(2\zeta+5)}\rho_\Theta(t)^{-2(2\zeta+3)}. \quad (A6)$$

In Figure A1 we show the size of the exponents of ρ_S, ρ_ν and ρ_Θ depending on the spectral index ζ. For instance, with a spectral index of $\zeta = 0.6$ we obtain

$$\frac{S_{xray}^{SSC}(t)}{S_{xray0}^{SSC}} \propto \rho_S^{-22.9}\rho_\nu^{-0.2}\rho_\Theta^{-8.4}. \quad (A7)$$

It is obvious that the evolution of S_{NIR} due to possible adiabatic expansion dominates the temporal behavior of S_{xray}^{SSC}.

References

Abod, C. P., Simon, J. B., Li, R., et al. 2019, ApJ, 883, 192
Baganoff, F. K., Bautz, M. W., Brandt, W. N., et al. 2001, Natur, 413, 45
Baganoff, F. K., Maeda, Y., Morris, M., et al. 2003, ApJ, 591, 891
Balick, B., & Brown, R. L. 1974, ApJ, 194, 265
Barrière, N. M., Tomsick, J. A., Baganoff, F. K., et al. 2014, ApJ, 786, 46
Beckert, T., & Falcke, H. 2002, A&A, 388, 1106
Bélanger, G., Goldwurm, A., Melia, F., et al. 2005, ApJ, 635, 1095
Boehle, A., Ghez, A. M., Schödel, R., et al. 2016, ApJ, 830, 17
Borkar, A., Eckart, A., Straubmeier, C., et al. 2016, MNRAS, 458, 2336
Bouffard, É., Haggard, D., Nowak, M. A., et al. 2019, ApJ, 884, 148
Bower, G. C., Broderick, A., Dexter, J., et al. 2018, ApJ, 868, 101
Boyce, H., Haggard, D., Witzel, G., et al. 2019, ApJ, 871, 161
Bremer, M., Witzel, G., Eckart, A., et al. 2011, A&A, 532, A26
Brinkerink, C. D., Falcke, H., Law, C. J., et al. 2015, A&A, 576, A41
Brown, R. L., & Lo, K. Y. 1982, ApJ, 253, 108
Cadolle Bel, M., Sizun, P., Goldwurm, A., et al. 2006, A&A, 446, 591
Capellupo, D. M., Haggard, D., Choux, N., et al. 2017, ApJ, 845, 35
Chiang, J., & Böttcher, M. 2002, ApJ, 564, 92
Dexter, J., Kelly, B., Bower, G. C., et al. 2014, MNRAS, 442, 2797
Dibi, S., Markoff, S., Belmont, R., et al. 2016, MNRAS, 461, 552
Do, T., Ghez, A. M., Morris, M. R., et al. 2009, ApJ, 691, 1021
Dodds-Eden, K., Porquet, D., Trap, G., et al. 2009, ApJ, 698, 676
Eckart, A., Baganoff, F. K., Morris, M., et al. 2004, A&A, 427, 1
Eckart, A., Baganoff, F. K., Schödel, R., et al. 2006, A&A, 450, 535
Eckart, A., Baganoff, F. K., Zamaninasab, M., et al. 2008, A&A, 479, 625
Eckart, A., Fazeli, N., Busch, G., et al. 2017, in Proc. XII Multifrequency
    Behaviour of High Energy Cosmic Sources Workshop (Palermo, Italy) 48,
    (doi:10.22323/1.306.0048)
Eckart, A., García-Marín, M., Vogel, S. N., et al. 2012, A&A, 537, A52
Eckart, A., Genzel, R., Ott, T., & Schödel, R. 2002, MNRAS, 331, 917
Eisenhauer, F., Genzel, R., Alexander, T., et al. 2005, ApJ, 628, 246
García-Marín, M., Eckart, A., Weiss, A., et al. 2011, ApJ, 738, 158
Genzel, R., Schödel, R., Ott, T., et al. 2003, Natur, 425, 934
Ghez, A. M., Wright, S. A., Matthews, K., et al. 2004, ApJL, 601, L159
Gillessen, S., Eisenhauer, F., Trippe, S., et al. 2009, ApJ, 692, 1075
Goldwurm, A., Brion, E., Goldoni, P., et al. 2003, ApJ, 584, 751
Goss, W. M., Brown, R. L., & Lo, K. Y. 2003, ANS, 324, 497
Gravity Collaboration, Abuter, R., Amorim, A., et al. 2018a, A&A, 618, L10
Gravity Collaboration, Abuter, R., Amorim, A., et al. 2018b, A&A, 615, L15
Haggard, D., Nynka, M., Mon, B., et al. 2019, ApJ, 886, 96
Herbst, T. M., Beckwith, S. V. W., Forrest, W. J., & Pipher, J. L. 1993, AJ,
    105, 956
Herrnstein, R. M., Zhao, J.-H., Bower, G. C., & Goss, W. M. 2004, AJ,
    127, 3399
Ho, L. C. 2008, ARA&A, 46, 475
Hornstein, S. D., Matthews, K., Ghez, A. M., et al. 2007, ApJ, 667, 900
Horrobin, M., Eisenhauer, F., Tecza, M., et al. 2004, AN, 325, 88
Karssen, G. D., Bursa, M., Eckart, A., et al. 2017, MNRAS, 472, 4422
Klinger, E., Rickert, D., & Hasenauer, J. 2018, Bioinformatics, 34, 3591
Koyama, K., Inui, T., Matsumoto, H., & Tsuru, T. G. 2008, PASJ, 60, S201
Lacy, J. H. 1980, HiA, 5, 163
Li, Y.-P., Yuan, F., & Wang, Q. D. 2017, MNRAS, 468, 2552
Li, Y.-P., Yuan, F., Yuan, Q., et al. 2015, ApJ, 810, 19
Marjoram, P., Molitor, J., Plagnol, V., & Tavaré, S. 2003, PNAS, 100, 15324
Markoff, S., Falcke, H., Yuan, F., & Biermann, P. L. 2001, A&A, 379, L13
Marrone, D. P., Baganoff, F. K., Morris, M. R., et al. 2008, ApJ, 682, 373
Marscher, A. P. 1983, ApJ, 264, 296
Marscher, A. P. 1987, in Superluminal Radio Sources, ed. J. A. Zensus &
    T. J. Pearson (New York: Cambridge Univ. Press), 280
Meisenheimer, K., & Heavens, A. F. 1986, Natur, 323, 419
Meisenheimer, K., Roeser, H.-J., & Schloetelburg, M. 1996, A&A, 307, 61
Meyer, L., Witzel, G., Longstaff, F. A., & Ghez, A. M. 2014, ApJ, 791, 24
Mościbrodzka, M., & Falcke, H. 2013, A&A, 559, L3
Mościbrodzka, M., Gammie, C. F., Dolence, J. C., Shiokawa, H., &
    Leung, P. K. 2009, ApJ, 706, 497
Mossoux, E., & Grosso, N. 2017, A&A, 604, A85
Mossoux, E., Grosso, N., Bushouse, H., et al. 2016, A&A, 589, A116
Mossoux, E., Grosso, N., Vincent, F. H., & Porquet, D. 2015, A&A, 573, A46

Subroweit, Mossoux, & Eckart

Narayan, R., Mahadevan, R., Grindlay, J. E., Popham, R. G., & Gammie, C. 1998, ApJ, 492, 554
Neilsen, J., Markoff, S., Nowak, M. A., et al. 2015, ApJ, 799, 199
Nowak, M. A., Neilsen, J., Markoff, S. B., et al. 2012, ApJ, 759, 95
Ponti, G., George, E., Scaringi, S., et al. 2017, MNRAS, 468, 2447
Porquet, D., Grosso, N., Predehl, P., et al. 2008, A&A, 488, 549
Revnivtsev, M. G., Churazov, E. M., Sazonov, S. Y., et al. 2004, A&A, 425, L49
Ryu, S. G., Nobukawa, M., Nakashima, S., et al. 2013, PASJ, 65, 33
Sabha, N., Witzel, G., Eckart, A., et al. 2010, A&A, 512, A2
Schechter, P. 1976, ApJ, 203, 297
Schlickeiser, R., & Röken, C. 2008, A&A, 477, 701
Schödel, R., Eckart, A., Mužić, K., et al. 2007, A&A, 462, L1
Schödel, R., Morris, M. R., Muzic, K., et al. 2011, A&A, 532, A83
Shahzamanian, B., Eckart, A., Valencia, S. M., et al. 2015, A&A, 576, A20
Shi, Y., Rieke, G. H., Hines, D. C., Gordon, K. D., & Egami, E. 2007, ApJ, 655, 781
Shields, G. A. 1999, PASP, 111, 661
Silk, J., & Mamon, G. A. 2012, RAA, 12, 917
Subroweit, M., García-Marín, M., Eckart, A., et al. 2017, A&A, 601, A80
Sunyaev, R., & Churazov, E. 1998, MNRAS, 297, 1279
Szekely, G., & Rizzo, M. 2004, InterStat, 5 http://interstat.statjournals.net/ YEAR/2004/abstracts/0411005.php
Székely, G. J., & Rizzo, M. L. 2013, Journal of Statistical Planning and Inference, 143, 1249

Terrier, R., Ponti, G., Bélanger, G., et al. 2010, ApJ, 719, 143
Toni, T., Welch, D., Strelkowa, N., Ipsen, A., & Stumpf, M. P. H. 2009, J. R. Soc. Interface, 6, 187
Tsuboi, M., Miyazaki, A., & Tsutsumi, T. 1999, in ASP Conf. Ser. 186, The Central Parsecs of the Galaxy, ed. H. Falcke et al. (San Francisco, CA: ASP), 105
van der Laan, H. 1966, Natur, 211, 1131
von Fellenberg, S. D., Gillessen, S., Graciá-Carpio, J., et al. 2018, ApJ, 862, 129
Witzel, G., Eckart, A., Bremer, M., et al. 2012, ApJS, 203, 18
Witzel, G., Martinez, G., Hora, J., et al. 2018, ApJ, 863, 15
Witzel, G., Morris, M., Ghez, A., et al. 2014, in IAU Symp. 303, The Galactic Center: Feeding and Feedback in a Normal Galactic Nucleus, ed. L. O. Sjouwerman, C. C. Lang, & J. Ott (Cambridge: Cambridge Univ. Press), 274
Yuan, Q., Wang, Q. D., Liu, S., & Wu, K. 2018, MNRAS, 473, 306
Yusef-Zadeh, F., Roberts, D., Wardle, M., Heinke, C. O., & Bower, G. C. 2006a, ApJ, 650, 189
Yusef-Zadeh, F., Wardle, M., Dodds-Eden, K., et al. 2012, AJ, 144, 1
Yusef-Zadeh, F., Wardle, M., Roberts, D. A., et al. 2006b, in VI Microquasar Workshop: Microquasars and Beyond (Como, Italy) 51, (doi:10.22323/1. 033.0051)
Zhang, S., Baganoff, F. K., Ponti, G., et al. 2017, ApJ, 843, 96

Paper III (in prep.): Ongoing Submm Observations of Sagitarius A* - No Indication for an Increased Flaring Acitivity between 2014 and 2017

6

In the previous two papers (Chaps. 4 and 5, Subroweit et al. 2017, 2020), I statistically analyzed radio, submm and X-ray lightcurves from Sgr A*. Using modified power-law models and Bayesian statistics, I was able to show *a)* that the observed emission from the radio to the NIR most likely is self-absorbed synchrotron emission and that the flux density distribution at these frequencies can be described by power-laws with a scaling index $\alpha \sim 4$ and *b)* that the observed X-ray radiation is in all likelihood produced by an SSC mechanism and that the X-ray count rate distribution follows a power-law with scaling index $\alpha \sim 1.6$.

Nevertheless, these results are not "cast in stone" but have to be taken with a grain of salt: first, the quality of every statistical investigation is closely related to the amount of available data. While the data coverage in the X-ray can be considered as sufficiently large, the data in the radio and submm regime, that was used for my analyses, is relatively sparse: in the X-ray, in total approximately 10000[1] single data points were available (3 Ms in total, binned to 300 s blocks), in the radio and in the submm, it was only 552 and 792, respectively. Secondly, it is not guaranteed that the emission mechanism of flares is describable as a stationary process. The environment around Sgr A* is a dynamical system, and physical events might lead to a significant long-term change of the system's parameters. Then, the former statistical description would be obsolete or at least had to be notably adjusted.

Such a change of the environment's parameters could be an altered accretion rate and therefore, e.g., a long-term variation in the electrons acceleration mechanism or the plasma densities. In the early 2010s, a source was detected which might lead to such a scenario: a putative gas cloud, labeled G2, on its way onto Sgr A*, "ready" to get disrupted and accreted onto the SMBH (Gillessen et al., 2012). In the following years, this object has been intensively monitored and a dispute about its nature started.

---

[1]The exact number is 9903.

An alternative interpretation of the available data was to identify that source as a dust enshrouded stellar object, also called dusty S-cluster object (DSO, Eckart et al. 2013). Such an object would not get disrupted at its flyby close to Sgr A*. Although the time of the closest encounter, the periapse, has been indisputably identified to have happened in spring 2014, the nature of this source has not yet been deciphered. Some groups claim to have observed an elongation of that object and a deviation from a Keplerian orbit (Pfuhl et al., 2015), others saw an always compact source on a regular Keplerian trajectory (Witzel et al., 2014a).

Our workgroup therefore proposed additional APEX/LABOCA observation of the GC to monitor Sgr A*'s submm variability. These observations were conducted in 2016 and 2017, i.e., after the periapse of G2/DSO and the data later reduced by the second author of the following manuscript, Shayoni Panja. I present a statistical analysis on this data, namely I compare the post- with the preperiapse data presented in my first paper (Subroweit et al. 2017). I show that the statistical properties of the pre- and the postperiapse data have not changed, i.e., that the power spectral densities and structure functions are, within the uncertainties, identical. Therefore, I conclude that the physical conditions around Sgr A* have not changed up to 2017, and that we thus have observed a stationary process between 2008 and 2017. For this reason, an influence of the flyby of G2/DSO up to 2017 can safely be ruled out. I also perform a Bayesian flux density distribution fit on the entire data between 2008 and 2017 and demonstrate that the power-law description with a scaling index of $\alpha \sim 4$ is still valid.

Ongoing Submm Observations of Sagitarius A* - No Indication for an Increased Flaring Acitivity between 2014 and 2017

Matthias Subroweit [ID],[1] Shayoni Panja,[1] and Andreas Eckart [ID][1, 2]

[1]*I. Physikalisches Institut, Universität zu Köln*
Zülpicher Str. 77
50937 Köln, Germany
[2]*Max-Planck-Institut für Radioastronomie*
Auf dem Hügel 69
53121 Bonn, Germany

ABSTRACT

We report on submillimeter (submm) observations of the flux density variations of Sagitarrius A* (Sgr A*) between 2014 and 2017 conducted with the Large APEX Bolometer Camera (LABOCA) at the Atacama Pathfinder EXperiment (APEX) telescope. It has been discussed whether the periapse of an infrared-excess object of unknown nature, called G2/DSO, in spring 2014 has changed the accretion and emission processes around Sgr A*. By statistically comparing the available data with already published lightcurves from 2008 to 2014 obtained with the same instrument, we find that the statistical parameters, i.e., the power spectral density and the structure function have not significantly changed. In addition, we show that the description of the flares with a power-law flux density distribution and a scaling parameter $\alpha \sim 4$ is still valid as we found in a previous paper for the 2008-2014 data. This means that up to 2017, the periapse of G2/DSO has not affected the flare physics of Sgr A*. In conclusion, our findings might strengthen the argument that G2/DSO is a stellar object which remained compact during and after its periapse and therefore has not affected the emission mechanism of Sgr A*.

Keywords: galaxies: active, Galaxy: center, galaxies: supermassive black holes, submillimeter: galaxies

1. INTRODUCTION

The gravitational center of our Galaxy coincides with the compact radio source Sagittarius A* (Sgr A*, Brown et al. 1981; Brown 1982). It is assumed that Sgr A* is the radiative counterpart of a supermassive black hole (SMBH) with a mass of $\sim 4.3 \times 10^6 M_\odot$ at a distance of ~ 8.2 kpc from our solar system (Gillessen et al. 2017; Gravity Collaboration et al. 2019). Sgr A* shows quasi-steady, so-called quiescent emission across the wavelength regime from radio to X-ray (Corrales et al. 2020; Zhao et al. 2001) with a peak of its spectral energy distribution in the submillimeter (submm) (Dexter et al. 2010). On top of the quiescent emission, Sgr A* also shows radiation outbursts, also referred to as flares, on minutes to hours time-scales at all observed frequencies (Witzel et al. 2021).

While the quiescent emission is well understood as mostly due to synchrotron emission and bremsstrahlung from the accretion flow (Yuan et al. 2002; Aitken et al. 2000), the mechanisms giving rise to flares are rather debatable. First, it is unclear where the matter and energy reservoir for the radiation outbursts physically stems from: magnetic reconnections and shocks in the accretion flow (Li et al. 2017; Okuda et al. 2019), tidal disruption of asteroids (Zubovas et al. 2012) or orbiting "hot spots" (Gravity Collaboration et al. 2018) are just a few examples of possible explanations for the driving physical mechanisms. Irrespective of the presumed specific physical particle acceleration process, most models include some combination of self-absorbed synchrotron and synchrotron self-Compton (SSC) emission to explain the spectral and temporal behaviour of the observed flares (Eckart et al. 2012; Gravity Collaboration et al. 2020).

During the past 30 years, statistics on Sgr A*s light curves at different wavebands has become an important tool to constrain the possible emission mechanisms. For instance, structure functions (SF) in the time- and periodograms in the frequency domain have been used to

Corresponding author: Matthias Subroweit
subroweit@ph1.uni-koeln.de

2   SUBROWEIT ET AL.

find possible periodicities and typical timescales in the
observed lightcurves (Beaklini & Abraham 2013; Witzel
et al. 2018). Flux density distributions have been in-
vestigated to describe the occurring flare magnitudes
(Witzel et al. 2012; Subroweit et al. 2020). In Sub-
roweit et al. (2017) (hereinafter referred to as Sub17),
we analyzed submm lightcurves obtained with the Large
APEX Bolometer Camera (LABOCA) at the Atacama
Pathfinder EXperiment (APEX) telescope from 2008 to
2014. We were able to describe the flux density dis-
tribution of the submm flares with a power-law with a
scaling index of ~ 4 and inferred that submm flares are
the predominantly optically thin part of an adiabati-
cally expanding, synchrotron emitting plasma.

At the beginning of the last decade, several authors
detected a - until that point - unknown source approach-
ing Sgr A* (Gillessen et al. 2012; Eckart et al. 2013).
Ongoing observations revealed, that this object had its
periapse to Sgr A* in spring 2014 (Valencia-S. et al.
2015; Plewa et al. 2017). Since its detection, there has
been an ongoing debate about the nature of this object.
One of the key questions is whether this object is a
core-less gas cloud, which should therefore be referred
to as G2 (according to the gas cloud G1, see McCourt
& Madigan 2016 and references therein) or a dust en-
shrouded stellar object (DSO) as proposed by Eckart
et al. (2013). In the gas cloud case, the object should
a) show a bright bow shock while approaching Sgr A*
(Narayan et al. 2012), b) then gets tidally stretched
at and disrupted after its closest approach to Sgr A*
(Pfuhl et al. 2015) and c) eventually release its tidal
remnants into the accretion flow onto Sgr A* which
then leads to an increased flaring activity (Gillessen
et al. 2012; Saitoh et al. 2014). In the DSO case a)
the object stays compact during its periapse passage
and b) therefore little material gets strapped away from
that object that infalls to Sgr A*, i.e., the impact on
the flaring activity should be marginal. It is beyond
the scope of this paper and the used statistical tools
to conclusively comment on that debate. Nevertheless,
it is important to note in which context the statistics
of the flaring activity was and currently still is discussed.

The goal of this paper is the following: as mentioned
earlier, in Sub17 we already published and analyzed
LABOCA/APEX data from 2008-2014, i.e., data before
the periapse of G2/DSO in spring 2014. For simplicity,
we call this data the preperiapse data. We fitted the
right tail, i.e., the bright flares part of the flux den-
sity distribution with a power-law with scaling index
$\alpha = 4.0 \pm 1.7$. In this paper, we present additional

data obtained with the same instrument, starting from
late 2014 up to 2017. We call it simply the postperiapse
data. We analyze the data with different statistical
tools, mainly Lomb-Scargle-Periodograms (LSP) and
structure functions (SF), and compare the postperi-
apse statistics with the preperiapse data. We find that
the statistical parameters and therefore the general be-
haviour of the emission process has not significantly
changed after 2014.

A note on the used fitting method throughout this
paper: all fits were conducted using an Approximation
Bayesian Computation (ABC) method implemented in
the Python package pyABC (Klinger et al. 2018). For
the function fits in Sects. 3.1 and 3.2 this may seem
unwieldy and over-complicated as regular least-square
fitting or simple MCMC methods would have also per-
formed well. However, the convolution of probability
distributions, as considered and needed in Sect. 3.3,
can be most conveniently fitted with ABC methods.
For simplicity and self-consistency, we used ABC for all
fits in this work.

Another note for the quick orientation on the used
color scheme throughout the paper: for all plots related
to preperiapse data, we used the color black. Postpe-
riapse data and related plots are shown in red, blue is
used for the entire dataset (pre- and postperiapse data
together).

2. OBSERVATIONS

We used the LABOCA bolometer array on the 12m
single dish APEX telescope located at the Llano de Cha-
jnantor Observatory in northern Chile to obtain on-the-
fly (OTF) maps of the Galactic center (GC) at 870 μm
(345 GHz). APEX has a bandwidth of 60 GHz and the
beam shape can be described as a circular Gaussian with
a full width half maximum (FWHM) $\sim$19". All data was
acquired between October 2014 and May 2017, after the
periapse of G2/DSO. A detailed list of observation dates
and their programme ids can be found in Tab. 1.

Primary calibrators such as Mars, Neptune and
Uranus, secondary calibrators such as G5.89, G10.62
and IRAS16293 and sky-dips were observed in between
the OTF maps of the GC to regularly check the opacity
of the sky. Secondary calibrators were chosen such that
they are close to the GC, in order to reduce the telescope
driving time. They were observed before and after ev-
ery GC observation. Sky-dips allowed us to determine
the overall opacity of the sky as a function of eleva-
tion. The GC maps were obtained with an inclination
of -10°, 0° and 10° with respect to an axis orthogo-

Table 1. Observations

Programme ID	Date
094.B-0015(B)	2014-10-04
	2014-10-05
	2014-10-06
098.B-0207(A)	2016-09-26
	2016-09-27
	2016-09-28
	2016-09-29
	2016-09-30
	2016-10-01
	2016-10-02
	2016-10-03
	2016-10-04
	2016-10-05
099.B-0108(A)	2017-04-24
	2017-04-25
	2017-04-28
	2017-04-29
	2017-04-30
	2017-05-01
	2017-05-02
	2017-05-03
	2017-05-04
	2017-05-05
	2017-05-07
	2017-05-08

Note—APEX/LABOCA GC observations conducted between October 2014 and May 2016 with their respective programme IDs.

nal to the Galactic plane to avoid scanning artefacts in the reconstruction of the extended thermal emission surrounding Sgr A*. The observations were conducted with a scanning speed of 3'/s, an integration time of 280 s and a mapping step of 30", yielding an rms (Root-Mean-Squared values of the fluctuations measured over time) noise level of 150 mJy/beam for each map of size 0.7×0.4 deg, with the fully sampled map of size 0.5×0.17 deg.

The data was reduced using the BOlometer Array Analysis (BOA) software package. The main objective was to achieve light curves of Sgr A*. Corrections were made during the reduction process for zenith opacity,

flat-fielding and noise removal of two kinds, i.e., correlated sky noise as well as noise caused by instrumental effects. For estimating the zenith opacity, two different methods were used: a precipitable water vapour (PWV) radiometer and sky-dips. Both method have their caveats, the radiometer tends to over-, the sky-dip to underestimate the opacity (for details see Sub17). Therefore, we used a weighted average to calculate the opacity of the zenith τ as given on the LABOCA calibration website[1]:

$$\tau = \frac{0.9\tau_{\mathrm{r}} + 1.3\tau_{\mathrm{s}}}{2}, \qquad (1)$$

where τ_{r} is the opacity obtained from the PWV radiometer and τ_s the opacity according to the skydip method. To obtain light curves of Sgr A*, the following procedure was used: all GC scans of one observation day were first co-added. A Gaussian point source was fitted on the co-added GC map at the position of Sgr A*. This was then subtracted from all the individual GC scans, leaving maps of the extended submm emission. These extended submm emission maps were co-added again to obtain a model of the extended GC submm emission with a high signal-to-noise ratio. This model was then again subtracted from each GC scan, providing us with maps of just the central point source. By doing so, we made sure that the background excess emission was removed, and we were able to better isolate the contribution made by Sgr A*. These maps were again fitted with a central Gaussian. The peak yielded the flux density of Sgr A* for each GC scan.
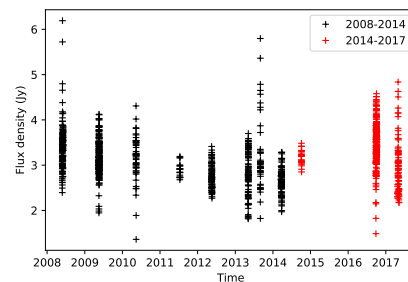
Figure 1. APEX/LABOCA lightcurves of Sgr A* between 2004 and 2014. The black markers indicate observations before April 2014 (preperiapse), red markers after April 2014 (postperiapse).
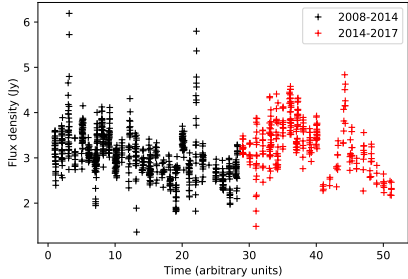
Figure 2. Concatenated APEX/LABOCA lightcurves of Sgr A* between 2004 and 2014. As in Fig. 1, black markers indicate preperiapse, red markers postperiapse observations. Time gaps greater than 1 day are replaced by 1 day.
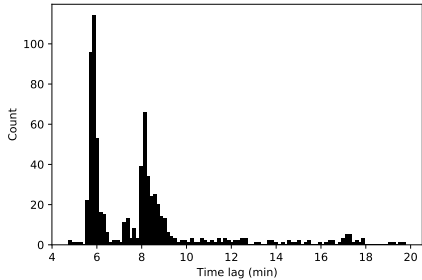
Figure 3. Histogram of time spans between consecutive observations up to 20 minutes in the preperiapse data. Most observations are either separated by ~ 5 or ~ 8 minutes lags.
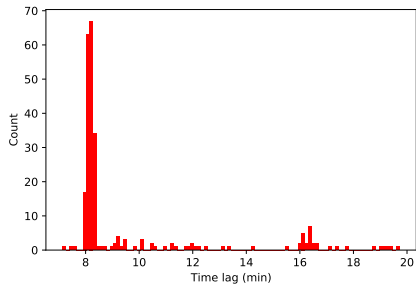
Figure 4. Histogram of time spans between consecutive observations up to 20 minutes in the postperiapse data. Most observations are separated by ~ 8 minutes time lags.

3. ANALYSIS

In Fig. 1, we show the total available submm data between 2008 and 2017, i.e., both the newly obtained postperiapse and the already published preperiapse data. The preperiapse data contains 782 single observations,

the postperiapse data 322. Fig. 2 shows a concatenated graph of both datasets, observation gaps longer than one day are replaced with a gap of one day.

In Figs. 3 and 4, we show the histograms of the time gaps between two consecutive observations (up to 20 minutes). In the preperiapse data, two peaks can be seen, one at about 6 minutes, another at about 8 minutes. This can be considered as the minimum time it takes between two full GC scans. The telescope operation mode has changed so that the minimal time gap between two full scans is always about 8 minutes in the postperiapse observations. This information is important in understanding the power spectrum analysis in the next section.

3.1. *Power spectral distributions*

A popular tool for the investigation of variability in light curves is the estimation of the power spectral distribution (PSD). PSDs contain information about the "color" of noise and, if present, about additional components in the frequency spectrum. For instance, periodicities appear as "spikes" in the PSD. If an object is monitored over a longer period, the comparison of PSDs for different sub-samples of the entire light curve may answer the question whether a stationary or a nonstationary process is observed. In the context of the DSO/G2-debate, this means that if major properties of the accretion and emission process had changed after periapse, the observed PSD should have significantly altered.

For evenly sampled data, the computation of the PSD can be simply performed by fitting a series of sinusoidals or discrete Fourier transform (DFT). In the unevenly sampled case, the PSD estimation is mathematically more tempting. A often used method is the Lomb-Scargle-periodogram (LS-periodogram). The LS-power is given by

$$P_{LS}(\omega) = \frac{1}{2\,\sigma^2}\left(\frac{\left(\sum_i (y_i - \bar{y})\cos\omega(t_i - \tau)\right)^2}{\sum_i \cos^2\omega(t_i - \tau)} \right. \qquad (2)$$

$$\left. + \frac{\left(\sum_i (y_i - \bar{y})\sin\omega(t_i - \tau)\right)^2}{\sum_i \sin^2\omega(t_i - \tau)} \right), \qquad (3)$$

where $\bar{y}$ is the mean and σ the variance of the data and τ a frequency dependent offset that guarantees that P_{LS} stays invariant against time-shifts (VanderPlas 2018). To obtain a decent coverage in the frequency domain, we constrain the PSD analysis to those observation nights which contain at least 20 data points. Less data might lead to spurious spikes in the PSD. For all this single observations, we calculate the PSD on a 2048

step frequency grid between 5 minutes and one day [2]. For each frequency, we calculate the mean value and its standard deviation by averaging over the single PSDs).

Figure 5 depicts the two averaged PSDs with the 1σ-uncertainty interval from the preperiapse data. By eye inspection of this plot, one can state that both PSDs seem to be "similar", i.e., the postperiapse PSD lies almost completely in the 1σ-uncertainty interval of the preperiapse PSD. The general behaviour of both PSDs can be described as follows: in the log-log-space, the LS-power seems to decrease linearly from lower to higher frequencies, up to a certain break-point from where on the PSD remains relatively stable at some plateau. For high frequencies, one can see significant spikes in the PSD. These spikes correspond to instrumental effects, namely the typical time lag between two consecutive observations. The preperiapse data shows two spikes at approximately 5 and 8 minutes, the postperiapse one spike at approximately 8 minutes (see Figs. 3 and 4). To statistically characterize and compare both datasets, we assume a broken power-law for the PSDs with $\mathrm{PSD}(f) = i \cdot f^s$ for frequencies f below some break frequency f_b and a constant value above f_b. Thus, the logarithmic PSD is given by

$$\log\mathrm{PSD}(f) = \begin{cases} s \cdot \log f + i & \text{for } f \leq f_b \\ s \cdot \log f_b + i & \text{otherwise} \end{cases}, \qquad (4)$$

where the symbols s, i and f_b indicate the slope, the intercept and the break frequency of the logarithmic PSD. We fit the model to the averaged PSD over the frequency range from $1/200$ to $1/16\,\mathrm{min}^{-1}$. The left boundary is given by the minimum total observation time of all averaged observation (all included observations cover at least a timespan of 200 min). The right boundary is given by the Nyquist-theorem: at a given sampling frequency of $f_s = 1/8\,\mathrm{min}^{-1}$ the maximum frequency which contains information in a spectral analysis is $f_{\max} = f_s/2$, thus $1/16\,\mathrm{min}^{-1}$. The fit was conducted using an ABC sampler, with uninformative priors on all parameters. A corner plot of the marginalized posteriors is shown in Fig. 6, the numerical values are summarized in Tab. 2. It can be seen that the parameters of the PSD model for the post- and preperiapse data are within uncertainties the same. The resulting broken power-law models on the fitting frequency domain are also shown in Fig. 7 which gives a good visual impression of the sim-

ilarity of both PSD models. The slope of both PSDs with $-2 \leq s \leq -1$ indicates a red noise process. Below the break timescales of $1/10^{-(1.39)}\,\mathrm{min} \approx 25\,\mathrm{min}$ and $1/10^{-1.37}\,\mathrm{min} \approx 23\,\mathrm{min}$, the flux density variations turn into white noise, i.e., they are dominated by non-flaring background variations and instrumental uncertainties.
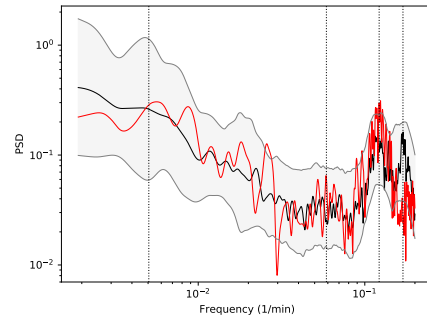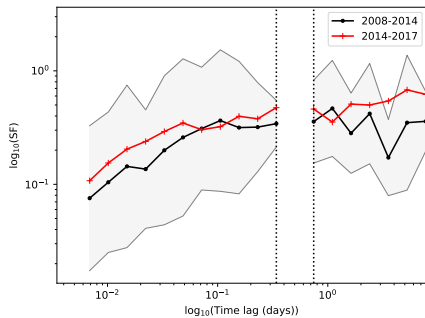

Figure 5. Averaged PSDs of the pre- (black) and postperiapse (red) data. The grey contours show the 1σ-confidence interval of the preperiapse data, calculated as the standard deviation in each frequency bin. Several characteristic timescales (in min^{-1}) are marked from right to left: the $1/5$ and $1/8$ timescale which corresponds to the temporal separation between consecutive observations, $1/16$ and $1/200$ as boundary frequencies for the PSD fit, see the text for details.
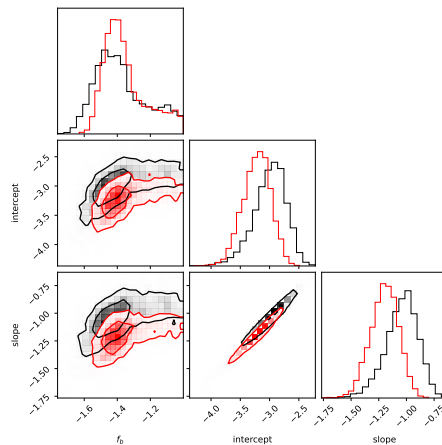
Figure 6. Overplot of marginalized posteriors for the pre- and postperiapse PSD models with 1 and $2\,\sigma$ credibility intervals in the 2D-histograms. The overlap of the $1\,\sigma$ credible intervals show that the PSD models for both datasets can be considered as identical.

---

[2] Of course there is no power on time scales above 8 hours, which is the maximum length of an observation night. We used the 24/2048 hours grid for computational convenience.

Table 2. Best fit parameters for the broken power-law PSD models

observation	slope	intercept	f_b
	$\log(\mathrm{Jy}^2/\mathrm{min}^{-1})$	$\log(\mathrm{Jy}^2)$	$\log(\mathrm{min}^{-1})$
2008-2014	$-1.03^{+0.16}_{-0.20}$	$-2.98^{+0.31}_{-0.38}$	$-1.39^{+0.26}_{-0.16}$
2014-2017	$-1.19^{+0.14}_{-0.17}$	$-3.21^{+0.27}_{-0.32}$	$-1.37^{+0.23}_{-0.11}$

Note—As visually indicated in Figs. 6 and 7, the best fit parameters are, within the uncertainties, consistent. The given logarithmic break frequencies of -1.39 and -1.37 correspond to a break timescale of approximately 24.5 and 23.4 in units of minutes.
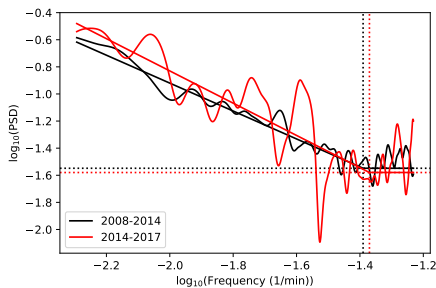
Figure 7. Observed PSDs and fitted broken power-law model for the pre- (black) and postperiapse (red) data. The dotted lines indicate the respective position of the break-points.

3.2. Structure functions

Another often used tool in the analysis of times series variability is the structure function (SF) with

$$\mathrm{SF}(\tau) = \frac{1}{N}\sum_{i=1}^{N}\left(x(t_i) - x(t_i + \tau)\right)^2 . \qquad (5)$$

It is a measure for the mean variance over all data points of the time series $x(t_i)$ separated by a time lag τ. Although it is by definition closely related to the PSD via the autocorrelation function (ACF), this relation is only unambiguous for evenly spaced data and an infinity time or frequency domain. We note that both conditions are not met in the underlying datasets, the consequences will be discussed later. In the context of this analysis, we use the SF for the following reasons:
First, as we have argued before, the PSD analysis only yields meaningful results if a single observation contains enough data points to make a decomposition into multiple frequency dependent sinusoidals justifiable. Therefore, the PSD analysis cannot yield the lower break frequency, i.e., the upper timescale, from where on the red

noise characteristics of the flaring flux density variations turn into long-term variations. The SF is not subjected to these limitations. The determination of the SF would even make sense if just two datapoints with an arbitrary time lag between them were given. As exhaustively discussed in Witzel et al. (2021), the SF is better suited to answer the question up to which timescale a time series "knows" about its previous states and from which timescale on the variations turn into a "memoryless" white noise process. Therefore, we can use the SF to get an estimate of the upper timescale of the flaring process. We thus follow the idea of Hughes et al. (1992) (see their Fig. 1) and model the SF as a broken power-law, where the break-timescale defines the transition between colored noise and the overall long-term variance of the signal:

$$\log \mathrm{SF}(\tau) = \begin{cases} s \cdot \log \tau + i & \text{for } \tau \le \tau_b \\ s \cdot \log \tau_b + i & \text{otherwise} \end{cases} . \qquad (6)$$

We fit the SF with an ABC sampler and uninformative priors over the range up to 8 hours, i.e., the maximum time of one observation run (see Fig. 8). The resulting marginalized posterior distributions are shown in Fig. 9, the corresponding best fit values are tabulated in Tab. 3. Just like the PSDs, no significant difference between both SFs can be stated. This is also visually underlined through Fig. 10. We can therefore conclude that the SFs for both the pre- and postperiapse data are approximately the same. The break timescales in days, as given in Tab. 3, correspond to ~ 109.2 and ~ 104.3 min, respectively. As mentioned before, a translation between SF and PSD parameters is not possible for unevenly sampled, limited data. Nevertheless, one often finds a relation between the SF slope β_s and the PSD slope β_p similar to $\beta_p \approx 2\beta_s$ (see, e.g., Hughes et al. 1992 or Do et al. 2009). This relation also approximately holds for

Table 3. Best fit parameters for the broken power-law SF models

observation	slope	intercept	τ_b
	$\log(\mathrm{Jy}^2/\mathrm{day})$	$\log(\mathrm{Jy}^2)$	$\log(\mathrm{day})$
2008-2014	$0.59^{+0.28}_{-0.22}$	$0.17^{+0.47}_{-0.33}$	$-1.12^{+0.32}_{-0.23}$
2014-2017	$0.49^{+0.21}_{-0.14}$	$0.15^{+0.37}_{-0.24}$	$-1.14^{+0.34}_{-0.24}$

Note—As visually indicated in Figs. 9 and 10 the best fit parameters are within uncertainties consistent. The given logarithmic break timescales of -1.12 and -1.14 correspond to approximately 109.2 and 104.3 in units of minutes.

the here estimated slopes, which might be taken as an indicator for the consistency of the analysis.

Figure 8. Structure functions of the pre- (black) and postperiapse (red) data. The grey contours show the 1σ-confidence interval of the preperiapse data, calculated as the standard deviation in each time lag bin. The dashed lines indicate the time gap between consecutive observing nights.

3.3. *Flux density distributions*

In the previous two subsections, we have shown that the pre- and postperiapse data show almost identical variability patterns in terms of similar PSDs and SFs. Another way of describing statistical characteristics of light curves are flux density distributions. Common non-parametric tests to check whether two data sets stem from the same underlying generating distribution are, for instance, the Kolmogorov-Smirnov (KS) or the Anderson–Darling (AD) test. Both tests define a distance metric between two empirical distribution functions and return a p-value as a measure for the statistical significance of observed differences. Low p-values indicate a high probability that both samples are not drawn from the same distribution. In this specific case, neither
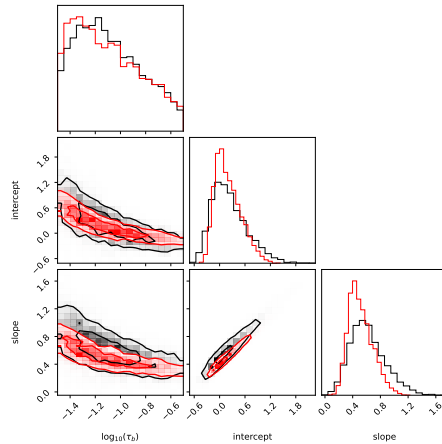
Figure 9. Overplot of marginalized posteriors for the pre- (black) and postperiapse (red) SF models. The overlap of the credible intervals indicate that the SF models for both datasets are consistent with each other.
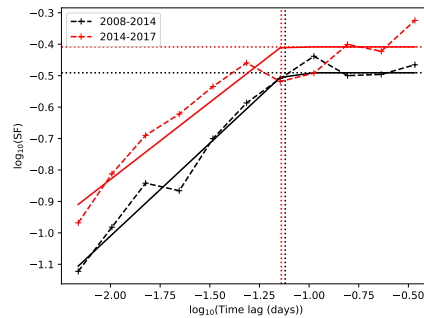
Figure 10. Observed SFs and fitted models for the pre- (black) and postperiapse (red) data. The dotted lines indicate the respective position of the breakpoints.

the KS nor the AD test yield unambiguous results: the KS test provides a p-value of 0.09, the AD test a significance level of 0.02. Both values lie in a range where it is difficult to decide whether both data sets are probably drawn from the same distribution (usually thresholds in the range between 0.01 and 0.05 are chosen).
In Sub17, we have shown that the preperiapse flux density distribution of submm flares can be described by a power-law with a scaling index $\alpha \sim 4$. A similar fit[3] to the postperiapse data yields a power-law index ~ 7, which would imply a different underlying flux density

---

[3] We omit the demonstration here.

8   Subroweit et al.

distribution. Nevertheless, this results has to be taken with a grain of salt as it is very counter-intuitive. The flaring activity of Sgr A* is expected to have stayed stable after the periapse of G2 (i.e., the power-law index should remain around 4) or to have increased. An increase of flaring activity would mean more bright flares, i.e., an enhancement of the high flux density tail of the distribution which would lead to a lower power-law index, i.e., $\alpha < 4$. We are not aware of any paper which reported on a decrease of flaring activity. Therefore, we interpret the resulting power-law index of ~ 7 as an indication for a under-sampled (low number of single measurements) flux density distribution after the periapse. This can be understood when looking at the light curve after 2014: no bright flares, i.e., flares with peak flux densities above 5 Jy have been observed. As there is no physical indication for a decrease in the flaring activity, we therefore compare the post- and preperiapse flux density distributions in a different manner: we address the question, whether the parameters of the flux density distribution fit change, if we first solely fit the preperiapse data and then the complete data set of the combined pre- and postperiapse data.

In Sub17, we chose a semi-analytic method introduced by Rácz et al. (2009) to fit the flux density distribution, namely fitting a so-called shifted power-law of the form

$$p(x) \propto (x - s)^{-\alpha}, \qquad (7)$$

where the shift parameter s summarizes the quiescent emission with a single value. We obtained $\alpha = 4.0 \pm 1.7$ and $s = (2.8 \pm 0.6)$ Jy. In this work, we enhance the fitting routine by modeling the entire submm flux distribution as the convolution of a Gaussian distribution $g(x|\mu, \sigma)$ (simulating the quiescent emission) and a power-law $f(x|x_{min}, \alpha)$ (representing flare emission):

$$p(x|\mu, \sigma, x_{min}, \alpha) = \int_{-\infty}^{\infty} g(z)f(x - z)dz. \qquad (8)$$

The best fit parameters $\mu, \sigma, x_{\min}$ and α are then estimated by an ABC routine with uniform, non-negative priors. The ABC sampler is set up such that each sequential population contains 5000 accepted particles. After the generation of 20 populations, the acceptance ratios became small and the estimated parameter distributions stable enough to be sure that the true posterior distributions of parameters are sufficiently approximated.[4] In Tab. 4, we summarize the fit results. For the preperiapse data, we obtain a scaling parameter $\alpha = 4.41^{+0.88}_{-0.81}$ which is in good agreement with the

---

[4] Details of an ABC fitting procedure are also described in Subroweit et al. (2020).

Table 4. Best ABC fit parameters for the flux density distribution

observation	μ	σ	x_{min}	α
	(Jy)	(Jy)	(Jy)	
2008-2014	$2.38^{+0.24}_{-0.27}$	$0.41^{+0.01}_{-0.01}$	$0.48^{+0.24}_{-0.21}$	$4.41^{+0.88}_{-0.81}$
2008-2017	$2.42^{+0.18}_{-0.20}$	$0.45^{+0.01}_{-0.01}$	$0.53^{+0.18}_{-0.15}$	$4.59^{+0.68}_{-0.58}$

NOTE—Results from the ABC fitting routine using a combined Gaussian and power-law model. All parameters for the pre- and postperiapse data, except σ are in excellent agreement, see the text for details.

result from Sub17. This may also taken as an indicator for the robustness of both fitting routines. A histogram of the preperiapse data, with the semi-analytic fit from Sub17 and the ABC fit from this work, is depicted in Fig. 12. The overplotted histogram of the postperiapse data shows the aforementioned abscence of bright flares with $S_\nu > 5$ Jy in that dataset.

In Tab. 4, we also list the ABC fit results for the entire dataset, i.e., all observations between 2008 and 2017. It shows that, within the uncertainties, the parameters μ, x_{min} and α stayed the same. Only the standard deviation of the Gaussian probability density changed significantly. A graphical representation of these facts can be seen in Fig 11. The discrepancy of the standard deviation though has to be put into perspective: first, their estimated uncertainties are very low, i.e., below 3% and might be underestimated by the fitting routine. An absolute difference of 0.04 Jy appears not significant. Secondly, this parameter only describes the scatter of the quiescent emission and therefore to some extent general uncertainties of the measurement process. As the data reduction with the BoA software package, as described in Sect. 2, includes some manual steps, it might be attributed to minor differences in the data reduction process such as opacity estimates or the Gaussian fit on the central regions in the GC scans. Therefore, it does not affect the description of the flaring emission, defined by the power-law parameters α and x_{min}. Thus, we can safely conclude that the parametric description of the flaring emission has not changed.

4. DISCUSSION AND CONCLUSIONS

In this paper, we have presented LABOCA/APEX observations of Sgr A* conducted between 2014 and 2017. All observations took place after the periapse of the G2/DSO object in spring 2014. We statistically analyzed these, and the lightcurves presented in Sub17, with PSDs and SFs to get typical timescales and noise
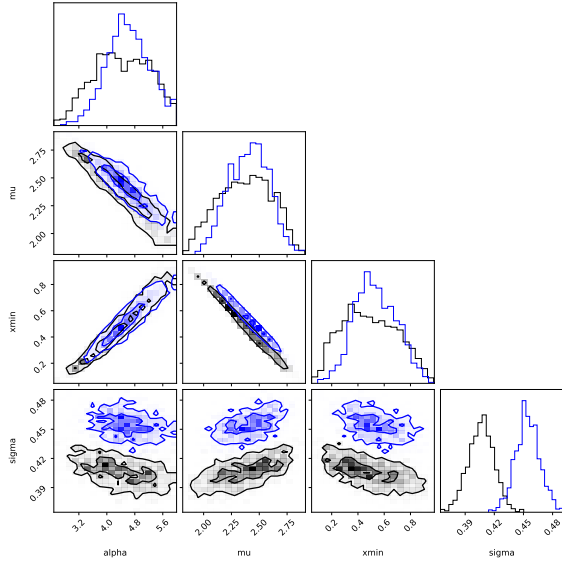
Figure 11. Overplot of marginalized posteriors of the combined Gaussian and power-law model with 1 and 2 σ credibility intervals in the 2D-histograms. In black the posteriors for the preperiapse data is shown, in blue for the entire dataset. All parameters except "sigma" are in excellent agreement, see the text for details.
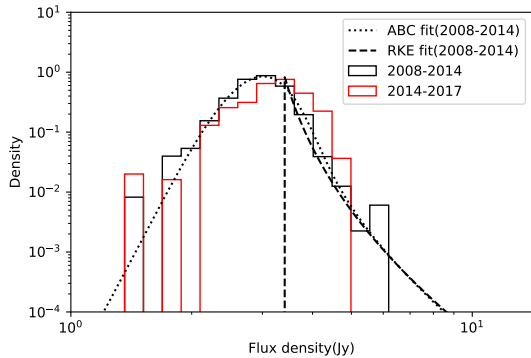
Figure 12. Histograms of the pre- (black) and postperiapse (red) data and best fits to the preperiapse data. The dashed and the dotted black show best fits to the preperiapse data: the former is the best fit with a semi-analytical model of a shifted power-law (RKE) according to Sub17, the latter is a combined Gaussian and power-law model ABC fit as worked out in this paper. The postperiapse data is not considered in the fits and is only shown for comparison.

Figure 13. Best fit for the flux density distribution with a combined Gaussian and power-law model. The dotted black line shows the fit on the postperiapse data as also shown in Fig. 12. In blue the histogram of the entire dataset and the best fit is depicted. It can be seen, that the model, i.e., the best fit parameters only slightly changed. The entire emission process between 2008 and 2017 can be described as a stationary process.

characteristics of the flaring activity. We find that all estimated postperiapse parameters show no significant deviations from the parameters describing the preperiapse data. Therefore, we conclude that the general properties of the emission process have not changed, and that we have observed a stationary process between 2008 and 2017. The relevance of this result is twofold:

first, in the context of the G2/DSO debate, this shows that the flyby of that object has not, or at least not yet changed the accretion and emission physics in the submm regime around Sgr A*. Nevertheless, we note that the impact of these findings for the question about the nature of the G2/DSO object is limited. We can only state that up to 2017 the periapse of this object has not yet influenced the flaring activity of Sgr A*. While this might strengthen the compact core argument, even with gas cloud models the time-scales on which increased flaring activity should appear are still not clear and highly model dependent. For instance, using viscosity arguments Murchikova (2021) calculated an infall time of leftover material between 6 and 10 years after periapse, Kawashima et al. (2017) estimate similar time scales based on magnetohydrodynamic simulations. This implies that even if the object G2/DSO was a gas cloud and a significant amount of matter was injected to the accretion flow onto Sgr A*, it does not necessarily mean that one should have observed increased flaring activity up to 2017.

Secondly, we can therefore claim that the flare generating process remained stationary and that the statistical description of this process has improved. We compiled a submm lightcurve of Sgr A* spanning over the period

of 9 years with 1104 data points in total. We can show that the emission process is a red noise process characterized by an PSD slope between -1.19 and -1.03 for timescales above 23.4 and 24.5 min, respectively. The SF slope is between 0.49 and 0.59 for timescales below 109.2 and 104.3 min, respectively. Considering the uncertainties, one can conclude that the flaring activity has typical timescales between 0.5 and 2 hours. Furthermore, the flux density distribution is described by a power-law with scaling index $\alpha \sim 4.6$. Within the uncertainties, this is consistent with the value of ~ 4 as we have found in Sub17. Moreover, it is also in agreement with the value of ~ 4.2 as found by Witzel et al. (2012)

in the infrared, strengthening the picture of a common physical origin of both emission processes.

In addition, we claim that the here presented observations (including the data from Sub17) is by itself a very valuable and unique dataset. We conducted long-term monitoring of Sgr A* in the submm with a single instrument over a period of 9 years. This dataset can be used in further, for instance multi-waveband, analyses of the emission processes of Sgr A*. The more consistent data is acquired the better we might understand the statistics and therefore the physical conditions in the close environment of a SMBH.

REFERENCES

Aitken, D. K., Greaves, J., Chrysostomou, A., et al. 2000, ApJL, 534, L173–L176, doi: 10.1086/312685

Beaklini, P. P. B., & Abraham, Z. 2013, MNRAS, 428, 2731–2740, doi: 10.1093/mnras/sts244

Brown, R. L. 1982, ApJ, 262, 110–119, doi: 10.1086/160401

Brown, R. L., Johnston, K. J., & Lo, K. Y. 1981, ApJ, 250, 155–159, doi: 10.1086/159356

Corrales, L., Baganoff, F. K., Wang, Q. D., et al. 2020, ApJ, 891, 71, doi: 10.3847/1538-4357/ab74df

Dexter, J., Agol, E., Fragile, P. C., & McKinney, J. C. 2010, ApJ, 717, 1092–1104, doi: 10.1088/0004-637X/717/2/1092

Do, T., Ghez, A. M., Morris, M. R., et al. 2009, ApJ, 691, 1021–1034, doi: 10.1088/0004-637X/691/2/1021

Eckart, A., García-Marín, M., Vogel, S. N., et al. 2012, A&A, 537, A52, doi: 10.1051/0004-6361/201117779

Eckart, A., Mužić, K., Yazici, S., et al. 2013, A&A, 551, A18, doi: 10.1051/0004-6361/201219994

Gillessen, S., Genzel, R., Fritz, T. K., et al. 2012, Nature, 481, 51–54, doi: 10.1038/nature10652

Gillessen, S., Plewa, P. M., Eisenhauer, F., et al. 2017, ApJ, 837, 30, doi: 10.3847/1538-4357/aa5c41

Gravity Collaboration, Abuter, R., Amorim, A., et al. 2018, A&A, 618, L10, doi: 10.1051/0004-6361/201834294

—. 2019, A&A, 625, L10, doi: 10.1051/0004-6361/201935656

—. 2020, A&A, 638, A2, doi: 10.1051/0004-6361/202037717

Hughes, P. A., Aller, H. D., & Aller, M. F. 1992, ApJ, 396, 469, doi: 10.1086/171734

Kawashima, T., Matsumoto, Y., & Matsumoto, R. 2017, PASJ, 69, 43, doi: 10.1093/pasj/psx015

Klinger, E., Rickert, D., & Hasenauer, J. 2018, Bioinformatics, 34, 3591–3593

Li, Y.-P., Yuan, F., & Wang, Q. D. 2017, MNRAS, 468, 2552–2568, doi: 10.1093/mnras/stx655

McCourt, M., & Madigan, A.-M. 2016, MNRAS, 455, 2187–2199, doi: 10.1093/mnras/stv2232

Murchikova, L. 2021, ApJL, 910, L1, doi: 10.3847/2041-8213/abeb70

Narayan, R., Özel, F., & Sironi, L. 2012, ApJL, 757, L20, doi: 10.1088/2041-8205/757/2/L20

Okuda, T., Singh, C. B., Das, S., et al. 2019, PASJ, 71, 49, doi: 10.1093/pasj/psz021

Pfuhl, O., Gillessen, S., Eisenhauer, F., et al. 2015, ApJ, 798, 111, doi: 10.1088/0004-637X/798/2/111

Plewa, P. M., Gillessen, S., Pfuhl, O., et al. 2017, ApJ, 840, 50, doi: 10.3847/1538-4357/aa6e00

Rácz, E., Kertész, J., & Eisler, Z. 2009

Saitoh, T. R., Makino, J., Asaki, Y., et al. 2014, PASJ, 66, 1, doi: 10.1093/pasj/pst003

Subroweit, M., García-Marín, M., Eckart, A., et al. 2017, A&A, 601, A80, doi: 10.1051/0004-6361/201628530

Subroweit, M., Mossoux, E., & Eckart, A. 2020, ApJ, 898, 138, doi: 10.3847/1538-4357/ab9947

Valencia-S., M., Eckart, A., Zajaček, M., et al. 2015, ApJ, 800, 125, doi: 10.1088/0004-637X/800/2/125

VanderPlas, J. T. 2018, ApJS, 236, 16, doi: 10.3847/1538-4365/aab766

Witzel, G., Eckart, A., Bremer, M., et al. 2012, ApJS, 203, 18, doi: 10.1088/0067-0049/203/2/18

Witzel, G., Martinez, G., Hora, J., et al. 2018, ApJ, 863, 15, doi: 10.3847/1538-4357/aace62

Witzel, G., Martinez, G., Willner, S. P., et al. 2021, ApJ, 917, 73, doi: 10.3847/1538-4357/ac0891

Yuan, F., Markoff, S., & Falcke, H. 2002, A&A, 383, 854–863, doi: 10.1051/0004-6361:20011709

Zhao, J.-H., Bower, G. C., & Goss, W. M. 2001, ApJL, 547, L29–L32, doi: 10.1086/318877

Zubovas, K., Nayakshin, S., & Markoff, S. 2012, MNRAS, 421, 1315–1324, doi: 10.1111/j.1365-2966.2011.20389.x

Summary, Conclusions and Outlook
7

In this thesis, I analyzed submm-, radio and X-ray emission coming from the direct vicinity of the Sgr A*. I statistically investigated these lightcurves and related the results with presumed emission models to check for their consistency. Detailed discussions of the specific results can be found in the conclusion sections of the respective papers. Here I will just list the main astrophysical results in a brief recap. The main conclusions of paper I (Chap. 4, Subroweit et al. 2017) can be summarized as follows:

- The 100 GHz radio data between 2010 and 2014 can be described by a power-law with scaling index $\alpha = 4.0 \pm 1.7$.

- The 350 GHz submm data between 2008 and 2014 yield a power-law with scaling index $\alpha = 4.7 \pm 0.8$.

- Both results are compatible with the NIR flux density distribution with $\alpha = 4.2 \pm 0.1$.

- All three emission types stem from the same source components, most likely from a self-absorbed synchrotron plasma.

- The results are comaptible with an expanding synchrotron blob model.

The central statements of paper II (Chap. 5, Subroweit et al. 2020) can be outlined by:

- The X-ray count rate distribution of the 2012's XVP campaign is best described by an exponentially truncated power-law, not a bounded power-law as other workgroups have suggested.

- Using this power-law model, one obtains a scaling index $\alpha = 1.66^{+0.07}_{-0.09}$.

- The power-law index fits very well to an SSC model explaining the X-ray emission.

- The presented statistics allows for brighter flares in the past and the future than those that have been observed so far.

The key messages of paper III (Chap. 6, Subroweit et al., in prep.) can be summed up with the following:

- The pre- (2008-2014) and the postperiapse (2014-2017) submm datasets are statistically similar.

- Both share a PSD with a slope between -1.19 and -1.03 and a lower break timescale between 23.4 and 24.5 min and a structure function with a slope between 0.49 and 0.59 and an upper break timescale between 109.2 and 104.3 min.

- The entire submm data between 2008 and 2017 can be described by a power-law with scaling index $\alpha = 4.59^{+0.58}_{-0.58}$. This is consistent with the previous results from paper I.

- The periapse of the G2/DSO object has not affected the emission mechanism of Sgr A* up to 2017.

The here presented statistical parameters are specifically fully compatible with the physical flare model as proposed and discussed in the attached publications: adiabatically expanding, self-absorbed synchrotron plasmas which produce X-ray emission through an SSC mechanism. The source regions probably have an angular diameter of approximately $1\,R_S$ and slowly expand at the speed of $\sim 0.01\,c$. Where pure synchrotron models require a demanding electron acceleration process, i.e., an electron population with γs of up to 10^4, the SSC mechanism predicts a less violent environment. Electron energies of $\gamma < 10^3$ are sufficient to explain the observed X-ray flares. On the other hand, an SSC model postulates electron densities above $10^9\,\mathrm{cm}^{-3}$ and therefore higher densities as typically found in the steady accretion flow onto Sgr A*. The physical mechanism that leads to those temporal overdensities still has to be investigated. Regardless of the concrete physical model which is used to explain the estimated statistical parameters: these parameters put additional constraints on and have to be explained by any physical theory of the accretion and emission mechanisms around Sgr A*. Therefore, I deem the statistical findings - independendly from the concretely assumed radiation model - as a very valuable outcome, possibly being adopted in future research.

The observational future in terms of monitoring Sgr A* seems to be very bright and promising at the moment. The Event Horizon Telescope (EHT), with a unpredecent resolution of less than $20\,\mu$as, has already produced ground breaking results with the observation of M87*, the SMBH at the very center of M87 (Event Horizon Telescope Collaboration et al., 2019). Observations of Sgr A* have already been conducted, the scientific community expects the first results to be published soon. With GRAVITY+, an upgrade of the Very Large Telescope Interferometer (VLTI), mas imaging and μas astrometry will be available soon (Eisenhauer et al., 2020). Stellar orbits and emission structures around Sgr A* will be resolved with an unpredecent accuracy. The James Webb Space Telescope (JWST, Kalirai 2018) will hopefully be launched by the end of 2021. Scientists will be able to observe the GC with a space-based facility unaffected by unavoidable disturbances of Earth-based observations. Finally, the Extremely Large

Telescope (ELT, Vernin et al. 2011) is being constructed at the moment. With an aperture diameter of 39 m and a collecting area of almost $1000 \, \text{m}^2$, it will outperform all existing optical telescopes in terms of resolution and sensitivity. This will allow for the detection of faint sources very close to Sgr A*. All four observational facilities will not only immensly improve the flare statistics in terms of numerical accuracy but will also provide insights in the spatial structure of the flare emitting source regions.

Finally, a personal remark and conclusion: not only the concrete astrophysical problems and objectives but also their computational solutions took a lot of passion, effort and time during my PhD-research. Computational capabilities and well developed software libraries allowed me to investigate physical problems with an accuracy and sofistication that I could not have imagined before the start of my work. Software development became an important part of my entire work. Especially the realm of Bayesian statistics, namely MCMC and ABC, was an entirely new experience for me. The benefits of this accumulated knowledge go far beyond the concrete physical results of this thesis. In my opinion, the adopted and developed tools can prove extremely valuable in future research also in other fields of astrophysics.

Bibliography

Adamic, L. A., Huberman, B. A., Barabási, A. L., Albert, R., Jeong, H., and Bianconi, G. (2000). Power-Law Distribution of the World Wide Web. *Science*, 287(5461):2115.

Ali, B., Paul, D., Eckart, A., Parsa, M., Zajacek, M., Peißker, F., Subroweit, M., Valencia-S., M., Thomkins, L., and Witzel, G. (2020). Kinematic Structure of the Galactic Center S Cluster. *ApJ*, 896(2):100.

Anderson, T. W. and Darling, D. A. (1952). Asymptotic Theory of Certain "Goodness of Fit" Criteria Based on Stochastic Processes. *The Annals of Mathematical Statistics*, 23(2):193 – 212.

Baganoff, F. K., Bautz, M. W., Brandt, W. N., Chartas, G., Feigelson, E. D., Garmire, G. P., Maeda, Y., Morris, M., Ricker, G. R., Townsley, L. K., and Walter, F. (2001). Rapid X-ray flaring from the direction of the supermassive black hole at the Galactic Centre. *Nature*, 413(6851):45–48.

Baganoff, F. K., Maeda, Y., Morris, M., Bautz, M. W., Brandt, W. N., Cui, W., Doty, J. P., Feigelson, E. D., Garmire, G. P., Pravdo, S. H., Ricker, G. R., and Townsley, L. K. (2003). Chandra X-Ray Spectroscopic Imaging of Sagittarius A* and the Central Parsec of the Galaxy. *ApJ*, 591(2):891–915.

Balick, B. and Brown, R. L. (1974). Intense sub-arcsecond structure in the galactic center. *ApJ*, 194:265–270.

Beaumont, M. A. (2010). Approximate Bayesian Computation in Evolution and Ecology. *Annual Review of Ecology, Evolution, and Systematics*, 41(1):379–406.

Beaumont, M. A., Zhang, W., and Balding, D. J. (2002). Approximate Bayesian Computation in Population Genetics. *Genetics*, 162(4):2025–2035.

Beckert, T., Duschl, W., Mezger, P., and Zylka, R. (1996). Anatomy of the Sagittarius A complex. V. Interpretation of the SGR A* spectrum. *Astronomy and Astrophysics*, 307:450–458.

Becklin, E. E. and Neugebauer, G. (1968). Infrared Observations of the Galactic Center. *ApJ*, 151:145.

Bélanger, G., Goldwurm, A., Melia, F., Ferrando, P., Grosso, N., Porquet, D., Warwick, R., and Yusef-Zadeh, F. (2005). Repeated X-Ray Flaring Activity in Sagittarius A*. *ApJ*, 635(2):1095–1102.

Berkson, J. (1980). Minimum Chi-Square, not Maximum Likelihood! *The Annals of Statistics*, 8(3):457 – 487.

Blumenthal, G. R. and Gould, R. J. (1970). Bremsstrahlung, Synchrotron Radiation, and Compton Scattering of High-Energy Electrons Traversing Dilute Gases. *Reviews of Modern Physics*, 42(2):237–271.

Bolton, J. G. and Stanley, G. J. (1948). Variable Source of Radio Frequency Radiation in the Constellation of Cygnus. *Nature*, 161(4087):312–313.

Bolton, J. G. and Westfold, K. C. (1950). Galactic Radiation at Radio Frequencies. III. Galactic Structure. *Australian Journal of Scientific Research A Physical Sciences*, 3:251.

Borkar, A., Eckart, A., Straubmeier, C., Kunneriath, D., Jalali, B., Sabha, N., Shahzamanian, B., García-Marín, M., Valencia-S, M., Sjouwerman, L., Britzen, S., Karas, V., Dovčiak, M., Donea, A., and Zensus, A. (2016). Monitoring the Galactic Centre with the Australia Telescope Compact Array. *MNRAS*, 458(3):2336–2349.

Boyce, H., Haggard, D., Witzel, G., Willner, S. P., Neilsen, J., Hora, J. L., Markoff, S., Ponti, G., Baganoff, F., Becklin, E. E., Fazio, G. G., Lowrance, P., Morris, M. R., and Smith, H. A. (2019). Simultaneous X-Ray and Infrared Observations of Sagittarius A*'s Variability. *ApJ*, 871(2):161.

Bremer, M., Witzel, G., Eckart, A., Zamaninasab, M., Buchholz, R. M., Schödel, R., Straubmeier, C., García-Marín, M., and Duschl, W. (2011). The near-infrared spectral index of Sagittarius A* derived from Ks- and H-band flare statistics. *A&A*, 532:A26.

Brinkerink, C. D. (2015). ALMA and VLA Measurements of Frequency-Dependent Time Lags in Sagittarius A*: Evidence for a Relativistic Outflow. In Iono, D., Tatematsu, K., Wootten, A., and Testi, L., editors, *Revolution in Astronomy with ALMA: The Third Year*, volume 499 of *Astronomical Society of the Pacific Conference Series*, page 167.

Brown, R. L. (1982). Precessing jets in Sagittarius A : gas dynamics in the central parsecof the galaxy. *ApJ*, 262:110–119.

Brown, R. L. and Lo, K. Y. (1982). Variability of the compact radio source at the Galactic Center. *ApJ*, 253:108–114.

Burke, B. F. (1965). Radio Radiation from the Galactic Nuclear Region. *ARA&A*, 3:275.

Chon, G., Böhringer, H., and Zaroubi, S. (2015). On the definition of superclusters. *A&A*, 575:L14.

Conselice, C. J., Wilkinson, A., Duncan, K., and Mortlock, A. (2016). The Evolution of Galaxy Number Density at z < 8 and Its Implications. *ApJ*, 830(2):83.

Cooper, A. P., Cole, S., Frenk, C. S., White, S. D. M., Helly, J., Benson, A. J., De Lucia, G., Helmi, A., Jenkins, A., Navarro, J. F., Springel, V., and Wang, J. (2010). Galactic stellar haloes in the CDM model. *MNRAS*, 406(2):744–766.

Devroye, L. (1986). *General Principles in Random Variate Generation*, pages 27–82. Springer New York, New York, NY.

Do, T., Witzel, G., Gautam, A. K., Chen, Z., Ghez, A. M., Morris, M. R., Becklin, E. E., Ciurlo, A., Hosek, Matthew, J., Martinez, G. D., Matthews, K., Sakai, S., and Schödel, R. (2019). Unprecedented Near-infrared Brightness and Variability of Sgr A*. *ApJ*, 882(2):L27.

Dodds-Eden, K., Porquet, D., Trap, G., Quataert, E., Haubois, X., Gillessen, S., Grosso, N., Pantin, E., Falcke, H., Rouan, D., Genzel, R., Hasinger, G., Goldwurm, A., Yusef-Zadeh, F., Clenet, Y., Trippe, S., Lagage, P. O., Bartko, H., Eisenhauer, F., Ott, T., Paumard, T., Perrin, G., Yuan, F., Fritz, T. K., and Mascetti, L. (2009). Evidence for X-Ray Synchrotron Emission from Simultaneous Mid-Infrared to X-Ray Observations of a Strong Sgr A* Flare. *ApJ*, 698(1):676–692.

Eckart, A. (2019). IBN RAḤĪQ'S TEXT ON THE MILKY WAY: PERCEPTION OF THE MILKY WAY IN THE EARLY ISLAMIC SOCIETY. *Arabic Sciences and Philosophy*, 29(2):227–260.

Eckart, A., Baganoff, F. K., Morris, M., Bautz, M. W., Brandt, W. N., Garmire, G. P., Genzel, R., Ott, T., Ricker, G. R., Straubmeier, C., Viehmann, T., Schödel, R., Bower, G. C., and Goldston, J. E. (2004). First simultaneous NIR/X-ray detection of a flare from Sgr A*. *A&A*, 427:1–11.

Eckart, A., Baganoff, F. K., Schödel, R., Morris, M., Genzel, R., Bower, G. C., Marrone, D., Moran, J. M., Viehmann, T., Bautz, M. W., Brandt, W. N., Garmire, G. P., Ott, T., Trippe, S., Ricker, G. R., Straubmeier, C., Roberts, D. A., Yusef-Zadeh, F., Zhao, J. H., and Rao, R. (2006). The flare activity of Sagittarius A*. New coordinated mm to X-ray observations. *A&A*, 450(2):535–555.

Eckart, A., García-Marín, M., Vogel, S. N., Teuben, P., Morris, M. R., Baganoff, F., Dexter, J., Schödel, R., Witzel, G., Valencia-S., M., Karas, V., Kunneriath, D., Straubmeier, C., Moser, L., Sabha, N., Buchholz, R., Zamaninasab, M., Mužić, K., Moultaka, J., and Zensus, J. A. (2012). Millimeter to X-ray flares from Sagittarius A*. *A&A*, 537:A52.

Eckart, A. and Genzel, R. (1996). Observations of stellar proper motions near the Galactic Centre. *Nature*, 383:415–417.

Eckart, A. and Genzel, R. (1997). Stellar proper motions in the central 0.1 PC of the Galaxy. *MNRAS*, 284(3):576–598.

Eckart, A., Genzel, R., Ott, T., and Schödel, R. (2002). Stellar orbits near Sagittarius A*. *MNRAS*, 331:917–934.

Eckart, A., Mužić, K., Yazici, S., Sabha, N., Shahzamanian, B., Witzel, G., Moser, L., Garcia-Marin, M., Valencia-S., M., Jalali, B., Bremer, M., Straubmeier, C., Rauch, C., Buchholz, R., Kunneriath, D., and Moultaka, J. (2013). Near-infrared proper motions and spectroscopy of infrared excess sources at the Galactic center. *A&A*, 551:A18.

Eisenhauer, F., Garcia, P. J. V., Genzel, R., Hönig, S. F., Kreidberg, L., Bouquin, J.-B. L., Léna, P., Paumard, T., Straubmeier, C., Amorim, A., Brandner, W., Carbillet, M., Cardoso, V., Clénet, Y., Davies, R. D., Defrère, D., de Zeeuw, T., Duvert, G., Eckart, A., Esposito, S., Fabricius, M., Schreiber, N. M. F., Gandhi, P., Gendron, E., Gillessen, S., Gratadour, D., Hofmann, K. H., Horrobin, M., Ireland, M. J., Kervella, P., Kraus, S., Lacour, S., Lai, O., Lopez, B., Lutz, D., Martinache, F., Meilland, A., Millour, F. A., Ott, T., Oudmaijer, R. D., Patru, F., Perraut, K., Perrin, G., Petrov, R. G., Quanz, S. P., Rabien, S., Riccardi, A., Saglia, R. P., Bermúdez, J. S., Schertl, D., Schubert, J., Soulez, F., Sturm, E., Tacconi, L. J., Tallon, M., Tallon-Bosc, I., Thiébaut, É., Vidal, F., Weigelt, G., Ziad, A., Absil, O., Alonso-Herrero, A., Bender, R., Benisty, M., Berger, J. P., Bañados, E., Boisson, C., Bouvier, J., Caselli, P., Cassan, A., Chazelas, B., Chiavassa, A., Combes, F., du Foresto, V. C., Dexter, J., Dougados, C., Henning, T., Herbst, T. M., Kammerer, J., Kishimoto, M., Labadie, L., Lagrange, A.-M., Marconi, A., Matter, A., Meliani, Z., Ménard, F., Monnier, J. D., Mourard, D., Netzer, H., Neumayer, N., Peterson, B. M., Petrucci, P.-O., Pott, J.-U., Rix, H.-W., Rouan, D., Sana, H., Ségransan, D., Sol, H., van Dishoeck, E. F., Vincent, F., Volonteri, M., and Zech, A. (2020). GRAVITY+: Towards Faint Science, All Sky, High Contrast, Milli-Arcsecond Optical Interferometric Imaging.

Ekers, R. D., van Gorkom, J. H., Schwarz, U. J., and Goss, W. M. (1983). The radio structure of SGR A. *A&A*, 122:143–150.

Elgarøy, Ø. (1982). Introduction to the 4th CESRA workshop on solar noise storms. In *Solar Radio Storms, CESRA Workshop #4*, page 1.

Evans, K. and Pounds, K. A. (1968). The X-Ray Emission Spectrum of a Solar Active Region. *ApJ*, 152:319.

Event Horizon Telescope Collaboration, Akiyama, K., Alberdi, A., Alef, W., Asada, K., Azulay, R., Baczko, A.-K., Ball, D., Baloković, M., Barrett, J., Bintley, D., Blackburn, L., Boland, W., Bouman, K. L., Bower, G. C., Bremer, M., Brinkerink, C. D., Brissenden, R., Britzen, S., Broderick, A. E., Broguiere, D., Bronzwaer, T., Byun, D.-Y., Carlstrom, J. E., Chael, A., Chan, C.-k., Chatterjee, S., Chatterjee, K., Chen, M.-T., Chen, Y., Cho, I., Christian, P., Conway, J. E., Cordes, J. M., Crew, G. B., Cui, Y., Davelaar, J., De Laurentis, M., Deane, R., Dempsey, J., Desvignes, G., Dexter, J., Doeleman, S. S., Eatough, R. P., Falcke, H., Fish, V. L., Fomalont, E., Fraga-Encinas, R., Freeman, W. T., Friberg, P., Fromm, C. M., Gómez, J. L., Galison, P., Gammie, C. F., García, R., Gentaz, O., Georgiev, B., Goddi, C., Gold, R., Gu, M., Gurwell, M., Hada, K., Hecht, M. H., Hesper, R., Ho, L. C., Ho, P., Honma, M., Huang, C.-W. L., Huang, L., Hughes, D. H., Ikeda, S., Inoue, M., Issaoun, S., James, D. J., Jannuzi, B. T., Janssen, M., Jeter, B., Jiang, W., Johnson, M. D., Jorstad, S., Jung, T., Karami, M., Karuppusamy, R., Kawashima, T., Keating, G. K., Kettenis, M., Kim, J.-Y., Kim, J., Kim, J., Kino, M., Koay, J. Y., Koch, P. M., Koyama, S., Kramer, M., Kramer, C., Krichbaum, T. P., Kuo, C.-Y., Lauer, T. R., Lee, S.-S., Li, Y.-R., Li, Z., Lindqvist, M., Liu, K., Liuzzo, E., Lo, W.-P., Lobanov, A. P., Loinard, L., Lonsdale, C., Lu, R.-S., MacDonald, N. R., Mao, J., Markoff, S., Marrone, D. P., Marscher, A. P., Martí-Vidal, I., Matsushita, S., Matthews, L. D., Medeiros, L., Menten, K. M., Mizuno, Y., Mizuno, I., Moran, J. M., Moriyama, K., Moscibrodzka, M., Müller, C., Nagai, H., Nagar, N. M., Nakamura, M., Narayan, R., Narayanan, G., Natarajan, I., Neri, R., Ni, C., Noutsos, A., Okino, H., Olivares, H., Ortiz-León, G. N., Oyama, T., Özel, F., Palumbo, D. C. M., Patel, N.,

Pen, U.-L., Pesce, D. W., Piétu, V., Plambeck, R., PopStefanija, A., Porth, O., Prather, B., Preciado-López, J. A., Psaltis, D., Pu, H.-Y., Ramakrishnan, V., Rao, R., Rawlings, M. G., Raymond, A. W., Rezzolla, L., Ripperda, B., Roelofs, F., Rogers, A., Ros, E., Rose, M., Roshanineshat, A., Rottmann, H., Roy, A. L., Ruszczyk, C., Ryan, B. R., Rygl, K. L. J., Sánchez, S., Sánchez-Arguelles, D., Sasada, M., Savolainen, T., Schloerb, F. P., Schuster, K.-F., Shao, L., Shen, Z., Small, D., Sohn, B. W., SooHoo, J., Tazaki, F., Tiede, P., Tilanus, R. P. J., Titus, M., Toma, K., Torne, P., Trent, T., Trippe, S., Tsuda, S., van Bemmel, I., van Langevelde, H. J., van Rossum, D. R., Wagner, J., Wardle, J., Weintroub, J., Wex, N., Wharton, R., Wielgus, M., Wong, G. N., Wu, Q., Young, K., Young, A., Younsi, Z., Yuan, F., Yuan, Y.-F., Zensus, J. A., Zhao, G., Zhao, S.-S., Zhu, Z., Algaba, J.-C., Allardi, A., Amestica, R., Anczarski, J., Bach, U., Baganoff, F. K., Beaudoin, C., Benson, B. A., Berthold, R., Blanchard, J. M., Blundell, R., Bustamente, S., Cappallo, R., Castillo-Domínguez, E., Chang, C.-C., Chang, S.-H., Chang, S.-C., Chen, C.-C., Chilson, R., Chuter, T. C., Córdova Rosado, R., Coulson, I. M., Crawford, T. M., Crowley, J., David, J., Derome, M., Dexter, M., Dornbusch, S., Dudevoir, K. A., Dzib, S. A., Eckart, A., Eckert, C., Erickson, N. R., Everett, W. B., Faber, A., Farah, J. R., Fath, V., Folkers, T. W., Forbes, D. C., Freund, R., Gómez-Ruiz, A. I., Gale, D. M., Gao, F., Geertsema, G., Graham, D. A., Greer, C. H., Grosslein, R., Gueth, F., Haggard, D., Halverson, N. W., Han, C.-C., Han, K.-C., Hao, J., Hasegawa, Y., Henning, J. W., Hernández-Gómez, A., Herrero-Illana, R., Heyminck, S., Hirota, A., Hoge, J., Huang, Y.-D., Impellizzeri, C. M. V., Jiang, H., Kamble, A., Keisler, R., Kimura, K., Kono, Y., Kubo, D., Kuroda, J., Lacasse, R., Laing, R. A., Leitch, E. M., Li, C.-T., Lin, L. C. C., Liu, C.-T., Liu, K.-Y., Lu, L.-M., Marson, R. G., Martin-Cocher, P. L., Massingill, K. D., Matulonis, C., McColl, M. P., McWhirter, S. R., Messias, H., Meyer-Zhao, Z., Michalik, D., Montaña, A., Montgomerie, W., Mora-Klein, M., Muders, D., Nadolski, A., Navarro, S., Neilsen, J., Nguyen, C. H., Nishioka, H., Norton, T., Nowak, M. A., Nystrom, G., Ogawa, H., Oshiro, P., Oyama, T., Parsons, H., Paine, S. N., Peñalver, J., Phillips, N. M., Poirier, M., Pradel, N., Primiani, R. A., Raffin, P. A., Rahlin, A. S., Reiland, G., Risacher, C., Ruiz, I., Sáez-Madaín, A. F., Sassella, R., Schellart, P., Shaw, P., Silva, K. M., Shiokawa, H., Smith, D. R., Snow, W., Souccar, K., Sousa, D., Sridharan, T. K., Srinivasan, R., Stahm, W., Stark, A. A., Story, K., Timmer, S. T., Vertatschitsch, L., Walther, C., Wei, T.-S., Whitehorn, N., Whitney, A. R., Woody, D. P., Wouterloot, J. G. A., Wright, M., Yamaguchi, P., Yu, C.-Y., Zeballos, M., Zhang, S., and Ziurys, L. (2019). First M87 Event Horizon Telescope Results. I. The Shadow of the Supermassive Black Hole. *ApJ*, 875(1):L1.

Falcke, H., Goss, W. M., Matsuo, H., Teuben, P., Zhao, J.-H., and Zylka, R. (1998). The Simultaneous Spectrum of Sagittarius A* from 20 Centimeters to 1 Millimeter and the Nature of the Millimeter Excess. *ApJ*, 499:731–734.

Foreman-Mackey, D., Hogg, D. W., Lang, D., and Goodman, J. (2013). emcee: The MCMC Hammer. *PASP*, 125:306.

Frater, R. H., Brooks, J. W., and Whiteoak, J. B. (1992). The Australia Telescope - Overview. *Journal of Electrical and Electronics Engineering Australia*, 12(2):103–112.

Friedman, E. and Landsberg, A. (2013). Hierarchical networks, power laws, and neuronal avalanches. *Chaos (Woodbury, N.Y.)*, 23:013135.

Friedman, H. (1963). Solar X-Ray Emission. In Evans, J. W., editor, *The Solar Corona*, volume 16, page 45.

Fritz, T. K., Chatzopoulos, S., Gerhard, O., Gillessen, S., Genzel, R., Pfuhl, O., Tacchella, S., Eisenhauer, F., and Ott, T. (2016). The Nuclear Cluster of the Milky Way: Total Mass and Luminosity. *ApJ*, 821(1):44.

Fuller, R. S., Anderson, M. G., Norris, R. P., and Trudgett, M. (2014). The Emu Sky Knowledge of the Kamilaroi and Euahlayi Peoples. *Journal of Astronomical History and Heritage*, 17(2):171–179.

Genzel, R., Eckart, A., Ott, T., and Eisenhauer, F. (1997). On the nature of the dark mass in the centre of the Milky Way. *MNRAS*, 291(1):219–234.

Genzel, R., Eisenhauer, F., and Gillessen, S. (2010). The Galactic Center massive black hole and nuclear star cluster. *Reviews of Modern Physics*, 82:3121–3195.

Genzel, R., Schödel, R., Ott, T., Eckart, A., Alexander, T., Lacombe, F., Rouan, D., and Aschenbach, B. (2003). Near-infrared flares from accreting gas around the supermassive black hole at the Galactic Centre. *Nature*, 425(6961):934–937.

Ghez, A. M., Becklin, E., Duchjne, G., Hornstein, S., Morris, M., Salim, S., and Tanner, A. (2003). Full Three Dimensional Orbits For Multiple Stars on Close Approaches to the Central Supermassive Black Hole. *Astronomische Nachrichten Supplement*, 324:527–533.

Ghez, A. M., Klein, B. L., Morris, M., and Becklin, E. E. (1998). High Proper-Motion Stars in the Vicinity of Sagittarius A*: Evidence for a Supermassive Black Hole at the Center of Our Galaxy. *ApJ*, 509:678–686.

Ghez, A. M., Wright, S. A., Matthews, K., Thompson, D., Le Mignant, D., Tanner, A., Hornstein, S. D., Morris, M., Becklin, E. E., and Soifer, B. T. (2004). Variable Infrared Emission from the Supermassive Black Hole at the Center of the Milky Way. *ApJ*, 601(2):L159–L162.

Ghisellini, G. (2013). *Radiative Processes in High Energy Astrophysics*, volume 873.

Gillessen, S., Eisenhauer, F., Quataert, E., Genzel, R., Paumard, T., Trippe, S., Ott, T., Abuter, R., Eckart, A., Lagage, P. O., Lehnert, M. D., Tacconi, L. J., and Martins, F. (2006). Variations in the Spectral Slope of Sagittarius A* during a Near-Infrared Flare. *ApJ*, 640(2):L163–L166.

Gillessen, S., Eisenhauer, F., Trippe, S., Alexander, T., Genzel, R., Martins, F., and Ott, T. (2009). Monitoring Stellar Orbits Around the Massive Black Hole in the Galactic Center. *ApJ*, 692:1075–1109.

Gillessen, S., Genzel, R., Fritz, T. K., Quataert, E., Alig, C., Burkert, A., Cuadra, J., Eisenhauer, F., Pfuhl, O., Dodds-Eden, K., Gammie, C. F., and Ott, T. (2012). A gas cloud on its way towards the supermassive black hole at the Galactic Centre. *Nature*, 481:51–54.

Gillessen, S., Plewa, P. M., Eisenhauer, F., Sari, R., Waisberg, I., Habibi, M., Pfuhl, O., George, E., Dexter, J., von Fellenberg, S., Ott, T., and Genzel, R. (2017). An Update on Monitoring Stellar Orbits in the Galactic Center. *ApJ*, 837:30.

Goldwurm, A., Brion, E., Goldoni, P., Ferrando, P., Daigne, F., Decourchelle, A., Warwick, R. S., and Predehl, P. (2003). A New X-Ray Flare from the Galactic Nucleus Detected with the XMM-Newton Photon Imaging Cameras. *ApJ*, 584(2):751–757.

González, R. E., Kravtsov, A. V., and Gnedin, N. Y. (2014). On the Mass of the Local Group. *ApJ*, 793(2):91.

Gould, R. J. (1979). Compton and synchrotron processes in spherically-symmetric non-thermal sources. *A&A*, 76(3):306–311.

Gravity Collaboration (2017). First Light for GRAVITY: A New Era for Optical Interferometry. *The Messenger*, 170:10–15.

Gravity Collaboration, Abuter, R., Amorim, A., Bauböck, M., Berger, J. P., Bonnet, H., Brandner, W., Clénet, Y., Coudé Du Foresto, V., de Zeeuw, P. T., Deen, C., Dexter, J., Duvert, G., Eckart, A., Eisenhauer, F., Förster Schreiber, N. M., Garcia, P., Gao, F., Gendron, E., Genzel, R., Gillessen, S., Guajardo, P., Habibi, M., Haubois, X., Henning, T., Hippler, S., Horrobin, M., Huber, A., Jiménez-Rosales, A., Jocou, L., Kervella, P., Lacour, S., Lapeyrère, V., Lazareff, B., Le Bouquin, J. B., Léna, P., Lippa, M., Ott, T., Panduro, J., Paumard, T., Perraut, K., Perrin, G., Pfuhl, O., Plewa, P. M., Rabien, S., Rodríguez-Coira, G., Rousset, G., Sternberg, A., Straub, O., Straubmeier, C., Sturm, E., Tacconi, L. J., Vincent, F., von Fellenberg, S., Waisberg, I., Widmann, F., Wieprecht, E., Wiezorrek, E., Woillez, J., and Yazici, S. (2018). Detection of orbital motions near the last stable circular orbit of the massive black hole SgrA*. *A&A*, 618:L10.

Gravity Collaboration, Abuter, R., Amorim, A., Bauböck, M., Berger, J. P., Bonnet, H., Brandner, W., Clénet, Y., Coudé Du Foresto, V., de Zeeuw, P. T., Dexter, J., Duvert, G., Eckart, A., Eisenhauer, F., Förster Schreiber, N. M., Garcia, P., Gao, F., Gendron, E., Genzel, R., Gerhard, O., Gillessen, S., Habibi, M., Haubois, X., Henning, T., Hippler, S., Horrobin, M., Jiménez-Rosales, A., Jocou, L., Kervella, P., Lacour, S., Lapeyrère, V., Le Bouquin, J. B., Léna, P., Ott, T., Paumard, T., Perraut, K., Perrin, G., Pfuhl, O., Rabien, S., Rodriguez Coira, G., Rousset, G., Scheithauer, S., Sternberg, A., Straub, O., Straubmeier, C., Sturm, E., Tacconi, L. J., Vincent, F., von Fellenberg, S., Waisberg, I., Widmann, F., Wieprecht, E., Wiezorrek, E., Woillez, J., and Yazici, S. (2019). A geometric distance measurement to the Galactic center black hole with 0.3% uncertainty. *A&A*, 625:L10.

Gravity Collaboration, Bauböck, M., Dexter, J., Abuter, R., Amorim, A., Berger, J. P., Bonnet, H., Brandner, W., Clénet, Y., Coudé Du Foresto, V., de Zeeuw, P. T., Duvert, G., Eckart, A., Eisenhauer, F., Förster Schreiber, N. M., Gao, F., Garcia, P., Gendron, E., Genzel, R., Gerhard, O., Gillessen, S., Habibi, M., Haubois, X., Henning, T., Hippler, S., Horrobin, M., Jiménez-Rosales, A., Jocou, L., Kervella, P., Lacour, S., Lapeyrère, V., Le Bouquin, J. B., Léna, P., Ott, T., Paumard, T., Perraut, K., Perrin, G., Pfuhl, O., Rabien, S., Rodriguez Coira, G., Rousset, G., Scheithauer, S., Stadler, J., Sternberg, A., Straub, O., Straubmeier, C., Sturm, E., Tacconi, L. J., Vincent, F., von Fellenberg,

S., Waisberg, I., Widmann, F., Wieprecht, E., Wiezorrek, E., Woillez, J., and Yazici, S. (2020). Modeling the orbital motion of Sgr A*'s near-infrared flares. *A&A*, 635:A143.

Guesten, R., Genzel, R., Wright, M. C. H., Jaffe, D. T., Stutzki, J., and Harris, A. I. (1987). Aperture Synthesis Observations of the Circumnuclear Ring in the Galactic Center. *ApJ*, 318:124.

Güsten, R., Nyman, L. Å., Schilke, P., Menten, K., Cesarsky, C., and Booth, R. (2006). The Atacama Pathfinder EXperiment (APEX) - a new submillimeter facility for southern skies -. *A&A*, 454(2):L13–L16.

Gutenberg, B. and Richter, C. (1956). Earthquake magnitude, intensity, energy, and acceleration (Second paper). *Bulletin of the Seismological Society of America*, 46.

Hastings, W. K. (1970). Monte Carlo Sampling Methods Using Markov Chains and Their Applications. *Biometrika*, 57(1):97–109.

Herbst, T. M., Beckwith, S. V. W., Forrest, W. J., and Pipher, J. L. (1993). Infrared Imaging Spectroscopy of the Galactic Center: Distribution and Motion of the Ionized Gas. *AJ*, 105:956.

Herrnstein, R. M., Zhao, J.-H., Bower, G. C., and Goss, W. M. (2004). The Variability of Sagittarius A* at Centimeter Wavelengths. *AJ*, 127(6):3399–3410.

Hollister, M. I. (2009). *SCUBA-2 instrument: an application of large-format superconducting bolometer arrays for submillimetre astronomy*. PhD thesis, The University of Edinburgh.

Hornstein, S. D., Matthews, K., Ghez, A. M., Lu, J. R., Morris, M., Becklin, E. E., Rafelski, M., and Baganoff, F. K. (2007). A Constant Spectral Index for Sagittarius A* during Infrared/X-Ray Intensity Variations. *ApJ*, 667(2):900–910.

Hubble, E. (1929). A Relation between Distance and Radial Velocity among Extra-Galactic Nebulae. *Proceedings of the National Academy of Science*, 15(3):168–173.

Jansky, K. (1932). Directional Studies of Atmospherics at High Frequencies. *Proceedings of the Institute of Radio Engineers*, 20(12):1920–1932.

Jansky, K. G. (1935). A Note on the Source of Interstellar Interference. *Proceedings of the Institute of Radio Engineers*, 23:1158–1163.

Kafle, P. R., Sharma, S., Lewis, G. F., and Bland-Hawthorn, J. (2014). On the Shoulders of Giants: Properties of the Stellar Halo and the Milky Way Mass Distribution. *ApJ*, 794(1):59.

Kalirai, J. (2018). Scientific discovery with the James Webb Space Telescope. *Contemporary Physics*, 59(3):251–290.

Kellermann, K. I. and Pauliny-Toth, I. I. K. (1967). Variations in the Flux Density of Some Quasi-stellar Sources. *Nature*, 213(5080):977–980.

Klinger, E., Rickert, D., and Hasenauer, J. (2018). pyABC: distributed, likelihood-free inference. *Bioinformatics*, 34(20):3591–3593.

Knuth, K. H. (2006). Optimal Data-Based Binning for Histograms. *arXiv Physics e-prints*.

Kolmogorov, A. (1933). Sulla Determinazione Empirica di una Legge di Distribuzione. *Giornale dell' Istituto Italiano degli Attuari*, 4:83–91.

Krabbe, A., Genzel, R., Eckart, A., Najarro, F., Lutz, D., Cameron, M., Kroker, H., Tacconi-Garman, L. E., Thatte, N., Weitzel, L., Drapatz, S., Geballe, T., Sternberg, A., and Kudritzki, R. (1995). The Nuclear Cluster of the Milky Way: Star Formation and Velocity Dispersion in the Central 0.5 Parsec. *ApJ*, 447:L95.

Kraus, J. D. (1963). The Large Radio Telescope of Ohio State University. *S&T*, 26:12.

Lacy, J. H., Townes, C. H., and Hollenbach, D. J. (1982). The nature of the central parsec of the Galaxy. *ApJ*, 262:120–134.

Lang, K. R. (1999). *Astrophysical formulae*.

Lau, R. M., Herter, T. L., Morris, M. R., Becklin, E. E., and Adams, J. D. (2013). SOFIA/FORCAST Imaging of the Circumnuclear Ring at the Galactic Center. *ApJ*, 775(1):37.

Launhardt, R., Zylka, R., and Mezger, P. G. (2002). The nuclear bulge of the Galaxy. III. Large-scale physical characteristics of stars and interstellar matter. *A&A*, 384:112–139.

Lee, S., Pak, S., Geballe, T. R., Lee, S.-G., Davis, C. J., Choi, M., Minh, Y. C., Herrnstein, R. M., and Ho, P. T. P. (2006). Shock interactions between Sgr A East and its environments. In *Journal of Physics Conference Series*, volume 54 of *Journal of Physics Conference Series*, pages 22–28.

Lemaître, G. (1931). The Beginning of the World from the Point of View of Quantum Theory. *Nature*, 127(3210):706.

Lo, K. Y. and Claussen, M. J. (1983). High-resolution observations of ionized gas in central 3 parsecs of the Galaxy: possible evidence for infall. *Nature*, 306(5944):647–651.

Lu, E. T. and Hamilton, R. J. (1991). Avalanches and the Distribution of Solar Flares. *ApJ*, 380:L89.

Lundgren, A., De Breuck, C., Siringo, G., Weiß, A., Agurto, C., Azagra, F., Belloche, A., Dumke, M., Durán, C., Eckart, A., González, E., Güsten, R., Hacar, A., Kovács, A., Kreysa, E., Mac-Auliffe, F., Martínez, M., Menten, K. M., Montenegro, F., Nyman, L. Å., Parra, R., Pérez-Beaupuits, J. P., Reveret, V., Risacher, C., Schuller, F., Stanke, T., Torstensson, K., Venegas, P., Wiesemeyer, H., and Wyrowski, F. (2020). An Era Comes to an End: The Legacy of LABOCA at APEX. *The Messenger*, 181:7–15.

Lundgren, A., Rabanus, D., Güsten, R., Menten, K., de Zeeuw, T., Olofsson, H., Kaufer, A., Nyman, L.-Å., Bergman, P., de Breuck, C., Wyrowski, F., Agurto, C., Azagra, F., Dumke, M., Mac-Auliffe, F., Martinez, M., Montenegro, F., Muders, D., Reveret, V., Risacher, C., Parra, R., Siringo, G., and Wieching, G. (2010). APEX: five years of operations. In Silva, D. R., Peck, A. B., and Soifer, B. T., editors, *Observatory Operations: Strategies, Processes, and Systems III*, volume 7737 of *Society of Photo-Optical Instrumentation Engineers (SPIE) Conference Series*, page 773708.

Malamud, B. D., Morein, G., and Turcotte, D. L. (1998). Forest fires: An example of self-organized critical behavior. *Science (New York, N.Y.)*, 281(5384):1840–1842.

Mar, J. W. and Liebowitz, H. (2003). *Structures Technology for Large Radio and Radar Telescope Systems*. The MIT Press.

Marjoram, P., Molitor, J., Plagnol, V., and Tavaré, S. (2003). Markov chain Monte Carlo without likelihoods. *Proceedings of the National Academy of Science*, 100(26):15324–15328.

Marrone, D. P., Baganoff, F. K., Morris, M. R., Moran, J. M., Ghez, A. M., Hornstein, S. D., Dowell, C. D., Muñoz, D. J., Bautz, M. W., Ricker, G. R., Brandt, W. N., Garmire, G. P., Lu, J. R., Matthews, K., Zhao, J. H., Rao, R., and Bower, G. C. (2008). An X-Ray, Infrared, and Submillimeter Flare of Sagittarius A*. *ApJ*, 682(1):373–383.

Marrone, D. P., Moran, J. M., Zhao, J.-H., and Rao, R. (2007). An Unambiguous Detection of Faraday Rotation in Sagittarius A*. *ApJ*, 654(1):L57–L60.

Marscher, A. P. (1983). Accurate formula for the self-Compton X-ray flux density from a uniform, spherical, compact radio source. *ApJ*, 264:296–297.

Marscher, A. P. (1987). Synchro-Compton emission from superluminal sources. In Zensus, J. A. and Pearson, T. J., editors, *Superluminal Radio Sources*, pages 280–300.

McHardy, I. (1988). EXOSAT observations of variability in active galactic nuclei. *Mem. Soc. Astron. Italiana*, 59:239–260.

McMillan, P. J. (2017). The mass distribution and gravitational potential of the Milky Way. *MNRAS*, 465(1):76–94.

McVinish, R. (2012). Improving ABC for quantile distributions. *Statistics and Computing*, 22(6):1199–1207.

Michelson, A. A. and Pease, F. G. (1921). Measurement of the Diameter of α Orionis with the Interferometer. *ApJ*, 53:249–259.

Minasandra, P. and Isvaran, K. (2018). Truncated power-law distribution of group sizes in antelope. *bioRxiv*.

Miyazaki, A., Tsutsumi, T., and Tsuboi, M. (2004). Intraday Variation of Sagittarius A* at Short Millimeter Wavelengths. *ApJ*, 611(2):L97–L100.

Moffet, A. T. (1975). *Strong Nonthermal Radio Emission from Galaxies*, page 211.

Montero-Castaño, M., Herrnstein, R. M., and Ho, P. T. P. (2009). Gas Infall Toward Sgr A* from the Clumpy Circumnuclear Disk. *ApJ*, 695(2):1477–1494.

Mościbrodzka, M., Falcke, H., Shiokawa, H., and Gammie, C. F. (2014). Observational appearance of inefficient accretion flows and jets in 3D GRMHD simulations: Application to Sagittarius A*. *A&A*, 570:A7.

Mossoux, E. and Grosso, N. (2017). Sixteen years of X-ray monitoring of Sagittarius A*: Evidence for a decay of the faint flaring rate from 2013 August, 13 months before a rise in the bright flaring rate. *A&A*, 604:A85.

Mossoux, E., Grosso, N., Bushouse, H., Eckart, A., Yusef-Zadeh, F., Plambeck, R. L., Peissker, F., Valencia-S., M., Porquet, D., Cotton, W. D., and Roberts, D. A. (2016). Multiwavelength study of the flaring activity of Sagittarius A in 2014 February-April. *A&A*, 589:A116.

Neilsen, J., Markoff, S., Nowak, M. A., Dexter, J., Witzel, G., Barrière, N., Li, Y., Baganoff, F. K., Degenaar, N., Fragile, P. C., Gammie, C., Goldwurm, A., Grosso, N., and Haggard, D. (2015). The X-Ray Flux Distribution of Sagittarius A* as Seen by Chandra. *ApJ*, 799(2):199.

Neumayer, N., Seth, A., and Böker, T. (2020). Nuclear star clusters. *The Astronomy and Astrophysics Review*, 28(1):4.

Oda, M., Gorenstein, P., Gursky, H., Kellogg, E., Schreier, E., Tananbaum, H., and Giacconi, R. (1971). X-Ray Pulsations from Cygnus X-1 Observed from UHURU. *ApJ*, 166:L1.

Papoulis, A. (1984). *Probability, random variables and stochastic processes*.

Pareto, V. (1964). *Cours d'économie politique*, volume 1. Librairie Droz.

Parsa, M., Eckart, A., Shahzamanian, B., Karas, V., Zajaček, M., Zensus, J. A., and Straubmeier, C. (2017). Investigating the Relativistic Motion of the Stars Near the Supermassive Black Hole in the Galactic Center. *ApJ*, 845(1):22.

Peißker, F., Eckart, A., Zajaček, M., Ali, B., and Parsa, M. (2020). S62 and S4711: Indications of a Population of Faint Fast-moving Stars inside the S2 Orbit—S4711 on a 7.6 yr Orbit around Sgr A*. *ApJ*, 899(1):50.

Penzias, A. A. and Wilson, R. W. (1965). A Measurement of Excess Antenna Temperature at 4080 Mc/s. *ApJ*, 142:419–421.

Pfuhl, O., Gillessen, S., Eisenhauer, F., Genzel, R., Plewa, P. M., Ott, T., Ballone, A., Schartmann, M., Burkert, A., Fritz, T. K., Sari, R., Steinberg, E., and Madigan, A.-M. (2015). The Galactic Center Cloud G2 and its Gas Streamer. *ApJ*, 798:111.

Piddington, J. H. and Minnett, H. C. (1951). Observations of Galactic Radiation at Frequencies of 1200 and 3000 Mc/s. *Australian Journal of Scientific Research A Physical Sciences*, 4:459.

Pilgrim, C. and Hills, T. T. (2021). Bias in Zipf's law estimators. *Scientific Reports*, 11(1):17309.

Planck Collaboration, Ade, P. A. R., Aghanim, N., Arnaud, M., Ashdown, M., Aumont, J., Baccigalupi, C., Banday, A. J., Barreiro, R. B., Bartlett, J. G., Bartolo, N., Battaner, E., Battye, R., Benabed, K., Benoît, A., Benoit-Lévy, A., Bernard, J. P., Bersanelli, M., Bielewicz, P., Bock, J. J., Bonaldi, A., Bonavera, L., Bond, J. R., Borrill, J., Bouchet, F. R., Boulanger, F., Bucher, M., Burigana, C., Butler, R. C., Calabrese, E., Cardoso, J. F., Catalano, A., Challinor, A., Chamballu, A., Chary, R. R., Chiang, H. C., Chluba, J., Christensen, P. R., Church, S., Clements, D. L., Colombi, S., Colombo, L. P. L., Combet, C., Coulais, A., Crill, B. P., Curto, A., Cuttaia, F., Danese, L., Davies, R. D., Davis, R. J.,

de Bernardis, P., de Rosa, A., de Zotti, G., Delabrouille, J., Désert, F. X., Di Valentino, E., Dickinson, C., Diego, J. M., Dolag, K., Dole, H., Donzelli, S., Doré, O., Douspis, M., Ducout, A., Dunkley, J., Dupac, X., Efstathiou, G., Elsner, F., Enßlin, T. A., Eriksen, H. K., Farhang, M., Fergusson, J., Finelli, F., Forni, O., Frailis, M., Fraisse, A. A., Franceschi, E., Frejsel, A., Galeotta, S., Galli, S., Ganga, K., Gauthier, C., Gerbino, M., Ghosh, T., Giard, M., Giraud-Héraud, Y., Giusarma, E., Gjerløw, E., González-Nuevo, J., Górski, K. M., Gratton, S., Gregorio, A., Gruppuso, A., Gudmundsson, J. E., Hamann, J., Hansen, F. K., Hanson, D., Harrison, D. L., Helou, G., Henrot-Versillé, S., Hernández-Monteagudo, C., Herranz, D., Hildebrandt, S. R., Hivon, E., Hobson, M., Holmes, W. A., Hornstrup, A., Hovest, W., Huang, Z., Huffenberger, K. M., Hurier, G., Jaffe, A. H., Jaffe, T. R., Jones, W. C., Juvela, M., Keihänen, E., Keskitalo, R., Kisner, T. S., Kneissl, R., Knoche, J., Knox, L., Kunz, M., Kurki-Suonio, H., Lagache, G., Lähteenmäki, A., Lamarre, J. M., Lasenby, A., Lattanzi, M., Lawrence, C. R., Leahy, J. P., Leonardi, R., Lesgourgues, J., Levrier, F., Lewis, A., Liguori, M., Lilje, P. B., Linden-Vørnle, M., López-Caniego, M., Lubin, P. M., Macías-Pérez, J. F., Maggio, G., Maino, D., Mandolesi, N., Mangilli, A., Marchini, A., Maris, M., Martin, P. G., Martinelli, M., Martínez-González, E., Masi, S., Matarrese, S., McGehee, P., Meinhold, P. R., Melchiorri, A., Melin, J. B., Mendes, L., Mennella, A., Migliaccio, M., Millea, M., Mitra, S., Miville-Deschênes, M. A., Moneti, A., Montier, L., Morgante, G., Mortlock, D., Moss, A., Munshi, D., Murphy, J. A., Naselsky, P., Nati, F., Natoli, P., Netterfield, C. B., Nørgaard-Nielsen, H. U., Noviello, F., Novikov, D., Novikov, I., Oxborrow, C. A., Paci, F., Pagano, L., Pajot, F., Paladini, R., Paoletti, D., Partridge, B., Pasian, F., Patanchon, G., Pearson, T. J., Perdereau, O., Perotto, L., Perrotta, F., Pettorino, V., Piacentini, F., Piat, M., Pierpaoli, E., Pietrobon, D., Plaszczynski, S., Pointecouteau, E., Polenta, G., Popa, L., Pratt, G. W., Prézeau, G., Prunet, S., Puget, J. L., Rachen, J. P., Reach, W. T., Rebolo, R., Reinecke, M., Remazeilles, M., Renault, C., Renzi, A., Ristorcelli, I., Rocha, G., Rosset, C., Rossetti, M., Roudier, G., Rouillé d'Orfeuil, B., Rowan-Robinson, M., Rubiño-Martín, J. A., Rusholme, B., Said, N., Salvatelli, V., Salvati, L., Sandri, M., Santos, D., Savelainen, M., Savini, G., Scott, D., Seiffert, M. D., Serra, P., Shellard, E. P. S., Spencer, L. D., Spinelli, M., Stolyarov, V., Stompor, R., Sudiwala, R., Sunyaev, R., Sutton, D., Suur-Uski, A. S., Sygnet, J. F., Tauber, J. A., Terenzi, L., Toffolatti, L., Tomasi, M., Tristram, M., Trombetti, T., Tucci, M., Tuovinen, J., Türler, M., Umana, G., Valenziano, L., Valiviita, J., Van Tent, F., Vielva, P., Villa, F., Wade, L. A., Wandelt, B. D., Wehus, I. K., White, M., White, S. D. M., Wilkinson, A., Yvon, D., Zacchei, A., and Zonca, A. (2016). Planck 2015 results. XIII. Cosmological parameters. *A&A*, 594:A13.

Plume, R., Fuller, G. A., Helmich, F., van der Tak, F. F. S., Roberts, H., Bowey, J., Buckle, J., Butner, H., Caux, E., Ceccarelli, C., van Dishoeck, E. F., Friberg, P., Gibb, A. G., Hatchell, J., Hogerheijde, M. R., Matthews, H., Millar, T. J., Mitchell, G., Moore, T. J. T., Ossenkopf, V., Rawlings, J. M. C., Richer, J., Roellig, M., Schilke, P., Spaans, M., Tielens, A. G. G. M., Thompson, M. A., Viti, S., Weferling, B., White, G. J., Wouterloot, J., Yates, J., and Zhu, M. (2007). The James Clerk Maxwell Telescope Spectral Legacy Survey. *PASP*, 119(851):102–111.

Ponti, G., George, E., Scaringi, S., Zhang, S., Jin, C., Dexter, J., Terrier, R., Clavel, M., Degenaar, N., Eisenhauer, F., Genzel, R., Gillessen, S., Goldwurm, A., Habibi, M., Haggard, D., Hailey, C., Harrison, F., Merloni, A., Mori, K., Nandra, K., Ott, T., Pfuhl,

O., Plewa, P. M., and Waisberg, I. (2017). A powerful flare from Sgr A* confirms the synchrotron nature of the X-ray emission. *MNRAS*, 468(2):2447–2468.

Porquet, D., Predehl, P., Aschenbach, B., Grosso, N., Goldwurm, A., Goldoni, P., Warwick, R. S., and Decourchelle, A. (2003). XMM-Newton observation of the brightest X-ray flare detected so far from Sgr A*. *A&A*, 407:L17–L20.

Powers, D. M. W. (1998). Applications and Explanations of Zipf's Law. In *New Methods in Language Processing and Computational Natural Language Learning*.

Pritchard, J. K., Seielstad, M. T., Perez-Lezaun, A., and Feldman, M. W. (1999). Population growth of human Y chromosomes: a study of Y chromosome microsatellites. *Molecular Biology and Evolution*, 16(12):1791–1798.

Quataert, E. (2002). A Thermal Bremsstrahlung Model for the Quiescent X-Ray Emission from Sagittarius A*. *ApJ*, 575(2):855–859.

Reber, G. (1940). Notes: Cosmic Static. *ApJ*, 91:621–624.

Ribas, I., Jordi, C., Vilardell, F., Fitzpatrick, E. L., Hilditch, R. W., and Guinan, E. F. (2005). First Determination of the Distance and Fundamental Properties of an Eclipsing Binary in the Andromeda Galaxy. *ApJ*, 635(1):L37–L40.

Richards, P. L. (1994). Bolometers for infrared and millimeter waves. *Journal of Applied Physics*, 76(1):1–24.

Rieke, G. H. and Low, F. J. (1973). Infrared maps of the galactic nucleus. *ApJ*, 184:415–425.

Rubin, D. B. (1984). Bayesianly Justifiable and Relevant Frequency Calculations for the Applied Statistician. *The Annals of Statistics*, 12(4):1151 – 1172.

Rybicki, G. B. and Lightman, A. P. (1979). *Radiative processes in astrophysics*.

Sabha, N., Witzel, G., Eckart, A., Buchholz, R. M., Bremer, M., Gießübel, R., García-Marín, M., Kunneriath, D., Muzic, K., Schödel, R., Straubmeier, C., Zamaninasab, M., and Zernickel, A. (2010). The extreme luminosity states of Sagittarius A*. *A&A*, 512:A2.

Salpeter, E. E. (1955). The Luminosity Function and Stellar Evolution. *ApJ*, 121:161.

Salvatier, J., Wiecki, T., and Fonnesbeck, C. (2016). Probabilistic programming in Python using PyMC3.

Schödel, R., Morris, M. R., Muzic, K., Alberdi, A., Meyer, L., Eckart, A., and Gezari, D. Y. (2011). The mean infrared emission of Sagittarius A*. *A&A*, 532:A83.

Schödel, R., Ott, T., Genzel, R., Hofmann, R., Lehnert, M., Eckart, A., Mouawad, N., Alexander, T., Reid, M. J., Lenzen, R., Hartung, M., Lacombe, F., Rouan, D., Gendron, E., Rousset, G., Lagrange, A.-M., Brandner, W., Ageorges, N., Lidman, C., Moorwood, A. F. M., Spyromilio, J., Hubin, N., and Menten, K. M. (2002). A star in a 15.2-year orbit around the supermassive black hole at the centre of the Milky Way. *Nature*, 419:694–696.

Serabyn, E., Lacy, J. H., Townes, C. H., and Bharat, R. (1988). High-Resolution [Ne ii] Observations of the Ionized Filaments in the Galactic Center. *ApJ*, 326:171.

Shahzamanian, B., Eckart, A., Valencia-S., M., Witzel, G., Zamaninasab, M., Sabha, N., García-Marín, M., Karas, V., Karssen, G. D., Borkar, A., Dovuciak, M., Kunneriath, D., Bursa, M., Buchholz, R., Moultaka, J., and Straubmeier, C. (2015). Polarized light from Sgr A* in the near-infrared K_s-band.

Shahzamanian, B., Eckart, A., Valencia-S., M., Witzel, G., Zamaninasab, M., Sabha, N., García-Marín, M., Karas, V., Karssen, G. D., Borkar, A., Dovčiak, M., Kunneriath, D., Bursa, M., Buchholz, R., Moultaka, J., and Straubmeier, C. (2015). Polarized light from Sagittarius A* in the near-infrared K_s-band. *A&A*, 576:A20.

Shimazaki, H. and Shinomoto, S. (2007). A method for selecting the bin size of a time histogram. *Neural computation*, 19(6):1503–1527.

Shimazaki, H. and Shinomoto, S. (2010). Kernel bandwidth optimization in spike rate estimation. *Journal of Computational Neuroscience*, 29(1):171–182.

Shklovskii, I. S. (1960). Secular Variation of the Flux and Intensity of Radio Emission from Discrete Sources. *Soviet Ast.*, 4:243.

Siringo, G., Kreysa, E., Kovács, A., Schuller, F., Weiß, A., Esch, W., Gemünd, H. P., Jethava, N., Lundershausen, G., Colin, A., Güsten, R., Menten, K. M., Beelen, A., Bertoldi, F., Beeman, J. W., and Haller, E. E. (2009). The Large APEX BOlometer CAmera LABOCA. *A&A*, 497(3):945–962.

Sisson, S. A., Fan, Y., and Tanaka, M. M. (2007). Sequential Monte Carlo without likelihoods. *Proceedings of the National Academy of Sciences*, 104(6):1760–1765.

Smith, I. L. and Wardle, M. (2014). An analysis of HCN observations of the Circumnuclear Disc at the Galactic Centre. *MNRAS*, 437(4):3159–3171.

Spergel, D. N., Bean, R., Doré, O., Nolta, M. R., Bennett, C. L., Dunkley, J., Hinshaw, G., Jarosik, N., Komatsu, E., Page, L., Peiris, H. V., Verde, L., Halpern, M., Hill, R. S., Kogut, A., Limon, M., Meyer, S. S., Odegard, N., Tucker, G. S., Weiland, J. L., Wollack, E., and Wright, E. L. (2007). Three-Year Wilkinson Microwave Anisotropy Probe (WMAP) Observations: Implications for Cosmology. *ApJS*, 170(2):377–408.

Subroweit, M., García-Marín, M., Eckart, A., Borkar, A., Valencia-S., M., Witzel, G., Shahzamanian, B., and Straubmeier, C. (2017). Submillimeter and radio variability of Sagittarius A*. A statistical analysis. *A&A*, 601:A80.

Subroweit, M., Mossoux, E., and Eckart, A. (2020). Synchrotron Self-Compton Scattering in Sgr A* Derived from NIR and X-Ray Flare Statistics. *ApJ*, 898(2):138.

Subroweit, M., Panja, S., and Eckart, A. (2021). Ongoing Submm Observations of Sagitarius A* - No Indication for an Increased Flaring Acitivity between 2014 and 2017. In preparation.

Toni, T., Welch, D., Strelkowa, N., Ipsen, A., and Stumpf, M. (2009). Toni T, Welch D, Strelkowa N, Ipsen A, Stumpf MPApproximate Bayesian computation scheme for parameter inference and model selection in dynamical systems. J R Soc Interface 6: 187-202. *Journal of the Royal Society, Interface / the Royal Society*, 6:187–202.

Trap, G., Goldwurm, A., Terrier, R., Dodds-Eden, K., Gillessen, S., Genzel, R., Pantin, E., Lagage, P. O., Ferrando, P., Bélanger, G., Porquet, D., Grosso, N., Yusef-Zadeh, F., and Melia, F. (2010). Soft gamma-ray constraints on a bright flare from the Galactic Center supermassive black hole. *Advances in Space Research*, 45(4):507–520.

Tsuboi, M., Kitamura, Y., Uehara, K., Tsutsumi, T., Miyawaki, R., Miyoshi, M., and Miyazaki, A. (2018). ALMA view of the circumnuclear disk of the Galactic Center: tidally disrupted molecular clouds falling to the Galactic Center. *PASJ*, 70(5):85.

Tsuboi, M., Miyazaki, A., and Tsutsumi, T. (1999). Flare of SGR A* at Short Millimeter Wavelengths. In Falcke, H., Cotera, A., Duschl, W. J., Melia, F., and Rieke, M. J., editors, *The Central Parsecs of the Galaxy*, volume 186 of *Astronomical Society of the Pacific Conference Series*, page 105.

Tully, R. B., Courtois, H., Hoffman, Y., and Pomarède, D. (2014). The Laniakea supercluster of galaxies. *Nature*, 513(7516):71–73.

Unsöld, A. (1947). Die Kurzwellenstrahlung der Milchstraße, der Sonne und des Mondes. *Naturwissenschaften*, 34(7):194–201.

van der Laan, H. (1966). A Model for Variable Extragalactic Radio Sources. *Nature*, 211(5054):1131–1133.

Vernin, J., Muñoz-Tuñón, C., Sarazin, M., Vazquez Ramió, H., Varela, A. M., Trinquet, H., Delgado, J. M., Jiménez Fuensalida, J., Reyes, M., Benhida, A., Benkhaldoun, Z., García Lambas, D., Hach, Y., Lazrek, M., Lombardi, G., Navarrete, J., Recabarren, P., Renzi, V., Sabil, M., and Vrech, R. (2011). European Extremely Large Telescope Site Characterization I: Overview. *PASP*, 123(909):1334.

von Fellenberg, S. D., Gillessen, S., Graciá-Carpio, J., Fritz, T. K., Dexter, J., Bauböck, M., Ponti, G., Gao, F., Habibi, M., Plewa, P. M., Pfuhl, O., Jimenez-Rosales, A., Waisberg, I., Widmann, F., Ott, T., Eisenhauer, F., and Genzel, R. (2018). A Detection of Sgr A* in the Far Infrared. *ApJ*, 862(2):129.

Weisskopf, M. C., Tananbaum, H. D., Van Speybroeck, L. P., and O'Dell, S. L. (2000). Chandra X-ray Observatory (CXO): overview. In Truemper, J. E. and Aschenbach, B., editors, *X-Ray Optics, Instruments, and Missions III*, volume 4012 of *Society of Photo-Optical Instrumentation Engineers (SPIE) Conference Series*, pages 2–16.

Wielebinski, R. (1970). 100 m Radio Telescope in Germany. *Nature*, 228(5271):507–508.

Wilson, W. E., Ferris, R. H., Axtens, P., Brown, A., Davis, E., Hampson, G., Leach, M., Roberts, P., Saunders, S., Koribalski, B. S., Caswell, J. L., Lenc, E., Stevens, J., Voronkov, M. A., Wieringa, M. H., Brooks, K., Edwards, P. G., Ekers, R. D., Emonts, B., Hindson, L., Johnston, S., Maddison, S. T., Mahony, E. K., Malu, S. S., Massardi, M.,

Mao, M. Y., McConnell, D., Norris, R. P., Schnitzeler, D., Subrahmanyan, R., Urquhart, J. S., Thompson, M. A., and Wark, R. M. (2011). The Australia Telescope Compact Array Broad-band Backend: description and first results. *MNRAS*, 416(2):832–856.

Witzel, G., Eckart, A., Bremer, M., Zamaninasab, M., Shahzamanian, B., Valencia-S., M., Schödel, R., Karas, V., Lenzen, R., Marchili, N., Sabha, N., Garcia-Marin, M., Buchholz, R. M., Kunneriath, D., and Straubmeier, C. (2012). Source-intrinsic Near-infrared Properties of Sgr A*: Total Intensity Measurements. *ApJS*, 203:18.

Witzel, G., Ghez, A. M., Morris, M. R., Sitarski, B. N., Boehle, A., Naoz, S., Campbell, R., Becklin, E. E., Canalizo, G., Chappell, S., Do, T., Lu, J. R., Matthews, K., Meyer, L., Stockton, A., Wizinowich, P., and Yelda, S. (2014a). Detection of Galactic Center Source G2 at 3.8 μm during Periapse Passage. *ApJ*, 796:L8.

Witzel, G., Morris, M., Ghez, A., Meyer, L., Becklin, E., Matthews, K., Lu, J. R., Do, T., and Campbell, R. (2014b). Near infrared variability of Sgr A* - spectral index measurements. In Sjouwerman, L. O., Lang, C. C., and Ott, J., editors, *The Galactic Center: Feeding and Feedback in a Normal Galactic Nucleus*, volume 303, pages 274–282.

Wollman, E. R., Geballe, T. R., Lacy, J. H., Townes, C. H., and Rank, D. M. (1977). Ne II 12.8 micron emission from the galactic center. II. *ApJ*, 218:L103–L107.

Wolter, H. (1952). Verallgemeinerte Schwarzschildsche Spiegelsysteme streifender Reflexion als Optiken für Röntgenstrahlen. *Annalen der Physik*, 445(4):286–295.

Wright, M. C. H. and Backer, D. C. (1993). Flux Density of Sagittarius A at lambda = 3 Millimeters. *ApJ*, 417:560.

Young, J. (1940). A statistical investigation of diameter and distribution of lunar craters. *J. Brit. Astron. Assoc*, 50(9):309326.

Yuan, F. and Narayan, R. (2014). Hot Accretion Flows Around Black Holes. *ARA&A*, 52:529–588.

Yuan, F., Quataert, E., and Narayan, R. (2003). Nonthermal Electrons in Radiatively Inefficient Accretion Flow Models of Sagittarius A*. *ApJ*, 598(1):301–312.

Yusef-Zadeh, F., Bushouse, H., Wardle, M., Heinke, C., Roberts, D. A., Dowell, C. D., Brunthaler, A., Reid, M. J., Martin, C. L., Marrone, D. P., Porquet, D., Grosso, N., Dodds-Eden, K., Bower, G. C., Wiesemeyer, H., Miyazaki, A., Pal, S., Gillessen, S., Goldwurm, A., Trap, G., and Maness, H. (2009). Simultaneous Multi-Wavelength Observations of Sgr A* During 2007 April 1-11. *ApJ*, 706(1):348–375.

Zernike, F. (1938). The concept of degree of coherence and its application to optical problems. *Physica*, 5(8):785–795.

Zhao, J., Ekers, R. D., Goss, W. M., Lo, K. Y., and Narayan, R. (1989). Long-Term Variations of the Compact Radio Source SGR a at the Galactic Center. In Morris, M., editor, *The Center of the Galaxy*, volume 136, page 535.

Zhao, J.-H., Blundell, R., Moran, J. M., Downes, D., Schuster, K. F., and Marrone, D. P. (2010). The High-density Ionized Gas in the Central Parsec of the Galaxy. *ApJ*, 723(2):1097–1109.

Zhao, J.-H., Goss, W. M., Lo, K. Y., and Ekers, R. D. (1992). Evidence for Intrinsic Activity of SGR A at the Galactic Center. In Filippenko, A. V., editor, *Relationships Between Active Galactic Nuclei and Starburst Galaxies*, volume 31 of *Astronomical Society of the Pacific Conference Series*, page 295.

Zhou, P., Leung, S.-C., Li, Z., Nomoto, K., Vink, J., and Chen, Y. (2021). Chemical Abundances in Sgr A East: Evidence for a Type Iax Supernova Remnant. *ApJ*, 908(1):31.

Zotti, G., Hoffmann, S. M., Wolf, A., Chéreau, F., and Chéreau, G. (2021). The Simulated Sky: Stellarium for Cultural Astronomy Research. *Journal of Skyscape Archaeology*, 6(2):221–258.

Zylka, R., Mezger, P. G., Ward-Thompson, D., Duschl, W. J., and Lesch, H. (1995). Anatomy of the Sagittarius A complex. IV. SGR A* and the Central Cavity revisited. *A&A*, 297:83–97.

List of Figures

List of Algorithms

List of Acronyms

ACIS Advanced CCD Imaging Spectrometer

ADS Astrophysics Data System

AO Adaptive Optics

ABC Approximate Bayesian Computation

AGN Active Galactic Nucleus

ALMA Atacama Large Millimeter Array

APEX Atacama Pathfinder EXperiment

ASKAP Australian Square Kilometre Array Pathfinder

ATCA Australia Telescope Compact Array

ATNF Australia Telescope National Facility

BB Big Bang

BPL Bounded Power-Law

CCD Charge-Coupled Device

CCDF Complementary Cumulative Distribution Function

CMB Cosmic Background Radiation

CDF Cumulative Distribution Function

CND Circum Nuclear Disk

CNR Circum Nuclear Ring

CONICA Near-Infrared Imager and Spectrograph

CXO Chandra X-ray Observatory

CSRIO Commonwealth Scientific and Industrial Research Organisation

DSO Dusty S-cluster Object

ELT Extremely Large Telescope

EHT Event Horizon Telescope

ERF Electron Rest Frame

ESA European Space Agency

ESO European Southern Observatory

EXOSAT European X-ray Observatory Satellite

FAST Five-hundred-meter Aperture Spherical radio Telescope

FoV Field of View

FIR Far-infrared

GBI Green Bank radio-link Interferometer

GBT Green Bank Telescope

GC Galactic Center

HETG High Energy Transmission Grating

HRC High Resolution Camera

IC Inverse Compton

IF Intermediate Frequency

IR Infrared

JWST James Webb Space Telescope

KDE Kernel Density Estimation

LABOCA LArge BOlometer CAmera

LC Local Supercluster

LETG Low Energy Transmission Grating

LG Local Group

LMC Large Magellanic Cloud

LO Local Oscillator

LTE Local Thermodynamical Equilibrium

M31 Andromeda galaxy

M33 Triangulum galaxy

MIR Mid-infrared

MCMC Markov Chain Monte Carlo

MHD Magnetohydrodynamic

MLE Maximum Likelihood Estimation

MW Milky Way

MPIfR Max Planck Institute for Radio astronomy

NaCo NAOS-CONICA

NAOS Nasmyth Adaptive Optics System

NASA National Aeronautics and Space Administration

NEFD Noise-Equivalent Flux Density

NEP Noise Equivalent Power

NIR Near-Infrared

NRAO National Radio Astronomy Observatory

NSC Nuclear Star Cluster

ORF Observer's Rest Frame

OSO Onsala Space Observatory

PDF Probability Density Function

PMF Probability Mass Function

PWV Precipitable Water Vapour

RIAF Radiative Inefficient Accretion Flow

SED Spectral Energy Distribution

Sgr A* Sagittarius A*

SMBH Supermassive Black Hole

SMC Sequential Monte Carlo, but also Small Magellanic Cloud

SSC Synchrotron Self-Compton

submm submillimeter

TER Total External Reflection

TPL exponentially Truncated Power-Law

UV Ultraviolet

VLBI Very Long Baseline Interferometry

VLT Very Large Telescope

XMM X-ray Multi-Mirror

XVP X-ray Visionary Project

Acknowledgements

First of all, I would like to thank Prof. Dr. Andreas Eckart for giving me the opportunity to write my PhD-thesis under his supervision on such an interesting topic. Many thanks for all the inspiring ideas, not only related to astrophysics, for always having an open door for any questions or issues, for giving me a lot of freedom in my research and in completing my thesis, for sharing his immense knowledge on physical and non-physical subjects and for teaching me, to deal with moments of scientific frustration with a good portion of serenity. It has been a great pleasure to work under his supervision.

I am really thankful to Prof. Dr. Peter Schilke for willingly agreeing to be the second referee for this thesis.

I would also like to thank Prof. Dr. Bülent Tezkan for taking the role to chair the defense committee.

I really appreciate having worked together with Macarena García-Marín, Enmanuelle Mossoux and Shayoni Panja and I thank them for having provided me with the data for my analyses.

My special thanks go to the proofreaders of this thesis for giving valuable comments and fruitful suggestions: Moritz Dannhoff, Lukas Steiniger, Basel Ali, Persis Misquitta and Elaheh Hosseini.

I would like to express my gratitude to all the people of the *aegroup*. I have enjoyed an outstanding team, with friendly and helpful people and a great atmosphere for scientific research.

Selbständigkeitserklärung

„Hiermit versichere ich an Eides statt, dass ich die vorliegende Dissertation selbstständig und ohne die Benutzung anderer als der angegebenen Hilfsmittel und Literatur angefertigt habe. Alle Stellen, die wörtlich oder sinngemäß aus veröffentlichten und nicht veröffentlichten Werken dem Wortlaut oder dem Sinn nach entnommen wurden, sind als solche kenntlich gemacht. Ich versichere an Eides statt, dass diese Dissertation noch keiner anderen Fakultät oder Universität zur Prüfung vorgelegen hat; dass sie - abgesehen von unten angegebenen Teilpublikationen und eingebundenen Artikeln und Manuskripten - noch nicht veröffentlicht worden ist sowie, dass ich eine Veröffentlichung der Dissertation vor Abschluss der Promotion nicht ohne Genehmigung des Promotionsausschusses vornehmen werde. Die Bestimmungen dieser Ordnung sind mir bekannt. Darüber hinaus erkläre ich hiermit, dass ich die Ordnung zur Sicherung guter wissenschaftlicher Praxis und zum Umgang mit wissenschaftlichem Fehlverhalten der Universität zu Köln gelesen und sie bei der Durchführung der Dissertation zugrundeliegenden Arbeiten und der schriftlich verfassten Dissertation beachtet habe und verpflichte mich hiermit, die dort genannten Vorgaben bei allen wissenschaftlichen Tätigkeiten zu beachten und umzusetzen. Ich versichere, dass die eingereichte elektronische Fassung der eingereichten Druckfassung vollständig entspricht."
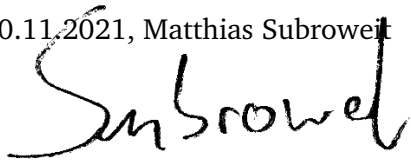
Teilpublikationen/eingebundene Artikel:

- Submillimeter and radio variability of Sagittarius A* - A statistical analysis (Subroweit et al., 2017)

- Synchrotron Self-Compton Scattering in Sgr A* Derived from NIR and X-Ray Flare Statistics (Subroweit et al., 2020)

Eingebundene Manuskripte in Vorbereitung:

- Ongoing Submm Observations of Sagitarius A* - No Indication for an Increased Flaring Acitivity between 2014 and 2017 (Subroweit et al., in prep.)

10.11.2021, Matthias Subroweit

Lebenslauf

Matthias Subroweit

Lebenslauf

Tempelstr. 54
50679 Köln
📱 +49 163 3830940
☎ +49 221 16829755
✉ subroweit@ph1.uni-koeln.de

Persönliche Daten

Geburtstag:	27.01.1977
Geburtsort:	Münster/Deutschland
Staatsangehörigkeit	**Deutsch**.

Ausbildung

Juni 1996	**Abitur**, *Städt. Aldegrevergymnasium, Soest.*
Januar 2002	**Gesellenbrief - Kälteanlagenbauer**, *Heinz Müller & Söhne oHG, Köln.*
März 2011	**Vordiplom - Physik**, *Universität zu Köln.*
September 2015	**Diplom - Physik**, *Universität zu Köln*, I. Physikalisches Institut.
Oktober 2015	**Beginn Promotionsstudium - Physik**, *Universität zu Köln*, I. Physikalisches Institut.

Refereed Publications

[1] Basel Ali u. a. "Kinematic Structure of the Galactic Center S Cluster". In: 896.2, 100 (Juni 2020), S. 100. DOI: 10.3847/1538-4357/ab93ae. arXiv: 2006.11399 [astro-ph.GA].

[2] S. Britzen u. a. "OJ287: deciphering the 'Rosetta stone of blazars". In: 478.3 (Aug. 2018), S. 3199–3219. DOI: 10.1093/mnras/sty1026.

[3] Florian Peißker u. a. "First Observed Interaction of the Circumstellar Envelope of an S-star with the Environment of Sgr A*". In: 909.1, 62 (März 2021), S. 62. DOI: 10.3847/1538-4357/abd9c6. arXiv: 2101.02077 [astro-ph.GA].

[4] M. Subroweit u. a. "Submillimeter and radio variability of Sagittarius A*. A statistical analysis". In: 601, A80 (Mai 2017), A80. DOI: 10.1051/0004-6361/201628530.

[5] Matthias Subroweit, Enmanuelle Mossoux und Andreas Eckart. "Synchrotron Self-Compton Scattering in Sgr A* Derived from NIR and X-Ray Flare Statistics". In: 898.2, 138 (Aug. 2020), S. 138. DOI: 10.3847/1538-4357/ab9947.

[6] G. Witzel u. a. "Rapid Variability of Sgr A* across the Electromagnetic Spectrum". In: 917.2, 73 (Aug. 2021), S. 73. DOI: 10.3847/1538-4357/ac0891. arXiv: 2011.09582 [astro-ph.HE].

[7] Michal Zajaček u. a. "Nature of the Galactic centre NIR-excess sources. I. What can we learn from the continuum observations of the DSO/G2 source?" In: 602, A121 (Juni 2017), A121. DOI: 10.1051/0004-6361/201730532. arXiv: 1704.03699 [astro-ph.GA].

Matthias Subroweit
Köln, 28. Oktober 2021